

Synthesis and Characterization of BaTiO₃-based Magnetoelectric Composites for Energy Storage Applications

Thesis

Submitted to
Delhi Technological University
in partial fulfilment for the requirements for the Degree of

DOCTOR OF PHILOSOPHY

in

APPLIED PHYSICS

by

S. SHANKAR SUBRAMANIAN

(Reg. No. 2K17/Ph.D./AP/09)

Under the Supervision
of

Dr. M. Jayasimhadri

Assistant Professor
Department of Applied Physics
Delhi Technological University
Bawana Road, Delhi-110042

Prof. O. P. Thakur

Professor
Department of Physics
Netaji Subhas University of Technology
Dwarka, Sec-3, New Delhi-110078



**DEPARTMENT OF APPLIED PHYSICS
DELHI TECHNOLOGICAL UNIVERSITY
DELHI-110 042, INDIA**

NOVEMBER-2020

©Delhi Technological University-2020
All rights reserved.



**DELHI TECHNOLOGICAL
UNIVERSITY**
Formerly Delhi College of Engineering
(Under Delhi Act 6 of 2009, Govt. of NCT of Delhi)
Shahbad Daulatpur, Bawana Road, Delhi-110042

CERTIFICATE

This is to certify that the thesis entitled "*Synthesis and Characterization of BaTiO₃-based Magnetoelectric Composites for Energy Storage Applications*" submitted to the Delhi Technological University, Delhi for the award of degree of Doctor of Philosophy is based on the original research work carried out by me under the supervision of Dr. M. Jayasimhadri, Department of Applied Physics, Delhi Technological University, Delhi and Prof. O. P. Thakur, Department of Physics, Netaji Subhas University of Technology, New Delhi. It is further certified that the work embodied in this thesis has neither been partially nor fully submitted to any other university or institution for the award of any degree or diploma.

S. Shankar Subramanian

Research Scholar
(Reg. No. 2K17/Ph.D/AP/09)

This is to certify that the above statement made by the candidate is correct to the best of our knowledge.

Dr. M. Jayasimhadri
Supervisor
Department of Applied Physics
Delhi Technological University,
Delhi- 110 042

Prof. O. P. Thakur
Co-Supervisor
Department of Physics
Netaji Subhas University of
Technology, New Delhi

Prof. Rinku Sharma
Head, Department of Applied Physics
Delhi Technological University,
Delhi-110 042

Dedicated to
my beloved family

ACKNOWLEDGEMENTS

*Thanks giving is a delightful job when sincerely expressed in words. It gives me great pleasure in expressing my gratitude to all who have supported me and made their contributions in making this thesis possible. First and foremost, I must acknowledge and thank the **Almighty**, for his blessing, protection and guiding me throughout this period.*

*At the outset, I would like to my profound sense of gratitude, indebtedness and reverence to my supervisor, **Dr. M. Jayasimhadri**, Department of Applied Physics, Delhi Technological University, Delhi, and my co-supervisor, **Prof. O. P. Thakur**, Department of Physics, Netaji Subhas University of Technology, New Delhi, who nurtured my research capabilities for a successful scientific career. It has been an honour to work under excellent, enthusiastic and distinguished supervisors. Their unrelenting encouragement, constant help, meticulous supervision and constructive criticism throughout the course of my study for carving another milestone in my academic journey. Their immense knowledge of the subject, analytic gaze, farsightedness and perseverance were a constant source of inspiration during the course of this thesis work.*

*I feel privileged to have worked under such a great supervision. I further stand ovated to **Prof. Rinku Sharma**, Head, Department of Applied Physics, DTU, for her valuable help and suggestions. My heartfelt recognitions for **Prof. S.C. Sharma**, DRC Chairman, former Head Department of Applied Physics, DTU, my SRC & DRC committee members for their enduring support and appropriate propositions. I express my sincere gratitude especially to **Prof. K. Srinivas**, University of Delhi, **Prof. G. Vijaya Prakash**, Indian Institute of Technology (IIT) Delhi, and **Prof. A. S. Rao**, DTU for their timely advice and support as SRC members.*

*I am very thankful to **Dr. Gyantosh Kr. Jha**, Principal, ARSD College, University of Delhi for providing me sufficient time for my research work.*

*It is my pleasure to express my sincere thanks to all the **faculty** members of Department of Applied Physics for their continuous encouragement and help during my research work. am also grateful **technical and non-technical staff** for their timely support and cooperation whenever required.*

*I express my sincere gratitude to our scientific collaborators; **Dr. Sukhvir Singh***

(NPL, New Delhi), **Dr. Avneesh Anshul** (AMPRI, Bhopal), **Prof. Anup Kumar Ghosh** (Banaras Hindu University), **Dr. Vinita Tuli** (ARSD College, University of Delhi) and **Dr. Manish Kumar** (ARSD College, University of Delhi) for their help, co-operation and fruitful discussions.

I sincerely thank my dear former and present labmates whose support helped in accomplishing my work. It is my pleasure to thank my seniors **Dr. Amit K. Vishwakarma**, **Dr. Kaushal Jha**, **Dr. Sumandeep**, and present labmates **Mr. Mukesh K. Sahu**, **Ms. Harpreet kaur**, **Ms. Deepali** for their support. I would also like to thank all the other research scholars of Department of Applied Physics, Delhi Technological University, Delhi for their help and advice. I wish to acknowledge the enjoyable company and suitable help rendered by my dear friends, **Mr. Prateek Sharma**, **Ms. Ritika Khatrri**, **Mr. Mohit Tyagi** and **Mr. Vijay**, for their help and support during this tenure. I am especially thankful to young friends from my lab **Mr. Indrajeet Maurya**, **Ms. Srishti Mittal**, **Mr. Vaibhav Joshi**, **Mr. Gaurav Gupta**, **Mr. Aditya Sharma**, **Mr. Amit** and **Mr. Mukund Jha** for their valuable suggestions and support during my research work. I thank my colleagues **Dr. Nutan Mishra**, **Dr. Ramswaroop**, **Mr. Lalit Kumar**, **Mr. Pawan Singh**, **Dr. Abid Hussain**, **Dr. Rita Singh**, **Dr. Arvind Kumar**, **Dr. Anjani Kumar Singh**, **Dr. Avanish Pratap Singh**, **Dr. Raghvendra Pandey**, **Mohd. Sadiq** and all other faculty members of ARSD College, who were always available with their all supports and encouragement whenever I needed their presence.

Finally, I thank my family for their support and motivation, every moment of my research period. With heartfelt gratitude and love, I express my gratefulness to my father **Mr. K. S. Nathan**, mother **Mrs. Vasantha Nathan** for their continual love and encouragement over the entire course of my life. I am thankful to my father-in-law **Late S. Rama Subramanian** and mother-in-law **Mrs. R. Vijaya Durga** for their valuable suggestions, care and gentle love. I am thankful to my mamaji **Mr. Prashant B Halyal** for continuous motivation. I thankful to my sweet wife **Aishwarya** for her endless support and my loving son **Akshit** for continuous encouragement.

I am thankful to my siblings **R. Meenakshi** and **S. Krishnamurthy** and their families for their valuable support. I express my thanks to chachiji **Mrs. B Kalpana** and chachaji **Mr. K. Balasubramanian** and their family for showing love and encouragement even in hard times. I am thankful to my extended maternal and paternal family for helping me maintain a positive attitude throughout my studies. I

always thankful to all my beloved friends across the globe for sharing my happiness and sorrow.

*I extend my gratitude to **Delhi Technological University** and staff in Administration, Accounts, Store & Purchase, Library and Computer Centre for their help and services.*

I thank one and all for helping me accomplish the successful realization of the thesis.

Thank you all!!!

S. Shankar Subramanian

LIST OF PUBLICATIONS

(Included in the thesis)

1. **S. Shankar**, M. Kumar, V. Tuli, O. P. Thakur and M. Jayasimhadri, “Energy storage and magnetoelectric coupling in ferroelectric–ferrite composites” **Journal of Material Science: Materials in Electronics** 29 (2018) 18352–18357. (*Impact Factor: 2.22*)
2. **S. Shankar**, O. P. Thakur and M. Jayasimhadri, “Conductivity behavior and impedance studies in $\text{BaTiO}_3\text{--CoFe}_2\text{O}_4$ magnetoelectric composites,” **Materials Chemistry and Physics** 234 (2019) 110–121. (*Impact Factor: 3.408*)
3. **S. Shankar**, M. Kumar, A. K. Ghosh, O. P. Thakur and M. Jayasimhadri, “Anomalous ferroelectricity and strong magnetoelectric coupling in CoFe_2O_4 -ferroelectric composites,” **Journal of Alloys and Compounds** 779 (2019) 918–925. (*Impact Factor: 4.65*)
4. **S. Shankar**, O. P. Thakur and M. Jayasimhadri, “Impedance Spectroscopy and Conduction Behavior in $\text{CoFe}_2\text{O}_4\text{--BaTiO}_3$ Composites,” **Journal of Electronic Materials** 49 (2020) 472–484. (*Impact Factor: 1.774*)
5. **S. Shankar**, O.P. Thakur and M. Jayasimhadri, “Structural, multiferroic, and magnetoelectric properties of $(1-x)\text{Bi}_{0.85}\text{La}_{0.15}\text{FeO}_3\text{--}x\text{BaTiO}_3$ composite ceramics,” **Journal of Material Science: Materials in Electronics** 31 (2020) 12226–12237. (*Impact Factor: 2.22*)
6. **S. Shankar**, O. P. Thakur and M. Jayasimhadri, “Magnetodielectric effect, impedance and magnetoelectric coupling in multiferroics $(1-x)\text{Co}_{0.5}\text{Ni}_{0.5}\text{Fe}_2\text{O}_4\text{--}x\text{BaTiO}_3$ bulk composites ($x=0, 0.10, 0.20$)”, Communicated to **Journal of Electroceramics**. (*Impact Factor: 2.58*)
7. **S. Shankar**, O. P. Thakur and M. Jayasimhadri, “Discursive investigations on structural, dielectric and multiferroic properties of $(\text{NdMnO}_3)_{1-x}\text{--}(\text{BaTiO}_3)_x$ composites”, Communicated to **Journal of Alloys and Compounds**. (*Impact Factor: 4.65*)

LIST OF PUBLICATIONS

(Other than thesis work)

1. **S. Shankar**, I. Maurya, Abhishek Raj, O. P. Thakur and M. Jayasimhadri, “Dielectric and tunable ferroelectric properties in $\text{BiFeO}_3 - \text{BiCoO}_3 - \text{BaTiO}_3$ ternary compound,” **Applied Physics A** 126 (2020) 686. (**Impact Factor: 1.81**)

ABSTRACT

The upsurge in energy usage in the field of electronics and communication has increased dependency on storage of energy from renewable as well as nonrenewable sources. Consequently, the major need of the world is to prepare efficient materials capable of storing and providing environment friendly sustainable and clean energy. Different research groups have put strenuous efforts for the preparation of advanced electronic materials as cheaper and alternative for energy storage elements in which batteries have up surged but the main focus is on the fabrication of dielectric materials with remarkable charging and discharging capacities and thermal stability. In context of energy storage devices, ceramics are found to exhibit outstanding electrical properties, prominent stability, and high rigidity under severe environmental conditions. The electrical energy storage application requires that these materials exhibit strong and large spontaneous polarization (P_s) as well as low remnant polarization. The dielectrics and ferroelectrics exhibit strong energy storage property and are subsequently desired in modern electrics and pulsed capacitors for power electronic system. Dielectric materials display excellent power density and strong discharge capability. In this context, oxide-based systems have inspired to show good results in these applications. In recent years, various types of lead-free ceramic materials based on titanate are extensively investigated because of their important applications in energy storage devices.

The probing of multifunctional materials with energy storage property is essential for technological advancements. Among these

materials, there exist unique magnetoelectric (ME) materials, which display controlling attribute of manipulation of ferroelectric ordering by applied magnetic field or ferromagnetic ordering by applied electric field. The first artificial ME material was an eutectic composite of BaTiO_3 and CoFe_2O_4 , which was formed by mixing the ferroelectric and ferromagnetic constituents. The implemented magnetic field and the voltage generated do not vary linearly as in the case of single-phased compounds due to the complexity of ME coupling amongst these phases. The research on ME coupling of composite materials has been thoroughly investigated.

An enormous effort has been focused on materials with large ME effect in the field of physics and material science for building new types of multistate memory devices. There are two classes of ME materials: Single phase magnetoelectrics and two-phase magnetoelectrics. Single phase ME materials show the coupling in a single phase material where the coupling arises out of two or more ferroic orders. Further, two phase magnetoelectrics or composite ME exhibit large magnitudes of the ME voltage and are therefore preferred over single phase magnetoelectrics. Usually, a ME composite consists of ferroelectric and ferromagnetic for piezoelectricity and magnetostriction to exhibit multiferroism. The composite ME materials exhibit tensorial product property as a consequence of mutually connected electric and magnetic phases resulting in indirect mechanical strain transfer at the interface of two phases and enhanced ME coupling.

Motivated by the above-mentioned facts, different magnetic material based - BaTiO_3 composites have been synthesized by solid state reaction

route by varying the composition to explore the magnetoelectric properties comprehensively. Dielectric, ferroelectric and energy storage properties have also been discussed in detail. Based on the extensive characterization and measured physical properties, the outcome of the research work has been organized into eight chapters and the chapter wise summary of the same is as follows:

Chapter 1 begins with a brief introduction, origin of problem, motivation for the research work and an overview of the current work. This chapter includes origin of magnetoelectricity and multiferroics. Subsequently, the types of magnetoelectric materials and importance of the composite materials have been discussed in detail. The following section describes about the structure of perovskite and spinel materials. The electrical and magnetic properties of materials have been discussed briefly. A short description on importance of BaTiO₃ and ferrimagnetic (CoFe₂O₄ and Co_{0.5}Ni_{0.5}Fe₂O₄), ferromagnetic (Bi_{0.85}La_{0.15}FeO₃) and antiferromagnetic (NdMnO₃) materials have also been discussed in this chapter. Finally, the objectives of the thesis based on the review of the literature have been incorporated.

Chapter 2 describes the synthesis procedure and characterization techniques used in the current thesis. The solid state reaction method has been used to synthesize desired perovskite BaTiO₃, magnetic constituents (CoFe₂O₄, Co_{0.5}Ni_{0.5}Fe₂O₄, Bi_{0.85}La_{0.15}FeO₃ and NdMnO₃) and their composites. The stoichiometry in these composites has been varied to enhance the obtained magnetoelectric coupling and energy storage

properties. This chapter elaborates the utility of many sophisticated experimental techniques such as x-ray diffraction (XRD), scanning electron microscopy (SEM), Fourier transform infrared spectroscopy (FT-IR), Raman spectroscopy, dielectric LCR meter and Impedance analyzer, vibrating sample magnetometer (VSM) and P-E ferroelectric hysteresis loop tracer in order to study the various properties such as structural, morphological, dielectric, magnetic, ferroelectric, magnetoelectric and energy storage properties, respectively.

Chapter 3 presents the comprehensive study on the composites of $\text{BaTiO}_3\text{-CoFe}_2\text{O}_4$ (BT-CFO) for energy storage and magnetoelectric applications. This chapter focuses on the basic ferroelectric BaTiO_3 (BT) and the effect of ferrite composition on magnetoelectric and energy storage properties of BT. The structural and morphological optimization of BT-CFO was systematically studied to obtain bi-phasic ferroelectric-ferrite system. The dielectric studies revealed Maxwell-Wagner polarization and thermal activated non-Debye type relaxation process in BT-CFO composites with 0.95BT - 0.05CFO composite exhibiting low dielectric loss ≈ 0.3 in frequency range of 100 Hz - 1 MHz and promised for industrial application. The maximum value of magneto-dielectric coupling achieved was 1.2 % at 7 kOe for 0.95BT - 0.05CFO composite. The impedance and conduction studies revealed high resistive nature in the composites and dominant polaron tunneling conduction mechanism. The ferroelectric P-E loop measurement confirmed the ferroelectric nature in BT-CFO composites. The maximum energy storage density and efficiency achieved for 0.95BT - 0.05CFO composite were 8.33 mJ/cm^3 and 59.7 % respectively. The

magnetoelectric coupling coefficient (α) was estimated by studying the effect of magnetic field on ferroelectric hysteresis loop measurements. The value of α was the highest for 0.95BT - 0.05CFO composite and was 13.33 mV/cm/Oe. The enhanced dielectric, ferroelectric, magnetoelectric characteristics suggest the scope of BT-CFO composites in energy storage applications. (The results of this chapter have been published in *Journal of Mater Sci: Mater Electron* 29 (2018) 18352–18357 (IF: 2.22) and *Materials Chemistry and Physics* 234 (2019) 110–121 (IF: 3.408)).

Chapter 4 describes the multiferroic and magnetoelectric properties of $\text{CoFe}_2\text{O}_4\text{-BaTiO}_3$ (CFO-BT) for energy storage and magnetoelectric applications. This chapter focuses on basic ferromagnetic CFO and the effect of ferroelectric BT concentration on magnetoelectric and energy storage properties of CFO. The composites of CFO-BT exhibited interplay of magnetism, ferroelectricity and display strong magnetoelectric behavior arising out of charge disordering. The structural analysis from the combination of XRD, Raman, and FT-IR measurements of CFO-BT composites established the co-existence of cubic and tetragonal phases. The dielectric measurements confirmed non-Debye type Maxwell-Wagner polarization and temperature-dependent relaxation in CFO-BT composites with 0.7CFO - 0.3BT composite showing an unexpected low dielectric loss ≈ 0.5 above 1 kHz and exhibited potential for device applications. The magnetic measurements revealed an enormous increase in the coercivity of 0.7CFO - 0.3BT composite, which was identified in terms of movement of ferromagnetic domains arising due to inclusion of trapping centers of BT in CFO. The impedance spectroscopy and conductivity measurements

confirmed high impedance behavior and crossover from barrier hopping to polaron conduction in CFO-BT composites. The addition of BT in CFO initiated the structural modification and resulted in conductivity cross-over with improved conductivity. The ferroelectric properties displayed a low leakage charge density of 0.0031 mC/cm^2 and prevalent asymmetry arising due to spatial disordering of charge distribution. The maximum energy storage density and efficiency achieved for 0.7CFO - 0.3BT composite were 3.009 mJ/cm^3 and 27.3 % respectively. The highest value of α obtained was 22 mV/cm/Oe at a field of 5000 Gauss for 0.9CFO - 0.1BT composite. These results were useful for exploring energy storage devices based on magnetoelectric CFO-BT composites. (The results of this chapter have been published in *Journal of Alloys and Compounds* 779 (2019) 918-925 (IF: 4.65) and *Journal of Electronic Materials* 49 (2020) 472–484 (IF: 1.774)).

Chapter 5 deals with magnetoelectric bulk composites of $\text{Co}_{0.5}\text{Ni}_{0.5}\text{Fe}_2\text{O}_4\text{-BaTiO}_3$ (CNFO-BT). The structural studies of CNFO-BT composites confirmed lattice distortion and enlarged strain owing to increasing BT in CNFO. The dielectric and impedance measurement exhibited conventional Maxwell-Wagner polarization and confirmed the existence of grain dominated non-Debye relaxations phenomena in CNFO-BT composites. The magnetic hysteresis curves revealed strong ferromagnetic behavior in all composites. The maximum energy storage density and efficiency achieved for 0.8CNFO - 0.2BT composite were 4.25 mJ/cm^3 and 31.6 % respectively. The highest value of magnetoelectric coupling obtained was 5 mV/cm/Oe at a field of 4000 Oersted for 0.8CNFO - 0.2BT composite. These results revealed lattice distortion, interfacial

charge polarization and restricted ferromagnetic domain wall rotation arising from substitution of BT in CNFO and indicate that CNFO-BT composites have potential for energy storage applications. (The results of this chapter have been communicated to *Journal of Electroceramics* (IF: 2.58)).

Chapter 6 focused on the comprehensive study of $\text{Bi}_{0.85}\text{La}_{0.15}\text{FeO}_3$ - BaTiO_3 (BLFO-BT) for magnetoelectric and energy storage applications. The structural analysis revealed phase purity in BLFO and a structural transformation from rhombohedral to cubic phase with increasing content of BT confirming the co-existence of composite phase with lattice compression. The dielectric measurements displayed peak broadening in temperature–permittivity plot and confirm relaxor behavior in BLFO-BT composite ceramics. The magnetic measurements confirmed the existence of weak ferromagnetism in BLFO-BT composites and novel superparamagnetism in 0.9BLFO - 0.1BT composite ceramic. The ferroelectric hysteresis P-E loop measurements produced unsaturated oval-shaped loops with high leakage and displayed a lossy dielectric nature. The 0.9BLFO - 0.1BT composite displayed an improved recoverable energy storage density of 16 mJ/cm^3 with an improved efficiency of 60 %. The highest value of magnetoelectric coupling obtained was 16 mV/cm/Oe at a field of 3000 Oersted for 0.9BLFO - 0.1BT composite. The superparamagnetic behavior and magnetic field-dependent energy storage capacity of BLFO-BT composite ceramics made them potential candidate for magnetoelectric devices. (The results of this chapter have been published in *Journal of Mater Sci: Mater Electron* 31 (2020) 12226–12237 (IF: 2.22)).

Chapter 7 is focused on the multiferroic magnetoelectric composites of NdMnO₃-BaTiO₃ (NMO - BT). The structural investigations revealed the evolution and co-existence of orthorhombic structure of NMO and tetragonal structure of BT in NMO-BT composites and confirm lattice stabilization in terms of symmetry. The dielectric measurements revealed step-like decrease in frequency dependent dielectric constant which confirmed improved conduction nature in NMO-BT composites. The addition of BT phase in NMO improved the remnant magnetization and saturated ferroelectric polarization owing from lattice stability establishing multiferroism in NMO-BT system. The impedance and conductivity measurements confirmed non-Debye type thermally activated conduction behavior and hopping assisted mechanism dominating in NMO-BT composites. The 0.8NMO - 0.2BT composite displayed an enhanced energy storage density of 1.544 mJ/cm³ with an improved efficiency of 50.4 %. The highest value of magnetoelectric coupling obtained was 22 mV/cm/Oe at a field of 5000 Oersted for 0.8NMO-0.2BT composite. The enhancement in energy storage efficiency of 0.8NMO-0.2BT composite and improved magnetoelectric coupling validates its potential for energy storage devices. (The results of this chapter have been communicated to *Journal of Alloys and Compounds* (IF: 4.65)).

Chapter 8 includes summary of the research work described in the previous chapters for optimization of efficient lead free ferroelectric BaTiO₃ based magnetoelectric composites for energy storage applications and outlines the future scope of this work.

CONTENTS

Acknowledgements.....	i
List of Publications	v
Abstract.....	vii
Contents.....	xv
List of Tables.....	xix
List of Figures.....	xxi
Chapter 1 Introduction and Overview.....	1
1.1. Introduction.....	2
1.2. Basics of Multiferroics and Magnetoelectricity.....	2
1.3. Magnetoelectric Coupling.....	5
1.3.1. Types of Magnetoelectric Coupling.....	6
1.3.1.1. Single Phase Magnetoelectrics.....	6
1.3.1.2. Two Phase or Bi-phase Magnetoelectrics and Heterostructures.....	7
1.4. Composites Materials.....	8
1.4.1. Types of Composite Materials.....	10
1.5. ABO₃ Perovskites.....	10
1.5.1. Structure of Perovskite.....	11
1.5.2. Classification of Perovskites.....	12
1.5.3. Properties of Perovskites.....	13
1.6. AB₂O₄ Spinel Ferrites.....	13
1.6.1. Structure of Spinel Ferrites.....	13
1.6.2. Properties of Spinel Ferrites.....	15
1.7. Electrical Properties of Materials.....	16
1.7.1. Ferroelectricity.....	16
1.7.2. Dielectrics.....	17
1.7.3. Impedance.....	19
1.8. Magnetic Properties of Materials.....	20
1.8.1. Orderings of Magnetic Materials.....	20
1.9. Materials and Applications.....	24
1.9.1. Materials for Magnetoelectric Composites.....	24
1.9.2. Materials for Energy Storage.....	28
1.10. Objective of the Thesis.....	30
Chapter 2 Experimental: Composite Synthesis and Characterization Techniques.....	33
2.1. Experimental.....	34
2.2. Chemicals Used	34
2.3. Composite Synthesis	35

2.4.	Characterization Tools and Working Principle.....	37
2.4.1.	X-ray Diffraction (XRD).....	37
2.4.2.	Scanning Electron Microscopy (SEM).....	39
2.4.3.	Energy Dispersive Absorption X-ray spectroscopy (EDAX).....	41
2.4.4.	Fourier Transform Infra-red spectroscopy (FT-IR).....	41
2.4.5.	Raman Spectroscopy.....	42
2.4.6.	Vibrating Sample Magnetometer (VSM).....	43
2.4.7.	Ferroelectric Loop Tracer.....	45
2.4.8.	Dielectric Measurements: LCR Meter and Impedance Analyzer...	45
Chapter 3	Effect of CoFe₂O₄ on Structural, Electrical and Magnetoelectric Properties of BaTiO₃-CoFe₂O₄ Composites.....	49
3.1.	Introduction.....	50
3.2.	Sample Preparation.....	51
3.3.	Results and Discussion.....	51
3.3.1.	Structural and Morphological Measurements.....	51
3.3.2.	Dielectric and Magnetodielectric Measurements.....	55
3.3.3.	Impedance and Modulus Measurements.....	57
3.3.4.	Conductivity Measurements.....	63
3.3.5.	Ferroelectric and Magnetoelectric Measurements.....	66
Chapter 4	Influence of BaTiO₃ on Structural, Electrical and Magnetoelectric Characteristics of CoFe₂O₄-BaTiO₃ Composites	71
4.1.	Introduction.....	72
4.2.	Sample Preparation.....	73
4.3.	Results and Discussion.....	74
4.3.1.	Structural and Morphological Measurements.....	74
4.3.2.	Dielectric and Magnetodielectric Measurements.....	76
4.3.3.	Impedance and Modulus Measurements.....	79
4.3.4.	Conductivity Measurements.....	84
4.3.5.	Magnetic Measurements	88
4.3.6.	Ferroelectric and Magnetoelectric Measurements.....	90
Chapter 5	Magnetodielectric Effect, Impedance and Magnetoelectric Coupling in Multiferroic Co_{0.5}Ni_{0.5}Fe₂O₄-BaTiO₃ Bulk Composites	95
5.1.	Introduction.....	96
5.2.	Sample Preparation.....	96
5.3.	Results and Discussion.....	97
5.3.1.	Structural Measurements.....	97

5.3.2.	Dielectric and Magnetodielectric Measurements.....	98
5.3.3.	Impedance Measurements.....	100
5.3.4.	Magnetic Measurements.....	102
5.3.5.	Ferroelectric and Magnetoelectric Measurements.....	103
Chapter 6	Structural, Multiferroic and Magnetoelectric Properties of Bi_{0.85}La_{0.15}FeO₃ BaTiO₃ Composites	105
6.1.	Introduction.....	106
6.2.	Sample Preparation.....	107
6.3.	Results and Discussion.....	107
6.3.1.	Structural and Morphological Measurements.....	107
6.3.2.	Dielectric Measurements.....	112
6.3.3.	Magnetic Measurements	114
6.3.4.	Ferroelectric and Magnetoelectric Measurements.....	117
Chapter 7	Discursive Investigations on Structural, Dielectric and Multiferroic Properties of NdMnO₃ - BaTiO₃ Composites.....	121
7.1.	Introduction.....	122
7.2.	Sample Preparation.....	123
7.3.	Results and Discussion.....	123
7.3.1.	Structural Measurements.....	123
7.3.2.	Dielectric Measurements.....	128
7.3.3.	Impedance Measurements.....	129
7.3.4.	Conductivity Measurements.....	130
7.3.5.	Magnetic Measurements	132
7.3.6.	Ferroelectric and Magnetoelectric Measurements.....	133
Chapter 8	Summary and Scope of Future Work.....	135
8.1.	Summary.....	135
8.2.	Important Findings of Research Work.....	136
8.3.	Future Scope of the Work.....	137
	References.....	139
	Curriculum Vitae	153

LIST OF TABLES

Tables	Table Captions	Page no.
Table 2.1.	List of chemicals used to prepare various magnetoelectric composites to carry out present thesis work.	35
Table 3.1.	Synthesis conditions of BaTiO ₃ , CoFe ₂ O ₄ and BaTiO ₃ - CoFe ₂ O ₄ composites.	51
Table 3.2.	Fitted parameters for Cole–Cole plots of BT-CFO composites.	59
Table 3.3.	Values of activation energy (E _a) in (eV) obtained from fitting of dc conductivity with 1000/T (K ⁻¹).	65
Table 4.1.	Synthesis conditions of BaTiO ₃ , CoFe ₂ O ₄ and CoFe ₂ O ₄ - BaTiO ₃ composites.	73
Table 4.2.	Fitted parameters for Cole–Cole plots of CFO-BT composites.	82
Table 4.3.	Values of activation energy (E _a) in (eV) obtained from fitting of dc conductivity with 1000/T (K ⁻¹)	86
Table 4.4.	Variation of Saturation magnetization (M _s), Remnant magnetization (M _r) and Coercivity (H _c) for CFO, CFO-10 BT and CFO-30 BT composites.	89
Table 5.1.	Synthesis conditions of BaTiO ₃ , Co _{0.5} Ni _{0.5} Fe ₂ O ₄ and Co _{0.5} Ni _{0.5} Fe ₂ O ₄ -BaTiO ₃ composites.	97
Table 5.2.	Fitted parameters for Cole–Cole plots of CNFO-BT composites.	102
Table 6.1.	Synthesis conditions of BaTiO ₃ , Bi _{0.85} La _{0.15} FeO ₃ and Bi _{0.85} La _{0.15} FeO ₃ -BaTiO ₃ composites.	107
Table 6.2.	EDAX table for percentage distribution of atomic weights of elements in BLFO-10BT and BLFO-20BT composites.	110
Table 6.3.	Raman peak positions of BLFO and BLFO-BT composites.	111
Table 7.1.	Synthesis conditions of BaTiO ₃ , NdMnO ₃ and NdMnO ₃ - BaTiO ₃ composites.	123
Table 7.2.	Variation of tolerance factor with BT concentration.	124
Table 7.3.	Fitted parameters for Cole–Cole plots of NMO-BT composites.	130

LIST OF FIGURES

Figures	Figure Captions	Page no.
Figure 1.1.	The four hysteresis loops, each characterizing ferroic orderings and categorized as (a) ferromagnetism, (b) ferroelectricity and (c-d) magnetoelectricity via cross-manipulation	3
Figure 1.2.	A schematic description of multiferroic and magnetoelectric materials based on their origins.	4
Figure 1.3.	The connectivity scheme of (a) (3-0) and (0-3) composite, (b) (2-2) laminate composites and (c) (1-3) multi-layered composites	9
Figure 1.4.	Crystal structure of ABO_3 type perovskite.	11
Figure 1.5.	Detailed classification of ABO_3 perovskite	12
Figure 1.6.	Structure of spinel ferrite	14
Figure 1.7.	Superexchange mechanism in ferrites.	14
Figure 1.8.	Distribution of spins in Fe_3O_4 .	15
Figure 1.9.	Isometric projection of $BaTiO_3$ unit cell.	17
Figure 1.10.	Polarization in $BiFeO_3$.	17
Figure 1.11.	Systematic representation of possible four type of polarization processes.	19
Figure 1.12.	Configurations of (a) paramagnetic (b) ferromagnetic (c) ferrimagnetic (d) antiferromagnetic and (e) superparamagnetic materials.	22
Figure 1.13.	Types of antiferromagnetism	23
Figure 1.14.	Applications of magnetoelectric materials on the basis of the origin of coupling and control mechanism.	28
Figure 1.15.	P-E loop of ferroelectric material.	29
Figure 2.1.	Schematic flow chart for the preparation of ferroelectric / ferrite constituent and composites.	36
Figure 2.2.	Bragg reflection from lattice planes	38
Figure 2.3.	X-ray diffractometer setup.	38
Figure 2.4.	JEOL Scanning Electron Microscopy.	40
Figure 2.5.	Schematic diagram of Scanning Electron Microscopy.	41
Figure 2.6.	Perkin Elmer FT-IR Setup.	42
Figure 2.7.	Renishaw Raman Spectrometer	43
Figure 2.8.	Vibrating Sample Magnetometer (VSM) setup.	44

Figure 2.9.	P-E loop tracer system with Sawyer-Tower circuit.	45
Figure 2.10.	Wayne Kerr LCR Meter setup with Wheatstone bridge circuit.	46
Figure 2.11.	Novo Control Broadband Dielectric / Impedance Spectrometer setup	46
Figure 3.1.	XRD patterns of BaTiO ₃ and BaTiO ₃ - CoFe ₂ O ₄ composites.	52
Figure 3.2.	SEM micrographs of (a) BT and (b) BT-CFO composites.	52
Figure 3.3.	EDAX patterns of BT and BT-CFO composites.	53
Figure 3.4	FT-IR spectra of BT and BT-CFO composites.	53
Figure 3.5.	Raman spectra of BT and BT-CFO composites.	54
Figure 3.6.	Frequency dependence of real part of dielectric constant (ϵ') for (a) BT, (b) BT-1CFO and (c) BT-5CFO composites.	55
Figure 3.7.	Frequency dependence of dielectric loss ($\tan \delta$) for (a) BT, (b) BT-1CFO and (c) BT-5CFO composites.	56
Figure 3.8.	Percentage change in dielectric constant of BT-1CFO and BT-5CFO composites as a function of magnetic field at 10 kHz.	57
Figure 3.9.	Nyquist plot for BT-CFO composites measured at different temperatures.	58
Figure 3.10.	Combined Nyquist plots of BT-CFO composites at different temperatures and their equivalent circuit measured.	58
Figure 3.11.	Frequency dependence of real part of impedance (Z') for BT and BT-CFO composites.	66
Figure 3.12.	Frequency dependence of complex part of impedance (Z'') for BT, BT-1CFO and BT-5CFO composites.	61
Figure 3.13.	Variation of M' with respect to frequency of BT-CFO composites.	62
Figure 3.14.	Variation of M'' with respect to frequency of BT-CFO composites.	62
Figure 3.15.	Plot of conductivity (σ) as function of frequency measured at different temperature for BT, BT-1CFO and BT-5CFO composites respectively.	63
Figure 3.16.	Plot of dc conductivity as a function of temperature ($10^3/T$) for BT, BT-1CFO and BT-5CFO composites respectively.	64
Figure 3.17.	Variation of exponent n as a function of temperature for BT, BT-1CFO and BT-5CFO composites	65
Figure 3.18.	P-E hysteresis loops of BaTiO ₃ and BaTiO ₃ – CoFe ₂ O ₄ composites.	67
Figure 3.19.	Variation of P-E hysteresis loop with magnetic field (upto 4200Oe) of BT-5CFO composite.	68
Figure 3.20.	Plot of maximum polarization with magnetic field and straight line fit of BT-5CFO composite.	68

Figure 4.1.	XRD patterns of CoFe_2O_4 and $\text{CoFe}_2\text{O}_4 - \text{BaTiO}_3$ composites.	74
Figure 4.2.	SEM micrographs of CFO and CFO-BT composites.	75
Figure 4.3.	Raman spectra of CFO and CFO-BT composite.	76
Figure 4.4.	FT-IR spectra of CFO and CFO-BT composites.	76
Figure 4.5.	Frequency dependence of real part of dielectric constant (ϵ') for (a) CFO, (b) CFO-10BT and (c) CFO-30BT composites	78
Figure 4.6.	Frequency dependence of dielectric loss ($\tan \delta$) for (a) CFO, (b) CFO-10BT and (c) CFO-30BT composites..	79
Figure 4.7.	Nyquist plot of CFO and CFO-BT composites measured at different temperatures.	81
Figure 4.8.	Combined Nyquist plots of (a-c) CFO, (d-f) CFO-10BT and (g-i) CFO-30BT composites at different temperatures and their equivalent circuit measured.	82
Figure 4.9.	Variation of Z' and Z'' with respect to the frequency of CFO and CFO-BT composites	83
Figure 4.10.	Variation of M' and M'' with respect to the frequency of CFO and CFO-BT composites	84
Figure 4.11.	Plot of conductivity (σ) as function of frequency measured at different temperature for CFO and CFO-BT composites respectively.	85
Figure 4.12.	Plot of dc conductivity as a function of temperature ($103/T$) for CFO and CFO-BT composites.	86
Figure 4.13.	Variation of exponent n as a function of temperature for CFO and CFO-BT composites.	87
Figure 4.14.	Room temperature magnetization curves (M vs H) for CFO, CFO-10 BT and CFO-30 BT composites. Inset shows the enlarged view of CFO, CFO-10 BT and CFO-30BT.	88
Figure 4.15.	Variation of dM/dH with respect to applied magnetic field for CFO and CFO-10BT for the confirmation of Coercivity. Inset shows the enlarged view of CFO-30BT composite	89
Figure 4.16.	P-E hysteresis loops of (a) CFO and CFO-10 BT and (c) CFO-30BT composites at frequency of 50 Hz.	91
Figure 4.17.	Plot of maximum polarization with magnetic field and best fit for CFO-BT composites.	93
Figure 4.18.	Variation of magnetoelectric coefficient (α) with respect to magnetic field for the CFO and CFO-BT composites.	94

Figure 5.1.	XRD patterns of CNFO and CNFO-BT composites.	97
Figure 5.2.	Variation of lattice parameter and lattice strain in CNFO-BT composites.	98
Figure 5.3.	Frequency dependence of real part of dielectric constant (ϵ') for CNFO and CNFO-BT composites at different temperatures.	99
Figure 5.4.	Percentage change in dielectric constant for CNFO and CNFO-BT composites as a function of magnetic field at 10 kHz.	100
Figure 5.5.	Nyquist plot of CNFO-BT composites measured at different temperatures along with their equivalent circuit measured.	101
Figure 5.6.	Room temperature magnetization curves (M vs H) for CNFO and CNFO-BT composites. Inset shows the enlarged view of CNFO and CNFO-BT composites.	103
Figure 5.7.	P-E hysteresis loops of CNFO and CNFO-BT composites.	103
Figure 5.8.	Variation of maximum polarization (P _{max}) with magnetic field for CNFO and CNFO-BT composites.	104
Figure 6.1.	XRD patterns of BLFO and BLFO-BT ceramics.	108
Figure 6.2.	Enlarged view of XRD of BLFO-BT ceramics in the $2\theta \approx 31.6$ - 32.5° .	108
Figure 6.3.	SEM micrograph and EDAX spectra of (a-b) BLFO-10BT and (c-d) BLFO-20BT, respectively.	109
Figure 6.4.	Raman spectra of BLFO and BLFO-BT composites	111
Figure 6.5.	Plot of dielectric constant with temperature for BLFO-BT composites.	113
Figure 6.6.	Variation of dielectric loss ($\tan \delta$) with frequency for BLFO-BT composites.	113
Figure 6.7.	Frequency dependence of dielectric permittivity at different temperature for BLFO-10BT composite.	114
Figure 6.8.	M-H curves of (a) BLFO, BLFO-20BT and BLFO-30BT composites. M-H curve of BLFO-BT composite ceramic fitted with Langevin function. Inset show the variation of dM/dH with respect to magnetic field of BLFO-10BT composite.	115
Figure 6.9.	Arrott plots of BLFO-BT ceramics.	116
Figure 6.10.	P-E hysteresis curves for BLFO-BT composite ceramics.	117
Figure 6.11.	Variation of useful recoverable energy density with frequency and magnetic field for BLFO- 10BT composite.	118
Figure 6.12.	Variation of maximum polarization and magnetoelectric interaction coefficient with magnetic field.	119

Figure 7.1.	XRD patterns of NMO, BT and NMO-BT composites	124
Figure 7.2.	(a) W-H plots of BT, NMO and NMO-BT composites (b) Variation of crystallite size of NMO and BT in NMO-BT composites.	125
Figure 7.3.	FT-IR spectra of NMO, BTO and NMO-BT composites	127
Figure 7.4.	Raman spectra of NMO-BT composites	127
Figure 7.5.	Frequency dependence of dielectric constant of NMO and NMO-BT composites	128
Figure 7.6.	Cole-Cole plots, equivalent spectra and fitted spectra of NMO and NMO-BT composites.	130
Figure 7.7.	Variation of $\log \sigma$ versus $\log \omega$ for NMO-20BT composite.	131
Figure 7.8.	Plot of DC conductivity versus temperature for NMO-20BT composite.	131
Figure 7.9.	Variation of power exponent n with temperature for NMO and NMO-BT composites.	132
Figure 7.10.	M-H hysteresis loops of NMO-BT composites. Inset shows enlarged M-H hysteresis loops of NMO and NMO-BT composites in the magnetic field range of ± 400 Oe.	133
Figure 7.11.	P-E hysteresis loops of NMO and NMO-20BT composite.	134
Figure 7.12.	Variation of maximum polarization versus magnetic field for NMO and NMO-BT composites	134
Figure 8.1.	Comparison of different composites based on energy storage parameter and magnetoelectric coupling.	136

Chapter - 1

Introduction and Overview

In the past decade, magnetic field driven electric polarization has been believed as the potential ability in composite materials to be used in energy storage systems. Magnetoelectric materials exhibit coupling of electric and magnetic orderings. The magnetoelectric composites additionally offer the product property, which significantly improves the coupling. This chapter is focused on the fundamentals of magnetoelectric materials, magnetoelectric coupling mechanism, composites and their properties. This chapter also provides a concise account of perovskite and spinel structures. Further, this chapter contains significance of BaTiO_3 - based magnetoelectric composites for the energy storage applications along with objectives of the present work.

1.1. Introduction

A vast increase in energy consumption for electronic and communication technology has the augmented need for storing energy of renewable and nonrenewable sources. Accordingly, the necessity for development of functional devices for storing and delivering sustainable and clean energy has grown tremendously [1,2]. Researchers around the globe consistently endeavored to develop advanced electronic systems as a substitute for energy storage component. Amongst such energy storage devices, the focus on lead based batteries have grown steadfastly. However, larger attention is given to prepare lead-free novel materials with outstanding charging and discharging capacities and thermal stability [2–8]. In this perspective, ceramic materials are preferred for their known excellent electrical properties, outstanding stability, and high rigidity under severe environmental conditions [1]. The requirements for electrical energy storage devices are robust and large spontaneous polarization (P_s) along with low remnant polarization [9]. Dielectric and ferroelectric materials strongly fulfill the requirements of energy storage devices and are, therefore, preferred in modern electronics and pulsed capacitors for power electronic systems [10,11]. In addition to dielectrics and ferroelectrics, few advanced materials such as oxides display excellent dielectric properties, power density and strong discharge capability along with magnetic or elastic or optical properties [3,4,19–21,5,12–18]. Among these oxides, lead-free titanate based systems are extensively investigated because of their important applications in the energy storage devices [22,23].

1.2. Basics of Multiferroics and Magnetoelectricity

The exploration of new materials and preparation of advanced materials including composites has become necessary from futuristic perspective of energy storage, sensing and other field of electronics. Advanced materials are advantageous over primary materials because of the improved properties like high dielectric, ferroelectric, magnetic, optical, thermal stability and mechanical strength. In addition, they offer novelty of sensing the variations in the ambient environmental conditions. These materials display versatility and can be used for next generation sensing as well as data storage and energy storage devices. Among these advanced materials, there exists unique magnetoelectrics which feature the manipulation of ferroelectric ordering

by applied magnetic field or ferromagnetic ordering by applied electric field as depicted in Fig. 1.1 [24].

The interaction between electricity and magnetism has strong and relevant significance for applications in devices with attractive tunability over the century. The coupling between electric and magnetic fields have existed from Oersted experiment for discovering the magnetic field by deflecting needle in the proximity of an electric field till the integration of unified electromagnetic theory by Faraday and Maxwell. The Maxwell's equations stand matched with the definition of magnetoelectric materials that inter-twin the electric and magnetic orderings. Magnetism appears in materials which have partially filled inner shells, whereas, electric order parameter originates from the atomic shifts which break inversion symmetry in a crystal. Thus, the existence of magnetoelectricity in single phase materials is critical as magnetic moment and electric dipole moment are inharmonious to each other. This inharmonicity is because the electric charges relate to the electric effects, while spin of electron decides the magnetism.

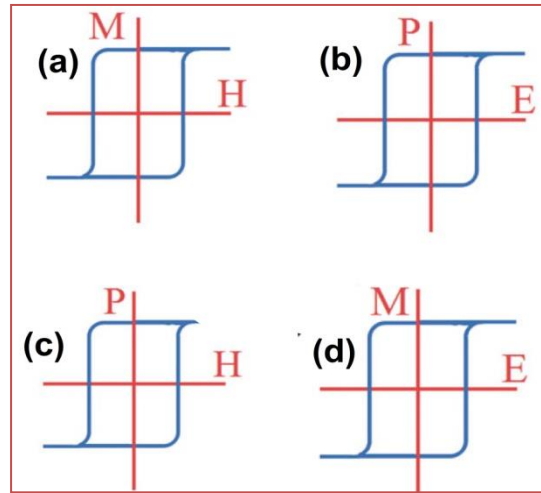


Figure 1.1. The four hysteresis loops, each characterizing ferroic orderings and categorized as (a) ferromagnetism, (b) ferroelectricity and (c-d) magnetoelectricity via cross-manipulation.

Magnetoelectrics have some relevance to the term multiferroic, which means the co-existence of two or more than two of ferroic orderings: ferroelectric, ferromagnetic and ferroelastic as shown in Fig. 1.2 [12–14]. Electrically polarizable materials consist of paraelectrics, ferroelectrics and antiferroelectrics whereas magnetically polarizable materials include paramagnets, ferromagnets and antiferromagnets. The purple and orange ellipses represent electrically polarizable and

magnetically polarizable materials, respectively. The green and orange circles represent ferroelectric and ferromagnetic materials respectively. The intersections of the two ferroelectric and ferromagnetic circles represent multiferroic materials and the smallest yellow circle represents magnetoelectric (ME) materials. These days, the term ferroic includes ferrotoroidicity along with the existing properties [25]. In addition to this, the definition of multiferroics has also been extended to include antiferromagnetic orderings. These multiferroics are rare due to the different chemistry of ferroelectricity and ferromagnetism [12]. ME materials, exhibit ME coupling and encompass

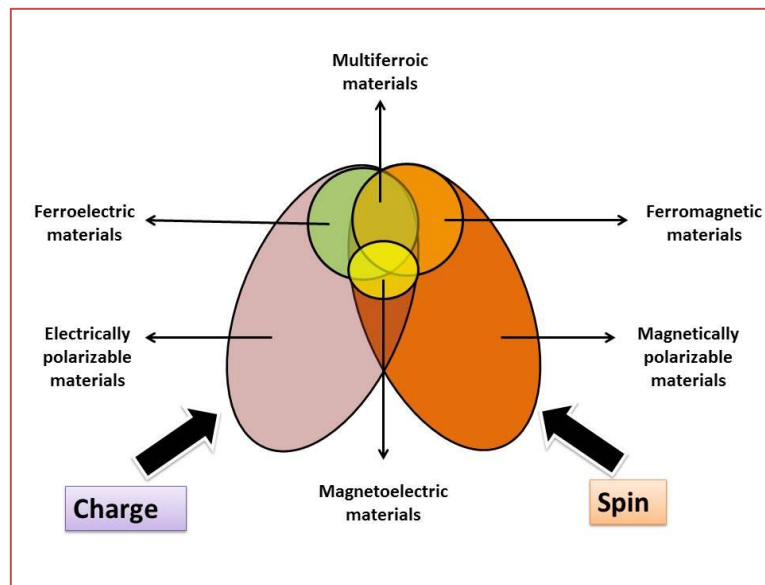


Figure 1.2. A schematic description of multiferroic and magnetoelectric materials based on their origins.

plethora of materials other than ferroic materials. So, one can say that ME materials are a broad class of materials, which include [24]:

- (i) Magnetically polarizable and electrically polarizable materials,
- (ii) Heterostructures of ferromagnets and ferroelectrics and
- (iii) Heterostructures of non-multiferroics materials.

Initially the multiferroics materials were made as single phase and were investigated for ME properties. The small magnetization generated low ME coupling in single phase systems, consequently, the discovery of unique multiferroics was established with broken inversion symmetry and a finite polarization [26–28]. The current development towards for miniaturizing devices has stimulated uniting magnetic and electrical orderings in the composite materials. The ME coupling in these systems

would lay the basis for novel devices capable of exhibiting electric field controlled magnetic memory data storage.

1.3. Magnetoelectric Coupling

B.D.H. Tellegen established the methodology of producing composite medium that demonstrated ME coupling [29]. The process was to allow mixing of macroscopic particles which possess electric as well as magnetic orderings and was otherwise not possible to be realized because of inharmonicity [30]. The first artificial ME material was an eutectic composite of BaTiO₃ and CoFe₂O₄ which was synthesized by mixing the electric and magnetic constituents [12–16]. The implemented magnetic field and the voltage generated in this composite did not vary linearly like in case of single-phased compounds due to complexity of the magnetoelectric coupling amongst constituent phases [14–16,31,32]. Following this idea of composite, the research of ME coupling of different composite materials (like BaTiO₃-CoFe₂O₄, metal-polymer matrix, LSMO-PZT and LSMO-BT) and laminates have been thoroughly investigated [33,34,43–50,35–42].

ME coupling in composites can be accomplished by union of electric and magnetic orderings, and also via strain. The ME coupling achieved through strain-mediation is found to be more prominent in composites, where ferroelectric and magnetic ordering appears as individually isolated phases and exhibit strong relation between them. The ME coupling in single phase materials and composites is quantified from Landau's Free energy expression in terms of electric fields as well as magnetic fields in the form [14]:

$$FE_L = F_0 - P_x E_y - M_x H_y - \frac{1}{2}(\epsilon_0 \epsilon_{xy} E_x E_y) - \frac{1}{2}(\mu_0 \mu_{xy} H_x H_y) - \alpha_{xy} E_x H_y - \frac{1}{2}(\beta_{xyz} E_x H_y H_z) - \frac{1}{2}(\gamma_{xyz} H_x E_y E_z) - \dots \quad (1.1)$$

The first order derivative provides ferroelectric polarization and magnetization as:

$$\text{Polarization } (P_x(\mathbf{E}, \mathbf{H})) = -(\partial F / \partial E_x) \quad (1.2)$$

$$= P_{os} + \epsilon_0 \epsilon_{xy} E_y + \alpha_{xy} H_y + \frac{1}{2}(\beta_{xyz} H_y H_z) + \gamma_{xyz} H_x E_y - \dots \quad (1.3)$$

$$\text{Magnetization } (M_x(\mathbf{E}, \mathbf{H})) = -(\partial F / \partial H_x) \quad (1.4)$$

$$= M_{os} + \mu_0 \mu_{xy} H_y + \alpha_{xy} E_y + \beta_{xyz} E_x H_y + \frac{1}{2}(\gamma_{xyz} E_y E_z) - \dots \quad (1.5)$$

where variables E, H, P_{os}, M_{os}, ϵ , μ , α , β and γ represent usual notations. For the presently studied materials, we assume that only linear ME interaction persists and thereby ignore higher orders and express coupling coefficient as $\alpha_{ME} = E/H$ or $\alpha_{ME} =$

$\delta E/\delta H$, where α_{ME} stands for linear ME coupling coefficient (α) = $\epsilon_0 \epsilon_r \alpha_E$. In case of binary systems, the enormity of interaction amongst the coupling components is connectivity and orientation dependent, and is computed by studying the behavior with changing electric as well as magnetic field [36]. The benefit of using two component system aims to strengthen the magnitude of coupling through interfacial strain. The physical electrostriction of ferroelectric phase mediates a strain in the magnetic component which in turn induces orientation dependent magnetic anisotropy. The enrichment in ME interaction originates from the multiplicative product of magnetostriction and electrostriction in binary systems.

1.3.1. Types of Magnetoelectric Coupling

On the basis of quantum mechanical approach, magnetoelectric materials are classified in two groups namely:

- (i) Single phase magnetoelectrics
- (ii) Two phase or bi-phase magnetoelectrics

1.3.1.1. *Single Phase Magnetoelectrics*

These materials show the coupling in a single-phase system where the coupling arises out of two or more ferroic orders. The origin of such type of coupling can be categorized as [24] :

- (a) Spin - orbit coupling
- (b) Spin - lattice coupling
- (c) Multiferroics

- (a) *Spin orbit coupling*: This kind of coupling is described on the basis of thermodynamics for explaining weak ferromagnetism. The coupling is postulated on the basis of an asymmetric exchange interaction. For e.g. in case of perovskite ABO_3 like $BiFeO_3$, distortion occurs due to the disparity between A and B ions, which tilt the O_6 octahedra. The exchange interaction is characterized by Dzyaloshinskii-Moriya interaction given by

$$H = \vec{D} \cdot (\mathbf{S}_i \times \mathbf{S}_j) \quad (1.6)$$

where H is applied magnetic field, \vec{D} is Dzyaloshinskii-Moriya (DM) vector and \mathbf{S}_i and \mathbf{S}_j are spin vectors. The cross product of spins represents the effective magnetic spin arising from bending of B-O-B bond [24].

- (b) *Spin or lattice coupling*: This type of interaction occurs via symmetry exchange mechanism which arises from shrinking or elongation of distance amongst neighboring parallel / antiparallel spin pairs and results in magnetically induced ferroelectric polarization. Based on the Ising model, the Hamiltonian (H) can be expressed in terms of the exchange coefficient J for nearest-neighbor sites as

$$H = \sum_{\langle ij \rangle} \left[J_{ij} \delta_{ij} (\mathbf{S}_i \cdot \mathbf{S}_j) + \frac{k}{2} (x_{ij} - x_0)^2 \right] = \sum_{n=4i} \left[4 \left. \frac{\partial J}{\partial x} \right|_{x_0} \delta + 2k\delta^2 \right] \quad (1.7)$$

where x , x_0 and k denote bond length, original length and coordination number respectively, J_0 is the exchange at x_0 , and $\delta = x - x_0$. For the parallel and antiparallel pairs of spin, the charge at i and $i+1$ site is not same and consequently, ferroelectric polarization is generated. Such an interaction is observed in compounds like $\text{Ca}_3\text{CoMnO}_6$ and is useful for applications in the high frequency region [24].

- (c) *Multiferroics*: Few materials like BiMnO_3 ferroelectricity permits alteration of ferroelectric domains offering electrically tunable magnetism via spin lattice interaction. Such materials are included in class of multiferroics. These materials provide room temperature magnetoelectric devices and magnetically controlled electro-optical response [24].

1.3.1.2. Two Phase or Bi-phase Magnetoelectrics and Heterostructures

Along with study on single phase magnetoelectric materials, the fabrication of unique magnetoelectric heterostructures from existing metallic compounds have also attracted lot of attention [24]. The interface effect present in these functional oxides is special because of its captivating physics which is not present in the individual components and have promising potential for applications. The origin of such coupling can be categorized as

- (a) Strain - mediated magnetoelectricity
- (b) Carrier mediated interfacial magnetoelectricity
- (c) Hybrid improper ferroelectricity in superlattices

- (a) *Strain-mediated magnetoelectricity*: This type of coupling involves quantum phenomena such as generation of strain in ferroelectric-ferromagnetic composites via piezoelectricity and piezomagnetism because of interface formation between constituent phases. This strain originates from preparation condition as observed in BaTiO₃, BaMnO₃ and LaAlO₃, strain drives ferromagnetism and ferroelectricity due to multivalency like in EuTiO₃ and lattice distortion drives magnetic anisotropy as observed in CoFe₂O₄ [24].
- (b) *Carrier-mediated interfacial magnetoelectricity*: The surfaces / interfaces that are involved in breaking the time-reversal symmetry enhance the magnetoelectric coupling. Such an interaction is achieved by carrier mediation via spin-dependent screening, bonding - oxidization like in PbZr_{0.2}Ti_{0.8}O₃ / La_{0.8}Sr_{0.2}MnO₃, Fe/BaTiO₃ / Pt and Fe / PbTiO₃ / Pt superlattices or electrical tuning of magnetocrystalline anisotropy like in BaTiO₃ / Fe₄ multilayers or ferroelectric control of magnetic phases like in CaRuO₃ / CaMnO₃ and LaSrMnO₃ or ferroelectric-magnetic tunneling junctions like in BaTiO₃ / La_{0.67}Sr_{0.33}MnO₃ [24].
- (c) *Hybrid improper ferroelectricity in superlattices*: Improper ferroelectricity arises on an account of mixing of non-polar distortion modes in hexagonal RMnO₃, RFeO₃, Ca₃Mn₂O₇, and Ca₃Ti₂O₇. This is achieved is by creating artificial superlattices such that two sites have different local symmetry like observed in Ca₃Mn₂O₇ [24].

1.4. Composite Materials

Composites are a class of materials, which provide scope of tailoring properties that are not possible amongst its constituents. Primarily, a composite exhibits traditional accumulative properties like density and stiffness, and the compositions are described by mass fraction or weight fraction. In addition, composites have tensorial product property discovered by Van Suchtelen, which is usually not present in its constituents [51].

One of the important applications of product property is exhibited as the ME coupling in composites which arise because of mutually connected electric and magnetic phases. The origin of ME coupling in binary composites can be described in

terms of piezoestriction and piezomagnetism. The implementation of magnetic field generates a deformation in piezomagnetic materials. This produces mechanical strain manipulates piezoelectric phases and generates a polarization. The opposite effect of generating magnetism in piezomagnetic phase is equally plausible. The overall consequence of product property i.e., ME coupling in all cases is tensorial in nature.

The ME coupling property especially in composites is decided by orientation amongst constituent ferroic orderings. There are different connectivity schemes possible in the bulk composites. Usually, the connectivity is described as (A-B), where A denotes ferromagnetic phase and B denotes ferroelectric phase in the matrix; and both A and B can take integer values between 0 and 3 [52,53]. Few examples of these connectivity structures are (0-3), (3-0) particulate composites, (2-2) laminate composites and (1-3) multi-layered composites. In Fig. 1.3., the connectivity scheme of these composites is shown [33]. Among these, the (0-3) and (3-0) composite are advantageous because of low cost and easy synthesis methods [54]. In addition, the manipulation of volume fractions of ferroelectric and ferromagnetic constituents is easily accessible in (0-3) composite structures [54,55]. The composite with (0-3) orientation is more resistive than (3-0) composite and offers strong polling of dipoles and generates enhanced magnetoelectric coupling. The composites with (3-0) connectivity is well studied in contrast to the sparsely studied composites with (0-3) connectivity, where ferroelectric phase is incorporated into ferromagnetic phase in spite of possessing higher conductivity.

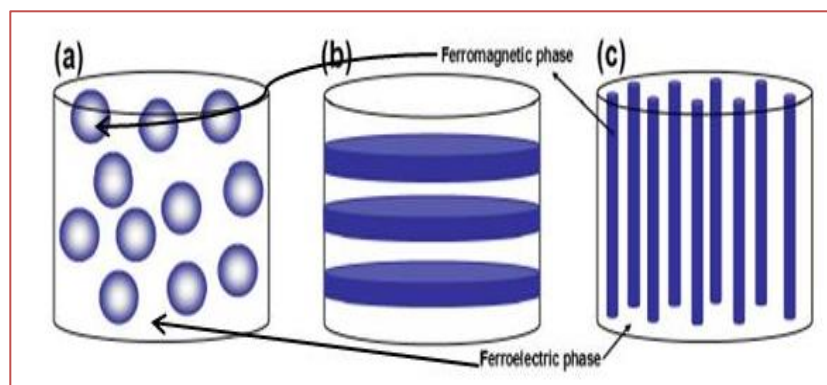


Figure 1.3. The connectivity scheme of (a) (3-0) and (0-3) composites, (b) (2-2) laminate composites and (c) (1-3) multi-layered composites.

1.4.1. Types of Composite Materials

Composites can be categorized based on the microstructure of the reinforcing components or in general of the composite, or the particle size (dimensions) of the reinforcing component. Composite materials can be grouped into three categories as [34] :

- (i) **Particle reinforced composites:** This kind of composites consist of particles like minerals, metal or amorphous type and are employed for making strengthened reinforced composites like ceramics and glasses.
- (ii) **Structural composites:** These types of composites are comprised of homogeneous as well as composites and provide additional features of tunable properties which depend on its constituent and orientation of structural elements.
- (iii) **Fiber reinforced composites:** This kind of composites are used for preparing metals, ceramics, glasses or polymers from converted graphite and are also called carbon fibers.

1.5. ABO₃ Perovskites

Perovskites acquire their nomenclature from Russian Scientist named Perovski for discovering calcium titanium oxide (CaTiO₃) in 1839 [56]. Generally, the perovskites are denoted by the chemical formula ABX₃, where A and B denote cations of dissimilar sizes and X is an anion binding these cations. The most common anion X is oxygen. The perovskite structure exists as

- (i) ABO₃ - Perovskite
- (ii) A₂BO₄ - Layered Perovskite
- (iii) A₂BB'O₆ - Double Perovskite

Perovskite materials are flexible to chemical substitutions at one or both of the cationic sites (A and B) as they retain their parental structure. Perovskites materials are a vastly studied class of materials in the field of condensed matter physics and it comprises of many metallic ions in the periodic table for different set of anions. This feature of perovskite, provides the chemical tailoring of materials and modifies the structural, microstructural, electrical and magnetic properties. These materials find their applications in various field of physics and chemistry. The most common perovskite with cubic structure is called an ideal perovskite. This class has great potential for

various applications, because of their basic structure and distinctive electrical properties.

1.5.1. Structure of Perovskite

Perovskite structures are denoted by chemical formula ABO_3 , with A and B as cation and O is the anion. The ionic radii of cation at A site is bigger than the cation at B site. The cations A and B have 12-fold and 6-fold co-ordination number, respectively. The basic unit cell of ABO_3 perovskite is shown in Fig 1.4.

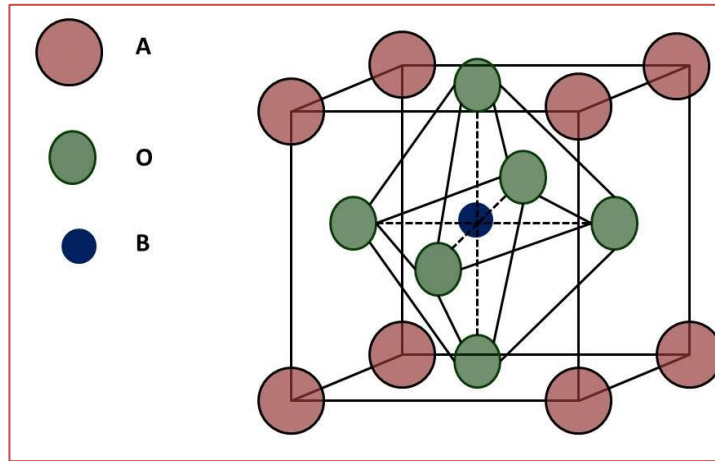


Figure 1.4. Crystal structure of ABO_3 type perovskite.

The divalent A cation occupies the corner position $(0, 0, 0)$ of the cube. The B cations are positioned at the body center position $(\frac{1}{2}, \frac{1}{2}, \frac{1}{2})$ and at the center of BO_6 octahedra. The oxygen anions are positioned at center of face in cubic lattice at $(\frac{1}{2}, \frac{1}{2}, 0)$. This unit cell is generally viewed as the three dimensional system of BO_6 octahedra connected at corners with B-O-B angles forming linear pair [57]. The formation of perovskite structure can be predicted by estimating the tolerance factor (γ) expressed as [58] :

$$\gamma = \frac{r_A + r_O}{\sqrt{2}(r_B + r_O)} \quad (1.9)$$

where r_i denote ionic radius of atoms $i = A, B$ and O respectively (in Angstroms). When $\gamma < 1$ produces tilting in BO_6 octahedra and when $\gamma > 1$ it shows shifting of B cation from center. The off-centering mainly occurs because of large variation between ionic radii of A and B ion leading to BO_6 octahedra contraction. The tolerance factor for ideal perovskite is unity and has space group $Pm\bar{3}m$ [59].

1.5.2. Classification of Perovskites

ABO_3 perovskite crystal structures are flexible owing to their ability of accommodating extensive choice of cations with altered oxidation states and cationic / anionic vacancies, which consequently provide pathway for a range of modified / substituted perovskites with diversified physical properties. The detailed classification of ABO_3 type perovskites is displayed in Fig. 1.5. The perovskite structures are categorized in two groups based on oxidation states as the

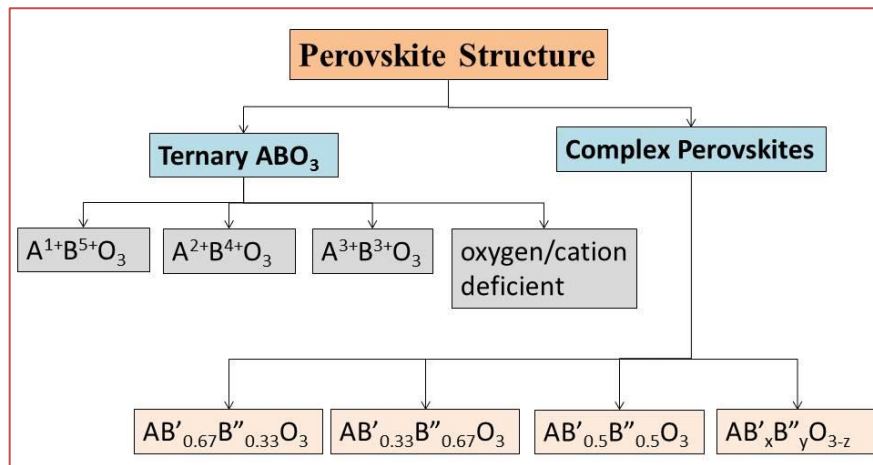


Figure 1.5. Detailed classification of ABO_3 perovskite

ternary ABO_3 type and the mixed complex perovskites $A(B'_xB''_y)O_3$ where B' and B'' are two distinct ions of distinct oxidation states such that $x + y = 1$.

- (i) The ternary oxides are classified as per the oxidation states with formulae $A^{1+}B^{5+}O_3$, $A^{2+}B^{4+}O_3$, $A^{3+}B^{3+}O_3$ and ion deficient compounds [60,61]. The best examples are $A^{1+}B^{5+}O_3$ - $AgTaO_3$, $A^{2+}B^{4+}O_3$ - $BaTiO_3$, $A^{3+}B^{3+}O_3$ - $BiMnO_3$ and ion deficient compound - $CaMnO_{3-\delta}$.
- (ii) The mixed complex perovskite type compounds, $A(B'_xB''_y)O_3$ can be classified into those which contain $2/3^{rd}$ and $1/3^{rd}$ amounts of B' and B'' elements as $A(B'_{0.67}B''_{0.33})O_3$, which consists of $1/3^{rd}$ and $2/3^{rd}$ amounts of B' and B'' elements as $A(B'_{0.33}B''_{0.67})O_3$, which consists of B' and B'' elements in equal quantities, $A(B'_{0.5}B''_{0.5})O_3$ and oxygen deficient compounds $A(B'_xB''_y)O_{3-z}$. The best examples are $A(B'_{0.67}B''_{0.33})O_3$ - $Ba(Nd_{0.67}W_{0.33})O_3$, $A(B'_{0.33}B''_{0.67})O_3$ - $Ba(Ca_{0.33}Nb_{0.67})O_3$ and $A(B'_{0.5}B''_{0.5})O_3$ - $Ba(Bi_{0.5}Ta_{0.5})O_3$.

1.5.3. Properties of Perovskites

Perovskites possess multifunctional properties owing to their cationic / anionic non-stoichiometry, cationic configuration disarrangement, and the mixed valency including the deficiency of oxygen. The sharing of BO_6 octahedra at the corner provides additional flexible feature in ferroelectric perovskite. This octahedral is subjected to the distortion exhibiting off-center shifting of cations, when modified by small B cations. The possible distortions based on cation movements along vertex, face and edge are tetragonal, rhombohedral and orthorhombic, respectively.

The off-centering of cations generate electric dipoles which align at adjacent unit cells via rotation and tilting of BO_6 octahedra and make the crystal produce electrical polarization. These ferroelectrics have spontaneous polarization. The polarization in the crystal disappears and becomes paraelectric, when the perovskite reaches a transition temperature. The perovskite displays giant dielectric constant. Below this transition temperature, the polarization can be reversed with hysteresis curve. These perovskite oxides displaying ferroelectricity and paraelectricity are found suitable for switching, actuating, transductive and capacitive applications. The ferroelectric perovskites due to non-zero hysteresis are useful in memory storage devices and tuning circuitry. These perovskites form an essential part of novel multiferroics and are fascinating to study due to their unique feature of electrical addressing of magnetic memory.

1.6. AB_2O_4 Spinel Ferrites

The spinel AB_2O_4 ferrites have attracted researchers due to their giant magnetostriction, modest saturation magnetization, chemical stability and notable mechanical hardness [62]. These ferrites are even treated as dielectrics because of higher conductivity owing from oxygen mediated electron exchange between Fe^{3+} / Fe^{2+} ions [63,64].

1.6.1. Structure of Spinel Ferrites

The spinel structure is derived from close-packed lattices. The spinels are formulated as AB_2X_4 , where A and B cations possess tetrahedral and octahedral coordination numbers, and X denotes an anion. The spinels have obtained its name from the mineral magnesium aluminate

MgAl_2O_4 . The usual chemical formula for oxide spinel is AB_2O_4 [65,66].

The typical spinel ferrite consists of cubic close-packed arrangement of oxygen ions. The A-site cations occupy $1/8^{\text{th}}$ of the tetrahedral voids and the B-site cations occupy half of the octahedral voids as shown in Fig. 1.6 [65,66]. On the contrary, the inverse spinels have an

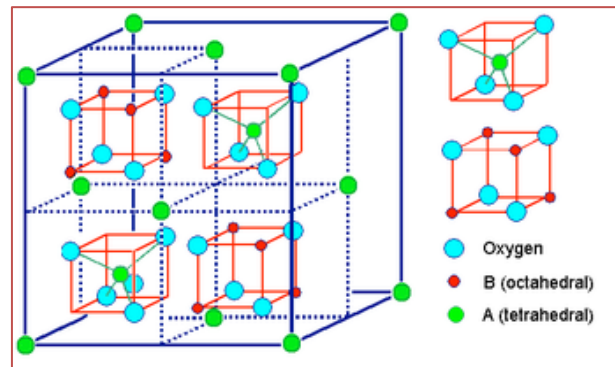


Figure 1.6. Structure of spinel ferrite.

akin d-structure consisting of the identical unit cell such that both the A-site and B-site cations exchange places. Therefore, the inverse spinels are denoted as $\text{B}(\text{AB})\text{O}_4$, where the AB ions in closed brackets occupy octahedral voids and the remaining B cations occupy tetrahedral voids. In addition, there exists another class of spinels namely mixed spinels whose structure lies midway between the normal and inverse spinels. The best fit example of spinel ferrite is Fe_3O_4 and inverse spinel is CoFe_2O_4 [65,66]. The preference of desired normal or inverse spinel structure is determined mainly by crystal field stabilization energy [65,66].

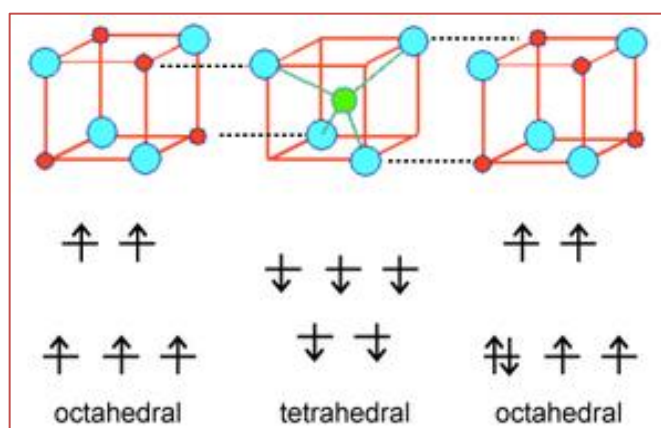


Figure 1.7. Superexchange mechanism in ferrites.

1.6.2. Properties of Spinel Ferrites

Spinel ferrites are very attractive from technological point of view owing to their distinct magnetic ordering, type of metal ions and either ferromagnetic for spinel ferrites or antiferromagnetic for inverse spinels. The inverse spinels Fe_3O_4 , CoFe_2O_4 , and NiFe_2O_4 are ferromagnetic in nature. Among these, CoFe_2O_4 is used in magnetic recording media and NiFe_2O_4 is used as deflection magnets.

The magnetism existing in ferrites can be explained by taking into consideration the coupling of unpaired spins of ions present in metal oxides. If the oxygen is connected with two metal ions, then their spins are coupled by superexchange interaction as shown at rightmost position of Fig. 1.7 [65,66]. The coupling of spins based on filling and symmetry of orbitals could be antiferromagnetic or ferromagnetic. The Goodenough-Kanamori rules predict the local magnetism arising from coupling of the electron spins in transition metal compounds resulting from superexchange interaction [65]. In case of ferrites, the coupling is very strong amongst ions of adjacent tetrahedral and octahedral voids, and the antiferromagnetism type local magnetism is displayed among these voids. These voids / sites are coupled identically both in spinels and inverse spinels, and therefore ions in the preferred orientation viz., spin down have on the tetrahedral sites and the other opposite orientation viz., spin up on octahedral sites respectively. If the number of spins on the tetrahedral as well as octahedral voids are equal, such a ferrite is antiferromagnetic. In case of number of unequal spins like in Fe_3O_4 , CoFe_2O_4 , and NiFe_2O_4 , then ferrite is ferrimagnetic. This distribution is explained for Fe_3O_4 in Fig. 1.8 [65,66]. Fe_3O_4 systems distributed as $(\text{Fe}^{2+}\text{Fe}^{3+})\text{O}_4$ consist of Fe^{3+} and Fe^{2+}

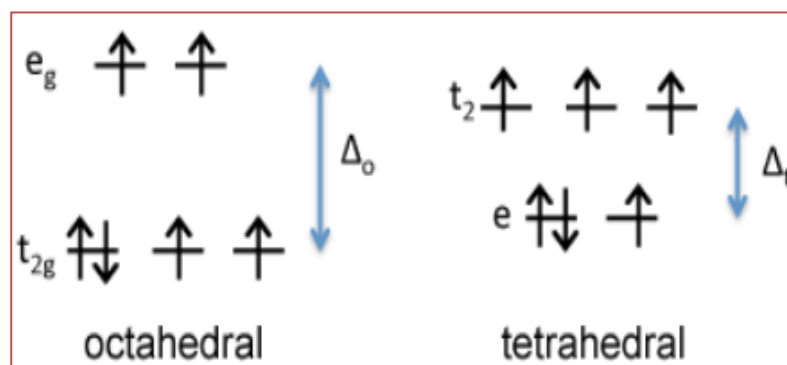


Figure 1.8. Distribution of spins in Fe_3O_4 .

ions. The former possesses large spin d^5 electrons and zero crystal field stabilization

energy indicating non-preference of occupancy at octahedral or tetrahedral sites, whereas the latter has large spin d^6 electrons with positive stabilization energy which dominates the positioning of Fe^{2+} ions at octahedral site rather than tetrahedral site. The spins on the Fe^{3+} in tetrahedral and octahedral voids are equal and opposite and consequently cancel. Conversely, due to the presence of free electrons on the Fe^{2+} ions aligned along the crystal directions makes Fe_3O_4 ferrimagnetic [65,66].

1.7. Electrical Properties of Materials

1.7.1. Ferroelectricity

Materials which undergo a phase transition from ordered symmetry (paraelectric) to a disordered symmetry (ferroelectric) from high to low temperature is known as ferroelectric material and has spontaneous macroscopic electric polarization. The electrical polarization is non-volatile and can be reversed with external electric field. The polarization change in ferroelectrics occurs with phase change at temperature known as Curie temperature (T_c). Spontaneously polarized ferroelectric materials show a hysteresis effect after applying the electric field (Fig. 1.1(b)) [67]. This effect is induced in the ferroelectric materials due to the presence of permanent dipole moment. The enhancements in dipole alignment i.e., increase in polarization is achieved after an increase of electric field. When the intensity of applied electric field is sufficiently high, then the dipoles align sharply along the applied field and saturate the polarization (P_s). As the electric field decreases to zero, the polarization is lowered to minimum. This non-zero polarization is called the remnant polarization (P_r). Electric field is reversed in negative direction to make this remnant polarization zero. The reversed electric field at which the electric polarization decreases to zero is known as coercive field (E_c). Extra negative field will provide saturation polarization (P_s) in the negative direction and hysteresis loop closes after reversal of the field.

The ferroelectricity in any material is established by the concept of electric polarization. Ferroelectric materials possess large dielectric constant and are suitable for the fabrication of electronic devices and energy storage materials. Nowadays, ABO_3 perovskite-structured oxides are most extensively studied and used as ferroelectrics. At higher temperatures, they exhibit typical cubic structure. The cubic ABO_3 perovskite structure consists of oxygen anions O, cation B of small size at oxygen octahedra and cation A of large size at the corner of unit cell. The spontaneous polarization in

ferroelectrics arises due to the non-centric shift of cation B during the phase transition from paraelectric to ferroelectric phase. There are different mechanisms which cause ferroelectricity in ABO_3 type materials:

- (i) The non-centric shift of the cation B gives origin for ferroelectric nature. This transition metal ion and oxygen atoms are connected via covalent bonding of empty d orbitals, e.g. $BaTiO_3$ unit cell is shown in Fig. 1.9 and shifting Ti^{4+} and O^{2-} ions from face center can be viewed [68].
- (ii) Stereo chemically active lone pair cations are another cause of ferroelectricity, e.g. Bi^{3+} in $BiFeO_3$ (Fig. 1.10) [69].

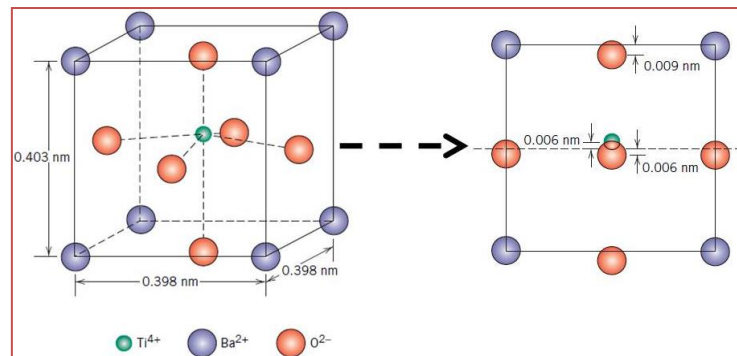


Figure 1.9. Isometric projection of $BaTiO_3$ unit cell.

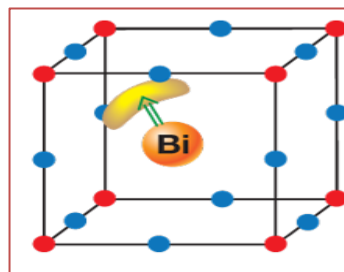


Figure 1.10. Polarization in $BiFeO_3$.

1.7.2. Dielectrics

Dielectrics are a class of electrical insulator, which possess only bound charges and does not contain free charges. It shows or can be made to show a polar state on the implementation of electric field. With the applied field, the charge centers of positive as well as negative charges are dislodged from their equilibrium position. Thus, a local electric dipole and local electric field in turn are generated. This phenomenon of creating electric dipoles from uncharged atoms and molecules is termed as electric polarization.

The polarization in an ideal dielectric material does not depend on temperature irrespective of its behavior in applied electric field. Therefore, when field is removed, the polarization becomes null. There are four important mechanisms (electronic, ionic, dipolar and space charge) for inducing polarization inside a dielectric material (Fig. 1.11) [70,71].

- (a) **Atomic or Electronic polarization:** When the application of electric field separates the centers of electron cloud and nucleus in opposite directions in a dielectric, electric polarization occurs. The field applied alters electron cloud of an atom such that a dipole pointing against the field is created [70].
- (b) **Ionic polarization:** This type of polarization appears in materials having crystal lattice with immobile anions and cations. In the absence of any field, there is null polarization due to the cancellation of dipole moments owing from crystal symmetry. On the application of electric field, an effective dipole moment or polarization is induced due to the small relative shift in the position of ions from equilibrium positions [70].
- (c) **Dipolar or orientational polarization:** The dipolar polarization occurs only in materials which possess permanent dipole moment. The electric dipole moment exists even when no field is applied due to the orientation / geometry of molecules. The dipoles existing in dielectric materials are randomized because of thermal agitation and are mobile in contrast to ionic polarization. Nevertheless, when electric field is implemented, the alignment of permanent dipoles of molecules present in the material results in appearance of dipolar polarization [70].
- (d) **Interface or space charge polarization:** The piling of opposite charges at grain boundaries or at the interface of electrode and material or both are the main causes of interfacial polarization. When an external field is implemented, these charges behaving as dipoles which tend to align due to fractional movement of charges [70].

The contribution of different polarization mechanisms can be understood by the plot of dielectric constant versus frequency of electric field as shown in Fig. 1.11. The polarization increases quantitatively in size from electronic to ionic to orientational polarization. It is obvious that particularly heavier entity will take more time to shift their place. The accumulated charges acting as dipoles and defects are involved in this kind of interface or space charge polarization. These entities are incapable to pursue the

oscillations of implemented electric field and thus space charge polarization appears for low frequencies up to 100 Hz.

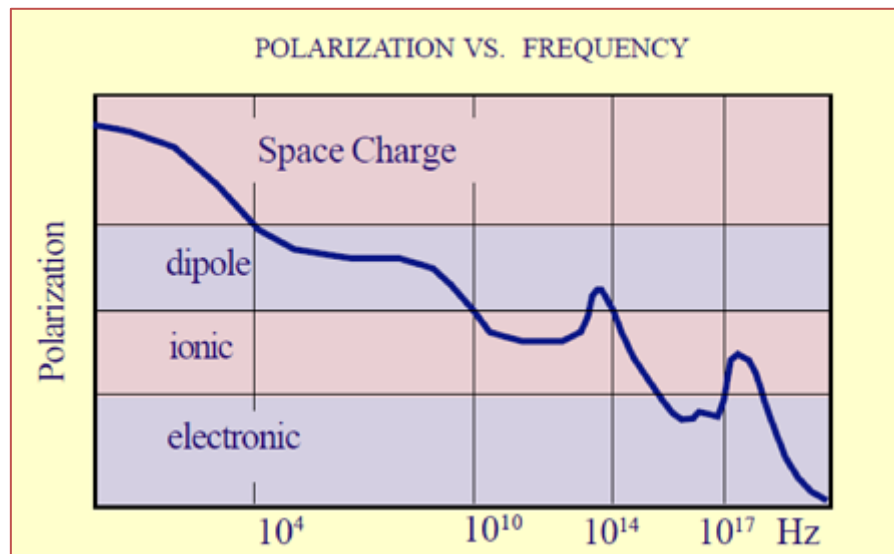


Figure 1.11. Systematic representation of possible four type of polarization processes.

The moments of molecular dipoles occur below 10^9 Hz in case of orientational polarization. On the other hand, ionic polarization is more rapid and usually occurs in the frequency range of 10^9 - 10^{13} Hz because of ionic contribution. Electronic polarization is the quickest and usually appears in the frequency range of 10^{13} - 10^{15} Hz due to the contribution of lighter electrons. The induction of polarization inside a material on the implementation of external electric field is referred to as dielectric behavior. When a dielectric material is inserted in between the parallel plates of a capacitor, the materials get polarized and increase the charge storage capacities. They are highly interesting for potential applications ranging from as transducers, condensers, and gear-switching, voltage rectifiers, frequency resonators, power amplifiers to electronic communication. These are also employed as memory storage devices for information in modern computers.

1.7.3. Impedance

Impedance spectroscopy is a new and interesting tool to extract the contributions of grains and/or grain-boundaries and / or electrode interface in the dielectric materials. To sort out the resistive and capacitive contributions, the sample is represented by the series combination of one or more parallel R-C circuits. Each of R-

C circuit elements relates to the respective contributions of grains and/or grain-boundaries and/or electrode interface. In the complex plane, the complex impedance can be expressed as $Z^* = Z' - jZ''$, where Z' and Z'' denote real and imaginary parts of total complex impedance (Z^*). In impedance analysis, the imaginary part is plotted against the real part Z' in the measured frequency range and such a plot is called Cole-Cole plot. Every R-C circuit generates one or more semicircles with each maxima corresponding to distinct single valued relaxation time (τ) expressed as $\tau = 1/\omega$, where ω denotes the angular frequency at maxima in Cole-Cole plot [72].

1.8. Magnetic Properties of Materials

1.8.1. Orderings of Magnetic Materials

On the basis of the collective interaction of atomic magnetic moments, the magnetic materials are classified in five major groups namely

- (i) Diamagnetism
- (ii) Paramagnetism
- (iii) Ferromagnetism
- (iv) Ferrimagnetism
- (v) Antiferromagnetism

Diamagnetic material consists of atoms having no net magnetic moment when no magnetic field is applied. On the application of external magnetic field (H), the precession of revolving electrons creates a magnetic moment opposite to applied field. Every material is usually diamagnetic in nature; however, the diamagnetic effect is screened by stronger paramagnetism or ferromagnetism. The susceptibility for diamagnets is independent of temperature [73].

Langevin describes paramagnetism as applicable for the systems containing non-interactive immobile electrons and the magnetic moment of every atom is presumed to be randomized due to thermal agitation. In the presence of magnetic field, the moments align and generate small net magnetization along the implemented field. With the increase in temperature, an increase in thermal agitation takes place and magnetic moments find it difficult to align due to decreased susceptibility. Such a decrease in magnetic susceptibility with temperature is termed as Curie law and is represented as

$$\chi = \frac{C}{T} \quad (1.10)$$

where C denotes Curie constant. The best example of a paramagnetic material is $\text{CuSO}_4 \cdot 5\text{H}_2\text{O}$ [73]. According to Pauli, the paramagnetic behavior is observed in materials consisting of mobile electrons and available to structure conduction band. When an external field is implemented, the mobile electrons used for conduction lose their balance with electrons of opposite spin due to alignment resulting in creation of small magnetic moment along the implemented field. As per Pauli model, susceptibility doesn't change with temperature; however, the alteration of band structures may be a cause for susceptibility change [69]. Due to incomplete d or f shells, some materials show ferromagnetic nature from paramagnetic nature, when they experience temperature change from high value to low value. Such a phase transition takes place below a unique temperature is known as Curie temperature (T_c). Magnetic order in these materials is achieved by exchange interactions between localized moments. The typical paramagnetic configuration is shown in Fig. 1.12(a) [74].

Often Curie law is considered as sub-kind of generalized Curie-Weiss law consisting expressed as

$$\chi = \frac{C}{T - \theta} \quad (1.11)$$

where θ is Weiss constant. This generalized law is derived on the basis of Weiss theory for ferromagnetic materials where exchange order among magnetic moments is permitted. The parameter θ can be zero, positive or negative. In case of $\theta = 0$, Curie-Weiss law reduces to Curie law of paramagnetism. Whenever $\theta \neq 0$, the neighboring magnetic moments display an interaction, and the material exhibits paramagnetic beyond transition temperature. Whenever θ is more than zero, it represents Curie temperature (T_c) below which the material exhibits ferromagnetism. If θ is negative, then it represents Néel temperature (T_N) below which the material exhibits antiferromagnetism and sometimes ferrimagnetism. This Curie-Weiss law holds true only for the materials exhibiting paramagnetism and does not hold good for multi-metal compounds or alloys due to virtue of unlocalized electrons generating the magnetic moment. Nevertheless this equation holds good in case of rare-earth based metals or compounds consisting of tightly bound 4f electrons [73].

When a ferromagnet is placed in an external magnetic field, it becomes magnetized and shows a characteristic loop called hysteresis loop as shown in Fig. 1.12(b) [74]. Such a ferromagnet gets magnetized in one particular direction with increasing the value of magnetic field, a saturated magnetization (M_s) is attained at

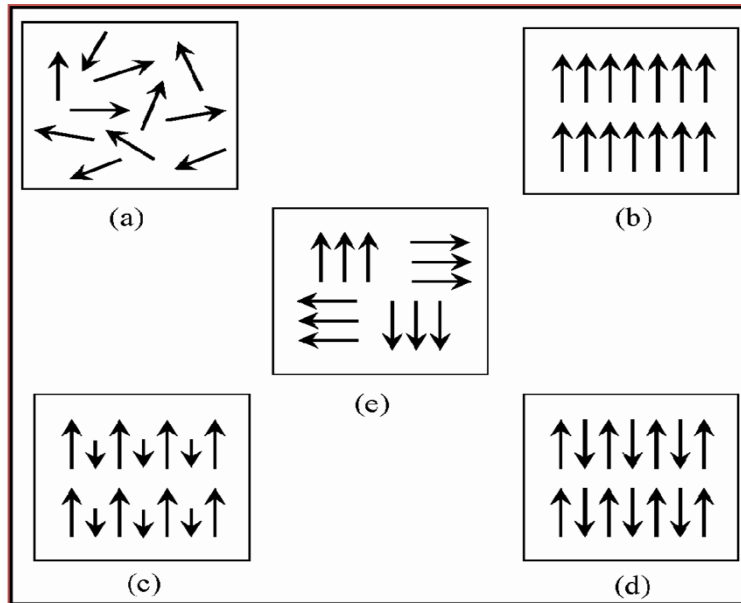


Figure 1.12 Configurations of (a) paramagnetic (b) ferromagnetic (c) ferrimagnetic (d) antiferromagnetic and (e) superparamagnetic materials.

which magnetization is maximum. On the removal of the field, the magnetization does not become zero and there is requirement of an extra magnetic field to relax the magnetization in negative direction. This type of non-zero magnetization at zero applied magnetic field is known as remnant magnetization (M_r) and the reverse magnetic field applied to make the magnetization zero is known as coercive field (H_c). The magnetization will sketch a hysteresis loop, if a cyclic field is used. The formation of ferromagnetic hysteresis loop in any magnetic material is because of magnetic domains present in the ferromagnet. The materials, which have comparatively high area in the magnetic hysteresis are termed hard magnets and exhibit more loss in the material, whereas the materials with less area in the magnetic hysteresis are termed known soft magnets and exhibit low loss. Ferromagnetic materials have long-range ordering which is the alignment of electron spins in the form of domains over longer lengths (Figure. 1.12(b)) [74]. The magnetic domains are oriented in different directions so that the ferromagnetic samples often have no macroscopic magnetization. There are two theories of ferromagnetism which explain numerous properties of ferromagnetic materials: Curie-Weiss for localization of magnetic moments and the Stoner band theory. In the Weiss's theory, electrons are localized and occupying certain energy levels. The electron energy depends on its angular momentum. The magnetic moments of electrons align parallel to each other due to the internal molecular field. The quantum mechanical exchange energy originates from this molecular field. According to the

Stoner theory, electrons can freely move in a periodic potential. The exchange energy of electrons will be minimized in the periodic potential if all the electrons have the same spin [69].

There exist some materials in which the magnetic moments are oriented anti parallel direction to one another. These materials are called ferrimagnetic materials. The strength of magnetic moment is different in both the directions as can be found in Fig. 1.12(c) [74]. Consequently, even when no magnetic field is implemented still a net magnetization exists in these materials. These materials are found to obey Curie-Weiss law for negative θ . An ideal example of ferrimagnet is spinel ferrite.

Now, if the antiferromagnetism is considered, the spins of electrons give no overall macroscopic magnetization in antiferromagnetic materials as shown in Fig. 1.12(d) [74]. This type of materials undergoes a transition from antiferromagnetic to paramagnetic state at higher temperatures. There are multiple states with different energies in antiferromagnetic interactions. The antiferromagnetic ordering is found in the transition metal compounds. There are at most three possible kinds of antiferromagnetic ordering inside a lattice, depending on the coupling in the plane and in between the planes couplings as shown in Fig. 1.13 [75]:

- (a) **A-antiferromagnet:** The ferromagnetic ordering exists in the planes and antiferromagnetic coupling exists between the planes.
- (b) **C-antiferromagnet:** The antiferromagnetic ordering exists in the planes and ferromagnetic coupling exists between the planes.
- (c) **G-antiferromagnet:** The antiferromagnetic ordering exists both in the planes and between the planes. The ideal example is perovskite ABO_3 with cubic structure where each 'B' magnetic atom has six-fold coordination number formed by antiferromagnetic atoms.

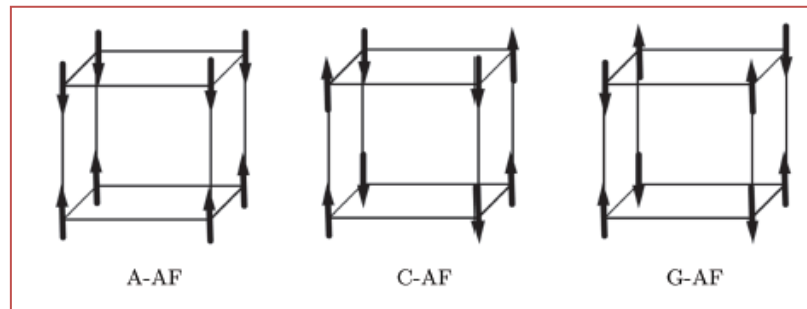


Figure 1.13. Types of antiferromagnetism.

There exists another unique class of magnetism namely superparamagnetism observed in materials containing small nanosized ferromagnetic particles. The size varies between 1-30 nm for different materials. The material exhibits very large saturation magnetization and very low coercivity. The large magnetization is presumed to be originating from a big dipole containing constituent magnetic moments of all existing nanoparticles. The sufficient increase in temperature assists in randomized flipping of dipoles. A typical configuration of superparamagnetism is shown in Figure 1.12(e) [74].

1.9. Materials and their Applications

1.9.1. Materials for Magnetoelectric Composites

Among the existing ABO_3 perovskites, Barium titanate ($BaTiO_3$) is a conventional ceramic with excellent ferroelectric and dielectric properties [76]. $BaTiO_3$ (BT) is widely used in electronic devices such as photoelectrodes, layered capacitors and sensors [76]. It is one of the best suitable material employed as dielectric in electronic devices and exhibits excellent piezoelectricity and ferroelectricity [77]. In addition, BT exhibits temperature dependent polymorphic i.e., structure changes from Rhombohedral to cubic when the temperature changes from $-90\text{ }^{\circ}\text{C}$ to $120\text{ }^{\circ}\text{C}$. The cubic structure follows ABO_3 structure of perovskite with $Pm3m$ space group [78]. The ferroelectric and dielectric properties can be tuned as desired based on preparation methods [78]. Through the substitution of specific dopants, the TiO_6 octahedra in BT can be distorted and is proved beneficial for achieving broadening of transition temperature (T_c) with improved dielectric and ferroelectric properties [78]. The shape and size of grains in BT control the physical parameters like crystal structure, T_c and optical properties [79]. These features make BT an ideal constituent for tunable energy storage devices [77].

Among the spinel AB_2O_4 ferrites, cobalt ferrite ($CoFe_2O_4$) is one of the most interesting spinel ferrite exhibiting spectacular physical properties like electric, magnetic, thermal, mechanical and optical properties [80,81]. $CoFe_2O_4$ (CFO) displays a special kind of ferrimagnetism i.e., superparamagnetism and is strongly attractive for sensor applications. In spite of such unique properties, CFO possesses lossy nature which makes it less useful for electrical device applications. This lossy behavior can be modified by the addition of strong ferroelectric material like lead free BT. The co-

existence of ferromagnetism as well as ferroelectricity is a fascinating concept for magnetoelectric devices and can be realized in composites of CoFe_2O_4 - BaTiO_3 (as CFO-BT or BT-CFO) due to different origins of respective ferroic orderings. The extent of coupling can be understood either qualitatively via directly measuring the change in ferroic order due to other or quantitatively via indirect measurements [82]. The quantification of direct measurements of magnetoelectricity for different order of coupling coefficients has been well established [12,27]. On the other hand, the indirect measurements reveal qualitatively the existence of coupling from the thermal dependence of dielectric parameter constant and magnetic parameters respectively [82,83]. However, these indirect studies reveal only the evidences of magnetoelectric coupling present in the system. In this work, we are interested in the preparation and optimization of CFO - BT and BT - CFO composites through mole ratio for superior magnetoelectricity employable in sensor devices. The composites of CoFe_2O_4 - BaTiO_3 with (3-0) connectivity scheme is expected to exhibit strong magnetoelectricity owing from individual phase contributions and product property. It is also pertinent to add that there have been commendably significant studies of BaTiO_3 - CoFe_2O_4 composites for investigating dielectric properties [84–86]. The BT based composite system usually suffers from tangent losses in microwave frequency regime. This BT-CFO composite with (0-3) connectivity scheme would be useful in improving the performance of BT in electronic devices. It would, therefore, be interesting to explore the effect of volume fraction on the magnetoelectricity in BaTiO_3 based composites as BaTiO_3 - CoFe_2O_4 and CoFe_2O_4 - BaTiO_3 system with (0-3) and (3-0) scheme, respectively.

The substitution of Ni^{2+} in the cubic structure of CFO is exciting due to improved resistive and magnetoelectric properties [43]. The recent studies on ferromagnetic $\text{Co}_{0.5}\text{Ni}_{0.5}\text{Fe}_2\text{O}_4$ (CNFO) have revealed that strong magnetostatic interactions arising from different magneto-crystalline anisotropy are countered by increased coercivity and decreased magnetic saturation [47,87,88]. There have been investigations on CNFO based composites for existence of magnetoelectric properties [49,54,89]. Furthermore, CNFO-BT system has showed some promising results in the magnetic properties [43–46]. Nevertheless, the origin of magnetodielectric, impedance and ferroelectric properties in CNFO-BT composites are not explored thoroughly. The $\text{Co}_{0.5}\text{Ni}_{0.5}\text{Fe}_2\text{O}_4$ - BaTiO_3 composites would be important from the viewpoint of stabilization of magnetodielectric effect, impedance and magnetoelectric coupling.

Another magnetic material of interest is the bismuth ferrite (BiFeO_3) which exhibits antiferromagnetism and is an excellent multiferroic [38,90–93]. BFO possesses ABO_3 type perovskite structure with distorted rhombohedral arrangement. BFO transforms its G-type antiferromagnetic nature to paramagnetic nature above $T_N \approx 365$ °C and ferroelectric - paraelectric phase transition above $T_c \approx 825$ °C. The antiferromagnetic orderings are due to the modulation of cycloid spin arising from super-exchange and spin-orbit interactions of metal-oxygen-metal owing to canting of sub-lattice formed by Fe^{3+} ions. On the contrary, the ferroelectricity arises from the non-centrosymmetric ordering along the principal diagonal axis [111] originating from stereochemical activity of 6s lone pair of electrons hybridized between 6p empty orbital of Bi^{3+} ions and filled 2p orbitals of O^{2-} ions. But there are some processing issues and as a result of which, there are some impurities like $\text{Bi}_2\text{Fe}_4\text{O}_9$, $\text{Bi}_{25}\text{FeO}_{39}$ etc. present in the material which shows unsaturated electrical hysteresis loop. The impurities of BFO are removed by doping at the Bi site with Gd^{3+} , La^{3+} and Sm^{3+} [94–97]. Partial modification at Bi site by lanthanum denoted by $\text{Bi}_{1-x}\text{La}_x\text{FeO}_3$ evades the possibility of formation of unwanted phases during synthesis and enhances the electrical and magnetic properties [3,93,98,99]. This La ion substitution is promising as its ionic radius is similar to that of Bi^{3+} which consequently stabilizes the structural owing to increased bond length, suppresses oxygen vacancies and enhanced magnetic anisotropy. The investigations on $\text{Bi}_x\text{La}_{1-x}\text{FeO}_3$ reveal that up to 12.5% mole ratio of La atoms, the rhombohedral $R3c$ structure remains unmodified and with 20% more ratio the cycloidal spin disappears [3,93,98,99]. $\text{Bi}_{0.85}\text{La}_{0.15}\text{FeO}_3$ ceramics show such distinct properties owing from structural modification which improvises the resistive nature and electrical remnant polarization, and make them suitable candidates for multiferroic applications [3,93,98–100]. The frequency dependent electrical properties of lanthanum-substituted BFO ceramics display a decreasing trend in dielectric properties with frequency attributing to a conventional dielectric relaxation process and temperature dependent broad dispersion in dielectric permittivity arising from modifications in the sample preparation methodology. This temperature dependent dispersion of dielectric permittivity and dielectric loss is usually detected to appear near to antiferromagnetic Neel temperature. Unexpectedly, the temperature dependence of conductivity has been studied thoroughly to understand the electrical properties [3,93,98,99]. Therefore, combining single phase multiferroic $\text{Bi}_{0.85}\text{La}_{0.15}\text{FeO}_3$ with ferroelectric BT as $\text{Bi}_{0.85}\text{La}_{0.15}\text{FeO}_3$ - BaTiO_3 composites is expected to bring a number

of important improvements in the physical properties like antiferromagnetic to ferromagnetic change, low coercive and countable maximum polarization of electric hysteresis loops for loss analysis.

Rare-earth manganites (RMnO_3) are fascinating materials due to their unusual strong coupling among charge, spin, and lattice dynamics and have extensively created enormous interest in research. These materials possess a striking feature of simultaneous occurrence of ferro to paramagnetic and metal to insulator transitions [101–103]. RMnO_3 finds their application in information storage devices owing from their broad antiferromagnetism Neel temperature range of 620-740 K [104]. These manganites possess distinctive fascinating electronic configuration due to the hybridization of 3d and 2p orbital of Mn and oxygen, respectively. In the category of RMnO_3 perovskites, NdMnO_3 is a unique rare-earth manganite possessing orthorhombic type structure and display antiferromagnetism [105,106]. NdMnO_3 (NMO) is considered novel due to inherent structural disordering arising from cognitive rotation of MnO_6 octahedra. This rotation decreases the Mn-O-Mn bond angles and supports in exhibiting a magnetic transition from A-type to E-type antiferromagnetism via partial incommensurate ordering and additionally causes multiferroism [102,107]. The prominent cause of magnetism in NMO is the superexchange mechanism of Mn^{3+} -O- Mn^{3+} causing the antiferromagnetic ordering in Mn, whereas the Nd ions retain their paramagnetism. The co-existence of electrical and magnetic ordering and the evidence of colossal magnetoresistance observed in Nd-manganite is on the basis of double exchange mechanism [108,109] which is explained in terms of correlation of Mn-O bond angle, charge-lattice behavior, Mn^{3+} / Mn^{2+} charge transfer mechanism, superexchange mechanism of t_{2g} spins and intersite interaction [110]. In recent years, the study of NMO based system has gained immense interest for the exploration of dielectric, magnetic and magnetoelectric properties [101,102,108,111–113]. The investigation of electric properties of NMO based composites has not been reported in the literature. The bulk composites of NdMnO_3 - BaTiO_3 will be an interesting work as it will involve the multiferroic magnetoelectric nature of NMO combined to the strong ferroelectric nature of BT.

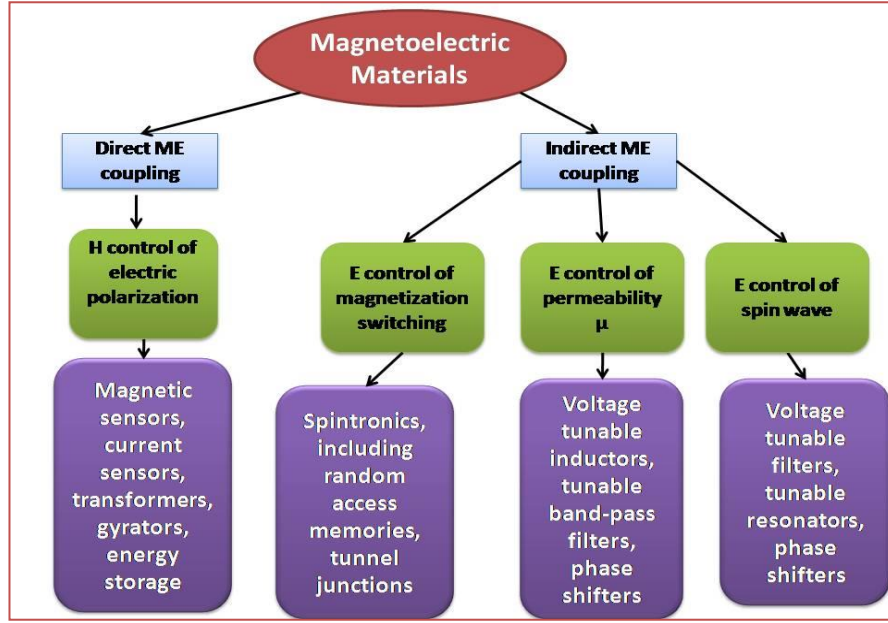


Figure 1.14. Applications of magnetoelectric materials on the basis of the origin of coupling and control mechanism.

The magnetoelectric materials especially composites possess various surprising features which enable them for potential applications like memory stage, gyration, sensing, filtering and resonating devices. The chief uniqueness in magnetoelectric materials is the control of one ferroic ordering by another which is the foundation for novel magnetoelectric based random access memory (MRAM). This MRAM would reform the existing technology with enormous speed, low cost and update computers, mobiles and all solid-state devices. Depending on the type of magnetoelectric coupling and control mechanism employed, the possible applications of magnetoelectric materials have been displayed in Fig. 1.14.

1.9.2. Materials for Energy Storage

Energy storage is a primordial subject of interest which emphasizes on the performance parameters of myriad class of materials and devices [114]. Dielectric materials display excellent power density and strong discharge capability needed for energy storage devices. In comparison to polymer based and electrolyte based capacitors, the dielectric capacitors generally have higher value of dielectric constants and small discharging time (ns) which makes them potential candidates for energy storage devices [115,116]. With the increase in miniaturization in recent years, high

energy density capacitors find applications in the fields of electric vehicles and mobile electronic communication [117].

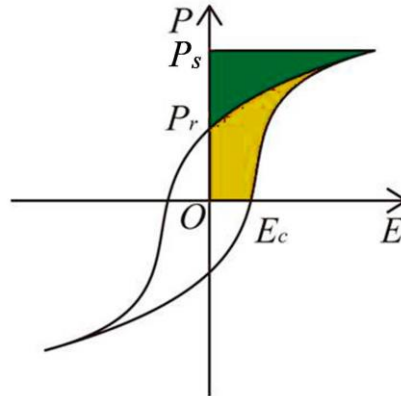


Figure 1.15. P-E loop of ferroelectric material.

A usual P-E loop of ferroelectric material is shown in Fig. 1.15. The yellow region represent energy lost and green region represents useful recoverable energy. The useful electrical energy storage density in any system is calculated by evaluating the integral area of the P–E hysteresis loop (charge and discharge curve are represented by lower and upper branch of P–E curve respectively) with the y-axis and is represented as

$$W_U = \int_0^{P_{max}} E dP \quad (1.12)$$

here E and P denote implemented electric field and generated polarization, respectively. The discharge and charge energy density are often referred as useful and total energy density (including energy stored and energy lost) per cycle. The energy conversion efficiency

$$\eta = \frac{W_U}{W_L + W_U} \quad (1.13)$$

here W_L represent energy lost [118]. This efficiency is beneficial for understanding the storage mechanisms in various dielectrics [118]. Higher the conversion efficiency, higher will be the useful energy density and dielectric constant. This effect implies that materials with high conversion efficiency will offer fast movement of charge carriers and will be prospective contenders for longstanding and durable energy source. Consequently, the materials having large polarization (P_{max}) and low remnant polarization (P_r) are preferred as suitable choice in high energy-storage capacitors [115,117]. Thus the antiferroelectric and relaxor ferroelectric materials based on $BaTiO_3$ and $PbTiO_3$ are found more appropriate for investigations [115,117,119]. These

systems have exhibited energy densities of upto $\approx 0.94 \text{ J/cm}^3$ and energy storage density of upto $\approx 72 \%$ at room temperature [120,121]. Keeping in mind the environmental concerns of PbTiO_3 , the studies on lead-free systems have gained more attention [122].

1.10. Objectives of the Thesis

The single phase magnetoelectrics are observed to have weaker coupling and are therefore not so useful for device applications as compared to two phase materials. So, in the present work attempts are made to fabricate two phase magnetoelectric composites of BaTiO_3 . In addition, the present work aims to optimize such composites with high energy storage density so as to make them as an alternative for lead - free energy storage devices. It is subsequently desired to choose materials with strong magnetic properties. Amongst the existing magnetic materials, the ones that exhibit explicit multiferroism and magnetoelectricity are ferrimagnetic (CoFe_2O_4), ferromagnetic ($\text{Bi}_{0.85}\text{La}_{0.15}\text{FeO}_3$) and antiferromagnetic (NdMnO_3). Therefore, based on literature, it is decided to prepare BaTiO_3 based bulk ceramic composites with these magnetic materials by varying the composition. The main focus would be given to enhancement and optimization of magnetoelectric properties and energy storage densities of BaTiO_3 based composites through stoichiometry. Furthermore structural, morphological, ferroelectric, dielectric, impedance and magnetic properties of BaTiO_3 based composites would be investigated. Thus, the discussion made in the previous sections and motivated by the above facts, the short-term specific objectives of the thesis are as follows:

- (i) To synthesize bulk composites of $\text{BaTiO}_3 - \text{CoFe}_2\text{O}_4$, $\text{CoFe}_2\text{O}_4 - \text{BaTiO}_3$, $\text{Co}_{0.5}\text{Ni}_{0.5}\text{Fe}_2\text{O}_4 - \text{BaTiO}_3$, $\text{Bi}_{0.85}\text{La}_{0.15}\text{FeO}_3 - \text{BaTiO}_3$ and $\text{NdMnO}_3 - \text{BaTiO}_3$ by using solid state reaction method to achieve required optimum structure and phase.
- (ii) To study phase formation, surface morphology by using XRD, SEM-EDAX, Raman, FT-IR techniques for better understanding of the properties in these composites.
- (iii) To investigate the dielectric, impedance, magnetic and ferroelectric properties of the synthesized BaTiO_3 based composites and its correlation with their structure in order to understand the fundamental physics.

- (iv) To reveal the quantification of magnetoelectric coupling coefficient in the synthesized BaTiO₃ based composites by studying the ferroelectric hysteresis (P-E) variation and the dielectric constant variation in the presence of magnetic field.
- (v) To optimize the energy storage density and efficiency of the synthesized BaTiO₃ based composites by analyzing the ferroelectric hysteresis (P-E).
- (vi) Finally, to develop efficient lead-free ferroelectric BaTiO₃ based composites for practical energy storage devices utilizing magnetoelectric properties.

Chapter - 2

Experimental : Composite Synthesis and Characterization Techniques

The synthesis of pure phase composites demands suitable understanding of different synthesis methods along with the appropriate characterization tools. The aim of the chapter is to describe several aspects of the experimental methods for the preparation of composites. The details of different characterization tools namely X-ray diffraction (XRD), scanning electron microscopy (SEM), energy dispersive absorption X-ray spectroscopy (EDAX), Fourier transform infra-red spectroscopy (FT-IR), Raman spectroscopy, vibrating sample magnetometer (VSM), ferroelectric loop tracer, dielectric measurements using LCR meter and impedance analyzer have been discussed along with their working principles.

2.1. Experimental

The primordial step in experimental research is the synthesis and characterization. This chapter is focused on the synthesis techniques and characterization techniques needed for validating the utilization of magnetoelectric composites for energy storage devices. Over the past decades, different researchers described numerous synthesis techniques for magnetic materials, ferroelectrics and magnetoelectric materials. These methods can be categorized as dry solid state ceramic route or wet methods like sol-gel and co-precipitation [123–126]. The dry solid state method has been discussed explicitly. The characterization tools such as X-ray diffractometer (XRD), Scanning electron microscopy (SEM), Fourier transform infrared spectroscopy (FT-IR), Raman spectroscopy, Vibrating sample magnetometer (VSM), Ferroelectric loop tracer and Dielectric measurements using LCR meter as well as impedance spectrometer are exploited to understand the structure, morphology, electrical, magnetoelectric and energy storage properties of the synthesized composites.

The extent of magnetoelectricity in the composites depends on the orientation amongst constituent phases. To synthesize magnetoelectric composites, several aspects are to be addressed carefully such as choice of magnetic phase, ferroelectric phase, desired phase purity of starting materials, calcination and sintering temperatures and sintering duration [127]. The solid state reaction route is usually chosen over other methods because of easy preparation and cost effectiveness. In addition to this, solid state route offers manipulation of mole ratio of constituents as well as temperature variation for sintering [127]. The basic underlying properties such as electrical and magnetic properties of the composite materials can be enhanced by modifying the chemical constitution, structure, size, orientation and morphology. The preparation of these composites plays a crucial role in achieving phase purity, unique electrical and magnetic properties. In other words, tuning of different parameters like sintering temperature and duration can assist in improving the quality of the composites [128]. The prepared composites and their modified morphology provide enrichment in dielectric and magnetoelectric properties owing to their product property [128].

2.2. Chemicals used

The preparation of various magnetoelectric composites requires individual magnetic and ferroelectric phase. The different chemicals used for synthesizing these

phases investigated in this thesis are mentioned below:

Table 2.1. List of chemicals used to prepare various magnetoelectric composites to carry out present thesis work.

S.No.	Name of the chemicals	Chemical Formula	Purity (%)	Supplier
1	Cobalt Oxide	Co_3O_4	99.90	Fisher Scientific
2	Iron Oxide	Fe_2O_3	99.90	Fisher Scientific
3	Barium Carbonate	BaCO_3	99.80	Fisher Scientific
4	Titanium Dioxide	TiO_2	98.00	CDH
5	Nickel Oxide	NiO	99.00	Fisher Scientific
6	Bismuth oxide	Bi_2O_3	99.00	CDH
7	Lanthanum Oxide	La_2O_3	99.99	Fisher Scientific
8	Neodymium Oxide	Nd_2O_3	99.99	CDH
9	Manganese Dioxide	MnO_2	92.00	CDH

2.3. Composite Synthesis

The commonly employed procedure for synthesis of composites is the solid state reaction method or dry media reaction method or mechano-chemical method. This technique is beneficial in producing large quantity of material with lower cost and within less time. Generally, in this technique, the starting materials of high purity in powder form are weighed stoichiometrically and are ground consistently with the help of agate mortar and pestle in water or acetone media. The mixture is pre-sintered or calcined for several hours in muffle furnace followed by pressing and sintering for assisting chemical reaction between the oxides and formation of the final product.

The composites are synthesis with the following steps:

- (i) Preparation of materials to form an “intimate mixture” of constituent A and constituent B so as to maintain the appropriate proportions of metal ions in the final product.
- (ii) The process of pre-sintering or calcinations involves heating the primary mixture of raw materials. This heating decomposes carbonates and higher oxides and removes the gaseous components in the sintering stage.

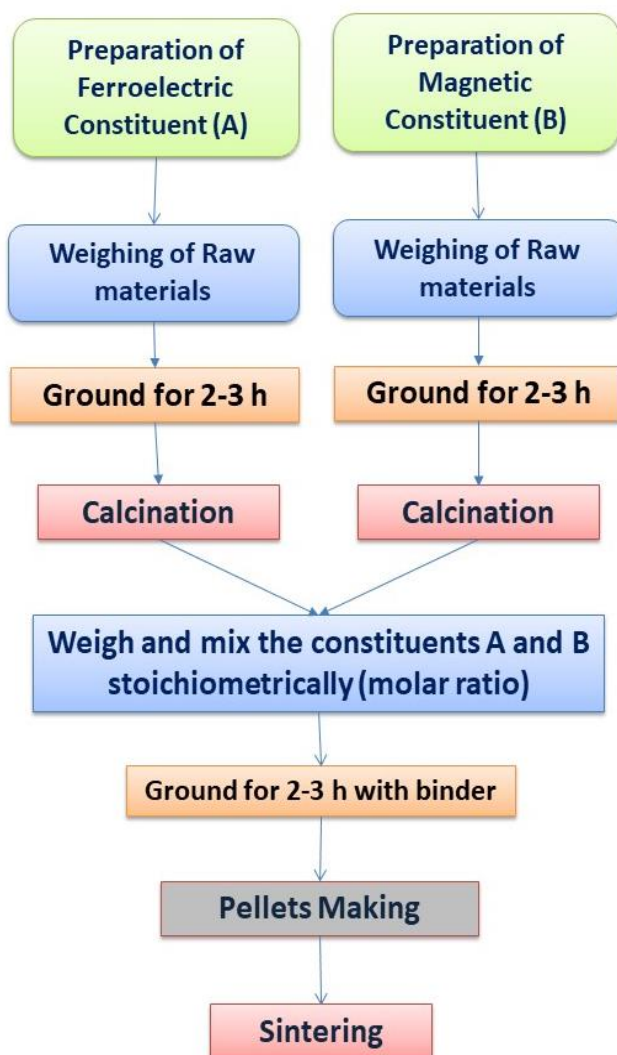


Figure 2.1. Schematic flow chart for the preparation of ferroelectric / ferrite constituent and composites.

- (iii) The calcined powder of constituents of A and B are ground to promote mixing unreacted oxides. The calcined power of constituent A is mixed with stoichiometrically with calcined powder of constituent B to prepare desired composites. The resultant powder of each composite is pressed into cylindrical pellets by using hydraulic press.
- (iv) The prepared composite pellets are sintered along with composite powder for obtaining good quality of composite pellets. The flow chart for synthesizing ferroelectric / ferrite constituent and composites is shown in Fig. 2.1.

2.4. Characterization Tools and Working Principle

2.4.1. X-Ray Diffraction (XRD)

X-ray diffraction is a non-destructive adaptable tool for identifying crystallite phase and analyzing structure of the synthesized composites [129]. This method provides the following information:

- (i) Constituent phases of composites
- (ii) Strain present in composites
- (iii) Crystallite size

For the present work, we have employed Bruker D8 X-ray diffractometer. This diffractometer consists of automatic tools and in-built software for ease of use. The radiation source of XRD had a wavelength of 1.5418 Å at a scanning rate of 0.4 sec/step.

The X-ray diffraction technique involves the observation of intensity variation of scattered X-ray beam incident on a sample with incident and scattering angle. In this technique, a monochromatic X-ray beam is implemented on a specimen sample consisting of randomly oriented particles. The scattered X-rays interfere constructively and produce diffraction pattern which are recorded using detectors or photographic films. The crystal planes of specimen sample satisfying Bragg's law allow certain diffraction to occur corresponding to specific inter-planar spacing of the crystal.

In the crystal structure, atoms are arranged in regular order. Fig. 2.2. shows set of lattice planes with inter-planar spacing 'd' [130]. When X-rays are incident on the crystal, these rays interact with the electrons present in the atoms and produce waves with spherical wave front in all directions. The waves scattering in all directions produce constructive and destructive patterns. The constructive interference is on the basis of Bragg's law which is expressed as [131]:

$$n\lambda = 2d\sin\theta \quad (2.1)$$

where the parameters n , λ , d and θ denote integral values, wavelength of incident X-ray radiation, inter-planar spacing, and glancing angle, respectively.

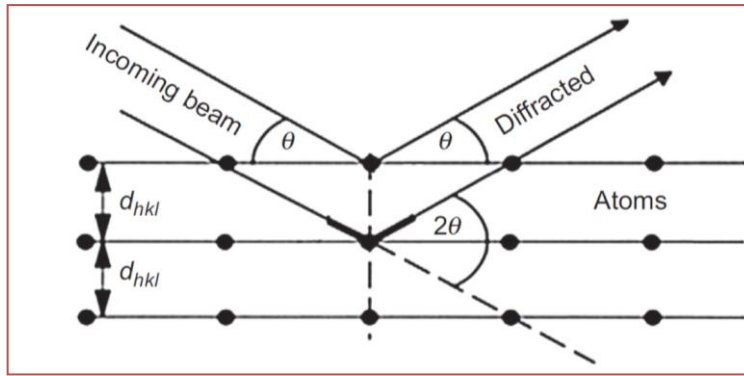


Figure 2.2. Bragg reflection from lattice planes.

In X-ray diffractometer, the position of detector is fixed with respect to specimen sample, which is usually achieved by either fixing detector and rotating the sample or rotating both specimen and detector with fixing position of incident X-rays. Only those crystal planes which are or nearly parallel to sample surface contribute to diffraction patterns. However, in the powder method, a number of combinations of inter planar spacings and the glancing angles satisfies the Bragg law. The image of X-ray diffractometer is shown in Fig. 2.3.



Figure 2.3. X-ray diffractometer setup.

The X-ray diffraction studies can help in estimating the following parameters [85,131,132] :

(a) **Lattice parameter:** In case of cubic lattice, the inter-planar distance (d) is related to lattice constant (a) and Miller indices (hkl) by the expression.

$$d = \frac{a}{\sqrt{h^2+k^2+l^2}} \quad (2.2)$$

(b) **Average crystallite size:** The average crystallite size in the composites can be estimated using Debye Scherrer's equation

$$D = \frac{k\lambda}{\beta \cos \theta} \quad (2.3)$$

where $k = 0.89$ (assuming the particles are spherical in shape), λ is the wavelength of X-ray, β is full width at half maximum (FWHM) of the diffraction peak and θ is angle of diffraction. The crystal lattice strain and average crystallite size were calculated using Williamson-Hall equation

$$\frac{\beta \cos \theta}{\lambda} = \frac{1}{\varepsilon} + \frac{\eta \cos \theta}{\lambda} \quad (2.4)$$

where ε and η denotes effective crystallite size and effective strain and the remaining terms have their usual meanings.

2.4.2. Scanning Electron Microscopy (SEM)

Scanning Electron Microscope (SEM) is a device used for imaging the surface morphology of any sample using secondary electrons [133]. A high-quality stream of electrons produced from electron gun is incident on sample surface which create secondary and back scattered electrons. The former ones are those which are removed from the surface due to excitation of incident primary electrons and latter ones are part of primary electrons backscattered by the sample. The electron beam is fully scanned over the specimen surface and images a map of surface based on the detected signals at different positions of beam. Depending on the types of electron beam signals, one can have backscattered electron imaging and secondary electron imaging. This device is capable of producing high-resolution mapped image of specimen surface. These images provide large depth of field beneficial for comprehending surface structure of sample. SEM imaging is also used for elemental analysis of the sample. For the present work, we have employed JEOL JSM 6610LV SEM 500 Instrument for obtaining SEM imaging with resolution 1.1 nm at 1 kV. The SEM Setup is shown in Fig. 2.4. The

electron emission is based on thermal field emission. The accelerating voltage and magnification vary in the range of 0.3 kV - 30 kV and 5x - 300000 x respectively.



Figure 2.4. JEOL Scanning electron microscope.

The picture of scanning electron microscope is shown in Fig. 2.5 [134]. The basic structure of SEM constitutes of an electron gun fitted to tungsten cathode. The electrons produced are accelerated with energy of 1 - 50 keV from anode. The accelerated electrons are focused with the help of a pair of condenser lens. The magnetic field of scanning coils deflects the beam along x and y axes for scanning the surface with the help of scanning circuit. The beam highly focused by objective lens scans the specimen surface in the raster pattern. The electron beam on interaction with the specimen tends to lose energy via random scattering and absorption within specimen resulting in the production of reflected energized electrons due to elastic scattering, secondary electrons due to inelastic scattering and the emission of electromagnetic radiation. Each of the electron beam generated can be detected by specific detectors. Electronic circuits are used to amplify the signals from beam current. The secondary electrons are using for mapping the surface image and backscattered electrons are used for providing contrast information about regions with different compositions. The magnification of SEM is very high as compared to optical microscope because of lower wavelength of electron beam with respect to optical microscope. This helps in achieving a resolution of about 1-20 nm. SEM technique is useful only for surface images and compositions up to a certain extent.

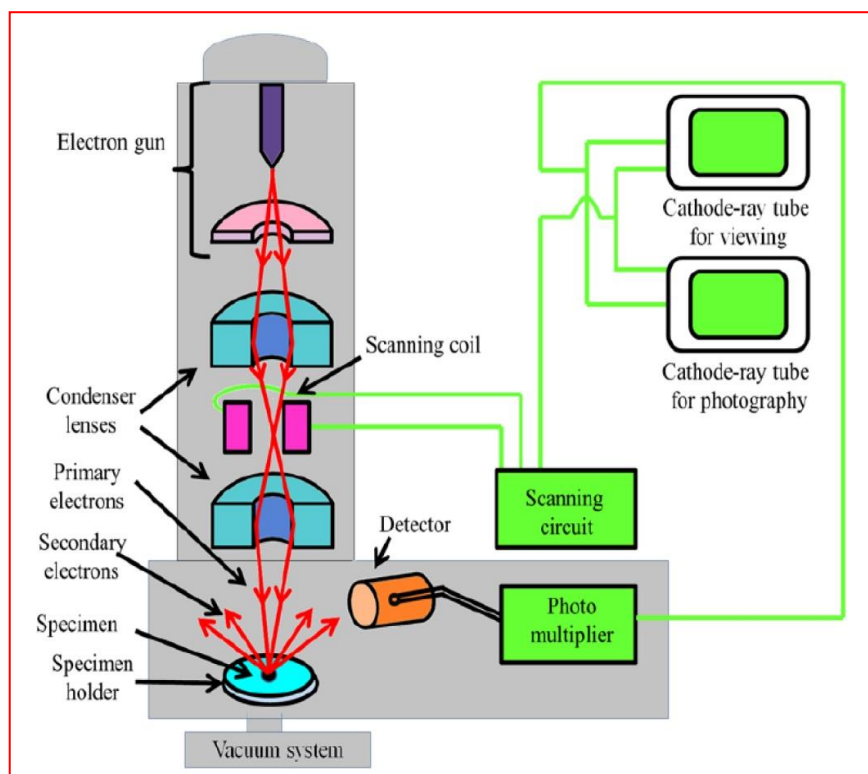


Figure 2.5. Schematic diagram of Scanning electron microscope.

2.4.3. Energy Dispersive Absorption X-Ray Spectroscopy (EDAX)

Many times, SEM is furnished along with energy dispersive absorption X-ray spectroscopy (EDAX) for gathering information about element composition in the composites. EDAX is a non-destructive technique which provides information related to material specifics, impurity content, and the relative ratio of chemical composition of specimen. The X-rays produced from the sample are placed under electron beam to lose excess energy. The X-rays are characteristic in nature i.e., their peak position or energies correspond to specific atoms in spectrum and height of peak corresponds to amount of element present. The information about compositions in sample can be obtained by X-ray mapping and line profiling.

2.4.4. Fourier Transform Infra-Red Spectroscopy (FT-IR)

This is a crucial technique which offers identification of functional groups present in a molecule / specimen. The peaks in IR spectra correspond to constituent of organic or inorganic specimen. The fundamental working principle of FT-IR technique is the characteristic feature of molecular bonds vibrating at specific frequencies corresponding to constituent of elements and their bonding structure. The molecular

vibrational energy lies in the IR range so when the specimen is made to incident with IR beam, it excites the molecule to attain high vibrational energy level. The FT-IR spectrometer consists of an IR source, interferometer, IR-detector and screen. The IR beam produced from IR source is modulated with the help of interferometer and incident on the specimen. The detector detects and records the transmitted radiation or reflected radiation with various wavelengths of IR beam and such a spectrum is termed interferogram. This interferogram can be converted to single beam IR spectrum by employing Fourier transform technique. The plot of FT-IR is a graph displaying percentage intensity of transmittance / absorbance of radiation from specimen with wave number. In the present work, the FT-IR spectra were recorded using Perkin Elmer RX1 FT-IR instrument operating in the wave number range of 400-4000 cm^{-1} and is shown in Fig. 2.6.



Figure 2.6. Perkin Elmer FT-IR Setup.

2.4.5. Raman Spectroscopy

Raman spectroscopy is a distinctive spectroscopic method which exploits the light-matter interaction and provides useful information regarding specimen characteristics. In this technique, electromagnetic radiation is made to interact with specimen resulting in Raman scattering with additional frequencies on either side of incident radiation as characteristic of specimen. This technique provides understanding of intra-molecular and inter-molecular vibration level present in the specimen. Along the advancement of laser sources, Raman spectroscopy has emerged as sensitive technique for the complex systems.

The fundamental working principle of Raman spectrometer is that when light strikes on liquid or solid, the incident photons are elastically scattered with same frequency and are termed as Rayleigh scattering. However, few photons are

inelastically scattered at frequencies other than incident frequency termed as Raman scattering. The change in frequency is related to change in molecular polarizability. The incident photon can often result in the deformation of electron cloud of molecule which causes change in polarizability. The vibrational energy of molecules corresponds to specific transitional levels linking to polarizability change and consequently only some Raman active modes are observed.



Figure 2.7. Renishaw Raman Microscope.

The essential components of Raman spectrometer are radiation source, mounting device, and detector. The laser light is focused at the sample with $1/3^{\text{rd}}$ of incident intensity onto the sample placed at mounting device. The beam scattered from the sample is collected by the detector which produces signal at certain frequencies. The intensity of scattered light varies as the fourth power of its frequency, intensity of incident radiation, scattering cross section and specimen quantity. For the present work, Renishaw Raman Microscope with laser excitation wavelength of 785 nm has been used and is shown in Fig. 2.7. The specimens discussed in this work were dissolved in chloroform.

2.4.6. Vibrating Sample Magnetometer (VSM)

The magnetic property viz., magnetization of any specimen is usually measured with the help of vibrating sample magnetometer (VSM). The VSM setup used in the present work is VSM Microsense EV9 as shown in Fig. 2.8. The fundamental working principle is based on the Faraday's Law of electromagnetic induction where a change in magnetic field generates an

electric field. Such an electric field is measurable and provides details of causal magnetic field.



Figure 2.8. Vibrating Sample Magnetometer (VSM) setup.

The VSM instrument measures magnetic content in the specimen. The specimen of interest is kept in a constant magnetic field. In case of magnetic specimen, the implemented field magnetizes the sample by forcing the domains to align along the field direction. Higher field would create stronger magnetization. This creates a magnetic field, often referred as stray field, around the specimen. When the sample begins to vibrate up and down, the stray field varies with time and creates an electric field following Faraday's Law. This electric field is detected by a set of pick-up coils and the magnitude of current depends on the strength of magnetization in the specimen. This current is converted to voltage with the help of transimpedance amplifier and is amplified with the help of lock-in amplifier using computer interface. This device provides information about magnetic property content and extent of magnetization in the specimen.

2.4.7. Ferroelectric Loop Tracer

The ferroelectric property of any material is measured on the basis of electric polarization. The ferroelectricity is typically displayed as a hysteresis loop of polarization developed versus electric field applied at a particular frequency. The hysteresis loop recording is based on an electric circuit employed by Sawyer and Tower which displayed phenomenal results on Rochelle salt. A modified Sawyer-Tower circuit used in all P-E hysteresis loop measurement along with the experimental setup is shown in Fig. 2.9 [135]. The sinusoidal electric signal of typically 50 Hz frequency implemented on the specimen is divided by potential divider circuit and consequently, current is stored in the form of charge in the capacitors. These voltages are thereby connected to oscilloscope which produce P-E hysteresis loop.

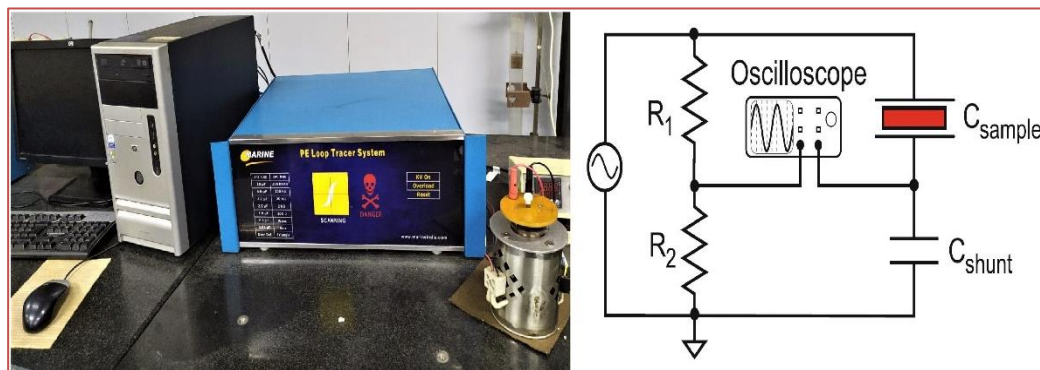


Figure 2.9. P-E loop tracer system with Sawyer-Tower circuit.

2.4.8. Dielectric Measurements: LCR Meter and Impedance Analyzer

The electrical properties like Inductance (L), Capacitance (C) and Resistance (R) of a specimen is measured using LCR meter. The working principle of LCR Meter is based on Wheatstone bridge. The schematic representation of Wheatstone bridge along with Wayne Kerr 6500P LCR meter is shown in Fig. 2.10. The value of unknown sample with impedance Z_x can be obtained using the relation expressed in Fig. 2.10., when the bridge is balanced i.e., the current through the galvanometer is zero. All these parameters are calculated by measuring Impedance of the specimen. These LCR circuits are unique because of characteristic current / voltage / impedance at resonance frequency. Consequently, such circuits are termed as tuning circuits because of attainment of maximum / minimum at certain chosen / rejected frequencies.

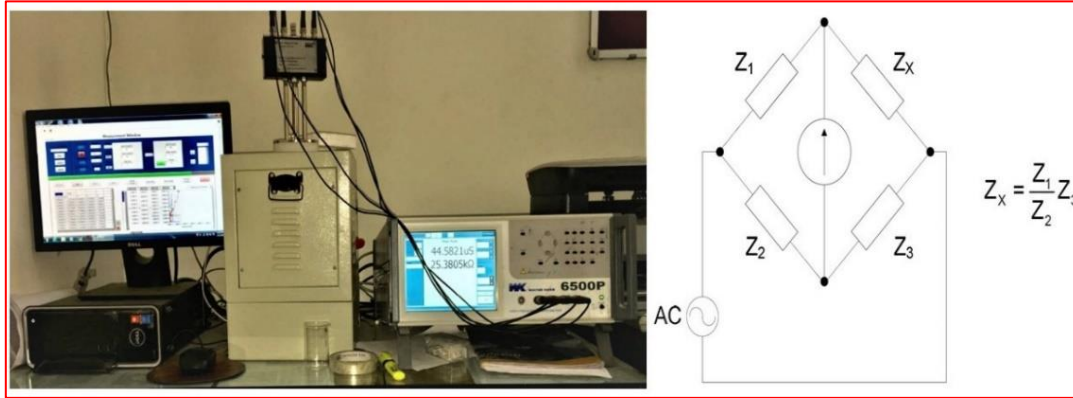


Figure 2.10. Wayne Kerr LCR Meter setup with Wheatstone bridge circuit.



Figure 2.11. Novo Control Broadband Dielectric / Impedance Spectrometer setup.

The series LCR circuit consists of component L, C, R in series and of parallel LCR circuit consists of parallel arrangement of L and C component with R in series with L. The LCR meter measures capacitance (C) and dielectric loss ($\tan \delta$). The following relations are used to obtain real (ϵ') and imaginary (ϵ'') parts of dielectric constant [136,137]

$$\varepsilon' = \frac{C \cdot t}{\varepsilon_0 \cdot A} \quad (2.5)$$

$$\tan \delta = \frac{\varepsilon'}{\varepsilon''} \quad (2.6)$$

where C, t and A denotes capacitance (in pico-farads), thickness (in cm) and, cross sectional area of sample pellet, respectively. For the present work, the composite specimens were hard pressed into circular shape with silver coating on opposite sides for making the specimen pellet better dielectric. The impedance and conductivity parameters were obtained from dielectric parameters using the following relation.

$$\varepsilon^* = \varepsilon' - j\varepsilon'' \quad (2.7)$$

$$Z^* = Z' - jZ'' = \frac{1}{j\omega C_0 \varepsilon^*} \quad (2.8)$$

$$M^*(\omega) = M' + jM'' = \frac{1}{\varepsilon^*} = j\omega C_0 Z^* \quad (2.9)$$

$$\sigma_{ac} = \omega \varepsilon' \varepsilon_0 \tan \delta \quad (2.10)$$

The dielectric, impedance and conductivity of different composites discussed in this work were measured using Wayne Kerr 6500 P high-frequency LCR meter and Impedance Analyzer (Novo Control) as shown in Figs. 2.10 and 2.11, respectively.

Chapter - 3

Effect of CoFe_2O_4 on Structural, Electrical and Magnetoelectric Properties of $\text{BaTiO}_3\text{-CoFe}_2\text{O}_4$ Composites

This chapter focusses on the comprehensive studies of ferroelectric - ferrite composites of BaTiO_3 - CoFe_2O_4 (BT-CFO) synthesized via solid state reaction method. XRD, FT-IR, SEM-EDAX and Raman studies confirm the pure phase of BT and BT-CFO composite formation. The dielectric measurements reveal the Maxwell-Wagner polarization and thermal activated relaxation process arising from movement of defects and ions in BT and BT-CFO composites. Particularly BT-5CFO composite exhibited a surprising low dielectric loss (≈ 0.3) over the frequency range of 100 Hz - 1 MHz and promises industrial application. The thermal variation of Impedance and modulus parameters revealed resistive nature of the composites and the presence of two thermally activated non-Debye type relaxation mechanism present in BT and BT-CFO composites. The conductivity measurements confirm polaron tunneling conduction mechanism in the composites. The P-E loop measurements confirmed the ferroelectric nature in BT-CFO composites with maximum energy storage of 8.33 mJ/cm^3 and efficiency of 59.7 % achieved for 0.95BT-0.05CFO composite. The Polarization (P) versus magnetic field (H) analysis confirmed the highest magneto-electric coefficient of 13.33 mV/cm/Oe for 0.95BT-0.05CFO composite. These results reveal magnetoelectric nature in BaTiO_3 - CoFe_2O_4 composites and could be beneficial in enhancing the properties of BT-CFO based energy storage systems.

3.1. Introduction

The weak coupling in single phase multiferroics owing due to atomic diffusion and undesirable chemical reactions [34] and their scarcity has motivated the research of composite materials [138]. ME composites with large magnitudes of the ME voltage coefficient have turned out to be better alternatives. These composites exploit the product property of piezomagnetic and piezoelectric phases or individual magnetostrictive and piezoelectric phases of the materials.

Usually, a magnetoelectric composite consists of ferroelectric and ferromagnetic for piezoelectricity and magnetostriction to exhibit multiferroism. The coupling in these magnetoelectrics arises due to the indirect mechanical strain transfer at the interface of two phases. The composites based on BaTiO_3 show greater enhancement in multiple properties such as dielectric constant, impedance, M-E coupling and energy storage by exploiting the distortions and orientations of cationic positions and are useful from technological point of view. Recently, many scientists reported even the electrical, impedance, dielectric modulus, ferroelectric, optical, multiferroic properties of lead titanate, and barium titanate based materials [20,139–142]. Perovskite BT is a good functional ceramic exhibiting polymorphic structure with interesting ferroelectric and optical properties. BT has found its applications in multilayer ceramic capacitors (MLCC), transducers, actuators, energy storage ferroelectric random access memories [77]. BT based materials are the basis for magnetoelectric devices and additionally provide the tunability in the tetragonal-cubic phase transition by adjusting the constituent contributions or doping which substituting at the Ba or Ti sites or both or composite formation. CoFe_2O_4 (CFO), a spinel ferrite, is well known for its remarkable electrical, optical, and magnetic properties, especially at nanometer scale [143]. The composites of BaTiO_3 – CoFe_2O_4 has exciting magnetoelectric properties due to the contribution of their individual phases limited to a certain extent [86,144]. Though the magnetoelectric coupling observed in these materials was very low due to the undesirable phases of CFO and microstructural distortion in the composites. One of the efforts to improve the performance in electronic devices based on barium titanate, is the BT - metal ferrite composites [84,85,151,86,143,145–150] by exploring the percolation threshold. A modest improvement in the permittivity has been detected at low levels on addition of the conducting ferrite phase [152]. However, the studies of addition of CFO in low

concentration to BT is not completely explored to observe the origin of coupling in BT-CFO composites. Furthermore, an intense study on electrical and dielectric properties of BT-CFO composites is essential for their scientific and technological advancements. In this regard, this chapter describes the synthesis of $\text{BaTiO}_3\text{-CoFe}_2\text{O}_4$ (BT-CFO) composite to study the effect of low stoichiometry of CFO on the structural, dielectric, conductivity, impedance, magneto-dielectric coupling, ferroelectric P-E and magnetoelectric properties of BT.

3.2. Sample Preparation

The $(1-x)\text{BT-xCFO}$ ($x = 0, 0.01$ and 0.05) composites were prepared by solid state reaction route as discussed in section 2.3 and as represented in Fig. 2.1. The AR grade of chemicals BaCO_3 , TiO_2 , Co_3O_4 and Fe_2O_3 were used as initial ingredients in stoichiometric ratio. The synthesis conditions have been tabulated in Table 3.1. The composites are named as BT (BaTiO_3), BT-1CFO ($0.99\text{BaTiO}_3 - 0.01\text{CoFe}_2\text{O}_4$) and BT-5CFO ($0.95\text{BaTiO}_3 - 0.05\text{CoFe}_2\text{O}_4$).

Table 3.1. Synthesis conditions of BaTiO_3 , CoFe_2O_4 and $\text{BaTiO}_3 - \text{CoFe}_2\text{O}_4$ composites.

Composition	Calcination temperature (°C)	Duration (h)	Sintering temperature (°C)	Duration (h)
BaTiO_3	1000	10	1100	12
CoFe_2O_4	900	8	-	-
BT-1CFO	-	-	750	10
BT-5CFO	-	-	750	10

3.3. Results and Discussion

3.3.1. Structural and Morphological Measurements

The phase purity and content for different compositions are shown in Fig. 3.1. The diffraction patterns were matched and indexed with JCPDS # 05-0626 for BT phase [6]. The tetragonality of BT is confirmed from the splitting of diffraction peaks at 2θ diffraction angles: 31° , 45° , 56° , 66° and 75° with miller indices (101), (002), (112), (202) and (103) for all the composites. The intensity of BT peaks didn't decrease significantly on increasing the concentration of cobalt ferrite. However, the small peaks

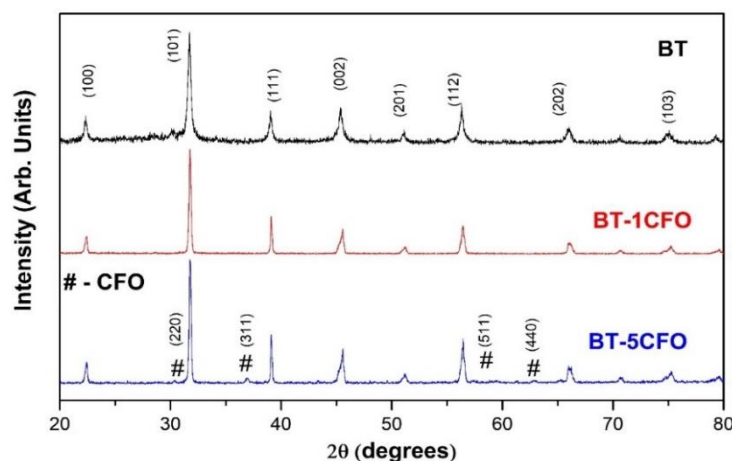


Figure 3.1. XRD patterns of BaTiO_3 and $\text{BaTiO}_3 - \text{CoFe}_2\text{O}_4$ composites.

due to cubic spinel cobalt ferrite matched with JCPDS # 22-1086 are observed in BT-5CFO sample (denoted by #). This confirms the co-existence of ferroelectric and ferromagnetic phases.

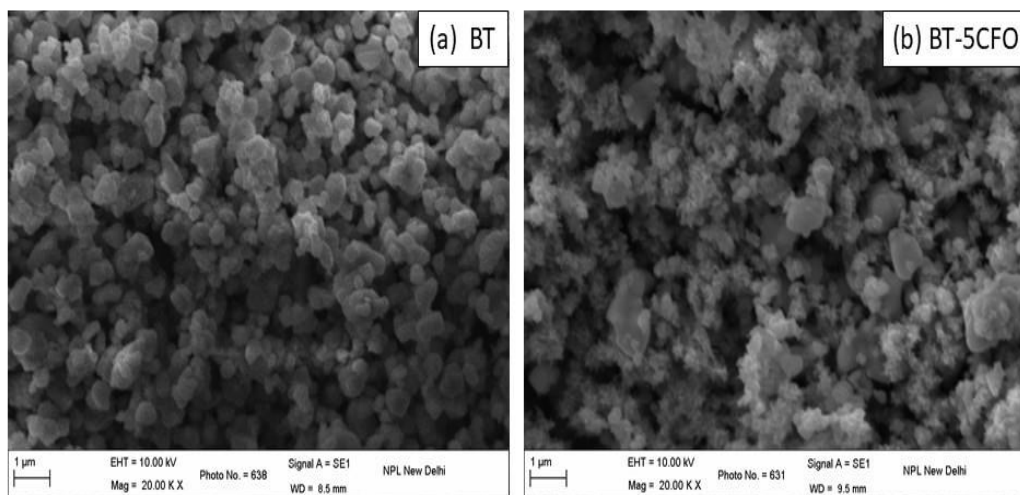


Figure 3.2. SEM micrographs of (a) BT and (b) BT-CFO composites.

The presence of CFO and formation of composite of BT-CFO have been verified by the scanning electron microscopy (SEM) and energy-dispersive X-ray absorption spectroscopy (EDAX). The SEM images of BT and BT-5CFO are shown in Fig. 3.2. The agglomeration at few places as corresponds to CFO and small white grain corresponds to BT of SEM images confirm the presence of two different domains of BT and CFO respectively in the BT-5CFO composite. The EDAX analysis confirms the presence of CFO in BT-5CFO sample due to clear percentage amount of CFO as seen in Fig. 3.3 and the strength of the peaks enhanced after the CFO addition in to BT.

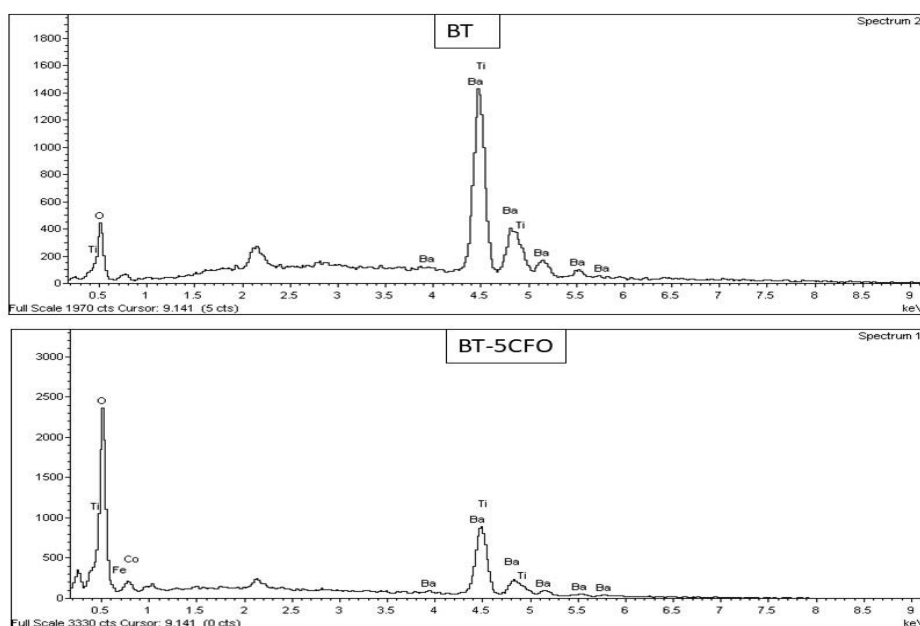


Figure 3.3. EDAX patterns of BT and BT-CFO composites.

High strength of the peaks of BT-5CFO comparative to pure BT is due to the magnetic nature of the CFO and also further confirms the composite formation [52,153–155].

The FT-IR spectra of BT and BT-CFO composites are presented in Fig. 3.4. The characteristic absorption band at 3486 cm^{-1} is assigned to the O-H stretching vibration in water and confirms that the existence of the water in the BT and BT-CFO composites. The presence of the band located at 542 cm^{-1} is specific to the vibration mode of the Ti-O bond in the TiO_6 octahedra [156]. In cobalt ferrite ceramic, the FT-IR spectrum has

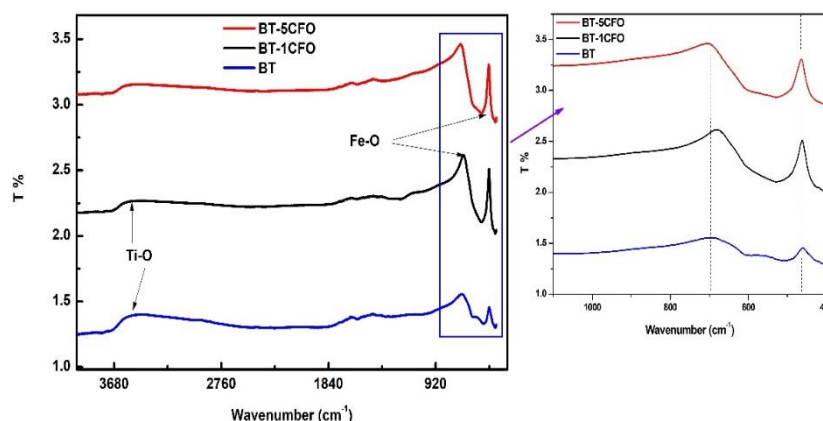


Figure 3.4. FT-IR spectra of BT and BT-CFO composites.

peaks near 600 and 450 cm^{-1} represent the characteristic peaks of Co_2O_3 [157]. The bands at these wavenumbers represent tetrahedral and octahedral clusters and also confirm the presence of Fe-O stretching vibration in cobalt ferrite. The shifting of peak

at 690 cm^{-1} and sharpening of peak at 458 cm^{-1} as in Fig. 3.4 are observed. The anomaly at bands near 600 and 400 cm^{-1} confirms the formation of BT-1CFO and BT-5CFO composites.

The optical vibrations in cubic perovskite structure are exhibited as triply degenerate F_{1u} and F_{2u} modes. The F_{1u} is Raman inactive because of lack of asymmetry in the cubic phase. In tetragonal phase F_{1u} and F_{2u} modes split into A, E and B modes respectively as $4E + 3A + B$. These modes exist as transverse and longitudinal modes due to electrostatic forces spread over long ranges. The Raman spectra of pure BT, BT-1CFO and BT-5CFO composites is displayed in Fig. 3.5. The BT, BT-1CFO and BT-5CFO composites exhibit optical modes at $181, 241, 306, 512, 716\text{ cm}^{-1}$ and confirm tetragonal $P4mm$ crystal symmetry [158]. The transverse mode A_T at 179 cm^{-1} correlates to the non-symmetric metal-oxygen vibration of phonons. The broad spectrum observed around $200 - 275\text{ cm}^{-1}$ is caused by lattice disorder in BT-1CFO and BT-5CFO composites due to the addition of CFO in BT [159]. The presence of longitudinal (E_L) and transverse (E_T) mode at 306 cm^{-1} and symmetric stretching A_L at 716 cm^{-1} resembles ferroelectric phase of tetragonal BaTiO_3 . The transverse A_T mode at 512 cm^{-1} corresponds to the symmetric stretching at TiO_6 octahedra [160]. The intensity of peaks reduces relatively in BT-CFO composites and is more dominant in BT-5CFO composite. The confirmation of composite is ensured from the appearance of peak near 680 cm^{-1} . The origin of high frequency peak at 680 cm^{-1} denote the symmetry mode vibration relating to the metal-oxygen movement at the tetrahedral sites in CoFe_2O_4 [161,162].

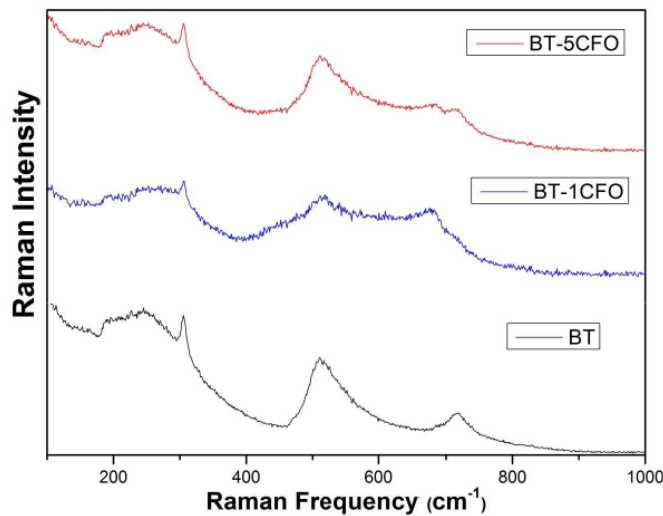


Figure 3.5. Raman spectra of BT and BT-CFO composites.

3.3.2. Dielectric and Magnetodielectric Measurements

The variation of real part of the dielectric constant (ϵ') with frequency for BT, BT-1CFO and BT-5CFO composites in the temperature range 50 °C - 450 °C are shown in Fig. 3.6. All the composites display large dielectric dispersion and exhibit the general Maxwell-Wagner polarization. It is interesting to note that ϵ' for BT drastically decreases with increase in temperature from 50 °C to 150 °C as shown in Fig. 3.6 (a). This decrease can be related to the ferroelectric-paraelectric phase transition at $T_c \approx 130$ °C [4]. A BT like behavior is also observed in BT-1CFO composite as shown in Fig. 3.6 (b). However, in case of BT-5CFO composite as shown in Fig. 3.6 (c) such a change in dielectric constant owing to ferroelectric-paraelectric transition is not observed. This is due to the lattice disorder in BT-CFO composite, as verified by Raman studies, arising from volumetric and piezoelectric strains generated in the BaTiO_3 phase with incorporation of CFO. The decrement in dielectric constant in the remaining temperature range (150 °C - 450 °C) is due to the space charge polarization arising from movement of defects and ions in the composite.

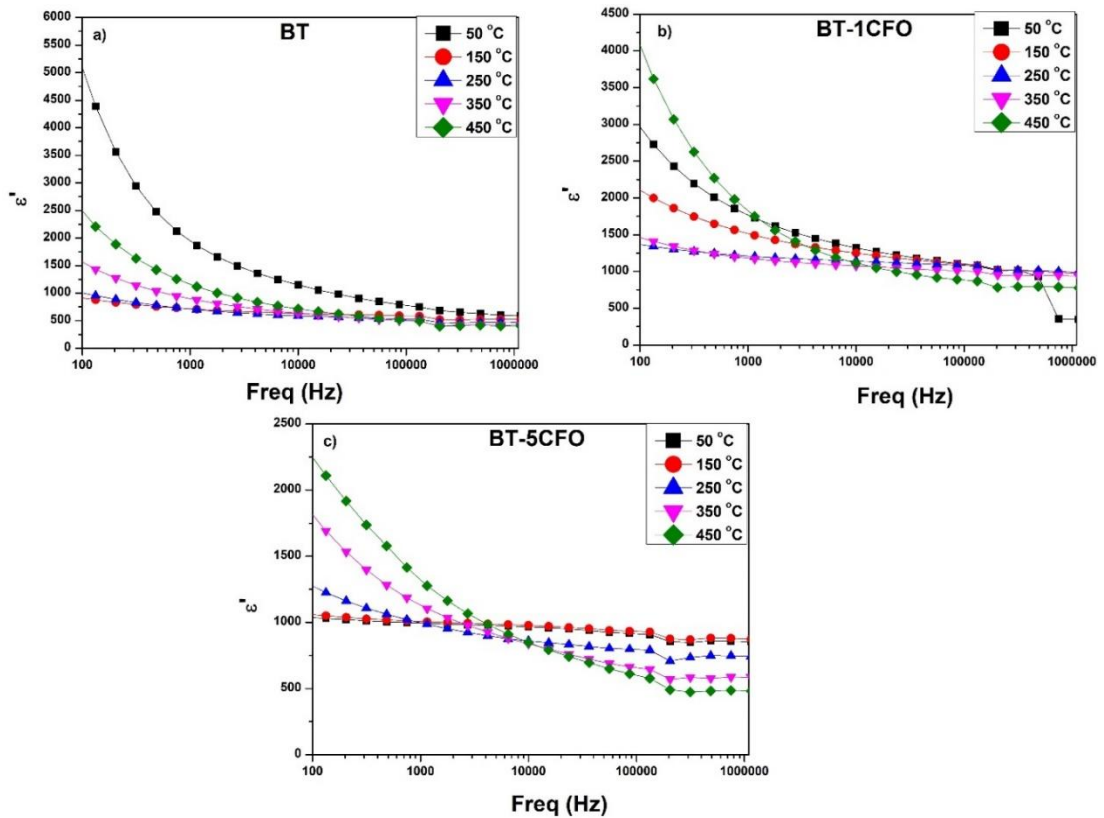


Figure 3.6. Frequency dependence of real part of dielectric constant (ϵ') for (a) BT, (b) BT-1CFO and (c) BT-5CFO composites.

The frequency dependence of dielectric loss ($\tan \delta$) for BT, BT-1CFO and BT-5CFO composites are shown in Fig. 3.7. The loss decreases with increase in frequency for all the compositions. It is exciting to note that the loss remarkably decreases from 4.2 (Fig. 3.7 (a)) to 0.3 (Fig. 3.7 (c)) for BT to BT-5CFO composite at 100 Hz. The value of $\tan \delta$ remains the same over the frequency range 100 Hz - 1 MHz for BT-5CFO composite at 50 °C and 100 °C making them suitable for device application over higher frequencies even at higher temperatures. The dielectric loss for BT, BT-1CFO and BT-5CFO composites shows temperature dependence like the dielectric constant behavior suggesting a thermally activated relaxation process. At 450 °C, the loss is enormous due to change in valency of Ti / Fe ions with different oxidation states creating oxygen vacancies and resulting in a high electrical leakage [163].

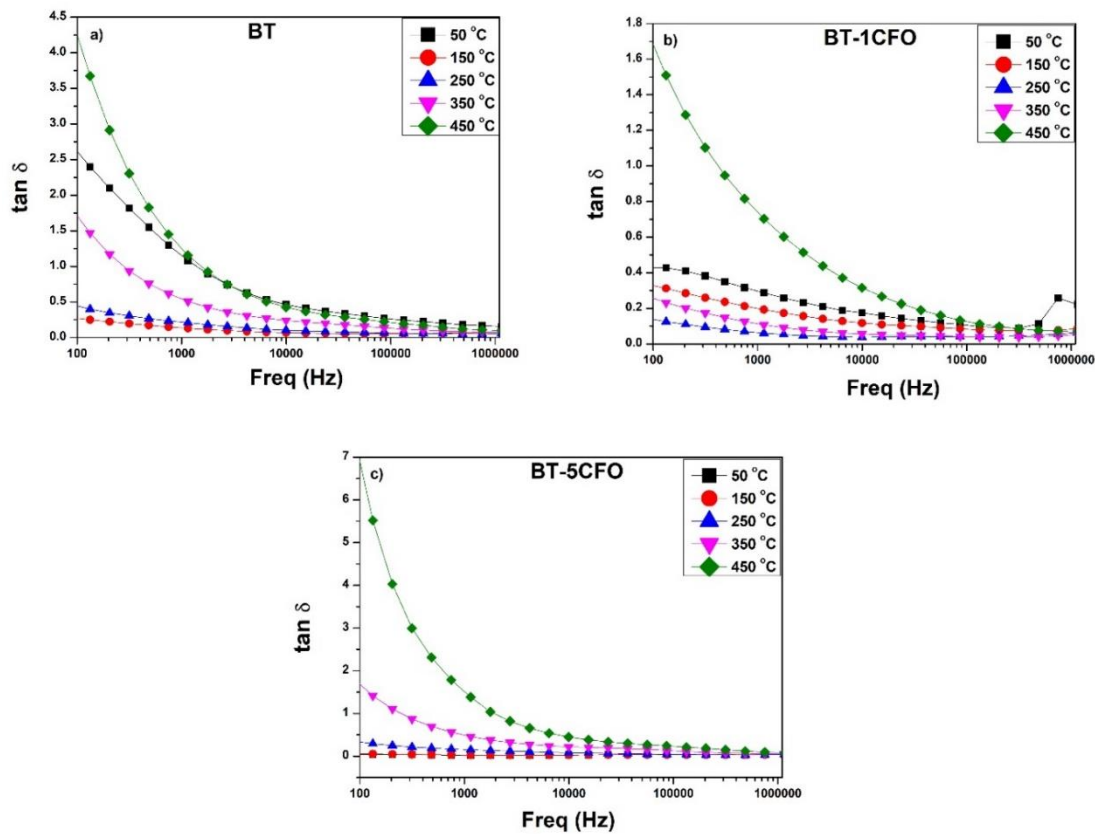


Figure. 3.7. Frequency dependence of dielectric loss ($\tan \delta$) for (a) BT, (b) BT-1CFO and (c) BT-5CFO composites.

In order to understand the impact of incorporation of CFO in BT, the magneto-dielectric coupling effect (% MD) which is quantified as the change in the value of dielectric constant (ϵ') in the presence of external magnetic field measured at fixed

frequency of 10 kHz for BT-1CFO and BT-5CFO composites are shown in Fig. 3.8. The MD is defined as:

$$\%MD = [\varepsilon'(H) - \varepsilon'(0)] / \varepsilon'(H) \times 100 \quad (3.1)$$

where $\varepsilon'(0)$ is the dielectric constant at zero magnetic field and $\varepsilon'(H)$ is the dielectric constant in the presence of magnetic field. Fig. 3.8 displays an increasing trend in the value of % MD with increasing magnetic field and gives an impeccable existence of magneto-dielectric coupling in BT-1CFO and BT-5CFO composites. The maximum value of % MD obtained are 0.3 and 1.2 for BT-1CFO and BT-5CFO composites, respectively. This coupling behavior could be attributed to the strain mediated coupling between the constituent phases. As the amount of CFO is increased the coupling between the phases increases and thus % MD is enhanced for BT-5CFO composite than BT-1CFO composite.

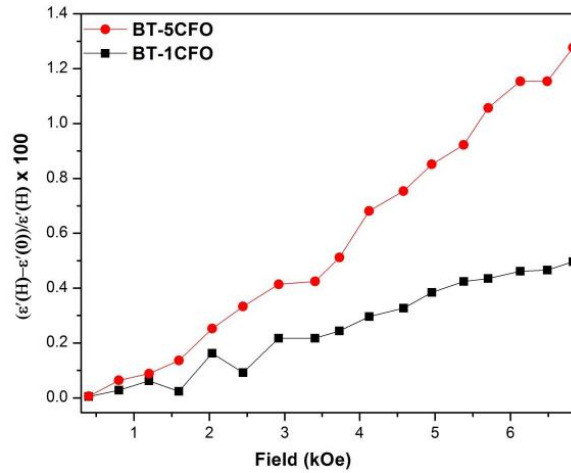


Figure 3.8. Percentage change in dielectric constant of BT-1CFO and BT-5CFO composites as a function of magnetic field at 10 kHz.

3.3.3. Impedance and Modulus Measurements

The impedance analysis helps to sort out the contributions from grains and grain boundaries by depicting the electrical behavior in Nyquist plot as semicircles which represent the individual contributions [164]. To understand the relaxation mechanism, the real and imaginary parts of impedance are plotted versus each other and the resulting Nyquist plots for BT-CFO composites are shown in Fig. 3.9. The Nyquist plots for BT, BT-1CFO and BT-5CFO composites distinctively depict a semicircle which begins from origin with intercept on the Z' axis. It can also be observed that plots of all the BT-CFO composites exhibit single circular arc and suggesting grain effect alone for all temperatures. The Nyquist plots of BT-CFO also give information regarding the grain

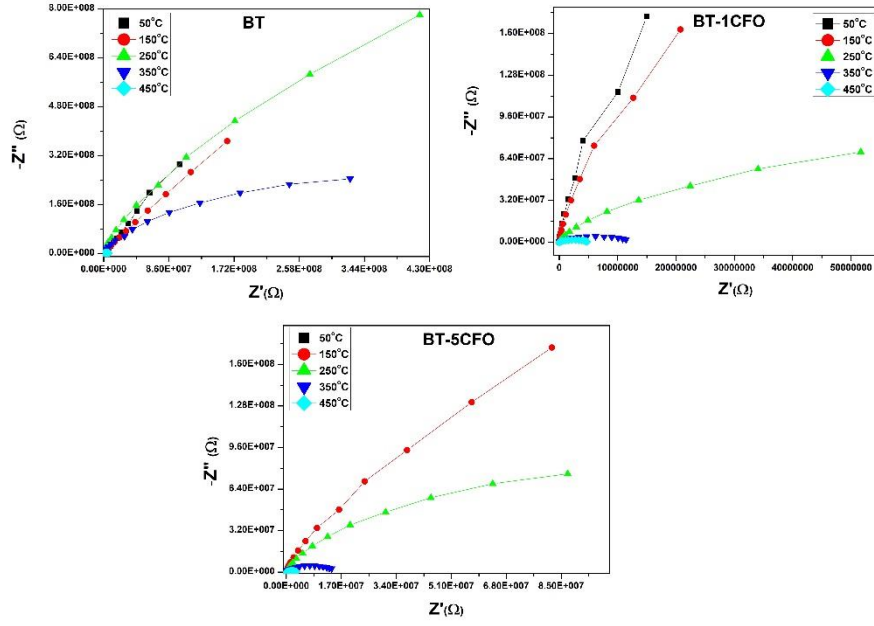


Figure 3.9. Nyquist plot for BT–CFO composites measured at different temperatures.

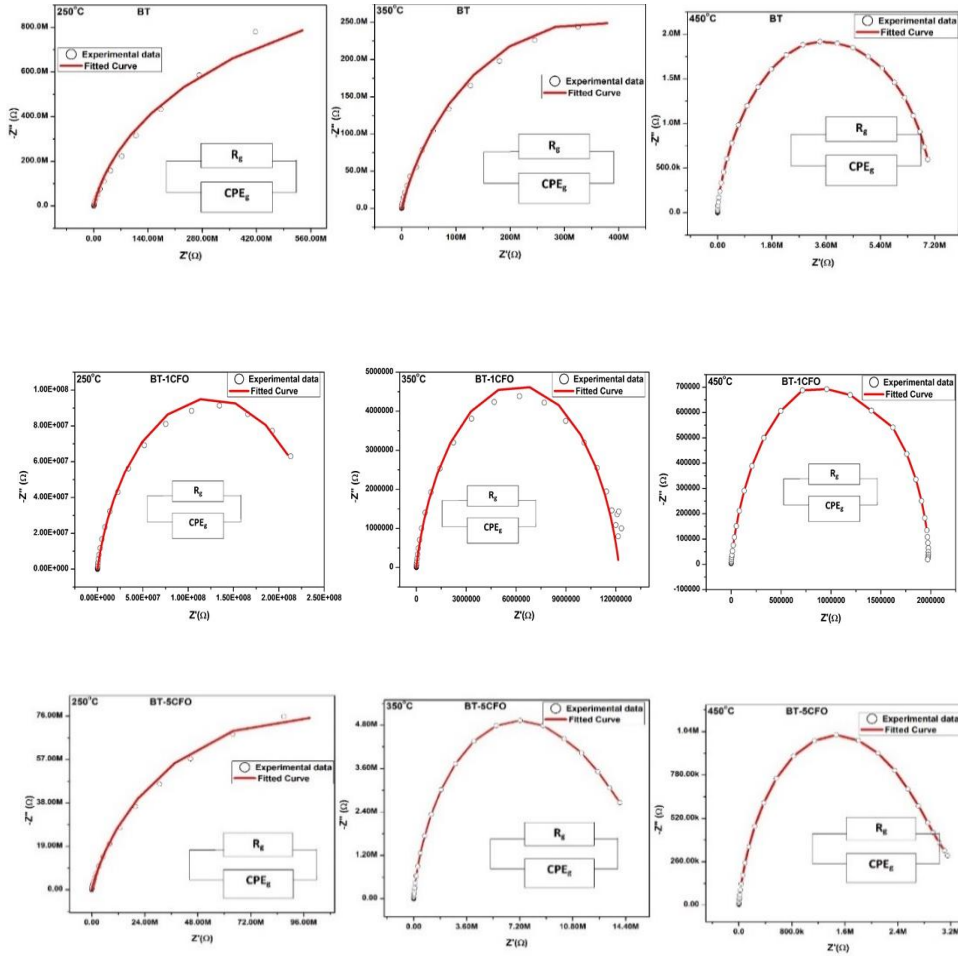


Figure 3.10. Combined Nyquist plots of BT-CFO composites at different temperatures and their equivalent circuit measured.

Table 3.2. Fitted parameters for Cole–Cole plots of BT-CFO composites

Temp (°C)	$R_g (\Omega)$	CPE_g	n_g
BT			
250	2.1×10^9	8.9×10^{-11}	0.92
350	7×10^8	3×10^{-8}	0.79
450	6×10^6	2×10^{-7}	0.72
BT-1CFO			
250	2.5×10^8	9×10^{-9}	0.83
350	1.22×10^7	3×10^{-9}	0.83
450	1.98×10^6	3×10^{-8}	0.81
BT-5CFO			
250	1.9×10^8	8×10^{-10}	0.85
350	1.38×10^7	8×10^{-9}	0.81
450	3×10^6	3×10^{-7}	0.78

resistance behavior. As the temperature is increased, there is a decrease in the radius of the semicircles suggesting a decrease in the resistivity. This thermal decrement of grain resistance suggested temperature dependent conduction mechanism present in BT-CFO composites. The grain resistance estimated from the non-zero intercept of the Nyquist plot on Z' axis is tabulated in Table 3.2. Furthermore, all the semi circles have their centers lie beneath the Z' axis. This low depression is owing to the presence of distributed relaxation times. This kind of curvature depression in semicircles is an evidential confirmation of statistically distributed relaxation times and confirms the non-Debye type relaxation in BT-CFO composites [165,166]. Factors like grain-grain boundaries distribution and vacancies / defects could be responsible for such non-ideal behavior in BT-CFO composites.

The modeling of deviation from Debye type relaxations in BT-CFO composites can be done using the modified brick layer model consisting of parallel combinations of resistance, capacitance and constant phase element (CPE) respectively [167–169]. The equivalent circuit contains a combination of two or more circuits representing the grains, grain boundaries and interface contributions where the individual sub-circuits contain resistor, CPE and / or capacitor connected in parallel. In case of BT-CFO composites, only one equivalent circuit consisting of R and constant phase element (CPE) is sufficient for fitting the Nyquist plots. Fig. 3.10 shows the correlation between the Nyquist (black circle symbols) plots and fitted data (solid red line). The values of

R and CPE obtained from fitting are tabulated in Table 3.2. It can be observed that the experimental data and fitted spectra are in good agreement with each other. Moreover, the non-Debye behavior present in BT-CFO composites is justified from the presence of CPE in the equivalent circuit which is related to the impedance by the equation $Z_{CPE} = 1/(j\omega)^n$ CPE.

The variation of real part of impedance Z' with frequency at different temperatures for the BT, BT-1CFO and BT-5CFO composites is shown in Fig. 3.11. respectively. It can be observed that, for all the compositions, Z' is high in the lower frequency region displaying frequency dispersion and declines constantly with frequency up to 100 kHz at all the temperatures and merges at 1 MHz. This suggests that space charge effect is dominant in the low frequency region and a possible release of space charge in the high frequency region. This sharp decrease in Z' over the

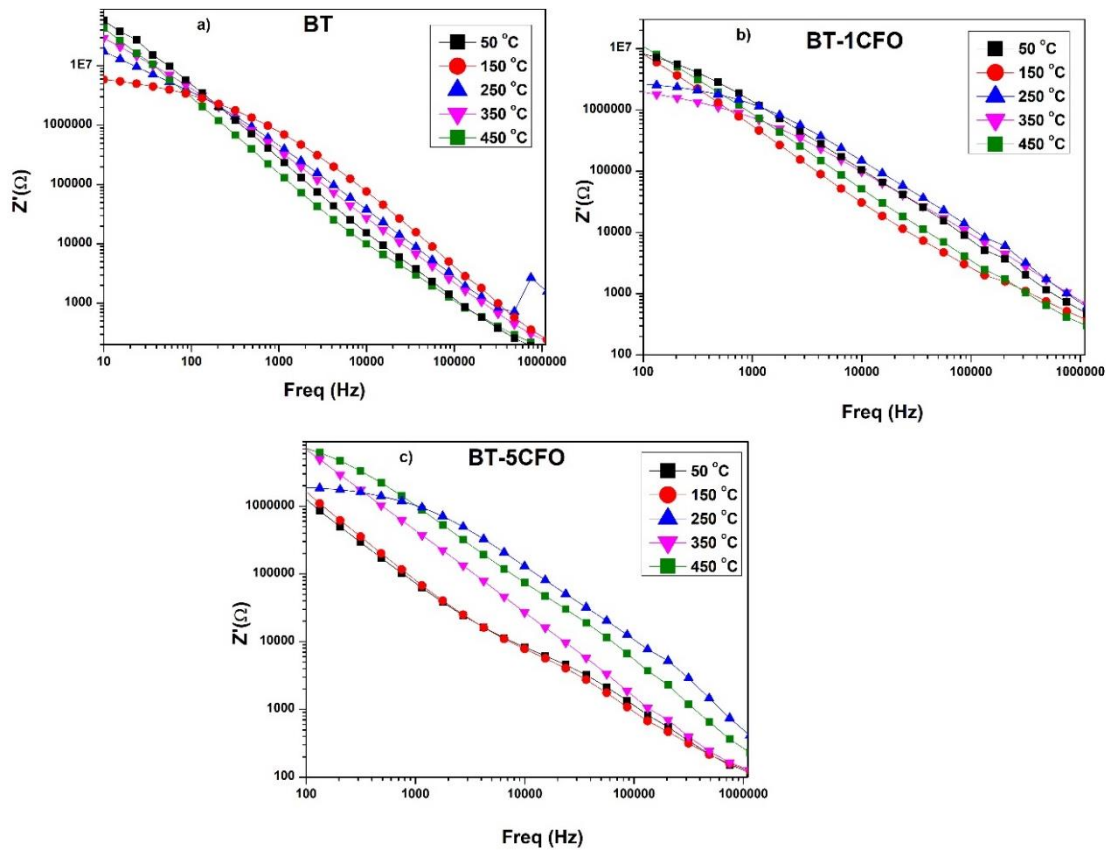


Figure 3.11. Frequency dependence of real part of impedance (Z') for BT and BT-CFO composites.

frequencies 100 Hz - 1 MHz confirm the resistive property in all the compositions. In addition to this, the increase in amount of CFO in BT reduces the impedance (Z') value

from 60 M Ω in BT to 1 M Ω in BT-5CFO composite at 100 Hz. It is also relevant to observe that Z' decreases with the increase in temperature confirming the temperature dependent behavior of the dispersion in the conductivity. This is mainly due to decrease in the grain and grain boundaries resistance [170].

The frequency dependence of complex part of impedance Z'' for BT, BT-1CFO and BT-5CFO composites are shown in Fig. 3.12. The plot of Z'' is crucial in inspecting the behavior of most resistive phase in the composites. It can be observed that the spectrum contains two peaks associated with two different relaxation times and are indicated by circles. This suggests the presence of more than one relaxation process present in BT-CFO composites. The lower frequency peaks correspond to the

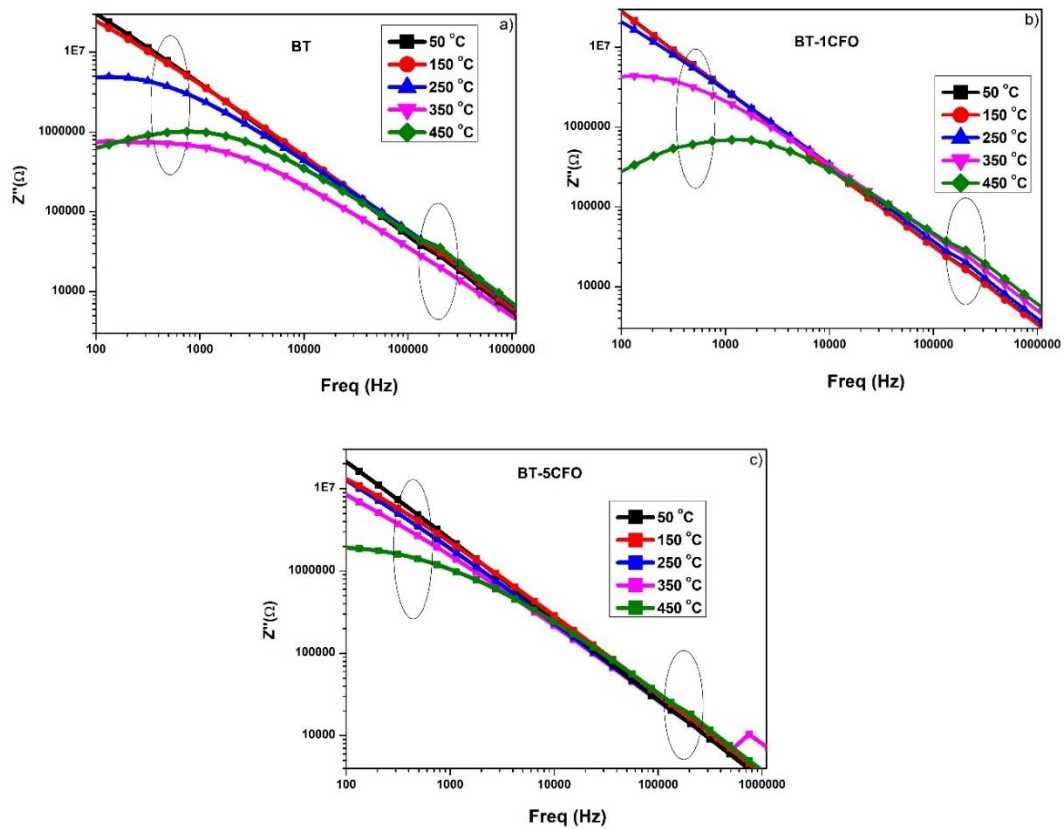


Figure 3.12 Frequency dependence of complex part of impedance (Z'') for BT and BT-CFO composites.

relaxation mechanism associated with grain boundaries and the other peaks attribute to the grain contributions. As the temperature is increased, the peaks tend to shift towards high frequency regime confirming the temperature dependent movement of charge carriers in both grains and grain boundaries [170]. On increasing the content of CFO in

BT, the second relaxation peak at high frequency diminishes suggesting the dominance of hopping mechanism for the charge carriers in BT-5CFO composite.

The modulus spectroscopy helps in differentiating the contribution of electrode polarization and grain boundaries to the conduction process. The complex electric modulus is related to complex impedance by Equation (2.9). Fig. 3.13 shows the

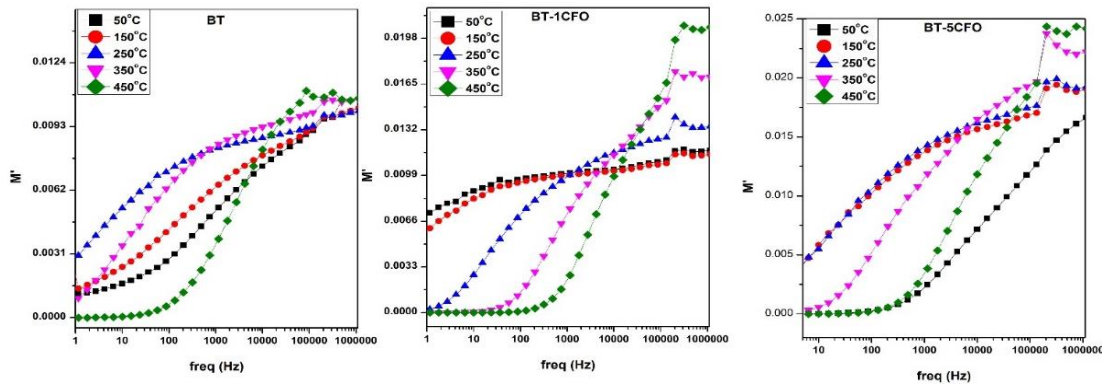


Figure 3.13. Variation of M' with respect to frequency of BT-CFO composites.

variation in real part of modulus (M') with frequency at the fixed different temperatures for BT-CFO composites. It can be seen from the Fig. 3.13 that M' starts from a very low near zero value in the low frequency regime and saturates to high value in higher frequency regime confirming the short-range conduction of charge carriers. On increasing the content of CFO in BT the saturation value decreases due to the localization of polarons. Fig. 3.14 shows the variation in the complex part of modulus (M'') as a function of frequency. It is observed from the graph that all the BT-CFO composites exhibit a peak at all the measured temperatures which shift with the rise in

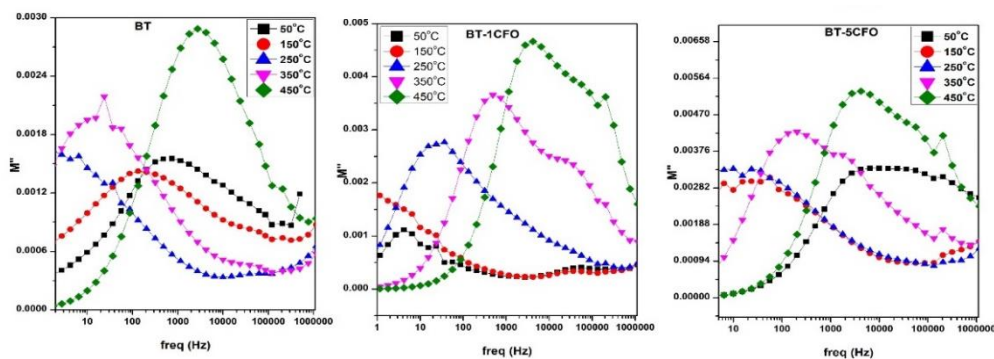


Figure 3.14. Variation of M'' with respect to frequency of BT-CFO composites.

temperature. All the peaks observed display an asymmetric broadening confirming the statistically distributed relaxation times and the non-Debye type behavior of BT-CFO

composites. In addition to this, at higher temperatures, the maxima shift towards higher frequency confirming the thermally activated conduction mechanism present in BT-CFO composites.

3.3.4. Conductivity Measurements

The variation of real part of conductivity (σ') with frequency at fixed different temperature for BT, BT-1CFO and BT-5CFO composites is represented in Fig. 3.15. The conductivity at low frequencies at 50 °C is nearly constant and represents the dc conductivity. This behavior is attributed to the charge carrier's movement across the insulating grain boundaries. Contrarily, in the high frequency regime, the conductivity sharply increases with frequency and display a strong frequency dispersion. This dispersion is attributed to enlarged mobility of charge carriers. In addition, at high frequencies, pronounced conduction mechanism could be generated between the Fe^{3+} /

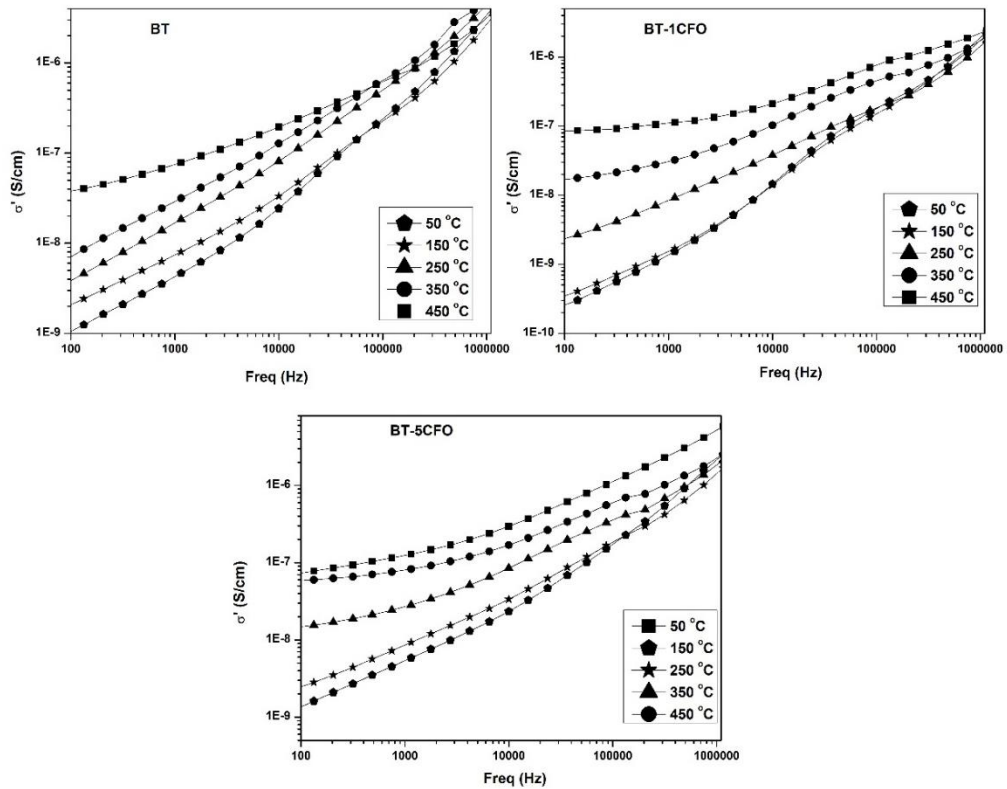


Figure 3.15. Plot of conductivity (σ') as function of frequency measured at different temperatures for BT and BT-CFO composites.

Fe^{2+} and $\text{Ti}^{4+} / \text{Ti}^{3+}$ ions. The conductivity (σ') decreases with increasing temperature in case of all the composites confirming thermally activated conduction mechanism. To explore the conduction mechanism in BT, BT-1CFO and BT-5CFO composites, the conductivity (σ') is expressed as [171]:

$$\sigma' = \sigma_{dc} + \sigma_{ac} = \sigma_{dc} + A\omega^n \quad (3.2)$$

where the constants A and n are temperature dependent. In order to obtain the dc and ac components of conductivity, the total conductivity for BT-5CFO composite was fitted as power function of the frequency.

The variation in the dc-conductivity (σ_{dc}) with temperature is used to estimate the activation energy (E_a) of the BT, BT-1CFO and BT-5CFO composites by employing the Arrhenius relation

$$\sigma_{dc} = \sigma_0 e^{-E_a/k_B T} \quad (3.3)$$

where σ_0 , k_B , T denote the pre-exponential factor, Boltzmann constant and absolute

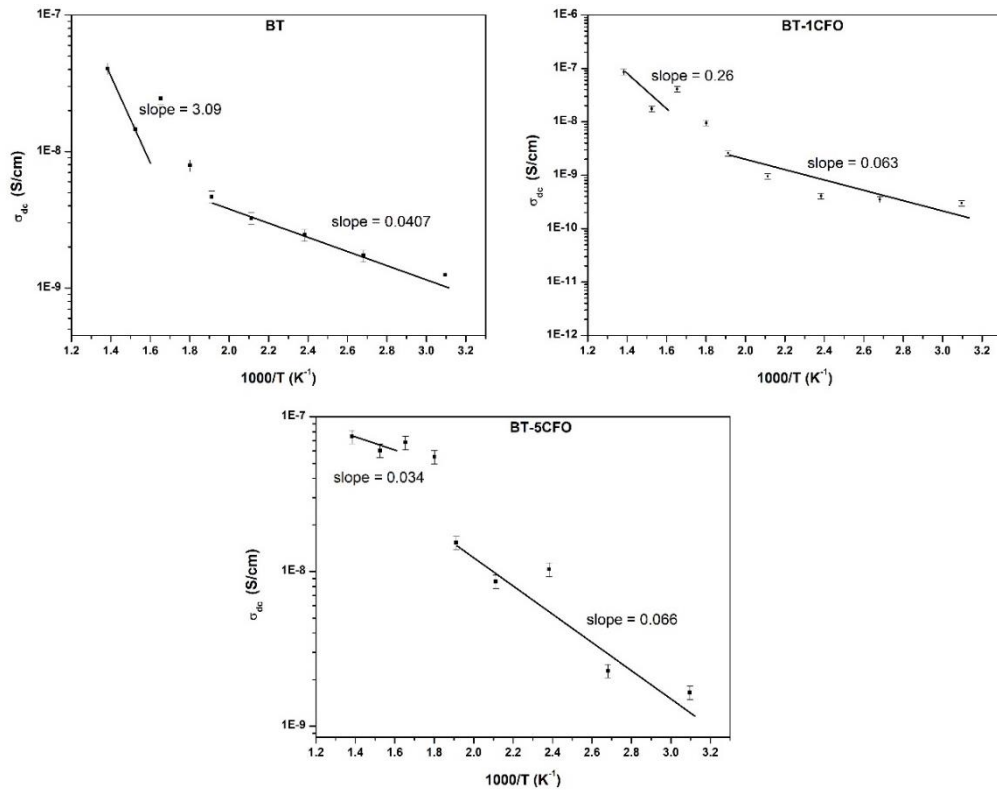


Figure 3.16 Plot of dc conductivity as a function of temperature ($10^3/T$) for BT, BT-1CFO and BT-5CFO composites.

temperature, respectively. The plot of σ_{dc} with temperature is shown in Fig. 3.16. Based on the temperature range, different slopes and activation energies have been estimated.

The activation energy estimated is tabulated in Table 3.3 for BT, BT-1CFO and BT-5CFO composites. It can be observed from Table 3.3 that the activation energy (E_a) for all the compositions obtained is much less than 1 eV, confirming the dominance of singly ionized oxygen in governing the thermal activated conduction process [172–174]. The oxygen vacancies are generated by the thermal excitations of electrons resulting in the reduction of Ti^{4+} to Ti^{3+} as given by Kroger-Vink equation of defects:



where V_o^{**} is the ionized metal. These defects generated during synthesis modify the interfacial resistance at grain / grain-boundary.

Table 3.3. Values of activation energy (E_a) in (eV) obtained from fitting of dc conductivity with $1000/T$ (K^{-1}).

Temp (°C)	BT (eV)	BT-1CFO (eV)	BT-5CFO (eV)
50-150	0.266	0.261	0.034
250-450	0.041	0.063	0.062

In order to realize the conduction behavior dominant in BT-CFO system, the temperature dependence of exponent n is shown in Fig. 3.17. As per Jonscher's power law, the ac-conductivity term $A\omega^n$ determines the kind of conductivity phenomena prevailing in the material. Depending on the change in the value of exponent n it is decided whether the mechanism is governed by QMT (quantum mechanical tunneling)

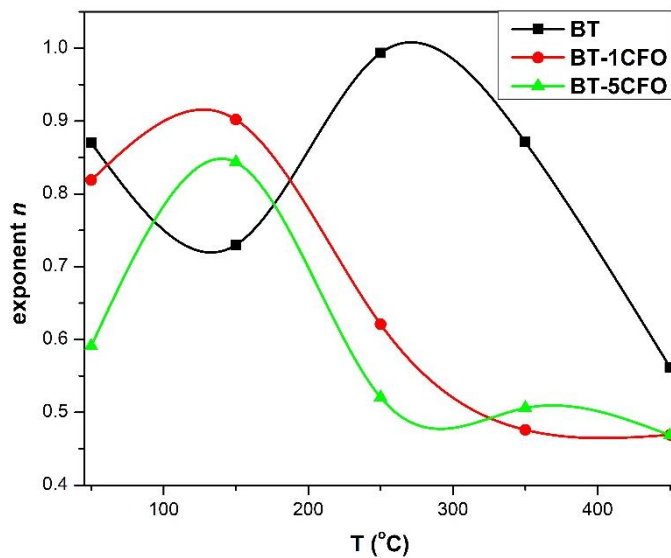


Figure 3.17. Variation of exponent n as a function of temperature for BT, BT-1CFO and BT-5CFO composites.

or CBH (correlated barrier hopping) or OLPT (overlapping large-polaron tunneling). If the exponent n remains almost equal to 0.8 and increases slightly with temperature or does not change with temperature then such a conduction phenomenon is related to QMT behavior through localized sites separated by the barriers. In QMT, the exponent n is temperature independent and frequency dependent. However, a temperature dependent frequency independent exponent n is expected in light of QMT by presuming that the charge carriers form non-overlapping small polarons and propagate via non-overlapping small polaron tunneling (NSPT). The NSPT model allows exponent n to be temperature dependent with increasing behavior. On the contrary, if the exponent n shows a decreasing trend with temperature, then the conduction is related to the CBH phenomenon concerning the same barrier. In OLPT, the exponent n displays both frequency and temperature dependence and reaches a minimum with increasing temperature. and increases with temperature beyond the minimum value [175]. From Fig. 3.17, it is observed that the exponent n shows a dispersive behavior with temperature confirming the presence of more than one type of conduction process present in BT and BT-CFO composites. The conductivity behavior for bulk BT follows OLPT model most suitably with exponent n reaching a minimum at 150 °C. Below $T \leq 150$ °C, the conduction phenomena for BT-1CFO composite strongly agrees with NSPT model. Also, for BT-5CFO composite, the conductivity behavior more or less follows NSPT model. The crossover in the conductivity from OLPT having delocalized polarons in BT to NSPT having localized polarons in BT-CFO composites could be due to the decreasing of electrical conductivity as a result of CFO addition in BT. For $T \geq 150$ °C, whereas both BT-1CFO and BT-5CFO follow CBH model and confirming that the hopping of electrons from one barrier site to another site takes place via thermal activation [164,176]. It is also important to observe that the exponent n remains less than 1 over the studied temperature range suggesting that the presence of translational motion.

3.3.5. Ferroelectric and magnetoelectric measurements

Polarization vs Electric field (P-E) hysteresis loops measured at fixed frequency of 50 Hz for BT, BT-1CFO and BT-5CFO composites are plotted in Fig. 3.18. These samples show the extensive ferroelectric nature at an applied field of 25 kV/cm. There is an observed decrease in maximum polarization of the samples with the increase in Cobalt ferrite content indicating the suppression of ferroelectric ordering [177]. The P-

E loops did not display any saturation, which could possibly be due to low value of electric field.

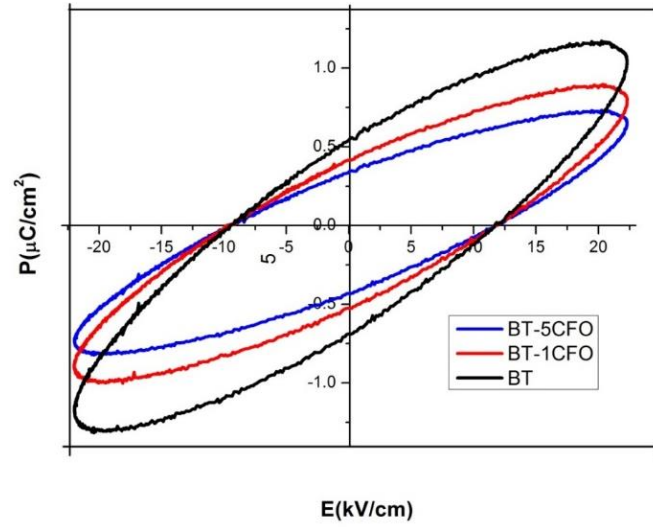


Figure 3.18. P-E hysteresis loops of BaTiO_3 and $\text{BaTiO}_3 - \text{CoFe}_2\text{O}_4$ composites.

The P-E loops have been exploited for estimation of energy storage density and discharge efficiency of BT-5CFO sample. The energy storage density and energy conversion efficiency of BT-5CFO composite are calculated using Equations (1.12) and (1.13), respectively. The unloaded sample of BT-5CFO displayed the energy density of 8.33 mJ/cm^3 and an efficiency of 59.7 %. The efficiency can be increased by studying the sample under mechanical stress and which is currently under investigation. The variation in P-E loop due to the field-induced structural transformation is an indicative of volumetric and piezoelectric strains in the BaTiO_3 phase.

In order to establish the magnetoelectric effect in the composites at room temperature, proving the ferroelectricity of the piezoelectric phase of barium titanate is essential. The hysteresis P-E loop of BT-5CFO composite exhibits a substantial variation with external magnetic field upto 4200 Oe as shown in Fig. 3.19. The remnant polarization is found to decrease and the coercive field do not change with increase in magnetic field. This display the tilting of P-E loops confirming the evidence of magneto-electricity due to increase in the content of CoFe_2O_4 in BaTiO_3 [83,178]. There was no variation in the P-E loop with magnetic field for BT-1CFO. This could be possibly due to less ferrite grains concentration in the composite which is incapable of generating magnetostriction in BaTiO_3 . The magnetoelectric coupling quantified by ME coefficient (α) is characterized by the appearance of an electric polarization (P) on applying magnetic field (H) as

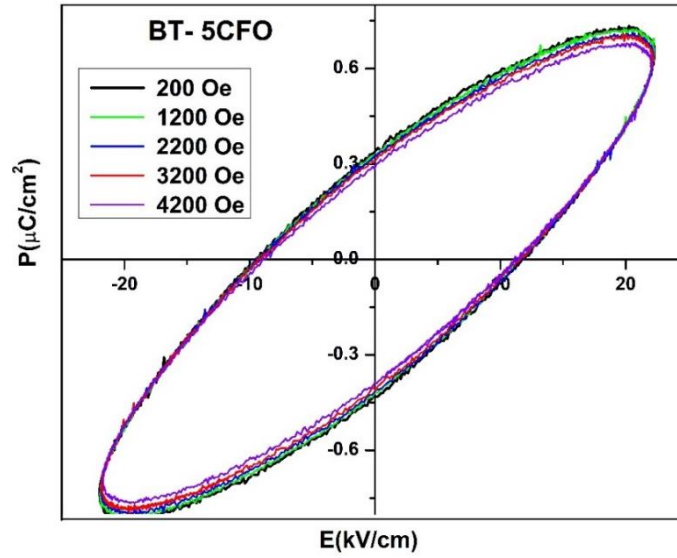


Figure 3.19. Variation of P-E hysteresis loop with magnetic field (upto 4200 Oe) of BT-5CFO composite.

$$\alpha = \delta E / \delta H \quad (3.5)$$

Fig. 3.20 shows the ME induced polarization as a function of the applied external magnetic field (dc). The slope of the curves is used for the estimation of the direct magnetoelectric coefficient. Considering only the linear effects, the polarization can be expressed as

$$P(E, H) = P_s + (dP/dH) \cdot H \quad (3.6)$$

where P_s denotes the spontaneous polarization at constant field. The values obtained from straight line fitting of P-H graph are $P_s = 0.78366 \mu\text{C}/\text{cm}^2$ and slope $dP/dH = -0.11801 \mu\text{C}/\text{cm}^2/\text{Oe}$. It can be seen that the coefficient is negative and low.

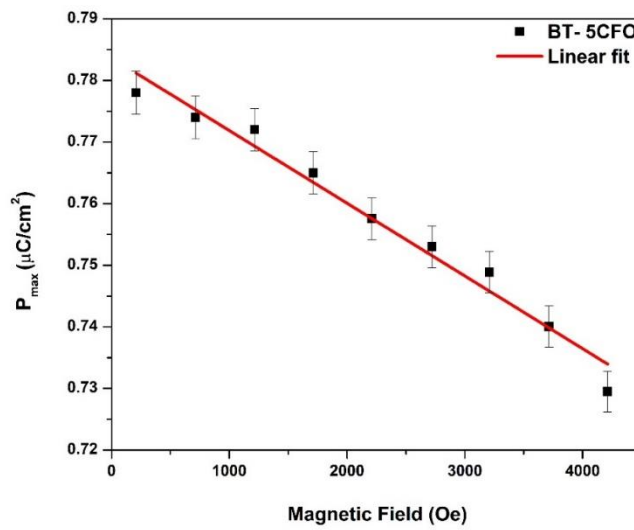


Figure 3.20. Plot of maximum polarization with magnetic field and straight line fit of BT-5CFO composite.

This decrease in induced polarization in biphasic composites could be explained by the effect of demagnetization arising from local strain. As the amount of magnetic phase is increased in BT, the polar domains of BT get surrounded by the magnetic CFO phase and hinder the domain wall rotation. On the application of magnetic field, a local magnetic field is generated around the BT domains resulting in an effective strain mediated magneto-electric coupling [49]. The M-E coupling coefficient for BT-5CFO composite is found to be 13.33 mV/cm/Oe which is relatively higher than reported values of 10 mV/cm/Oe and 12 mV/cm/Oe for 0.8BaTiO₃ - 0.2CoFe₂O₄ and 0.7BaTiO₃ - 0.3CoFe₂O₄ respectively [7].

Chapter - 4

Influence of BaTiO₃ on Structural, Electrical and Magnetoelectric Characteristics of CoFe₂O₄ - BaTiO₃ Composites

This chapter describes the extensive investigations of biphasic composites of CoFe₂O₄–BaTiO₃ (CFO-BT) prepared using solid state reaction method. The structural analysis from the combination of XRD, Raman, and FT-IR measurements of CFO-BT composites established the co-existence of cubic and tetragonal phases. The dielectric and impedance measurements confirmed non-Debye type Maxwell-Wagner polarization in CFO-BT composites with 0.7CFO-0.3BT composite showing an unexpected low dielectric loss (≈ 0.5) above 1 kHz and exhibited potential for device applications. The conductivity measurements confirmed improved conductivity with BT and crossover from barrier hopping to polaron conduction in CFO-BT composites. The magnetic measurements revealed an enormous increase in the coercivity of 0.7CFO-0.3BT composite due to the movement of ferromagnetic domains. The ferroelectric properties displayed a low leakage charge density of 0.0031 mC/cm² and asymmetric nature of P-E loop was due to spatial disordering of charge distribution. The optimum energy storage density and efficiency were 3.009 mJ/cm³ and 27.3 %, respectively for 0.7CFO-0.3BT composite. The maximum magnetoelectric coupling of 22 mV/cm/Oe was achieved for 0.9CFO-0.1BT composite. These results were useful for exploring energy storage devices based on magnetoelectric CFO-BT composites.

4.1. Introduction

The ME composites have limitations which create obstacles in the path of achieving high ME coupling in composites. Firstly, it is very difficult to prepare the highly insulating samples to stop the leakage current problem, which decline the measurement of ferroelectric polarization loops [179,180] and the second problem is to prepare single domain states, if the domains are present in the material [180,181]. The optimization of the sample preparation is, therefore, an important solution of such type of problems. In addition, the extent of coupling can be modified by tuning the connectivity and orientations between these phases and thereby rendering ME materials useful for scientific and technological devices [36].

It can be recalled from section 1.4. that for getting improved resistivity in the bulk composite, (0-3) connectivity is an important factor as it provides good electric polling process as well as better magnetoelectric coupling in the samples [52,53]. The previous chapter comprehensively discussed about BaTiO₃ - CoFe₂O₄ composites with (0-3) connectivity scheme. The composites displayed maximum ME coupling of 13.33 mV/cm/Oe with energy density of 8.33 mJ/cm³. These results suggest a scope of improvement in ME coupling of composites via modifying connectivity and constituent contribution. In this context, the (3-0) connectivity (ferroelectric phase in to ferromagnetic phase) is an important scheme due to its larger conductivity and has not been studied more till now. There are plethora of applications possible in this (3-0) scheme like control on electric polarization i.e. switching or modulation by a magnetic field, materials with magnetically tunable dielectric permittivity, or microwave absorbing materials [182,183].

The choice of typically strong magnetic phase with appropriate point group symmetry is important for the magnetoelectric behavior of a material since the ME coefficients acquire the symmetry of the material [26,184,185]. CoFe₂O₄ (CFO) is one of the most interesting spinel ferrite, which shows outstanding physical properties viz electrical, dielectric, optical, mechanical, thermal and magnetic properties due to their cationic distribution amongst the two interstitial octahedral and tetrahedral sites [80,81]. In order to examine the enhanced multiferroic, magnetoelectric coupling and to induce the electric nature inside the magnetic spinel ferrite CFO, there is a need of some modifications. Significant efforts for improving the properties of CFO have been focused on partially substituting the Fe³⁺ ions [186,187], composites with ferroelectric

/ piezoelectric materials [188], nanoparticles [132] and core / shell structures [189]. Among these heterostructure systems, CFO based composites combining the ferromagnetic CFO with ferroelectric phase stand out distinctively because of their outstanding ME coupling. In the light of these modification the composites of CFO and barium titanate (BaTiO_3) are observed to give promising results for magnetoelectricity in both bulk and nano systems [166,190,191]. The incorporation of perovskite BaTiO_3 in spinel CFO is observed to bring structural modification and lattice disorder [167], which may affect the electrical behavior and impedance properties in CFO-BT composites. There is a good advantage to combine the BT with CFO as CFO-BT composite has the spinodal decomposition of this binary system and as a result of which, it puts off the reaction between constituents throughout the high temperature processing. Moreover, bulk composites will have enlarged mechanical strength based on the volume fractions of the two phases. This chapter describes the synthesis of CoFe_2O_4 - BaTiO_3 (CFO-BT) composites under (3-0) connectivity scheme to examine the influence of BT in CFO on multiferroic properties, magnetoelectric coupling, dielectric, conductivity, impedance and ferroelectric properties for the use in various electronic device applications.

4.2. Sample Preparation

The $(1-x)\text{CFO}-x\text{BT}$ ($x = 0, 0.1$ and 0.3) were prepared by solid state reaction route as discussed in section 2.3 and as represented in Fig. 2.1. The AR grade of chemicals Co_3O_4 , Fe_2O_3 , BaCO_3 and TiO_2 , were used as initial ingredients in stoichiometric ratio. The synthesis conditions have been tabulated in Table 4.1. The composites are named as CFO (CoFe_2O_4), CFO-10BT ($0.9\text{CoFe}_2\text{O}_4 - 0.1\text{BaTiO}_3$) and CFO-30BT ($0.7\text{CoFe}_2\text{O}_4 - 0.3\text{BaTiO}_3$).

Table 4.1. Synthesis conditions of BaTiO_3 , CoFe_2O_4 and CoFe_2O_4 - BaTiO_3 composites.

Composition	Calcination temperature ($^{\circ}\text{C}$)	Duration (h)	Sintering temperature ($^{\circ}\text{C}$)	Duration (h)
BaTiO_3	1100	10	-	-
CoFe_2O_4	1000	12	1200	10
CFO-10BT	-	-	1300	10
CFO-30BT	-	-	1300	10

4.3. Results and Discussion

4.3.1. Structural and Morphological Measurements

The structure as well as phase analysis of the samples were confirmed from the powder XRD spectra. Fig. 4.1 shows the powder XRD patterns of CFO and CFO-BT composites. The XRD patterns show that the sample CFO is in single phase and no trace of other impurities have been found. All the peaks have been indexed using the standard JCPDS # 22-1086 for single phase cubic spinel structure with space group $Fd3m$ of cobalt ferrite. The indexing of BT with tetragonal structure in CFO-BT composites is indexed using standard JCPDS # 05-0626 [183]. The evolution of BT peaks in CFO-BT is indicated by '#'. XRD patterns of CFO-10BT and CFO-30BT composites clearly show the hkl values of both the phases and confirm the composite formation without any impurity phase, indicating negligible inter-diffusion among the phases indicating the ferroelectric state in all CFO-BT composites.

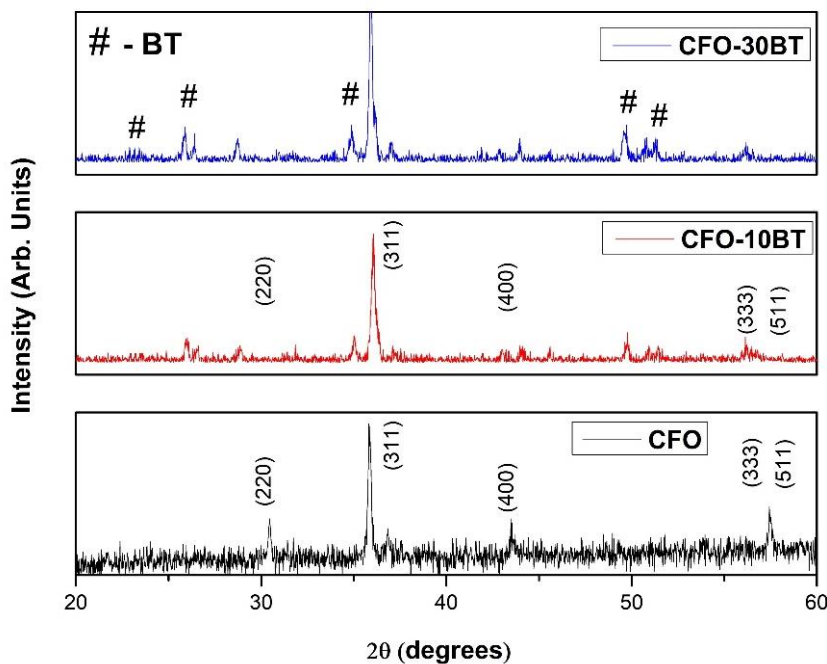


Figure 4.1. XRD patterns of CoFe_2O_4 and $\text{CoFe}_2\text{O}_4 - \text{BaTiO}_3$ composites.

The magnetic moment of the ferrites is determined by the distribution of cations at the lattice. The cationic distribution in the cubic spinel structure appears at (220) and (400) planes on the tetrahedral and octahedral sites [192,193]. There is a shift and splitting in the (311) major peak position to higher 2 theta side of XRD spectra with the increase of BT constituent in CFO as shown in the Fig. 4.1. The possible reason behind the shifting and splitting may be due to the increase of the distortion in the lattice of

pure cubic structure [194] and the distortion is due to the different ionic radii of Co^{2+} (0.78 Å) and Ba^{2+} (1.35 Å) which distort the interstices of the ferrite lattice. Thus, it is possible that some amount of different ionic radii may enter in to interstices and distort the structure and rest amount form the composite (cubic-perovskite composite). The different stoichiometry formation of CFO confirms the shifting and splitting of (311) peak position by 0.13° . The lattice parameters of CFO and CFO-BT composites are calculated from the powder XRD spectra (hkl) and found to decrease from 10.7 Å to 8.5 Å. The lattice parameter of the unit cell of cobalt ferrite phase has in good conformity with the values reported in the literature [195].

Fig. 4.2 (a-c) shows the SEM images of CFO, CFO-10BT and CFO-30BT composites respectively. The SEM images display uniform, homogenously dispersed structure with more or less narrow grain size distribution. In addition, some amount of coagulation can be observed in the SEM pictures due to strong magnetism in CFO. It can also be observed from the SEM images, that all the composites are tightly bound with low porosity and has average grain size of $(5 \pm 1) \mu\text{m}$.

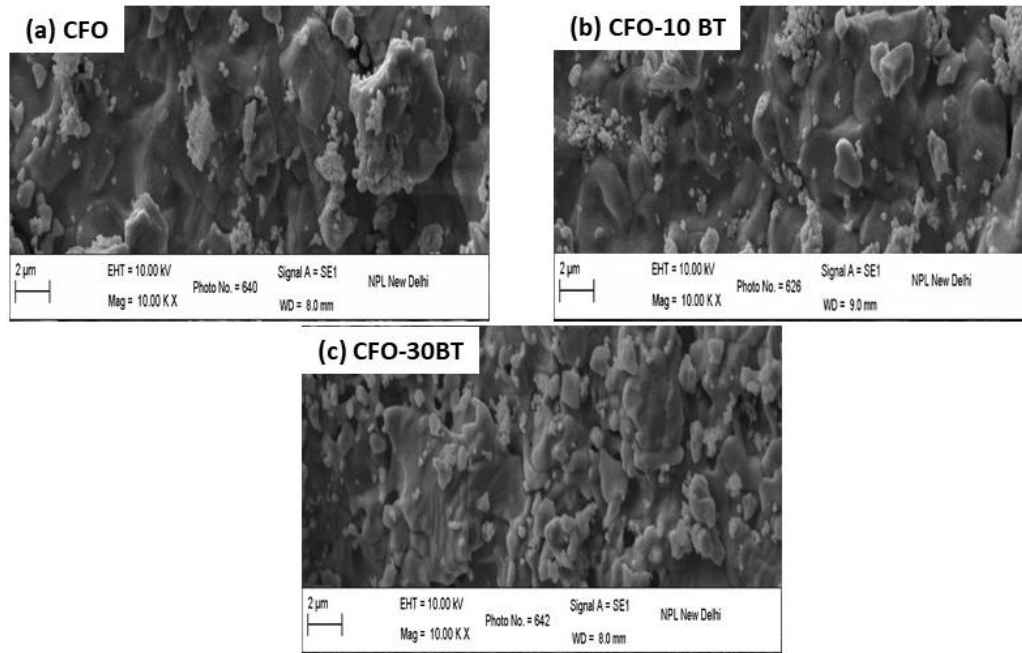


Figure 4.2. SEM micrographs of CFO and CFO-BT composites.

The phase contribution, cation distribution and the state of strain is explored using the Raman spectroscopy. The Raman spectra for CFO and CFO-30BT composites are shown in Fig. 4.3 in the frequency range of $200 - 1000 \text{ cm}^{-1}$. The peaks in CFO-30BT composite has slightly shifted as compared to CFO which could be due to

decrease in particle size in the composite. The spectrum consists of five Raman active modes namely $E_g + A_{1g} + 3T_{2g}$ representing the motion of 'O' ions and both octahedral and tetrahedral sites ions in CoFe_2O_4 spinel structure [161]. The spectrum consists of broad peaks centered at 294, 470, 672 cm^{-1} and 294, 470, 560, 610, 672 cm^{-1} for CFO and CFO-30BT composites, respectively. The low frequency mode at 294 cm^{-1} and at 560 cm^{-1} are assigned to T_{2g} and E_g modes reflecting the stretching in tetrahedral sites [162]. The peak at frequency of 470 cm^{-1} denotes the T_{2g} mode and indicates oxygen motion at the Fe-O and Co-O lattice sites. The high frequency peak at 672 cm^{-1} denotes the A_{1g} (to $A_{1g}(1)$ and $A_{1g}(2)$) symmetry mode and is attributed to the metal-oxygen motion in the tetrahedral sites. The splitting of peak at 610 and 672 cm^{-1} is caused by the partial cationic distribution and can be ascribed to $A_{1g}(\text{Fe}^{3+} - \text{O})$ and A_{1g} sub-band ($\text{Co}^{2+} - \text{O}$) respectively. The relative increase in the peaks at 610 and 672 cm^{-1} in CFO-BT as compared to CFO is due to the content of BT in CFO [196].

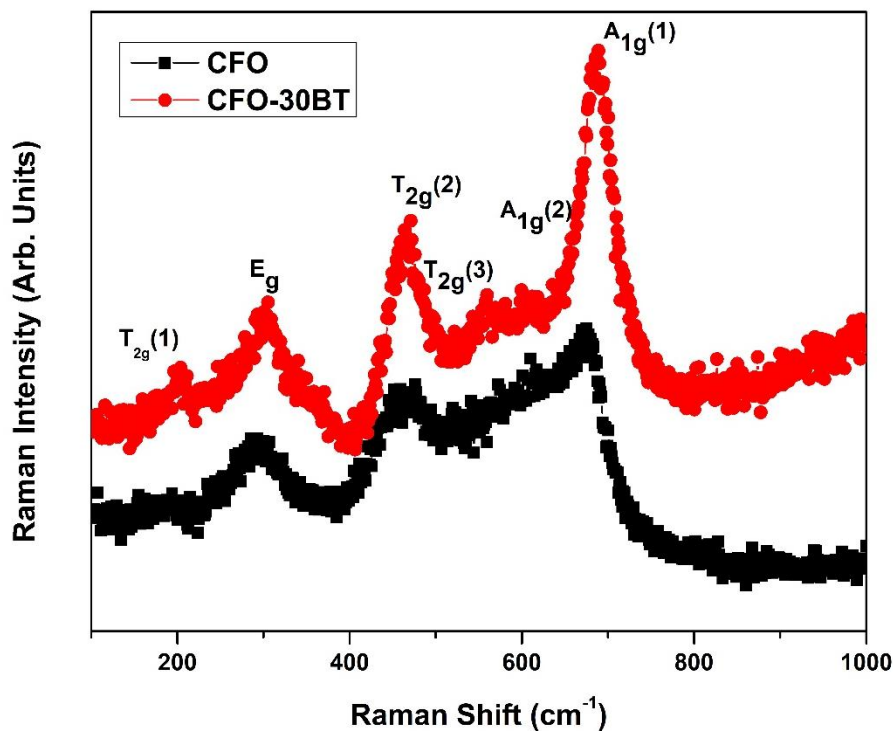


Figure 4.3. Raman spectra of CFO and CFO-BT composite.

The FT-IR spectra of CFO, CFO-10BT and CFO-30BT are recorded in the range of 4000 to 500 cm^{-1} as shown in Fig. 4.4. The bands present near the 564 cm^{-1} and 686 cm^{-1} indicate that a spinel structure of CFO is crystallized [197]. In case of CFO, the peaks at 564 and 686 cm^{-1} corresponds to Fe in the tetrahedral sites and stretching vibration mode associated with the metal-oxygen absorption band

respectively. The bands at 654 cm^{-1} and 686 cm^{-1} wavenumbers also correspond to tetrahedral and octahedral clusters and also authenticate the presence of Fe-O stretching vibration in CFO. A broad band at 3415 cm^{-1} correspond to O-H group in free and absorbed water and band at 1593 cm^{-1} corresponds to the symmetric C-H stretching. The peaks at 1027 , 1282 and 2344 cm^{-1} are due to C-O bending vibrations [198]. The peaks observed between the wavenumber of 500 to 700 cm^{-1} in case of CFO and became a single sharp peak near 686 cm^{-1} in case of CFO-BT. The band at 686 cm^{-1} in CFO-BT corresponds to typically Ti-O vibrations and confirm the presence of BT in CFO-BT composites [199].

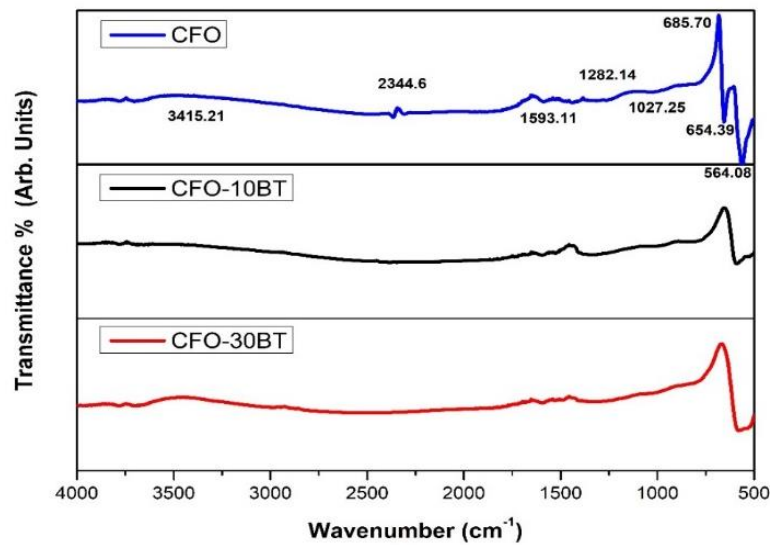


Figure 4.4. FT-IR spectra of CFO and CFO-BT composites.

4.3.2. Dielectric Measurements

The variation of dielectric constant (ϵ') with frequency for CFO, CFO-10BT and CFO-30BT composites at fixed different temperatures is shown in Fig. 4.5 (a-c), respectively. The composites of CFO-BT display a decrease in dielectric permittivity with frequency arising from the presence of conventional dielectric relaxation process and following Maxwell-Wagner polarization. The decrease is mainly caused by inability of electric dipoles to cope up with the change in frequency of applied electric field [93]. It can be observed from Fig. 4.5 that the permittivity increases with temperature and BT content in CFO. The dispersion in permittivity at low frequencies as well as at high frequency region confirms the presence of space charge polarization [93]. The composites of CFO-BT display higher permittivity than pure CFO. The dielectric constant increases from 450 to 700 at 100 Hz and 100 °C for CFO and

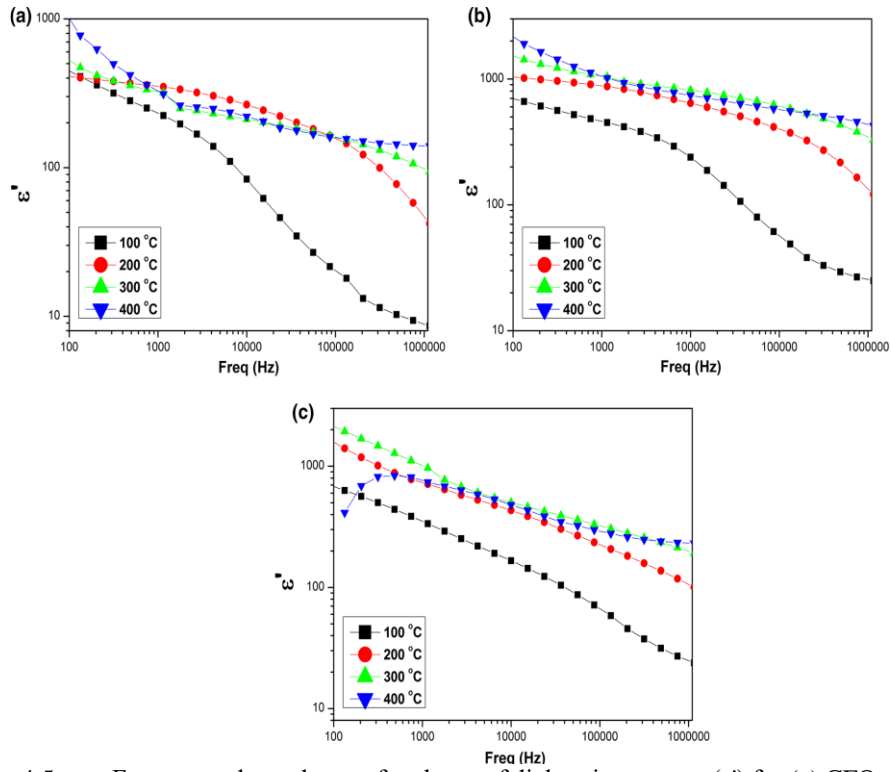


Figure 4.5. Frequency dependence of real part of dielectric constant (ϵ') for (a) CFO, (b) CFO-10BT and (c) CFO-30BT composites.

CFO-30BT composite. Fig. 4.6 (a-c) displays change of loss ($\tan \delta$) with frequency for CFO, CFO-10BT and CFO-30BT composites, respectively. The high dielectric loss in CFO is attributed to hopping of divalent charge carrier $\text{Fe}^{2+} / \text{Fe}^{3+}$ ions. This prominent feature decides the dielectric parameters in CFO-BT composites despite the strong dielectric nature of BT [189]. It is surprising to find that the dielectric loss declines prominently from 10 to less than unity for CFO and CFO-30BT composite, respectively. The minimum loss obtained is 0.5 for CFO-30BT composite at 1000 Hz which remains more or less constant over the experimentally studied frequency range.

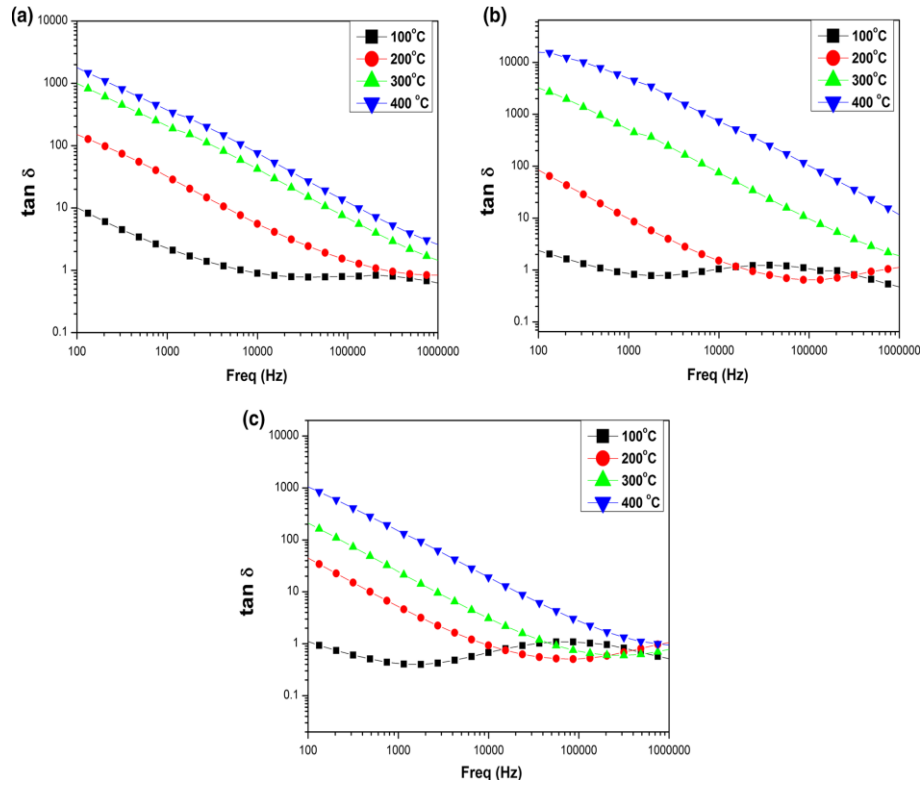


Figure 4.6. Frequency dependence of dielectric loss ($\tan \delta$) for (a) CFO, (b) CFO-10BT and (c) CFO-30BT composites.

4.3.3. Impedance and Modulus Measurements

Complex impedance spectroscopy is a useful technique to understand electrical behavior and electrical relaxation processes by dividing the grain-grain boundary contributions and other sources. The Nyquist plot or Cole-Cole plots of CFO, CFO-10BT and CFO-30BT composites are displayed in Fig. 4.7. All Nyquist plots start from origin at 100 °C suggesting the dominant grains contributions. The increase in the temperature from 100 °C to 200 °C sets in significant contributions of grains and grain boundaries in all the compositions. As the temperature reaches 400 °C, the samples CFO and CFO-BT composites tend to exhibit dominant contributions from the grain boundaries along with a small extension in the low frequency region. The radius of the semicircle increases on addition of BT in CFO upto 10% due to the dielectric nature of BT. However, the CFO-30BT composite display a relative decrease in Nyquist semicircle radius as compared to CFO-10BT composite which could be possibly due to extensive hopping of Fe ions. Furthermore the radius of the semicircles in Nyquist plots decrease invariably with temperature for CFO and CFO-BT composites owing to presence of statistically distributed relaxation processes [165,166].

The centers of semicircles in Nyquist plots for CFO and CFO-BT composites

lie below the Z' axis and suggest a typical non-Debye behavior in CFO based materials [188]. Moreover, based on the assumption that the semicircle of Nyquist plot is composed of combinations of RC circuits connected in parallel and using the frequency equation $f = 1/2\pi RC$, the relaxation time (τ) can be estimated as the reciprocal of frequency in the maxima of Nyquist plots [191].

The non-Debye behavior and grains/grain boundary contributions present in CFO and CFO-BT composites can be assessed by modeling the Nyquist plots as R-C equivalent circuits respectively employing altered brick layer model [167–169]. The equivalent electric circuit may consist of an arrangement of more than one circuit, comprising of resistor, and/or CPE and/or capacitor connected in parallel, representing the contributions arising from grains, grain boundaries and interfaces. The Nyquist plots of CFO and CFO-BT composites are fitted using Zview software and two equivalent circuits containing resistance and constant phase element are found suitable in following the plots. Fig. 4.8 (a-i) shows correspondence between the Nyquist plots and fitted data indicated by black circle and solid red line respectively for CFO and CFO-BT composites. The parameters obtained from fitting of Nyquist plots are tabularized in Table 4.2. The experimental results and fitted graphs as seen in Fig. 4.8 are in consonance with each other. The occurrence of CPE combinational electric circuit governed by equation $Z_{CPE} = 1/(j\omega)^n$ CPE confirms the non-Debye behavior exhibited by CFO and CFO-BT composites.

The change in impedance Z' with frequency for CFO, CFO-10BT and CFO-30BT composites at fixed temperatures is shown in Fig. 4.9 (a-c). The plots in Fig. 4.9 show that Z' is large at low frequencies region and reduces continually with frequency for the studied temperature range. It can be observed that Z' in CFO and CFO-BT composites coincides at higher temperatures as well as at higher frequencies due to reduction in hopping potential barrier and subsequent release of space charge. With the increase in BT content and temperature, Z' decreases confirming the thermal dependence in dispersion of conductivity existing in CFO-BT composites. This is dominantly attributed to the reduction in resistance of grain/grain boundaries [200]. Fig. 4.9 also shows the variation in complex part of impedance Z'' with frequency for CFO, CFO-10BT and CFO-30BT composites respectively. Variation of complex Z'' are essential in examining presence of impedance phase in composites. From Fig. 4.9, it can be observed that Z'' attain peaks at all measured temperatures for all the

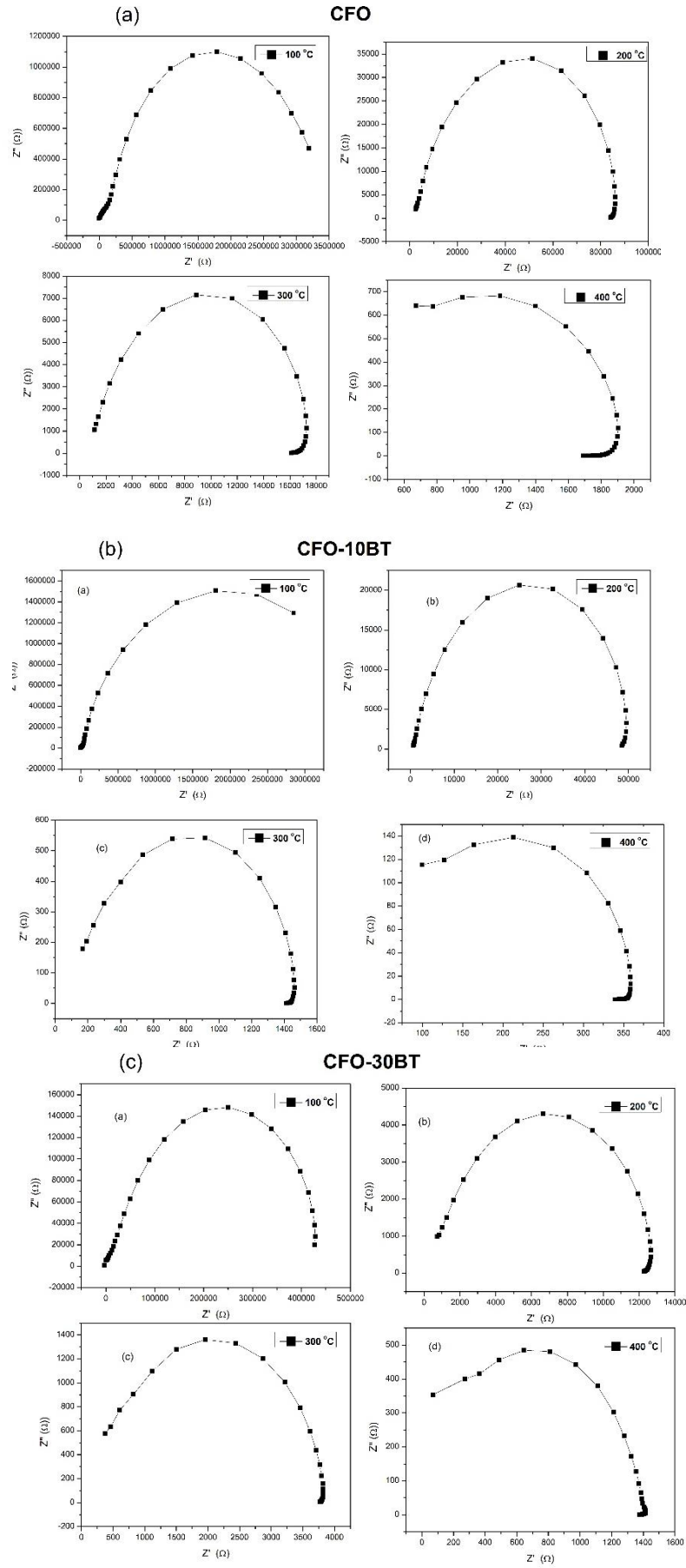


Figure 4.7. Nyquist plot of CFO and CFO-BT composites measured at different temperatures.

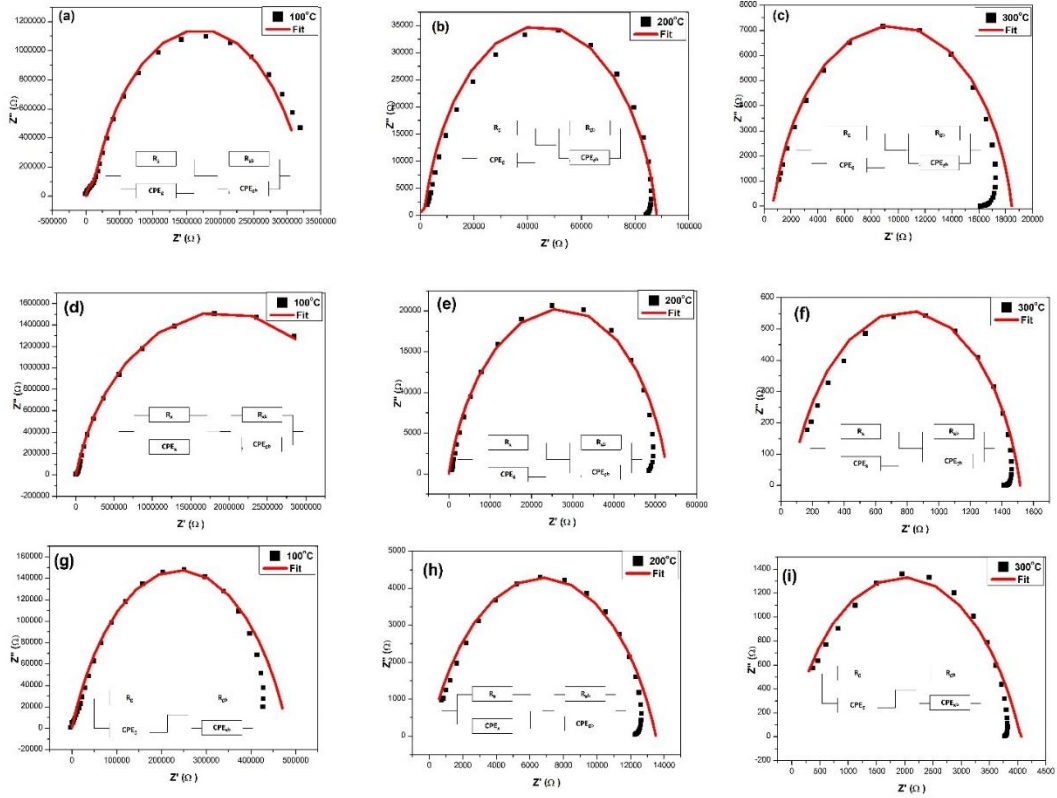


Figure 4.8. Combined Nyquist plots of (a-c) CFO, (d-f) CFO-10BT and (g-i) CFO-30BT composites at different temperatures and their equivalent circuit measured.

Table 4.2. Fitted parameters for Cole–Cole plots of CFO-BT composites

Temp (°C)	$R_g (\Omega)$	CPE_g	n_g	$R_{gb} (\Omega)$	CPE_{gb}	n_{gb}
CFO						
100	3200000	1.3×10^{-8}	0.79	100000	2×10^{-9}	0.86
200	86600	6.9×10^{-9}	0.87	1500	9×10^{-10}	0.90
300	17660	7.5×10^{-9}	0.87	800	6×10^{-7}	0.40
CFO-10BT						
100	3000000	2×10^{-9}	0.90	800000	2×10^{-8}	0.70
200	9500	2×10^{-8}	0.70	43500	2×10^{-8}	0.80
300	80	8×10^{-9}	0.70	1435	2×10^{-9}	0.84
CFO-30BT						
100	480000	3×10^{-9}	0.70	1300	2×10^{-7}	0.90
200	13500	2×10^{-9}	0.72	13	2×10^{-9}	0.50
300	4050	4×10^{-9}	0.70	13	2×10^{-5}	0.99

compositions. The maxima of Z'' (Z''_{max}) drifts to high frequency regime indicating the existence of thermally activated relaxation processes in CFO and CFO- BT composites arising from thermal agitation of charges present in grains and at the grain boundaries

[200]. The Z'' peak exhibit thermal decrement with broadening which confirms the thermal activated relaxation mechanism related to the existence of static charges and defects/vacancies at low and high temperatures.

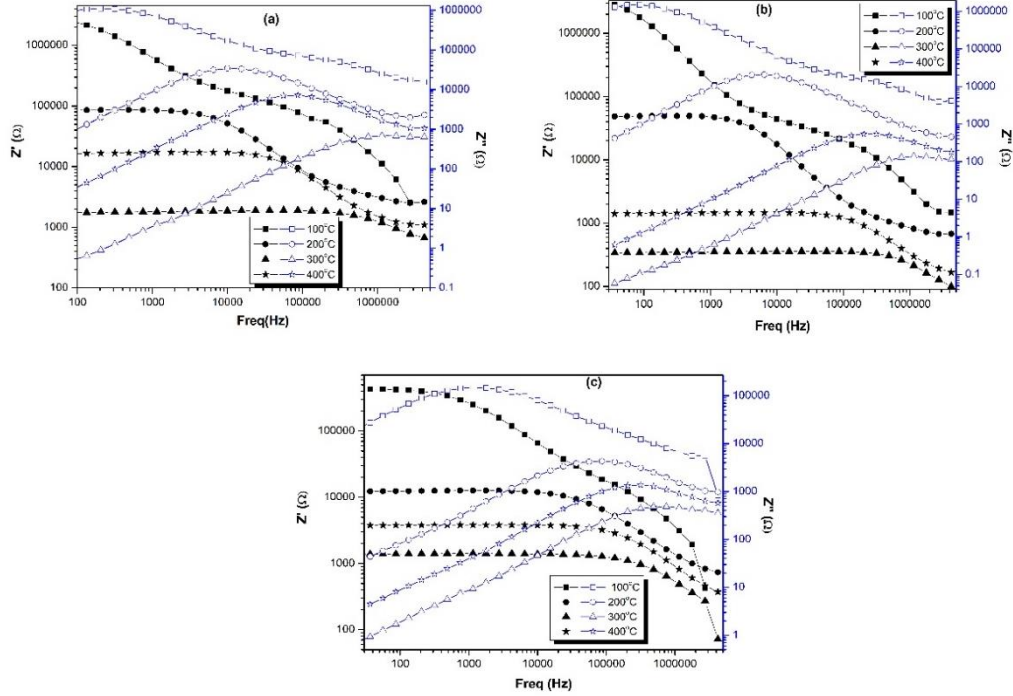


Figure 4.9. Variation of Z' and Z'' with respect to the frequency of (a) CFO, (b) CFO-10BT and (c) CFO-30BT composites.

The electrical response can be analyzed using the modulus spectroscopy analysis. Fig. 4.10 (a-c) depicts the frequency dependency of real part of modulus (M') for CFO, CFO-10BT and CFO-30BT composites respectively. Fig. 4.10 shows that M' is negligible at low frequencies and becomes saturated at high frequencies owing from the movement of short-range charge carriers. As the amount of BT is increased in CFO, a decrease in the saturated value is observed due to the localization of charge carriers. The variation of complex modulus (M'') with frequency is also shown in Fig. 4.10. It can be seen that all the samples display maxima at 100 °C, which broadens and shift to high frequency with rise in temperature and confirms the presence of temperature dependent conductivity behavior in CFO and CFO-BT composites. All the peaks are asymmetric in nature owing to the presence of multi-relaxation process and usual non-Debye nature of CFO based samples.

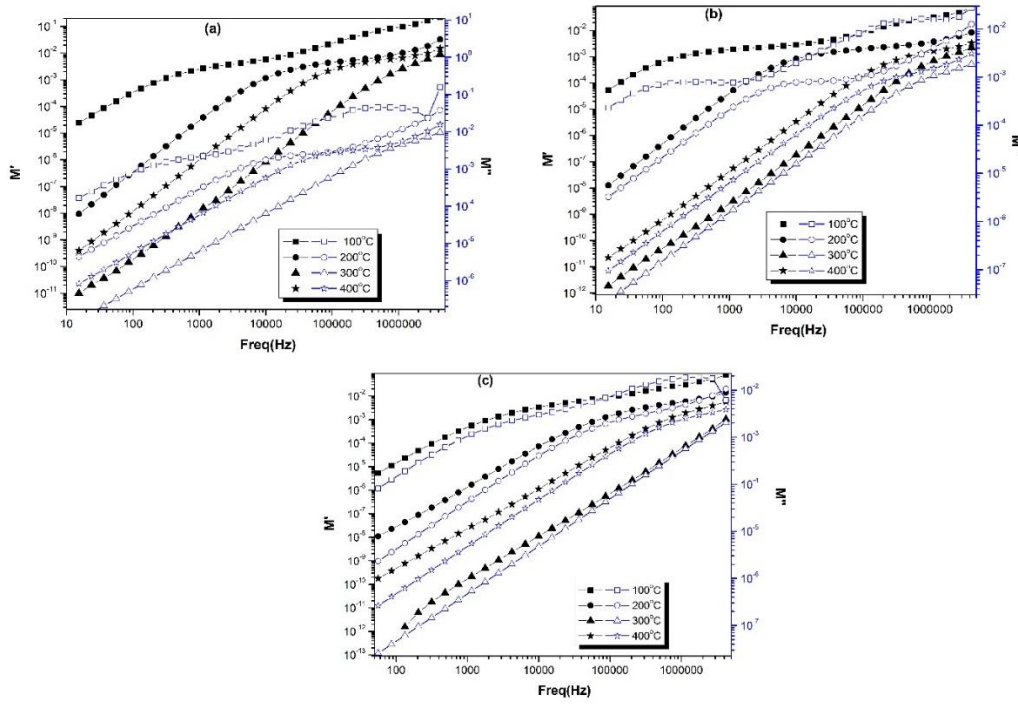


Figure 4.10. Variation of M' and M'' with respect to the frequency of (a) CFO, (b) CFO-10BT and (c) CFO-30BT composites.

4.3.4. Conductivity Measurements

The variation of real part of conductivity (σ') for CFO, CFO-10BT and CFO-30BT composites with temperature as well as frequency is shown in Fig. 4.11 (a-c). At low frequencies up to 1 kHz, the conductivity spectra show negligible variation and are frequency independent. This contribution originates from the dc conductivity and is accredited to the movement of charge around grain boundaries. The data shows dispersion at higher frequencies for CFO and CFO - BT composites, suggesting the onset of ac conductivity. This dispersion is aroused from increased mobility in charges. For temperatures except 100 °C, the spectra tend to merge at high frequency regime which is an indicative of structural disordering. At higher temperatures, the frequency dispersion reduces radically due to dominant dc conductivity part. It can also be observed from the data that conductivity increases with BT content as a result of increase in conduction path due to structural distortion in CFO-BT composites. Moreover, all the composites display thermally activated conduction mechanism. It can be assumed that whenever the conductivity increases and saturates at high frequencies then a single particle is hopping to and fro in a double well with infinite barriers [201,202].

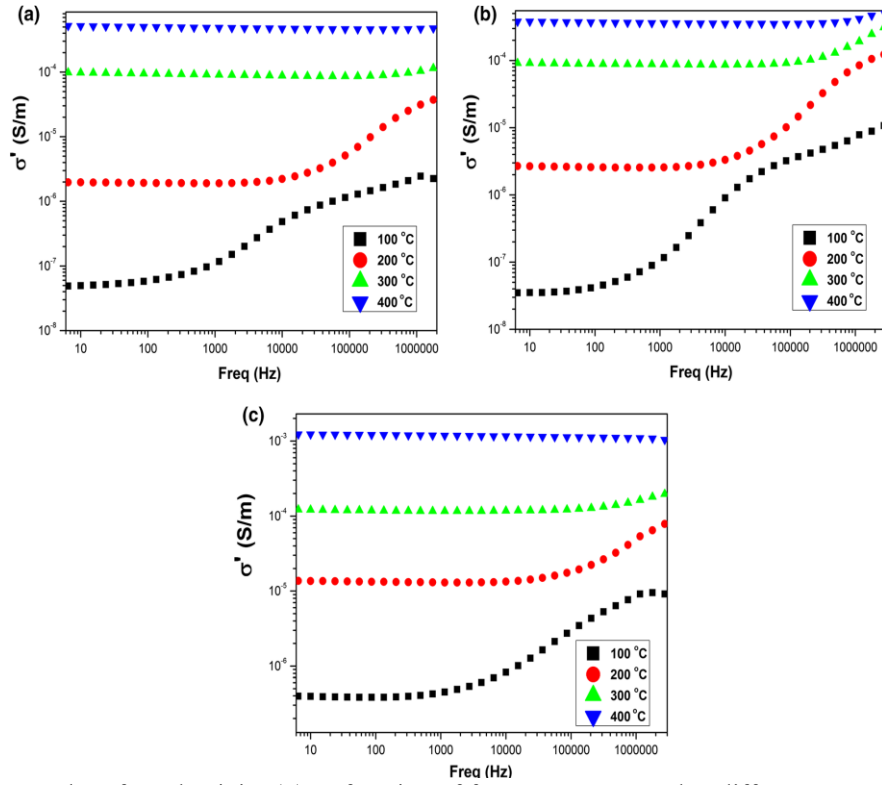


Figure 4.11. Plot of conductivity (σ) as function of frequency measured at different temperature (a) CFO, (b) CFO-10BT and (c) CFO-30BT composites.

The conductivity behavior in CFO, CFO-10BT and CFO-30BT can be understood by separating the dc and ac conductivity from the real part of conductivity (σ') as presented in Equation (3.2). The thermal variation of σ_{dc} – dc conductivity can be exploited to determine the activation energy (E_a) in CFO and CFO-BT composites and is governed by Equation (3.3). The thermal dependence of σ_{dc} and its linear fit is represented in Fig. 4.12. On the studied temperatures, separate slope values and activation energies have been obtained for CFO, CFO-10BT and CFO-30BT composites respectively and are tabulated in Table 4.3. The activation energies (E_a) obtained are found to be less than one in case of CFO and CFO-BT composites which affirms that thermal activated conductivity is controlled by singly ionized oxygen [172–174]. These oxygen ions / defect vacancies are produced during the synthesis at high temperatures which reduce the Ti^{4+} ions to Ti^{3+} ions following the Kroger-Vink defect Equation (3.4). These defects produced affect the inter-granular impedance.

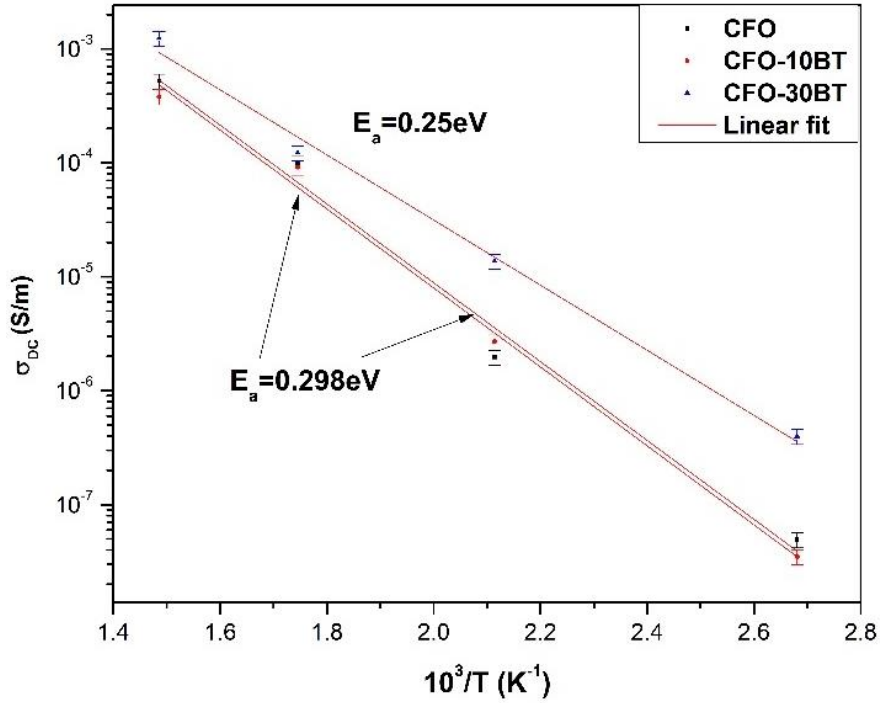


Fig. 4.12: Plot of dc conductivity as a function of temperature ($10^3/T$) for CFO and CFO-BT composites.

Table 4.3. Values of activation energy (E_a) in (eV) obtained from fitting of dc conductivity with $1000/T$ (K^{-1})

Activation Energy	CFO	CFO-10BT	CFO-30BT
E_a (eV)	0.250	0.298	0.298

The ac conductivity term usually follows the Jonscher's power law of frequency as given by

$$\sigma_{ac} = A\omega^n \quad (4.1)$$

where A and n vary with temperature. However, in case of CFO and CFO-BT composites Jonscher's law alone did not yield complete positive fit for ac conductivity. To supersede this condition, the modified Jonscher's law consisting of multiple relaxations was used:

$$\sigma_{ac} = A\omega_1^{n1} + B\omega_2^{n2} \quad (4.2)$$

where the constants A , B , $n1$ and $n2$ are temperature dependent. These terms ω_1 ($= \omega/\omega_1$) and ω_2 ($= \omega/\omega_2$) denote the low and high hopping frequencies. The exponents $n1$ and $n2$ represent restricted ion hopping and two level systems.[203] The modified Jonscher's law yielded satisfactory fit. The obtained values of $n1$ and $n2$ are plotted in Fig. 4.13. The conductivity phenomena present in CFO-BT composites can be understood by observing the frequency and temperature dependence of exponent $n1$.

The temperature-independent nature upto ω_1 is due to the diffusive nature of charge carriers in uniform potentials which gets sub-diffusive above ω_1 and below ω_2 . It can be realized that the vacancies accumulated at interfaces become conducting by recovering the oxygen vacancies from interfacial traps. The Jonscher's law for conductivity describes that the variation in exponent n (in present case for nI) is used for understanding the conduction behavior present in samples. Usually there are three kinds of conductivity phenomena which exist viz., quantum mechanical tunneling (QMT), correlated barrier hopping (CBH) and overlapping large-polaron tunneling (OLPT) depending on exponent n variation. In case when the value of exponent n is nearly 0.8, or n remains constant with temperature, and changes with frequency alone, then QMT behavior occurring via barrier localized sites is present. The thermal dependence of exponent n can be explained on the basis of QMT by assuming that the charge carriers form and move by means of non-overlapping small polaron tunneling

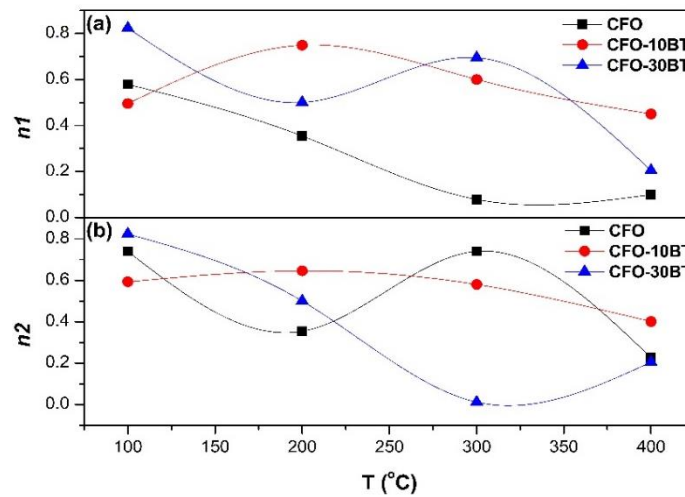


Figure 4.13. Variation of exponent n as a function of temperature for CFO and CFO-BT composites.

(NSPT). As per this theory, n increases with temperature. However, a decreasing variation in exponent n with temperature implied the CBH conduction existing in the sample. Lastly, whenever the exponent n exhibits frequency as well as thermal variation by obtaining a minima on increasing the temperature and increases thereafter implies an OLPT dominated conduction behavior [204].

It is seen from Fig. 4.13 that exponent nI display thermally dominated dispersion and confirms the existence of two or more different conductivity phenomena in CFO-BT composites. The conduction phenomena for CFO and CFO-10BT composite display the usual CBH of charges between barriers [164,176]. Interestingly,

in case of CFO-30BT composite, a crossover from CBH to OLPT in the conductivity behavior is observed arising from structural distortion [205]. Most importantly, the values of exponent nI is below 1 and confirms the dominant translational motion.

4.3.5. Magnetic Measurements

The magnetization (M) with respect to applied magnetic field intensity (H) hysteresis (M-H) loops of CFO-BT composites are measured at room temperature and an applied field of 15000 Oe, as shown in the Fig. 4.14. It can be observed from Fig. 4.14 that the magnetization of the CFO-BT composites increases rapidly at low field

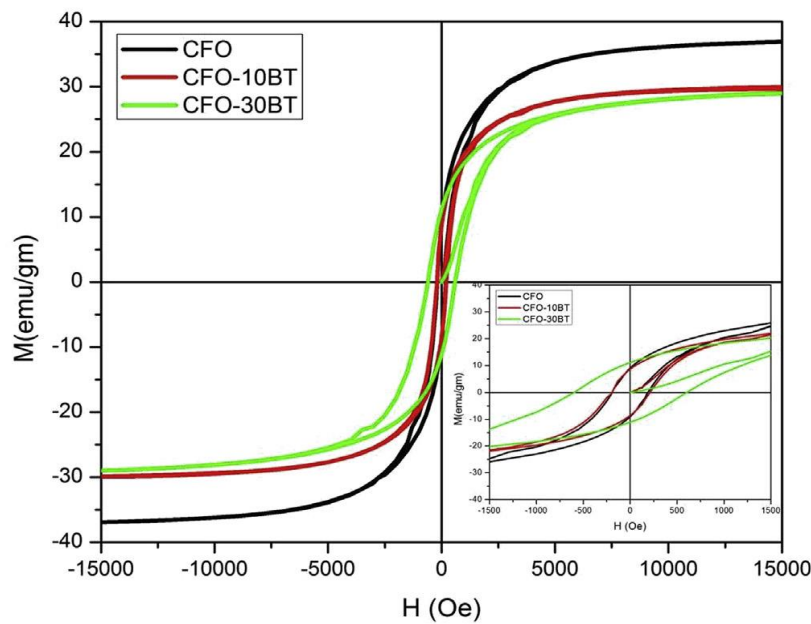


Figure 4.14. Room temperature magnetization curves (M vs H) for CFO, CFO-10 BT and CFO-30 BT composites. Inset shows the enlarged view of CFO, CFO-10 BT and CFO-30BT.

(up to 5000 Oe) and tends to saturate at higher fields (5000-15000 Oe). The saturation magnetization (M_s) decreases after the increase of ferroelectric phase in to CFO as shown in the Table 4.4 and follow the trend as reported in literature for $\text{CoFe}_2\text{O}_4\text{--Ba}_{0.8}\text{Sr}_{0.2}\text{TiO}_3$ composite system [206]. The magnetization in CFO-BT composite system is mainly due to the magnetic phase of CFO only because of the individual CFO grains acts as centers of magnetization. The incorporation of strong ferroelectric phase of BT breaks the magnetic circuit of CFO and the magnetic properties decreases with the increase of electric nature of the CFO-BT composite system.

The interesting part of the M-H hysteresis loops is remnant magnetization, which remains same for CFO and CFO-10BT and enhances with the increase of BT

concentration in to CFO (for CFO-30BT) as shown in the Table 4.4 and can be clearly seen from the enlarged view of the M-H hysteresis loops (inset of Fig. 4.14). Remnant magnetization is the good indicator for memory applications and CFO-30BT composite is therefore an ideal choice for memory devices.

Table 4.4. Variation of Saturation magnetization (M_s), Remnant magnetization (M_r) and Coercivity (H_c) for CFO, CFO-10 BT and CFO-30 BT composites.

Composition	Saturation Magnetization (M_s) (emu/gm)	Remnant Magnetization (M_r) (emu/gm)	Coercivity (H_c) (Oe)
CFO	36.88	9.00	190
CFO-10BT	30.02	9.00	190
CFO-30BT	28.80	11.3	600

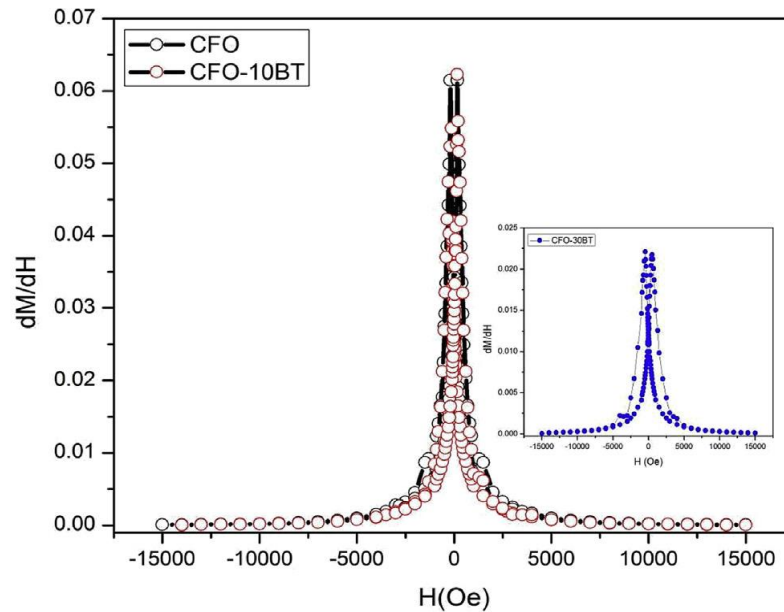


Figure 4.15. Variation of dM/dH with respect to applied magnetic field for CFO and CFO-10BT for the confirmation of Coercivity. Inset shows the enlarged view of CFO-30BT composite.

The coercivity (H_c) values of the CFO-BT composites are shown in the enlarged view of the M-H hysteresis loops (inset of Fig. 4.14) and also verified from the butterfly nature of dM/dH curve in Fig. 4.15 and inset of Fig. 4.15. The coercivity values obtained from M-H hysteresis loops are exactly same as obtained from the dM/dH curve. The coercivity values remain almost same up to CFO-10BT and increases nearly three times in case of CFO-30BT composite. It should be pointed out that the coercivity

value changes after the addition of high amount of BT in to CFO (i.e. CFO-30BT) but remains same in case of low amount of non-magnetic phase of BT (i.e. CFO-10BT). As per the fact available in the literature for the magnetic materials [206,207], the movement of ferromagnetic domains of CFO remains close to each other in CFO-10BT due to which the cooperation between the domains remain unchanged. So that the coercivity does not change for low concentration of BT. But in case of high concentration of BT in CFO-30BT in to CFO, the situation becomes opposite and the ferromagnetic domain walls move far away from each other and also the cations present at octahedral and tetrahedral shift negligibly but countable part to each other owing to their different ionic radii. As per the matter of these facts, the cooperation between the CFO domains become started and the countable replacement of cations at the tetrahedral and octahedral sites distort the structure, and as a result of these facts coercivity increases. So, it may be pointed out that the low amount of BT does not affect the intrinsic property of the CFO but high amount of BT changes the intrinsic property of CFO.

Another magnetic parameter, magnetic moment per unit (n_b) in Bohr magneton can be calculated as follows [208]:

$$n_b = \frac{M \times M_s}{5585} \quad (4.3)$$

where, M is the molecular weight of particular composition and M_s is the saturation magnetization (emu / gm). It has been observed that n_b decreases at room temperature as BT concentration increases from CFO-10BT to CFO-30BT. The increase in the value of magnetic moment may be due to the fact that when the non-magnetic phase of BT increases in CFO, the molecular weight and saturation magnetization decreases.

4.3.6. Ferroelectric and Magnetoelectric Measurements

Sawyer-Tower technique is used for the study of ferroelectric properties of materials for polarization switching [209]. The measured Polarization vs Electric field P-E loops for pure CFO, CFO-10BT and CFO-30BT at room temperature and frequency of 50 Hz are shown in Fig. 4.16. The modification in the structure through the addition of BT in to CFO is an interesting part of the material preparation, which may radically affect the polarization as well as the loss in case of CFO-BT composites. The mixing of the cations i.e Fe^{3+} with Ti^{4+} at the octahedral site and Ba^{2+} with Co^{2+} at tetrahedral site of the cubic spinel structure and significant replacement of one to other

due to their different ionic radii lead to structural distortion and induces strain. As a result of induced strain, the polarization increases as well as the area under the PE loop decreases after the increase of BT percentage in to CFO as shown in the Fig. 4.16 [210].

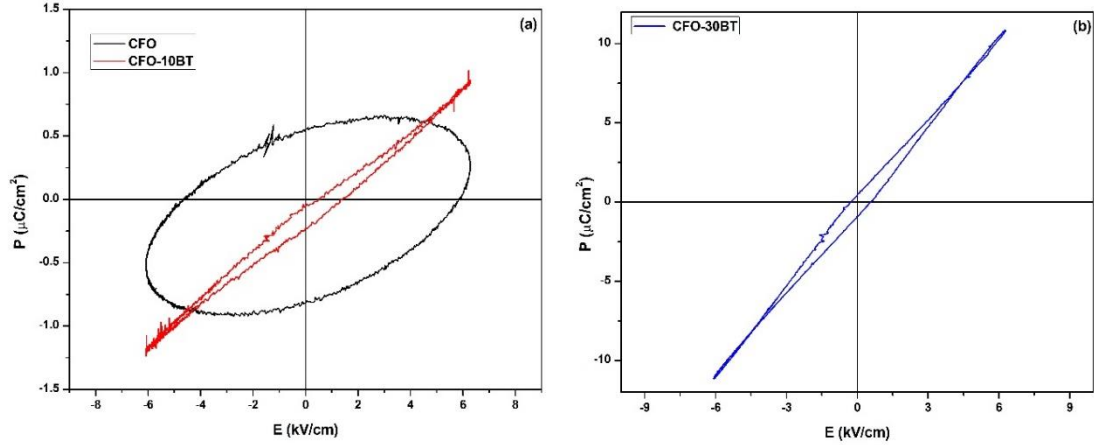


Figure 4.16. P-E hysteresis loops of (a) CFO and CFO-10 BT and (c) CFO-30BT composites at frequency of 50 Hz.

CFO is a semiconducting / superparamagnetic material and leakage current is mainly connected to the CoFe_2O_4 medium. The CFO particles are collective in nature with each other due to the strong magnetization of them and consequently create spatial channels of magnetic particles. The loop of CFO and CFO-10BT indicate high leakage and loop of CFO-30BT indicate relatively weak ferroelectricity and unusually low loss. The reason behind such type of lossy hysteresis loops in CFO may be due to high amount of magnetic phase in the composite and such high leakage current reduces after increase of the BT content. Though, the leakage current can stalwartly influence the measurements in case of such conducting materials. For the measurement of leakage current of CFO-30BT, the total charge of the composite materials (q_{total}) is measured by Sawyer–Tower technique and expressed as [52,83]:

$$q_{\text{total}} = P(E(t)) * A + \int_0^{\tau-\text{cycle}} dt i_{\text{leak}}(t) \quad (4.4)$$

where P is the polarization, E is the electric field, A is the sample electrode area, i_{leak} is the leakage current, and t is time. The estimation of leakage current is done by dividing the applied voltage $v(t)$ by the earlier calculated resistance (r_{leak}) of the CFO-30BT sample. This resistance is supposed to be independent of time. After the calculation from the Equation (4.4), the polarization due to the leakage in CFO-30BT is found to

be very low ($\sim 0.0031 \mu\text{C}/\text{cm}^2$). Such a low leakage current is very useful to achieve high magnetoelectric coupling and use in spintronics and sensing device applications.

An anomalous asymmetry in the P-E hysteresis loops is also the prominent observation of the present study, which is clearly observed in case of CFO-30BT composite. The charge distribution at the interfaces of the material is an interesting parameter to decide the symmetry / asymmetry in the ferroelectric P-E hysteresis loops, which can be relevant in various applications like rational design of memory, sensors and photonic devices [211]. Fig. 4.16 clearly shows the asymmetry in the P-E hysteresis loop of CFO-30BT in terms of different coercivity values ($\Delta E_c = E_c^+ - E_c^- = \text{positive value}$) and gets the positive coercivity ($E_c^+ \approx + 0.5627 \mu\text{C}/\text{cm}$) and negative coercivity ($E_c^- \approx -0.2749 \mu\text{C}/\text{cm}$). It is seen from the coercivity calculation of CFO-30BT that E_c^- is almost half of the E_c^+ , which is the good indication for the use of the material in device applications. It is possible that the value of ΔE_c may change for different spatial regions of the sample i.e. the position of the sample interface with respect to the electrode interface. It is because of the different space charge densities present at different parts of the sample [44]. The charge distributions (also the charge density) at interfaces which decay exponentially towards the interior of the material are resulted as the induced asymmetric potentials in the material. As a result of such induced asymmetric potentials, local electric field is generated that may be the cause of asymmetric P-E hysteresis loop in the CFO-30BT composite. T. Putzeys et.al. assumed and provided an additional mechanism of electron trapping in the interface through negative electrode, as a result of which coulomb trap takes place which is not present in positive electrode and provide the weaker response of the polarization in comparison to the negative electrode. So the pronounced asymmetry is experiential between the positive and negative electrode interfaces of the CFO-30BT composite [212].

The estimation of energy storage density and discharge efficiency of CFO-30BT composite have been done from the P-E hysteresis loop. The energy storage density and the efficiency of a ferroelectric material are calculated as discussed in the section 1.9.2. The composite of CFO-30BT exhibited an enhanced energy density of $3.009 \text{ mJ}/\text{cm}^3$ as compared to $0.5 \text{ mJ}/\text{cm}^3$ for CFO. An improved efficiency of 27.3 % for CFO-30BT was observed as compared to 10 % for CFO. The improvement in the efficiency of energy storage in CFO-30BT is a clear indication of its usefulness in the energy storage devices.

The quantification of ME coupling coefficient (α) is studied by variation of P-E hysteresis loops in the presence of external magnetic fields for all the CFO-BT composites as shown in the Fig. 4.17. The variation of maximum polarization with

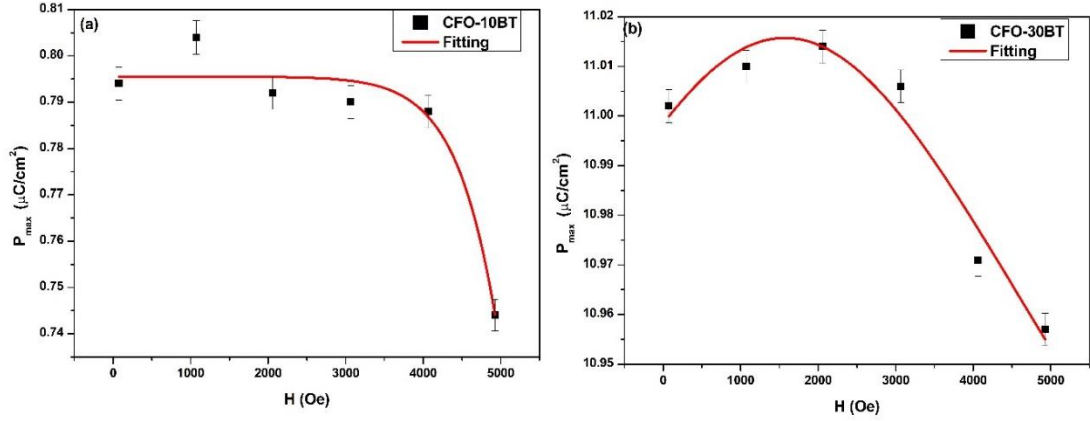


Figure 4.17. Plot of maximum polarization with magnetic field and best fit for (a) CFO-10BT and (b) CFO-30BT composites.

external magnetic field for CFO-10BT composite is shown in the Fig. 4.17(a). It can be seen that the polarization remains constant upto a field of 4 kOe. The variation in P_{max} with H is fitted numerically with Gaussian fit to estimate the magnetoelectric coupling coefficient in the following relation with adjusted R-square value = 0.87641.

$$P_{max} = P_{max0} + \left(\frac{A}{w\sqrt{\pi/2}} \right) e^{\left(-2 * \left(\frac{H-H_c}{w} \right)^2 \right)} \quad (4.5)$$

where P_{max0} , H_c , A and W represent the initial maximum polarization ($H=0$), critical field and constants.

The M-E coupling coefficient α is estimated as $\alpha = dP_{max}/dH$, which can be expressed as:

$$\alpha = \frac{dP_{max}}{dH} = \left(\frac{-4A(H-H_c)}{w^2\sqrt{\pi/2}} \right) e^{\left(-2 * \left(\frac{H-H_c}{w} \right)^2 \right)} \quad (4.6)$$

Fig. 4.17(b) shows the variation of P_{max} with external magnetic field for CFO-30BT composite. The polarization decreases continuously with magnetic field. The variation in P_{max} with H is fitted numerically with Lorentzian fit to estimate the magneto-electric coupling coefficient in the following relation with adjusted R - square value = 0.91197

$$P_{max} = P_{max0} + \left(\frac{2A}{\pi} \right) * \left(\frac{w}{(4 * (H-H_c)^2 + w^2)} \right) \quad (4.7)$$

The M-E coupling coefficient α is estimated as $\alpha = dP_{max}/dH$, which can be expressed as:

$$\alpha = \frac{dP_{max}}{dH} = P_{max} = \left(\frac{-2 \cdot A \cdot w}{\pi} \right) * \left(\frac{H - H_c}{((4 \cdot (H - H_c)^2) + w^2)^{3/2}} \right) \quad (4.8)$$

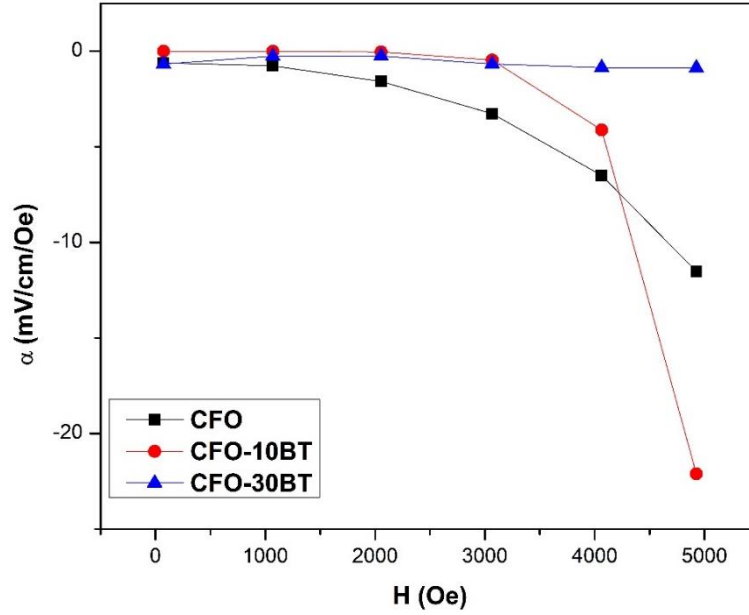


Figure 4.18. Variation of magnetoelectric coefficient (α) with respect to magnetic field for the CFO and CFO-BT composites.

The M-E coupling coefficient (α) obtained from the above analysis is plotted in Fig. 4.18. It can be seen that α decreases with increase in magnetic field. It is very important to note that the effect of BT in CFO. The value of α is more in CFO-10BT as compared to CFO and with further addition of BT, α decreases in CFO-30BT. The maximum value of magnetoelectric coefficient ($\alpha = 17.04$ mV/cm/Oe) was reported in the case of $0.5\text{CoFe}_2\text{O}_4 + 0.5\text{BaTiO}_3$ composite [213]. The highest α in the present study is achieved for CFO-10BT as 22 mV/cm/Oe at a field of 5000 Oe, which is higher than the reported values for CFO-BT systems [214,215].

Chapter - 5

Magnetodielectric Effect, Impedance and Magnetoelectric Coupling in Multiferroic $\text{Co}_{0.5}\text{Ni}_{0.5}\text{Fe}_2\text{O}_4\text{-BaTiO}_3$ Bulk Composites

This chapter is focused on the magnetoelectric bulk composites of $\text{Co}_{0.5}\text{Ni}_{0.5}\text{Fe}_2\text{O}_4\text{-BaTiO}_3$ (CNFO-BT) prepared employing solid state reaction method. The structural properties of CNFO-BT composites discussed by X-ray diffraction method, which confirms the lattice distortion and enlarged strain owing to BT substitution in CNFO. The dielectric and impedance measurement exhibit conventional Maxwell-Wagner polarization and confirm the existence of grain dominated non-Debye relaxations phenomena in CNFO-BT composites. The magnetodielectric change and variation of ferroelectric polarization with magnetic field reveal lattice distortion, interfacial charge polarization and restricted ferromagnetic domain wall rotation arising from substitution of BT in CNFO. The magnetic hysteresis curves reveal strong ferromagnetic behavior in all composites. The maximum energy storage density and an efficiency achieved for 0.8CNFO-0.2BT are 4.25 mJ/cm^3 and 31.6 %, respectively. The P vs H analysis confirmed the highest magneto-electric coefficient of 5 mV/cm/Oe for 0.8CNFO-0.2BT composite.

5.1. Introduction

The magnetoelectric composites are engineered artificially by mixing separately the ferroelectric and ferromagnetic phases for enhancing the magnetoelectric coupling at room temperature [47,50]. The extent of coupling can be maximized by involving piezoelectric and/or piezomagnetic materials, which acquaint in achieving strain mediated coupling and good connectivity at the electric and magnetic phase [50].

The previous chapter comprehensively discussed about CoFe_2O_4 - BaTiO_3 composites with (3-0) connectivity scheme. The composites displayed maximum ME coupling of 22 mV/cm/Oe with energy density of 3.009 mJ/cm^3 . These results suggest a scope of improvement in ME coupling of composites via improving the resistivity of constituents. The properties of CoFe_2O_4 are usually synthesis procedure as well as grain size dependent and can also be altered by addition of foreign atoms. The substitution of Ni^{2+} in the cubic structure of CFO is exciting due to improved resistive and magnetoelectric properties [43]. The recent studies on $\text{Co}_{0.5}\text{Ni}_{0.5}\text{Fe}_2\text{O}_4$ (CNFO) have revealed that strong magnetostatic interactions arising from different magneto-crystalline anisotropy are countered by increased coercivity and decreased magnetic saturation [47,87,88]. In addition, there have been investigations on CNFO based composites for existence of magnetoelectric properties [49,54,89]. Furthermore system of CNFO-BT has showed some promising results in magnetic properties [43–46]. Nevertheless, the origin of magnetodielectric, impedance and ferroelectric properties in $\text{Co}_{0.5}\text{Ni}_{0.5}\text{Fe}_2\text{O}_4$ - BaTiO_3 composites are not explored thoroughly. In this regard, this chapter describes the synthesis of $\text{Co}_{0.5}\text{Ni}_{0.5}\text{Fe}_2\text{O}_4$ - BaTiO_3 (CNFO-BT) composite to study the effect of BT on the structural, dielectric, impedance and magneto-dielectric coupling ferroelectric P-E and magneto-electric properties of CNFO.

5.2. Sample Preparation

The $(1-x)\text{CNFO}-x\text{BT}$ ($x = 0, 0.1$ and 0.2) were synthesized by solid state reaction route as discussed in section 2.3 and as represented in Fig. 2.1. The AR grade of chemicals BaCO_3 , TiO_2 , Co_3O_4 , NiO and Fe_2O_3 were used as initial ingredients in stoichiometric ratio. The synthesis conditions have been tabulated in Table 5.1. The composites are named as CNFO ($\text{Co}_{0.5}\text{Ni}_{0.5}\text{Fe}_2\text{O}_4$), CNFO-10BT ($0.9\text{Co}_{0.5}\text{Ni}_{0.5}\text{Fe}_2\text{O}_4$ - 0.1BaTiO_3) and CNFO-20BT ($0.8\text{Co}_{0.5}\text{Ni}_{0.5}\text{Fe}_2\text{O}_4$ - 0.2BaTiO_3).

Table 5.1. Synthesis conditions of BaTiO₃, Co_{0.5}Ni_{0.5}Fe₂O₄ and Co_{0.5}Ni_{0.5}Fe₂O₄-BaTiO₃ composites.

Composition	Calcination temperature (°C)	Duration (h)	Sintering temperature (°C)	Duration (h)
BaTiO ₃	1000	12	-	-
Co _{0.5} Ni _{0.5} Fe ₂ O ₄	1000	12	1200	8
CNFO-10BT	-	-	1200	8
CNFO-20BT	-	-	1200	8

5.3. Results and Discussion

5.3.1. Structural Measurements

The X-ray diffraction patterns of CNFO and CNFO-BT composites are shown in Fig. 5.1. The XRD plot of CFO is referred from previous chapter. The XRD pattern of CNFO

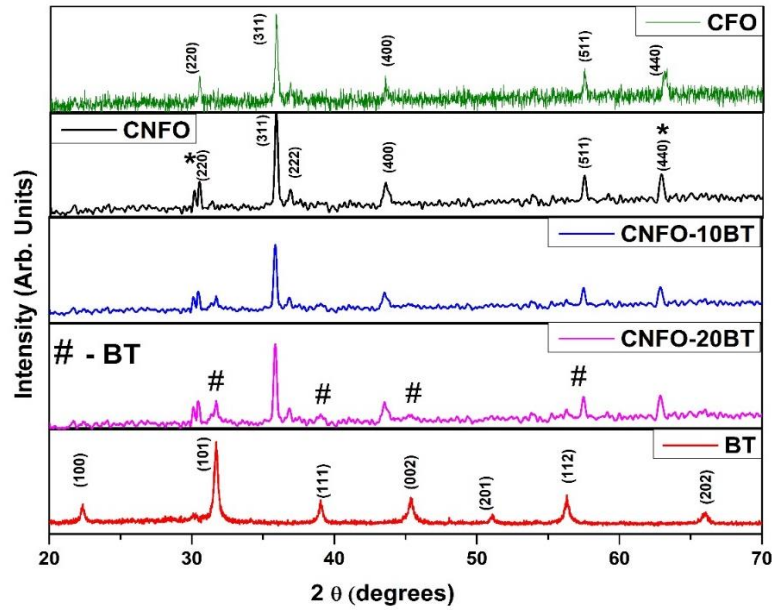


Figure 5.1. XRD patterns of CNFO and CNFO-BT composites.

is matched with JCPDS # 22-1086 and confirms the spinel cubic structure with space group (*Fd3m*). The splitting and broadening of peaks in XRD of CNFO in comparison to that of CFO at $2\theta \sim 30^\circ$ and 62.5° are matched with JCPDS # 10-0325 for NiFe₂O₄ [216] and is marked by '*' symbol in Fig. 5.1. This occurrence of NiFe₂O₄ peaks confirms the formation of CNFO. The XRD patterns of CNFO-BT system are matched with JCPDS # 22-1086 for CNFO and JCPDS card # 05-0626 for BaTiO₃ (BT) and

confirm the formation of CNFO-BT composites. The ferroelectric BT phase in the composite at $2\theta \sim 32^\circ$ and at other higher values is indicated by ‘#’ symbol in Fig. 5.1.

The effect of BT addition in CNFO is observed by studying the lattice parameter variation and lattice strain estimations. The variation of lattice parameter was obtained using Debye-Scherrer Equation (2.3) and lattice strain was obtained from Williamson-Hall Equation (2.4) and were plotted in Fig. 5.2. It can be observed that the lattice parameter obtained for CNFO is 8.325 Å is lower than that of CoFe_2O_4 (10.7 Å) as at both octahedral / tetrahedral sites, ionic radii of Ni^{2+} (0.745 / 0.55 Å) is less than Co^{2+} (0.69 / 0.58 Å) [217]. The lattice parameters in Fig. 5.2 decrease from 8.325 Å to 7.967 Å for CNFO to CNFO-BT composites due to lattice distortion arising on account of trapping centers formed by BT substitution. This lattice distortion is also accompanied by the increase in the lattice strain as shown in Fig. 5.2.

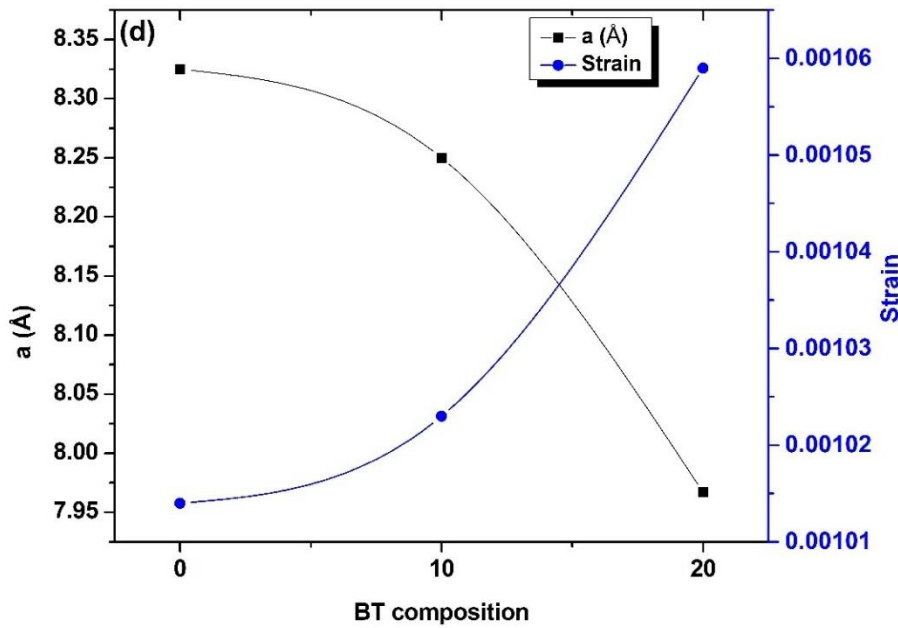


Figure 5.2. Variation of lattice parameter and strain in CNFO-BT composites.

5.3.2. Dielectric and Magnetodielectric Measurements

The dielectric analysis is an ideal technique for correlation of most of the properties of ferrites with preparation, composition and temperature. The frequency dependency of dielectric constant for CNFO and CNFO-BT composites is shown in Fig. 5.3. The graphs show usual behavior of dielectric materials with CNFO and CNFO-BT composites possessing large dielectric constant values [218] at low frequencies and the dielectric constant decreases at higher frequencies. The main reason to show such a decreasing trend is due to the presence of interfacial polarization as predicted by

Maxwell-Wagner [219] and arises because of the charge accumulation on sample-electrode interface. The exchange of electrons among multivalent $\text{Fe}^{2+} / \text{Fe}^{3+}$, creates a spatial displacement of Fe ions along with electric field resulting in the polarization. The high value of dielectric permittivity at low frequencies is because of the presence of multivalent Fe ions, its related oxygen vacancies and defects. The decrement in the value of dielectric permittivity with frequency is because the dipoles cannot follow the electric field oscillations at higher fields. As per Koops theory, the contribution of dielectric constant at lower frequency originates from grain boundaries as they possess high impedance at grain boundary region [220]. The contribution to dielectric permittivity at high frequencies originates from low resistive grains. Thus, the presence of multivalent Fe ions is responsible for polarization in CNFO. The dielectric constant increases with BT content and suggests enhancement in electrical nature of CNFO-BT composites. For all composites, the increase in temperature from 100 °C to 400 °C onsets the space charge polarization linked to ionic defect movements and decreases the dielectric constant [85].

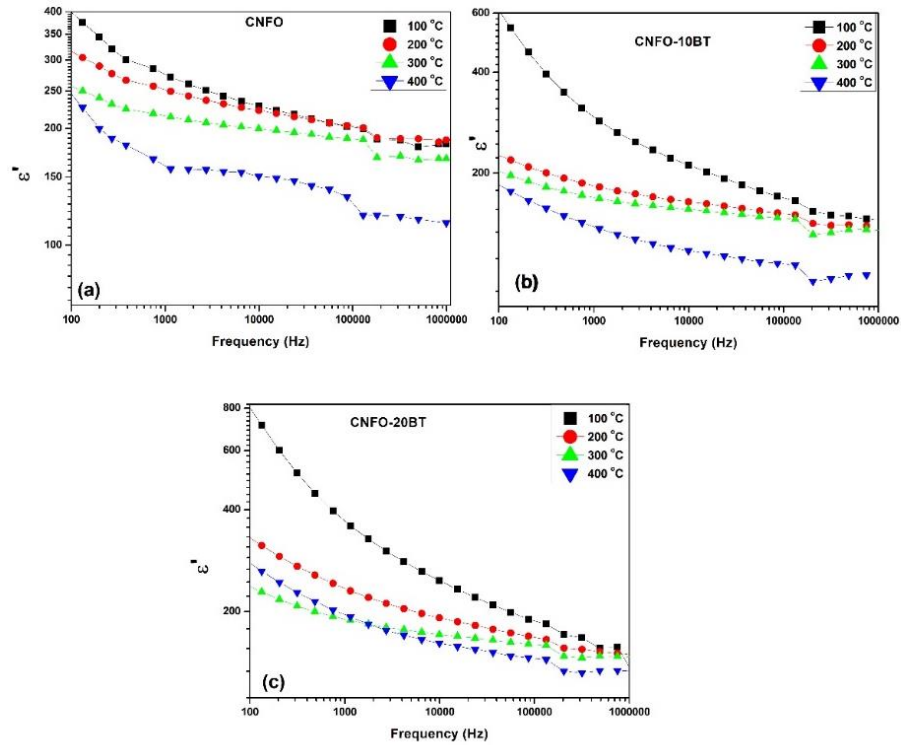


Figure 5.3: Frequency dependence of real part of dielectric constant (ϵ') for CNFO and CNFO-BT composites at different temperatures.

The magnetodielectric coupling constant (MD) is studied by measuring the dielectric properties at different magnetic fields and at a frequency of 10 kHz as shown

in Fig. 5.4 and is quantified as Equation (3.2). The composition of magnetic-ferroelectric phase is an important factor for deciding the magnetodielectric response. The variation in dielectric constant is less for CNFO and significantly increases with BT content. This enhancement could be possibly due to the modification of spatial charge distribution and restricted ferromagnetic domain wall rotation originating from BT substitution in CNFO. With increasing magnetic field, the change in dielectric constant drastically decreases due to alignment of domain walls in CNFO. Surprisingly, all CNFO-BT composites indicate stability in magnetodielectric coupling by displaying non-zero MD value at even higher fields. It is important to note that the magnetodielectric response in CNFO as well as CNFO-BT composites originates due to the contribution of magnetostriction of CNFO. This occurs due to the strain induced in CNFO phase on application of magnetic field creating a mechanical coupling between dielectric and magnetic phases and can be expressed as strain mediated magnetodielectric response. Additionally, the interfacial polarization effect in CNFO-BT can also induce magnetodielectric behavior based on the impedance of grain or grain boundary with application of magnetic field [221].

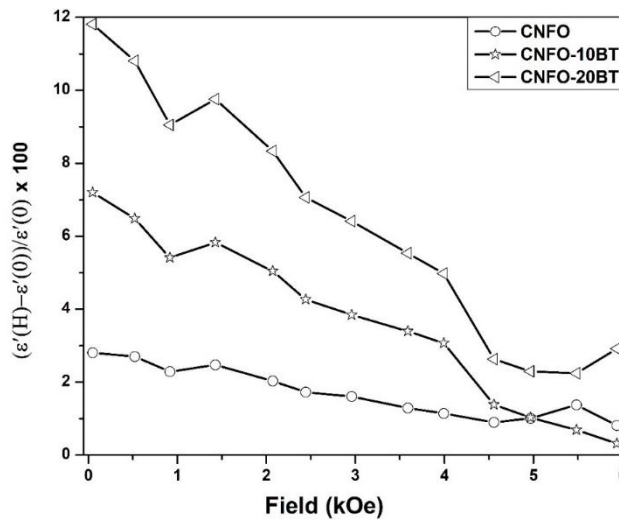


Figure 5.4. Percentage change in dielectric constant for CNFO and CNFO-BT composites as a function of magnetic field at 10 kHz.

5.3.3. Impedance Measurements

Fig. 5.5 shows Nyquist plots of CNFO and CNFO-BT composites. All the composites display single semicircular arc starting from the origin whose radius decreases with temperature suggesting dominance of grains contribution and negative temperature coefficient of resistance [93]. It is noted that the impedance value in the

composites increase with BT suggesting highly resistive nature of CNFO-BT composites [40]. CNFO is a weak ferroelectric and poor dielectric material. Thus, the significant contribution in the dielectric and impedance properties is due to the effective content of BTO. Increasing the amount of BTO in CNFO-BT composite therefore increases the net impedance of CNFO-BT composite [40]. The centers of semicircles are observed to be positioned below the Z' axis owing from spread relaxation times

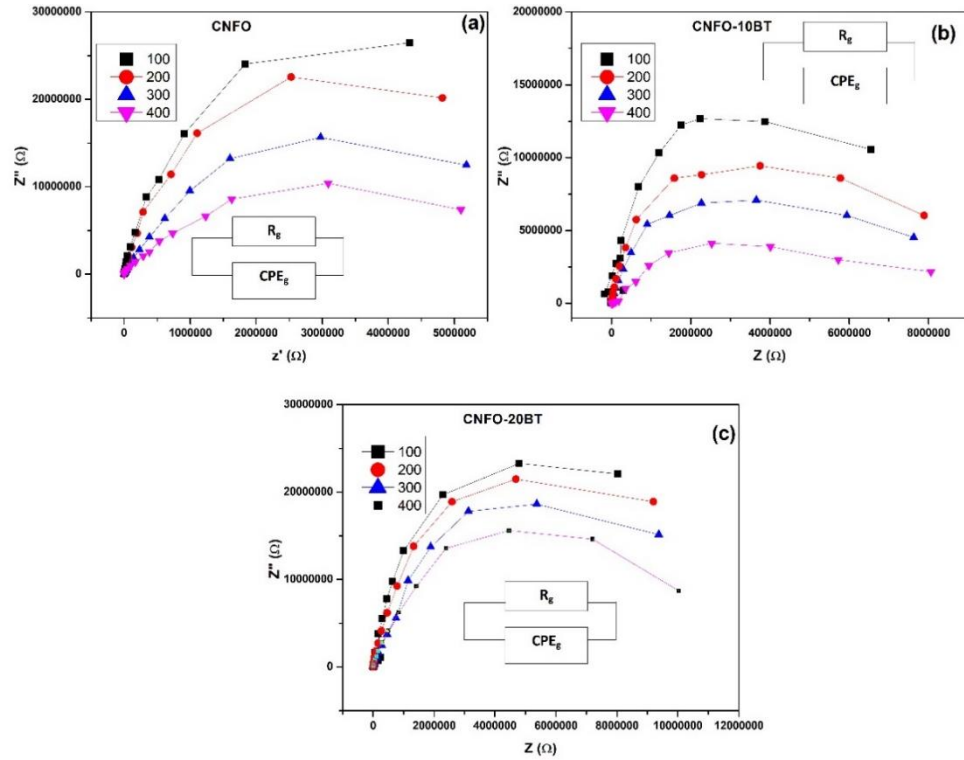


Figure 5.5. Nyquist plot of CNFO-BT composites measured at different temperatures along with their equivalent circuit measured.

and indicate the existence of non-Debye relaxations in CNFO-BT composites [137]. The non-Debye relaxations can be understood by representing the Nyquist plots in terms of modified R-C electric circuits. These electric circuits contain arrangement of one or more subarray of resistance (R), capacitance (C) and constant phase element (CPE) with each subarray denoting the contributions of grains and grain boundary. The non-Debye behavior present in BT-CFO composites is justified from the presence of CPE in the equivalent circuit, which is related to the impedance by the equation $Z_{CPE} = 1/(j\omega)^n$ CPE. The corresponding fitted parameters are displayed in Table 5.2. The impedance spectra of CNFO-BT composites are fitted with one R-CPE parallel combination and are in agreement with each other. The fitting also confirms the dominance of grain resistance in the conduction phenomena.

Table 5.2. Fitted parameters for Cole–Cole plots of CNFO-BT composites.

Temp (°C)	$R_g (\Omega)$	CPE_g	n_g
CNFO			
200	6.1×10^6	2×10^{-8}	0.65
300	4.3×10^6	6×10^{-9}	0.78
400	1.9×10^6	9×10^{-10}	0.86
CNFO-10BT			
200	8.2×10^6	1.2×10^{-9}	0.62
300	5.3×10^6	5×10^{-9}	0.70
400	3.1×10^6	7×10^{-10}	0.79
CNFO-20BT			
200	8.9×10^6	3×10^{-8}	0.55
300	5.4×10^6	7×10^{-8}	0.69
400	2.9×10^6	4×10^{-9}	0.75

5.3.4. Magnetic Measurements

Fig. 5.6 shows magnetic hysteresis curves for CNFO and CNFO-BT composites. Inset of Fig. 5.6 shows the enlarged view of M-H curves at low magnetic fields. All composites display systematically strong ferromagnetic behavior. The saturation magnetization for CNFO is comparable to the earlier reported work [88]. The magnetic retentivity is found to decrease with increase in content of BT. This re-emphasizes structural distortion induced in CNFO lattice owing to BT substitution. Contrarily, the coercivity is large for CNFO-10BT and least for CNFO-20BT as compared to CNFO. The increased value of coercivity in CNFO-10BT composite is due to enhancement in magnetoelectric coupling, however, such coupling is limited by lattice distortion and weakens the ferromagnetic nature in CNFO-BT composite. On further increasing the BT content as in case of CNFO-20BT, enlarged strain mediated magnetoelectric coupling at the piezoelectric-piezomagnetic interface enhances the ferromagnetic nature.

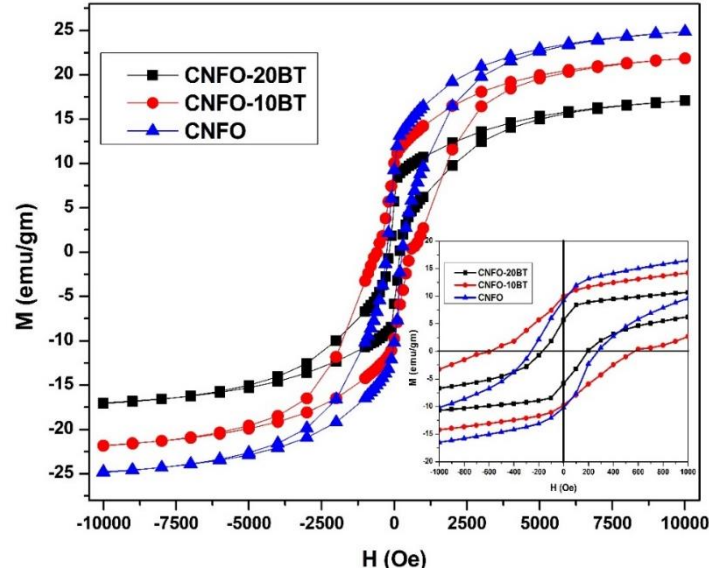


Figure 5.6. Room temperature magnetization curves (M vs H) for CNFO and CNFO-BT composites. Inset shows the enlarged view of CNFO and CNFO-BT composites.

5.3.5. Ferroelectric and Magnetoelectric Measurements

The ferroelectric hysteresis P-E loops of CNFO-BT composites are plotted in Fig. 5.7. All the loops show weak P-E ferroelectric polarization loop because of spatially distributed electric dipoles. The unsaturated lossy P-E loop is due to the fact of relatively high-leakage current. The magnetic nature of CNFO particles tends to

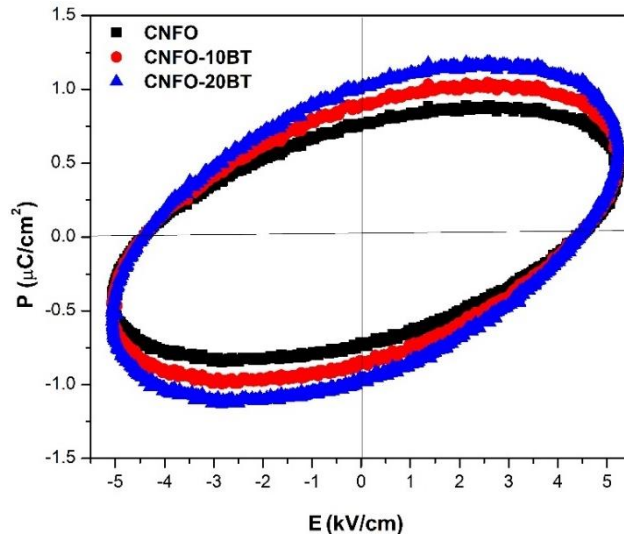


Figure 5.7. P-E hysteresis loops of CNFO and CNFO-BT composites.

agglomerate and thereby induces weak ferroelectricity [222,223]. As the content of BT phase is increased in CNFO, the maximum polarization is increased due to increased conductivity. The energy storage and efficiency is estimated using Equations (1.12) and

(1.13). The unloaded sample of CNFO and CNFO-20BT displayed the energy density of 2.1 and 4.25 mJ/cm³ respectively with an efficiency of 17 and 31.6 %, respectively.

The magnetoelectricity in CNFO-BT composites can be understood well by examining the variation of maximum electric polarization versus applied electric field hysteresis graphs as a function of external magnetic field [83]. Fig 5.8 shows the variation in maximum polarization measured from P-E hysteresis loop at different magnetic fields for CNFO and CNFO-BT composites at room temperature with fixed frequency of 50 Hz. The maximum polarization observed decreases with increasing magnetic field suggesting strong magnetoelectric character in CNFO composites. The largest change in maximum polarization of 20 % is observed in CNFO-20BT composite, making it most suitable for magnetoelectric devices [224]. This enhanced magnetoelectric effect is correlated to lattice shrinkage on BT substitution resulting in strain mediated magnetoelectric coupling at the piezoelectric-piezomagnetic interface [49]. In order to obtain the ME coupling coefficient, the variation of P_{\max} was linearly fitted with magnetic field H . The error bars obtained from linear fit are also incorporated in the experimental data plot. The maximum magnetoelectric coupling coefficient (α) was achieved for CNFO-20BT composite as 5 mV/cm/Oe. This magnetoelectric response of CNFO-BT composite agrees with some reported results [40,46].

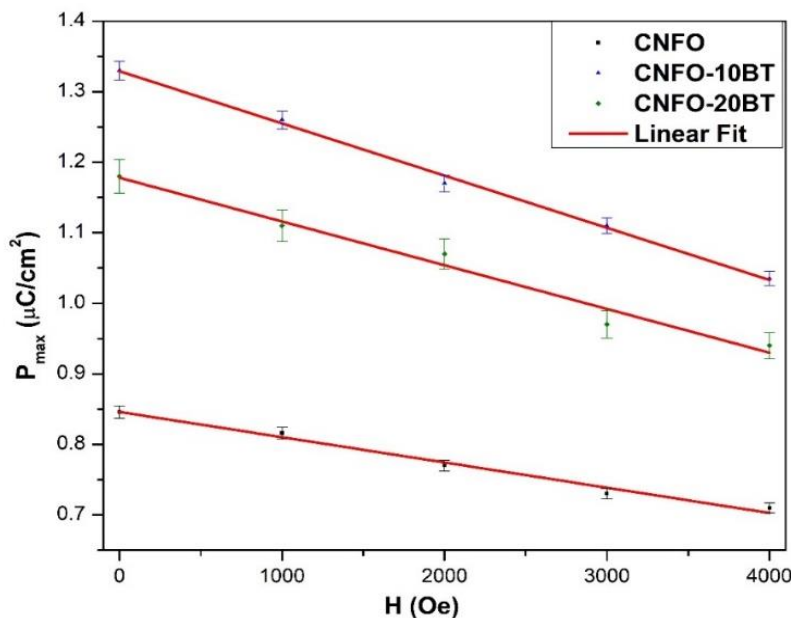


Figure 5.8. Variation of maximum polarization (P_{\max}) with magnetic field for CNFO and CNFO-BT composites.

Chapter - 6

Structural, Multiferroic and Magnetoelectric Properties of Bi_{0.85}La_{0.15}FeO₃ - BaTiO₃ Composites

This chapter discussed on the comprehensive study of Bi_{0.85}La_{0.15}FeO₃-BaTiO₃ by coalescing ferroelectric, dielectric, magnetic and magnetoelectric properties with structural and microstructural characterizations to explore the effect of BaTiO₃ (BT) in Bi_{0.85}La_{0.15}FeO₃ (BLFO) and forming composite ceramics. The structural investigations reveal structural transformation from rhombohedral to cubic phase along with lattice compression on increase BT content. The room temperature M-H hysteresis curve shows the existence of weak ferromagnetism in BLFO-BT composites and superparamagnetism in BLFO-10BT ceramic. The curve fitting of M-H curve for 0.9BLFO-0.1BT showed the existence of superparamagnetic particles. The ferroelectric hysteresis P-E loop measurements produced unsaturated oval shaped loops with high leakage and displayed a lossy dielectric nature. The effect of magnetic field on polarization versus electric field curve reveals the interfacial interaction due to the origin of magnetoelectric interaction in BLFO-BT composite ceramics. All the samples display peak broadening in temperature-permittivity plot and confirm relaxor behavior. The 0.9BLFO-0.1BT composite exhibited maximum energy storage density of 16 mJ/cm³ with an efficiency of 60 % associated with maximum magnetoelectric coupling of 16 mV/cm/Oe and is a potential candidate for magnetoelectric devices.

6.1. Introduction

The miniaturization and discovery of novel materials for advanced functional devices have been fascinating for research in the recent times [225–230]. Among these novel materials, magnetoelectrics are studied extensively as the coupling between the orders promotes in achieving magnetic control of electrical polarization and electric control of magnetization [231]. This feature is invariably explored in the design of technological advancements in the areas of electrically controlled magnetic storages, sensing and high-speed optoelectronics. The single phase multiferroics though exhibit magnetoelectricity, are not completely exploited in industrial applications due to weak magnetoelectric coupling in them [14–16,31,32]. Subsequently in recent years, intensive research has been focused in finding systems based on single phase multiferroics such as solid solutions [90,232,233], composite systems [38–42] and thin films [234–236] for achieving enhancement in magnetoelectric coupling both in bulk and nanoscale regime [92,154,237].

The previous chapter comprehensively discussed about $\text{Co}_{0.5}\text{Ni}_{0.5}\text{Fe}_2\text{O}_4$ - BaTiO_3 composites with (3-0) connectivity scheme. The composites displayed maximum ME coupling of 5 mV/cm/Oe with energy density of 5 mJ/cm³. The comprehensive results of previous chapters help in understanding that in order to achieve higher magnetoelectric coupling, a conciliation on energy storage becomes obligatory and vice versa. This mutually exclusive improvement in ME coupling at the expense of energy storage suggests a new choice of host with improved properties for the preparation of composites. As per literature, BiFeO_3 (BFO) manifests as promising candidate for exorbitant novel magnetoelectric applications due to its prevailing multiferroism at room temperature [38,90–93]. It has also been discussed in the section 1.9.1 that $\text{Bi}_{0.85}\text{La}_{0.15}\text{FeO}_3$ (BLFO) is one of the stable structures which display single phase and enhanced ferroelectric and magnetic properties along with dielectric anomaly near the magnetic transition temperature [3,93,98,99]. In addition, BLFO based composites have been investigated for structural, dielectric and multiferroic properties [42,238–240]. The extent of magnetoelectric coupling in modified BFO and BLFO based systems still needs to be improved. Furthermore, there has not been enough focus on the multiferroic and magnetoelectric properties of composite ceramics of BLFO and BT. In this regard, this chapter describes the synthesis $\text{Bi}_{0.85}\text{La}_{0.15}\text{FeO}_3$ - BaTiO_3 (BLFO-

BT) composite to study the effect of BT in BLFO on the structural, dielectric, and magneto-dielectric coupling ferroelectric P-E and magneto-electric properties.

6.2. Sample Preparation

The (1-x)BLFO-xBT ($x = 0, 0.1, 0.2$ and 0.3) were prepared by solid state reaction route as discussed in section 2.3 and as represented in Fig. 2.1. The AR grade of chemicals Bi_2O_3 , Fe_2O_3 , La_2O_3 , BaCO_3 and TiO_2 were used as initial ingredients in stoichiometric ratio. The synthesis conditions have been tabulated in Table 6.1. The composites are named as BLFO ($\text{Bi}_{0.85}\text{La}_{0.15}\text{FeO}_3$), BLFO-10BT ($0.9\text{Bi}_{0.85}\text{La}_{0.15}\text{FeO}_3$ - 0.1BaTiO_3), BLFO-20BT ($0.8\text{Bi}_{0.85}\text{La}_{0.15}\text{FeO}_3$ - 0.2BaTiO_3), and BLFO-30BT ($0.7\text{Bi}_{0.85}\text{La}_{0.15}\text{FeO}_3$ - 0.3BaTiO_3).

Table 6.1. Synthesis conditions of BaTiO_3 , $\text{Bi}_{0.85}\text{La}_{0.15}\text{FeO}_3$ and $\text{Bi}_{0.85}\text{La}_{0.15}\text{FeO}_3$ - BaTiO_3 composites.

Composition	Calcination temperature (°C)	Duration (h)	Sintering temperature (°C)	Duration (h)
BaTiO_3	1000	10	-	-
$\text{Bi}_{0.85}\text{La}_{0.15}\text{FeO}_3$	800	10	950	10
BLFO-10BT	-	-	950	10
BLFO-20BT	-	-	950	10
BLFO-30BT	-	-	950	10

6.3. Results and Discussion

6.3.1. Structural and Morphological Measurements

Fig 6.1 shows the X-ray diffraction pattern of the sintered BLFO and BLFO-BT ceramics. It is clearly perceptible from the XRD spectra that the samples exhibit composite as well as solid solution behavior. The XRD graphs display polycrystalline nature of all samples and indexing of diffraction peaks is as per distorted rhombohedral structure with $R3c$ space group. The XRD pattern of BLFO are matched with JCPDS # 86-1518 and show very few traces of impurities $\text{Bi}_{25}\text{FeO}_{39}$ at $2\theta \approx 28^\circ$ as indicated by symbol '*'. Additionally, no trace of impurities of $\text{Bi}_2\text{Fe}_4\text{O}_9$ was not observed in BLFO ceramic, which suggests that incorporation of La in BFO suppresses the unwanted

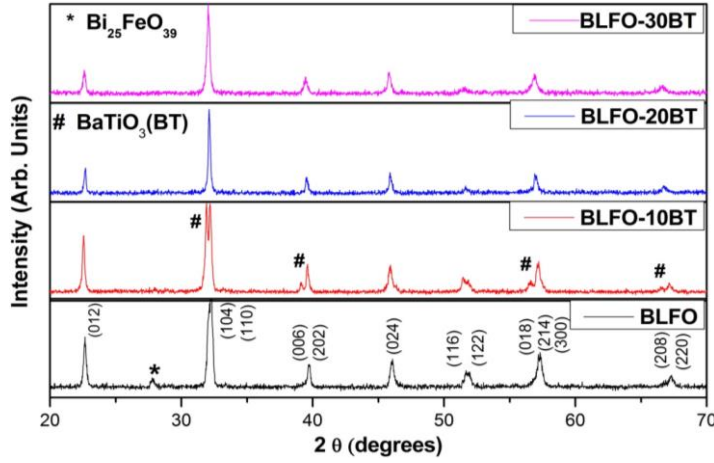


Figure 6.1. XRD patterns of BLFO and BLFO-BT ceramics.

secondary phases and results in phase purity [3,93,241]. The XRD pattern of BLFO-10BT shows a peculiar splitting in the peaks around $2\theta \approx 32^\circ$, 40° and 58° exhibiting the co-existence of rhombohedral La modified BFO as well as tetragonal BT and suggests composite formation. The splitting is more visible in enlarged view of XRD of BLFO-10BT in Fig. 6.2. The XRD patterns of BLFO-10BT for are indexed with JCPDS # 05-0626 for tetragonal phase of BaTiO_3 and are indicated by symbol ‘#’. This splitting in the peaks vanishes in case of BLFO-20BT and BLFO-30BT ceramics and peaks become sharper indicating the formation of cubic structure. Furthermore, the peaks $2\theta \approx 32^\circ$ in BLFO-20 and BLFO-30BT solid solution shift to lower 2θ angle due to A-site substitution of large atom of Ba^{2+} (ionic radius: 1.35 \AA) in place of Bi^{3+} atom (ionic radius: 0.605 \AA) resulting in lattice compression.

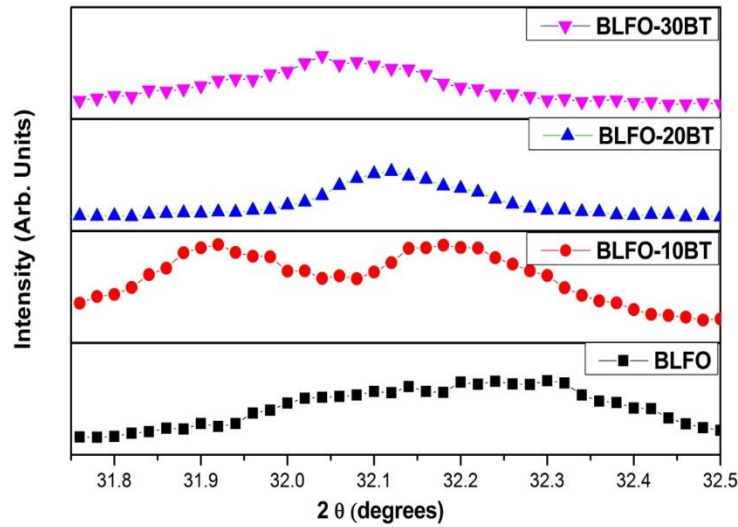


Figure 6.2. Enlarged view of XRD of BLFO-BT ceramics in the $2\theta \approx 31.6-32.5^\circ$.

Fig. 6.3 (a and c) show SEM images of BLFO-10BT and BLFO-20BT ceramics. The SEM images display high density structure with non-uniform grain sizes. The density is found to increase relatively in case of BLFO-20BT in comparison to BLFO-10BT. The grains may be categorized as small grains which are more or less spherical of size nearly 5 μm and large grains of lump shape of size more than 5 μm . It can also be observed that small grains quantity increases with BT content. If we assume that large grains and small grains have different phase for contribution then we can estimate the formation of BLFO-10BT and BLFO-20BT from EDAX spectra as shown in Fig. 6.3 (b and d), respectively. The corresponding values for elemental composition are tabulated in Table 6.2. The increasing content of Ba and Ti follows the distribution of molar ratio for composites and confirms the formation of BLFO-10 and BLFO-20BT composites.

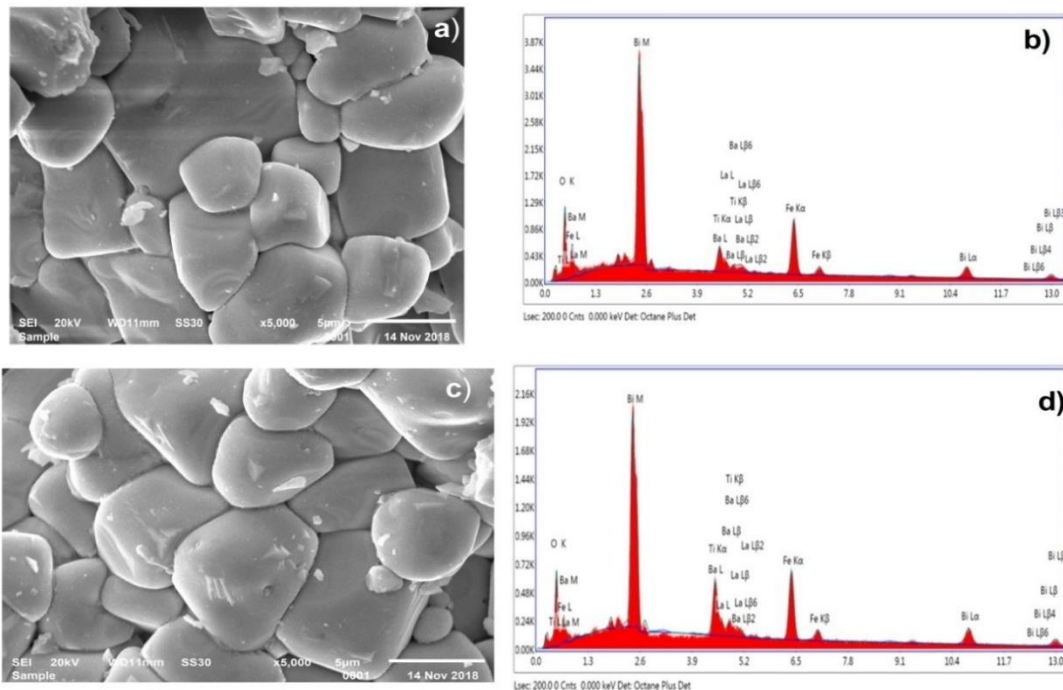


Figure 6.3. SEM micrograph and EDAX spectra of (a-b) BLFO-10BT and (c-d) BLFO-20BT, respectively.

Table 6.2. EDAX table for percentage distribution of atomic weights of elements in BLFO-10BT and BLFO-20BT composites.

Element	BLFO-10BT	BLFO-20BT
O K	60.93	55.37
Bi M	11.81	10.57
Ba L	1.81	5.56
Ti K	3.25	7.83
La L	2.21	2.03
Fe K	19.99	18.64

Raman spectroscopy is an important study for understanding the phase formation. Raman scattering is used for detection of any alteration in crystal lattice including atomic displacements by probing the deviation in frequency, bandwidth and intensity of the Raman peaks. The Raman spectra for BLFO and BLFO-B,T ceramics were studied at room temperature. BiFeO₃ possesses rhombohedral structure with $R3c$ space group and contains 18 phonon modes classified as $\Gamma = 4A_1 + 5A_2 + 9E$ as given by the group theory [39]. Out of these 18 modes, the Raman active modes are 4A₁ and 9E. In the present study, BLFO Raman spectra have only 5 out of 13 observed Raman peaks as shown in Fig. 6.4. The peaks of BLFO spectra are fitted with Lorentzian function using Fityk software and their corresponding positions obtained are presented in Table 6.3. A peculiar increase in peak position (blueshift) as compared with earlier reported literature in BLFO compared to BFO due to lowering of reduced mass occurring on account of substitution of low atomic mass La ion in place of Bi ion. This shift in peak position can also be expressed using the relation

$$f = \frac{1}{2\pi} \sqrt{\frac{k}{m}} \quad (6.1)$$

where f is frequency of the Raman modes, m is reduced mass, and k is force constant [39]. The Raman spectra of polycrystalline materials consisting of smaller unit cells display all Raman modes. In the present study, some of the Raman modes of BiFeO₃ are absent due to merging of low wavenumber Raman modes as well as symmetry-forbidden scattering.

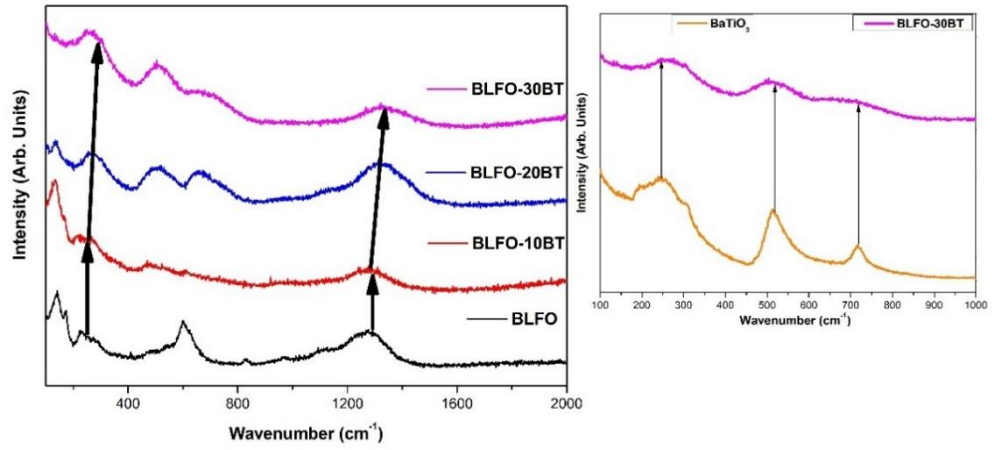


Figure 6.4. Raman spectra of BLFO and BLFO-BT composites.

The Raman spectra of BLFO-BT ceramics are also represented in Fig. 6.4. The Raman modes associated with constituent BLFO and BT phases can be tracked in the Raman spectra of BLFO-BT. Except for a few significant peaks, most of the peaks are merged in the BLFO-BT due to the Raman active modes of BT. The growth of the E4 mode in BLFO-10BT ($\sim 470 \text{ cm}^{-1}$) can be construed to alterations in the movement of

Table 6.3. Raman peak positions of BLFO and BLFO-BT composites.

BLFO		BLFO-10BT		BLFO-20BT		BLFO-30BT	
Wave number (cm ⁻¹)	Phase	Wave number (cm ⁻¹)	Phase	Wave number (cm ⁻¹)	Phase	Wave number (cm ⁻¹)	Phase
141.275	A1-1 (BLFO)	133.836	A1-1 (BLFO)	133.836	A1-1 (BLFO)	249.588	ETO (BT)
173.429	A1-2 (BLFO)	168.49	A1-2 (BLFO)	254.477	ETO (BT)	503.436	ETO (BT)
228.778	A1-3 (BLFO)	225.1	A1-3 (BLFO)	519.992	ETO (BT)	655.834	ELO (BT)
602.25	E-9 (BLFO)	470.217	E-4 (BLFO)	660.476	ELO (BT)	1400	E-9 (BLFO)
1330	E-9 (BLFO)	522.354	ETO (BT)	1378	E-9 (BLFO)		
		1330	E-9 (BLFO)				

Bi ions and the tilting of FeO_6 octahedra. The evolution of Raman modes ETO at 249, 503 and 655 cm^{-1} associated with tetragonal BaTiO_3 in BLFO-30BT can be observed from the inset of Fig. 6.4. The shift in Raman active mode E9 of BLFO (1330 cm^{-1}) with BT concentration to higher wavenumber as tabulated in Table 6.3 is correlated to lattice compression arising on an account of Ba^{2+} replacing Bi^{3+} ion as also verified by XRD results. The Raman spectra of BLFO-10BT and BLFO-20BT ceramics display the presence of both constituent phases confirming composite formation along with higher wavenumber modes shifted to higher side and lower wavenumber modes shifted to lower side displaying blueshift and redshift simultaneously. The blueshift associated with Bi-O bond is dominant than redshift and agrees well with the increase in dielectric transition temperature observed.

6.3.2. Dielectric Measurements

The dielectric properties are studied with concentration of BT in BLFO. The variation of dielectric constant (ϵ') for BLFO-BT composite ceramics at 100 Hz as a function of temperature is shown in Fig. 6.5. The permittivity plot shows maximum in the vicinity of 360°C , the ferroelectric / antiferroelectric transition T_c of BLFO [99]. As the temperature crosses the transition temperature T_c , the dielectric constant decreases with temperature which suggest the presence of bulk permittivity. The anomaly is observed in all the compositions exhibit near 360°C . The anomaly peak of permittivity shifts to the lower temperature with increasing content of BT indicating the effect of BT substitution in bringing the T_c of BLFO-BT composites close to room temperature and confirms the presence of relaxor behavior.

For the composite ceramics, the dielectric contribution arises from the parent ferroelectric component as well as the interfacial polarization originating due to different resistance of ferroelectric and ferromagnetic phase. The variation of dielectric loss ($\tan \delta$) with frequency is shown in Fig. 6.6 for BLFO-BT composites. A constant high value of $\tan \delta$ at low frequencies in all the composites are attributed to space charge polarization originating from non-homogenous dielectric structure consisting of defects, porosity and grain distribution [42].

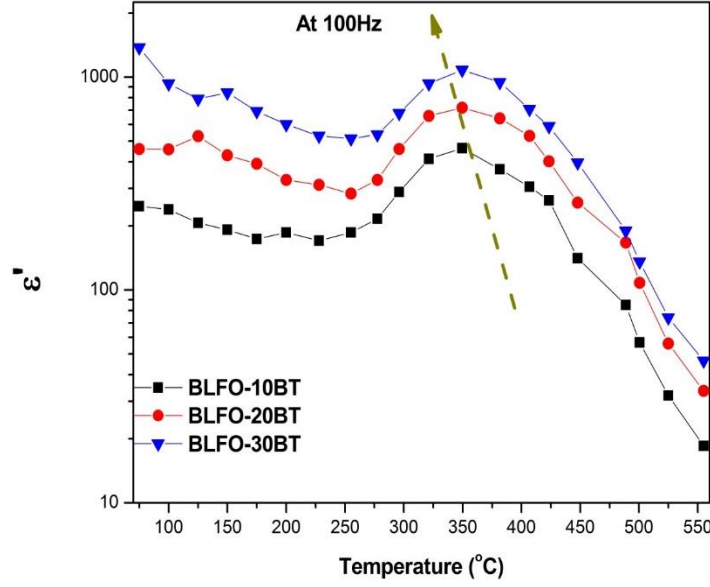


Figure 6.5. Plot of dielectric constant with temperature for BLFO-BT composites at frequency of 100 Hz.

The loss decreases with increasing BT mole fraction and this indicates an ordering between BT and dielectric behavior. The dielectric properties of all the BLFO-BT composites display similar permittivity and $\tan \delta$ behavior. The variations in the dielectric constant (ϵ') for BLFO-10BT composite ceramic at room temperature are shown in Fig. 6.7. The plot displays that ϵ' decreases with increase in frequency. In the frequency region up to 10 kHz, ϵ' decreases quickly and indicating frequency dispersion

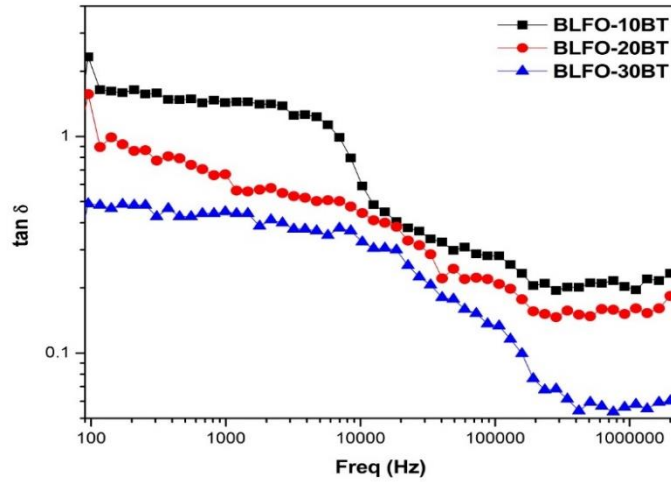


Figure 6.6. Variation of dielectric loss ($\tan \delta$) with frequency for BLFO-BT composites.

in the BLFO-BT composites. The possession of high value of ϵ' and $\tan \delta$ at low frequencies is due to the presence of interfacial polarization in BLFO-BT ceramics [242,243]. The value of ϵ' decreases gradually as the electric dipoles are unable to

follow the oscillations of applied field. The contributors for high dielectric constant at low frequency are interfacial polarization, and that for low dielectric value at higher frequency is electronic polarization [244–246]. Furthermore, as the temperature increases from 100 °C to 400 °C, the dipoles gain higher kinetic energy and their ability to follow the oscillations of electric field decreases thereby decreasing the value of dielectric constant. However, an anomaly is observed at temperature of 300 °C, where the dielectric constant is higher and is related to dielectric / ferroelectric transition temperature.

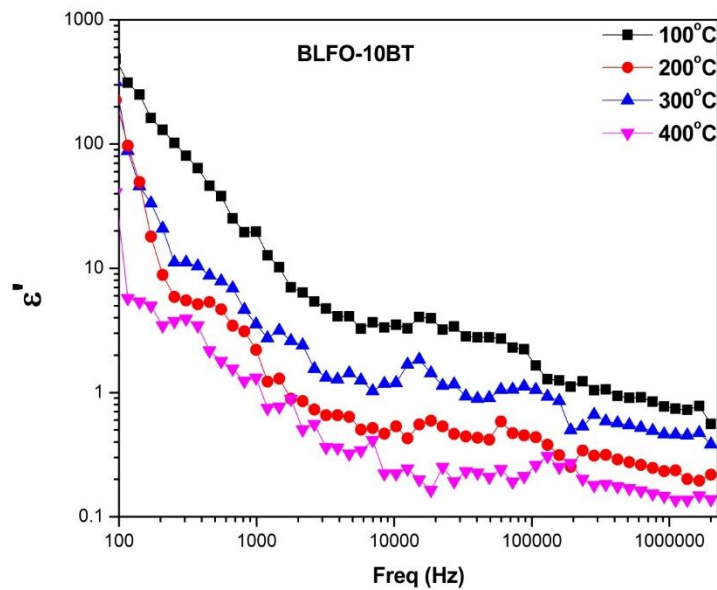


Figure 6.7. Frequency dependence of dielectric permittivity at different temperature for BLFO-10BT composite.

6.3.3. Magnetic Measurements

The room temperature variation of magnetization with applied magnetic field upto 10 kOe obtained from vibrating sample magnetometer is shown in Fig. 6.8. The M-H plot of BLFO, BLFO-20BT and BLFO-30BT composite ceramics in Fig. 6.8(a) exhibit weak ferromagnetism which tends to saturate at higher magnetic field. In a typical BFO, the antiferromagnetism is usually overcome by incommensurate cycloidal spin structure. When the A site is substituted with a foreign atom, a canted spin structure is generated resulting in weak ferromagnetic behavior as observed for La substituted BFO or BLFO [69,247]. The strength of magnetic moment induced is dependent on the size of foreign atoms and level of distortion of FeO_6 octahedra. This is the possible reason of observed weak ferromagnetism in BLFO as compared to antiferromagnetic BFO. It has also been observed that ferromagnetism is more prominent in BiFeO_3 and

BLFO based systems and this strain induced structural distortion generates large magnetization [240,248,249]. So, when BLFO lattice is modified by BaTiO₃, the substitution of bigger sized Ba²⁺ ions result in enhancement in the magnetization of BLFO-10BT. This enhancement in the magnetization could also be due to interfacial coupling between the constituent phases [40]. The measured maximum magnetization gets lowered with further increase in BT concentration in BLFO. The addition of further ferroelectric BT generates larger spatial alteration in BLFO lattice, which decreases the maximum magnetization in BLFO-BT composite ceramics. The remnant magnetization is also found to decrease with BT content in BLFO-BT composites. The improved magnetization of BLFO-10BT shows potential for memory device applications. As BT is ferroelectric in nature, the net magnetization in these BLFO-BT composite ceramics is mainly due to BLFO concentration.

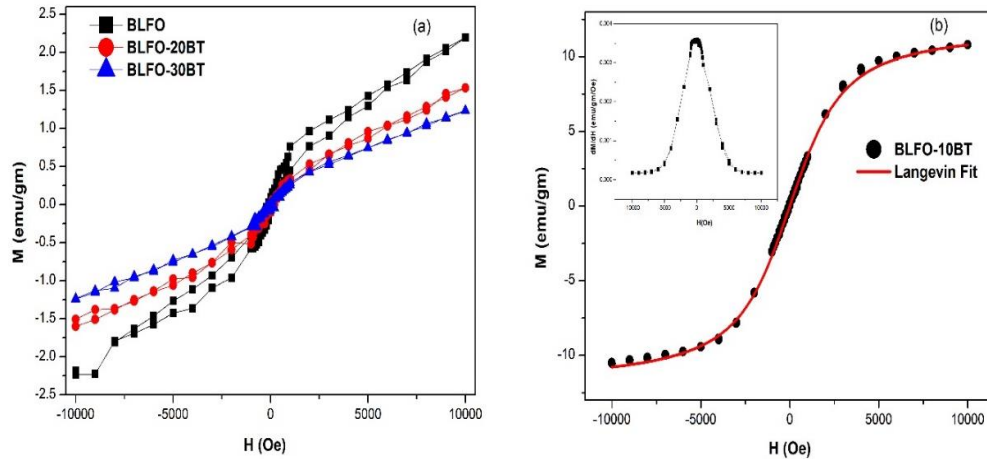


Figure 6.8. M-H curves of (a) BLFO, BLFO-20BT and BLFO-30BT composites (b) M-H curve of BLFO-10BT composite ceramic fitted with Langevin function. Inset show the variation of dM/dH with respect to magnetic field of BLFO-10BT composite.

An anomalous superparamagnetic M-H curve is observed in case of BLFO-10BT composite ceramic as shown in Fig. 6.8(b). This is possible whenever the size of grains span around the threshold superparamagnetic limit in the composite system [247]. To analyze the extent of superparamagnetic behavior, the M-H curve was fitted for BLFO-10BT composite with the following Langevin function

$$M = n\mu \left\{ \coth \left(\frac{\mu H}{kT} \right) - \frac{kT}{\mu H} \right\} \quad (6.2)$$

where μ is net magnetic moment per particle, k is Boltzmann constant, T is temperature and n is number of particles per unit mass. The volume V obtained from μ/M_s by including the density of BLFO-10BT and M_s is $1.899 \times 10^{-17} \text{ emu/cm}^3$. If we assume that the particles are spherical in shape then the estimate diameter radius of the particle is 18.6 nm. Furthermore, the superparamagnetic particle size limit can be obtained from relation between volume V and anisotropy constant (k_u) as $V = 25kT/k_u$, where k represents Boltzmann constant and T is temperature. The anisotropy constant can be obtained using the coercivity (H_c) as

$$H_c = 0.48 \frac{2k_u}{M_s} \quad (6.3)$$

The coercivity of 661.25 Oe of BLFO-10BT was obtained from the first order differentiation of M-H hysteresis curve as dM/dH curve as plotted in inset of Fig. 6.8. The resultant anisotropy constant is 5435 erg/cm^3 . The values of coercivity are estimated from M-H loops and dM/dH curves are in good agreement with each other. The critical volume obtained is $1.89 \times 10^{-16} \text{ cm}^3$ which is more than the estimated particle size and thus supports the existence of superparamagnetic particles in BLFO-10BT composite ceramic. This behavior is not observed in BLFO-20BT and BLFO-30BT composite ceramics, because the number of superparamagnetic particles gets lowered w.r.t. threshold limit with increase in BT content.

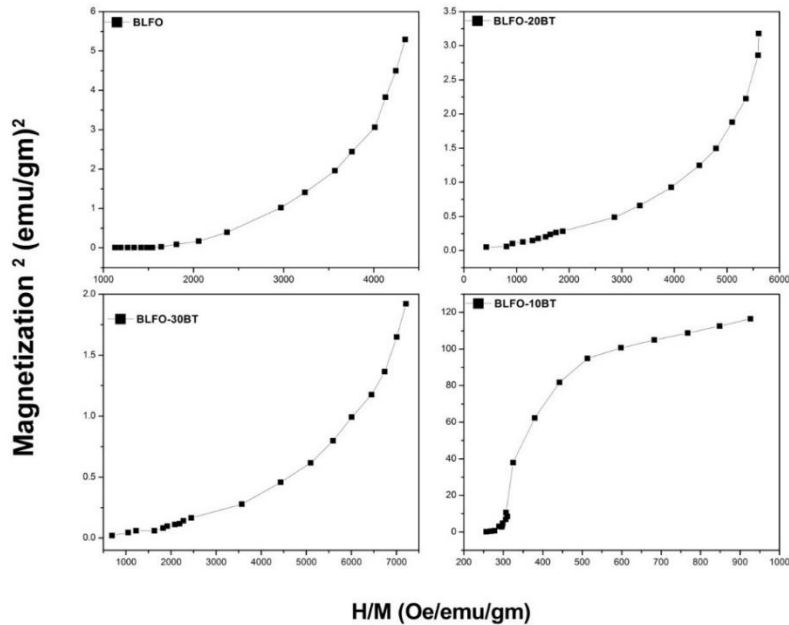


Figure 6.9. Arrott plots of BLFO-BT ceramics.

To estimate the extent of ferromagnetic orderings and the magnetic transition order in BLFO-BT ceramics due to BT substitution, the Arrott plots (M^2 vs. H/M curve) have been prepared as shown in Fig. 6.9. The occurrence of curvature and positive slope at high fields in the Arrott plots of BLFO and BLFO-BT composite ceramics show the existence of weak ferromagnetic ordering and second-order meta-magnetic transition [250]. The positive curvature in case of BLFO-10BT ceramic indicates superparamagnetic behavior which could be due to spin interactions at the interfaces of the BLFO and BT grains.

6.3.4. Ferroelectric and Magnetoelectric Measurements

The ferroelectric hysteresis loops help in validating composite ceramics for polarization switching applications. The P-E hysteresis loop for BLFO-BT ceramics is studied employing the Sawyer–Tower technique [209] and are displayed in Fig. 6.10. All the loops show similar unsaturated behavior and exhibit high leakage current. It is expected that BT incorporation in BLFO should enhance the P-E loop. In the present studied system, this behavior is not observed which could be attributed to increase oxygen vacancies destroying the pinning of ferroelectric domains. The P-E loop of BLFO-10BT show the largest polarization among all the composite ceramics, which could possibly be due to incorporation of ferroelectric domain walls in the rhombohedral lattice of BFO. The P-E loop of BLFO-20BT and BLFO-30BT show

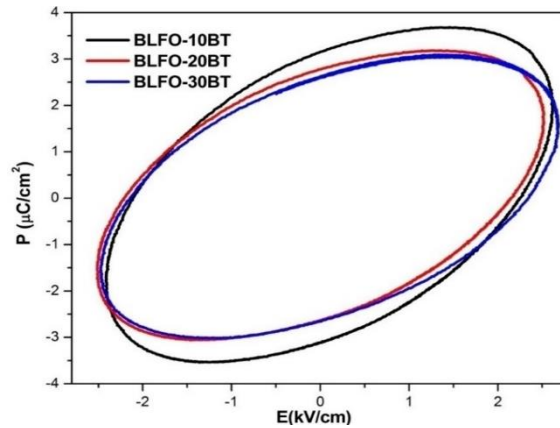


Figure 6.10. P-E hysteresis curves for BLFO-BT composite ceramics.

akin pattern with nearly same coercive field of 1.5 kV/cm due to large leakage current arising from vacancies created by multivalent ions. The BLFO-10BT composite displays an improved recoverable energy storage density of 16 mJ/cm³ with an

improved efficiency of 60 %, whereas BLFO-30BT displays energy density of 10 mJ/cm³ and efficiency of 40 %. The enhancement in energy storage efficiency of BLFO-10BT composite validates its potential for energy storage devices.

The P-E loops for BLFO-10BT were also observed by varying the frequency as well as magnetic field. The estimated values of recoverable useful energy storage density with frequency as well as magnetic field is plotted in Fig. 6.11. The energy density of BLFO-10BT decreases with frequency as the dipoles do not have the ability to cope with the oscillations of the electric field. The decrement in the energy density of BLFO-10BT composite with magnetic field indicates the presence of magnetoelectric interaction in the composites. The qualitative

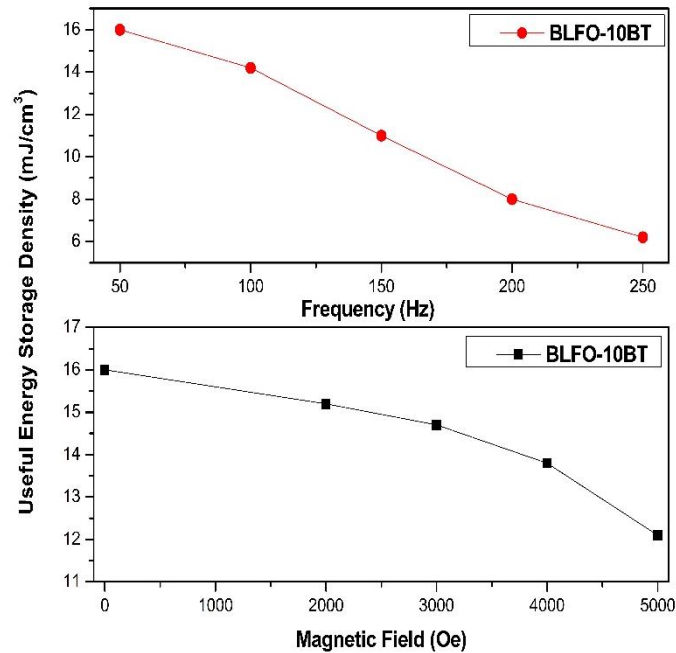


Figure 6.11. Variation of useful recoverable energy density with frequency and magnetic field for BLFO- 10BT composite.

evidence of magnetoelectricity originates from the variation in maximum polarization P_{\max} with external magnetic field. The variation of maximum polarization with magnetic field for BLFO-10BT and BLFO-30BT composite and their corresponding magnetoelectric coupling coefficient computed as

$$\alpha = \frac{dE}{t \cdot dH} \quad (6.4)$$

where t is thickness, are displayed in Fig. 6.12. The polarization decreases with magnetic field because the composites are unable to sustain larger magnetic field. The relative variation of 48% and 45% in P_{\max} versus H was observed for BLFO-10BT and

BLFO-30BT composites, respectively. Interestingly, α is observed to increase with magnetic field emphasizing that the composites are able to show multiferroism and magnetoelectricity at high magnetic fields as required for sensor applications. The origin of the magnetoelectric interaction comes from the interfacial coupling between the constituent phases as confirmed from magnetization studies [40].

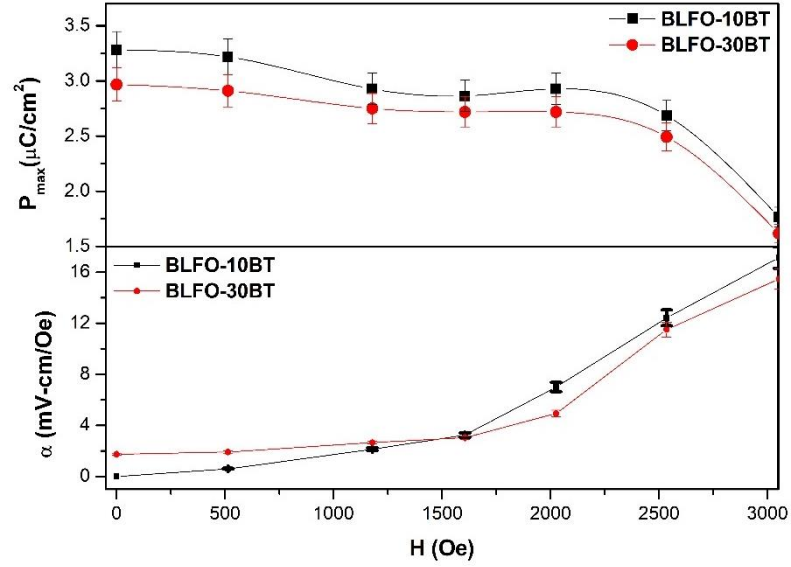


Figure 6.12. Variation of maximum polarization and magnetoelectric interaction coefficient with magnetic field.

Chapter - 7

Discursive Investigations on Structural, Dielectric and Multiferroic Properties of NdMnO₃- BaTiO₃ Composites

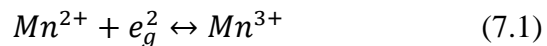
Tunable multiferroic composites are advantageous for device applications because of their controllable electrical and magnetic properties. This chapter discusses the investigations on the structural, multiferroic, electrical and magnetoelectric properties of NdMnO₃-BaTiO₃ composites synthesized employing conventional solid state reaction from initial components NdMnO₃ (NMO) and BaTiO₃ (BT). The XRD, Raman and FT-IR studies reveal the evolution and co-existence of NMO and BT phase in NMO-BT composites and confirm lattice stabilization in terms of symmetry. The dielectric measurements reveal step-like decrease in frequency dependent dielectric constant which confirm improved conduction nature in NMO-BT composites. The impedance measurements confirm non-Debye type thermally activated conduction behaviour. The conductivity measurements confirm the hopping assisted mechanism dominating in NMO-BT composites. The addition of BT phase in NMO improves the remnant magnetization and saturates ferroelectric polarization owing from lattice stability establishing multiferroism in NMO-BT system. The maximum energy density was achieved for 0.8NMO-0.2BT of 1.544 mJ/cm³ with an efficiency of 50.4 % associated with maximum magnetoelectric coupling of 22 mV/cm/Oe.

7.1. Introduction

Multiferroic magnetoelectric composite materials have substituted for single-phase multiferroics in the last decades [137,251]. The magnetoelectric coupling in multiferroic composites is enticed via mechanical strain mediated interaction between ferroelectric and ferromagnetic phases and are ascribed as piezo / magneto-striction [12,14,32]. Large number of composites from ferrites and manganites for the ferromagnetic phase and barium/lead based titanates for the ferroelectric phase have been investigated for multiferroics and magnetoelectric properties [47–50].

The previous chapter broadly discussed about $\text{Bi}_{0.85}\text{La}_{0.15}\text{FeO}_3\text{-BaTiO}_3$ composites with (3-0) connectivity scheme. The composites displayed maximum ME coupling of 16 mV/cm/Oe with energy density of 16 mJ/cm³. These results suggest a scope of improvement in ME coupling of composites via a new choice of host with improved insulating properties for preparation of composites.

Rare earth manganites ReMnO_3 (Re = Rare earth) are vastly studied systems due to the occurrence of captivating features like magnetic orderings, metal-insulator transition, colossal magnetoresistance and multiferroism originating from charge spin and lattice dynamics [101–103]. These manganites exhibit peculiar structural and charge conductivity transport phenomena that are governed by the behavior of transitional metal (Mn) ions with the neighboring (Re) ions. Manganites of La, Pr or Nd usually exhibit orthorhombic structure having *Pnma* space group [105,106]. In recent years, the magnetoelectric and magnetodielectric explorations in ReMnO_3 have enticed enormous interest due to the presence of different origins of multiferroics properties, the most common being the double exchange interaction (DE) arising from the presence of mixture of Mn^{2+} / Mn^{3+} ions as given below [108,109].



The hopping of doubly degenerate e_g^2 electron induces the magnetic transition. Amongst the existing mixed valent manganites, NdMnO_3 (NMO) is the best possible candidate to exploit for enhancement in ME properties due to the existence of structural disordering originating from tilting of MnO_6 octahedra. This tilting provides an antiferromagnetic A to E - type magnetic transition required for spontaneous multiferroism [102,107]. NMO exhibits insulating ferromagnetic nature which can be tailored by doping Nd^{3+} site or Mn^{3+} site by divalent atoms such as Ba^{2+} , Sr^{2+} , Cd^{2+} , Ca^{2+} , Cu^{2+} and Zn^{2+} ions [101,102,108,111]. The studies on NMO doped systems have

shown interesting results, however, the composite study of NMO is barely countable. The studies on NMO based composites show the advantage of composite system instead of parent NMO [112,113]. Furthermore, the composites of bulk ferromagnetic NMO with ferroelectrics are expected to show strong magnetoelectric coupling close to room temperature owing to the product property of multiferroics magnetoelectric composites.

In this regard, this chapter describes the synthesis NdMnO₃ - BaTiO₃ (NMO-BT) composite to study the effect of BT in NMO on the structural, dielectric, magnetic, and ferroelectric P-E and magneto-electric properties.

7.2. Sample Preparation

The (1-x)NMO-xBT (x = 0, 0.1 and 0.2) were prepared by solid state reaction route as discussed in section 2.3 and as represented in Fig. 2.1. The CDH grade of chemicals Nd₂O₃, MnO₂, BaCO₃ and TiO₂ were used as initial ingredients in stoichiometric ratio. The synthesis conditions have been tabulated in Table 7.1. The composites are named as NMO (NdMnO₃), NMO-10BT (0.9NdMnO₃ – 0.1BaTiO₃) and NMO-20BT (0.8NdMnO₃ – 0.2BaTiO₃).

Table 7.1. Synthesis conditions of BaTiO₃, NdMnO₃ and NdMnO₃ - BaTiO₃ composites.

Composition	Calcination temperature (°C)	Duration (h)	Sintering temperature (°C)	Duration (h)
BaTiO ₃	1000	8	-	-
NdMnO ₃	900	8	950	10
NMO-10BT	-	-	950	10
NMO-20BT	-	-	950	10

7.3. Results and Discussion

7.3.1. Structural Measurements

XRD spectra of NMO, BT and NMO-BT composites have been recorded at room temperature and plotted in Fig.7.1. The XRD patterns have been indexed the perovskite NdMnO₃ and BaTiO₃ phase with JCPDS # 25-1149 for orthorhombic phase

and JCPDS # 05-0626 for tetragonal phase, respectively. The XRD patterns of NMO and BT samples show pure decomposed single phase with no presence of any Nd, Ba, Mn and Ti oxides. The sharpened peaks in the XRD spectra are owing to the strong crystallinity in NMO and BT compounds. The XRD patterns of NMO-10BT and NMO-20BT show the evolution and co-existence of both individual phase of NMO and BT, which confirms the formation of NMO-BT composites.

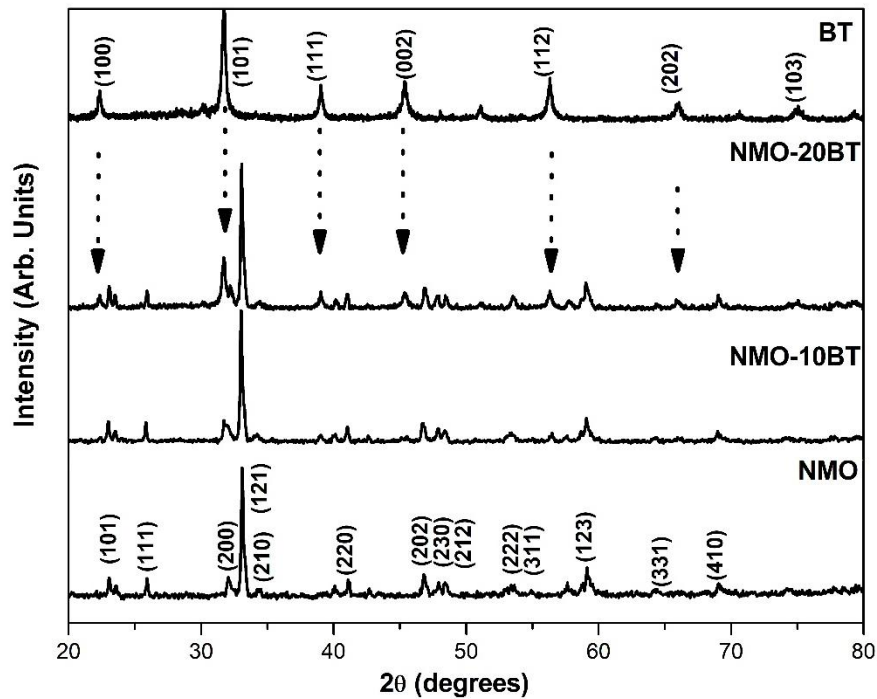


Figure 7.1. XRD patterns of NMO, BT and NMO-BT composites

Table 7.2. Variation of tolerance factor with BT concentration.

Element	Ionic radii (Å)	Composition	Tolerance Factor γ
Nd	1.16		
Mn	0.83	BT	1.06
Ba	1.38	NMO	0.81
Ti	0.605	NMO-10BT	1.011
O	1.42	NMO-20BT	0.84

The impact of BT addition in NMO is understood by using the Debye Scherrer Equation (2.3) and Williamson-Hall Equation (2.4). The W-H equation is used to obtain accuracy in crystallite size and strain. Fig. 7.2 (a) shows the W-H plot for BT, NMO and NMO-BT composites. There is a decreasing trend in the strain obtained from W-H

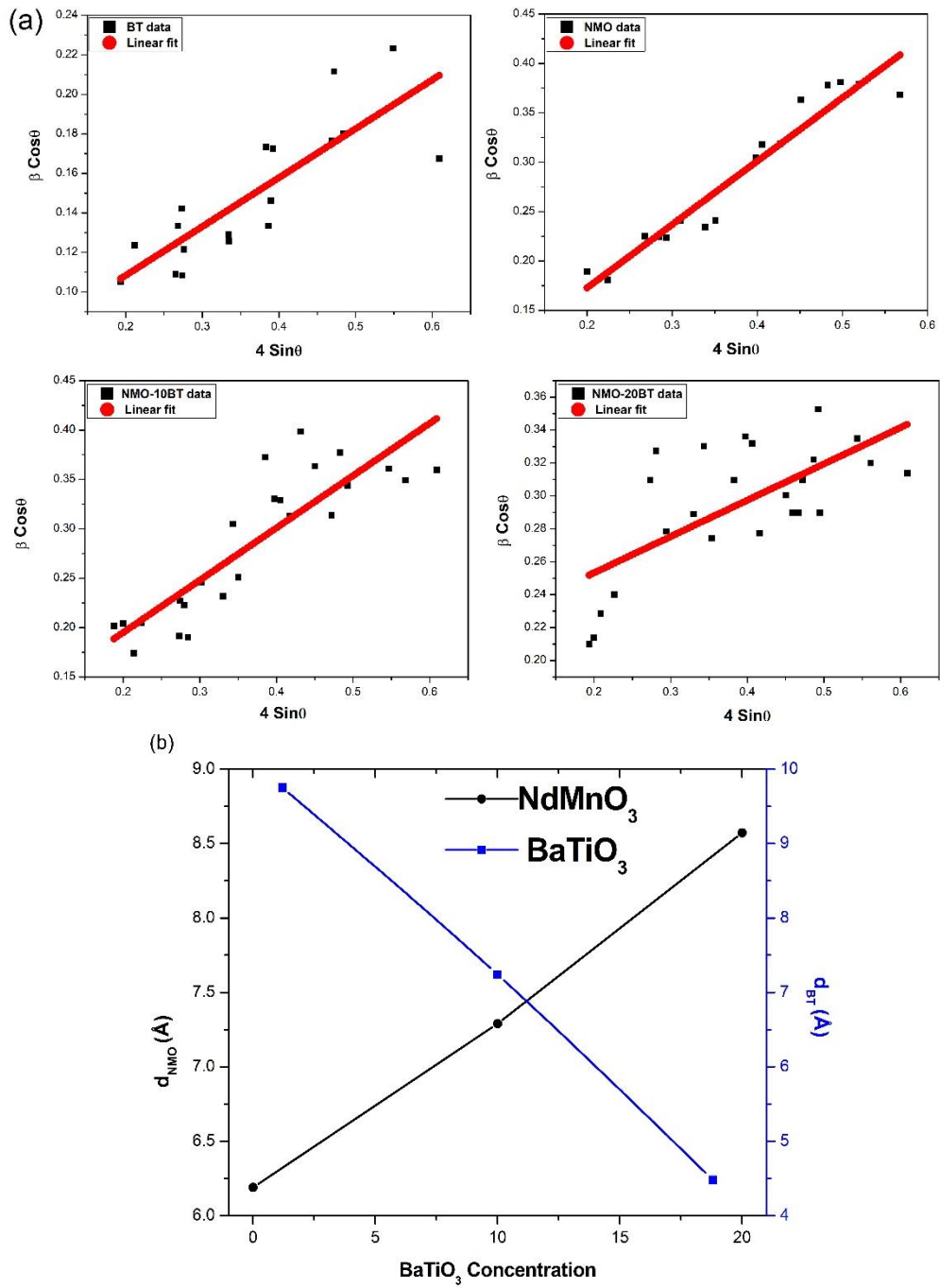


Figure 7.2. (a) W-H plots of BT, NMO and NMO-BT composites (b) Variation of crystallite size of NMO and BT in NMO-BT composites.

plot indicating that the incorporation of BT in NMO lattice has led to stabilization. The crystallite size obtained from Scherrer equation is plotted in Fig. 7.2 (b). The crystallite size (d_{NMO}) in NMO is found to increase in NMO-BT composite as compared to NMO and similarly the crystallite size (d_{BT}) in BT is found to decrease suggesting a lattice distortion. Moreover, the crystallite size obtained from W-H plot is in agreement with

the crystallite size obtained using Scherrer equation. The crystal lattice distortion can be explained on the basis of tolerance factor formula of ABO_3 type perovskites expressed as Equation (1.19). The calculated tolerance factor based on ionic radii is tabulated in Table 7.2 along with corresponding ionic radii used. It can be seen from the table that tolerance factor of NMO and BT lie in their respective range of orthorhombic ($0.75 < \gamma < 0.9$) and tetragonal ($\gamma > 1$) phases. On addition of BT in NMO lattice the tolerance factor increases to 1.014 indicating a tetragonal dominated structure with lattice distortion and which subsequently decreases for NMO-20BT composite to the initial range of orthorhombic structure which counts for the lattice stabilization in terms of symmetry.

FT-IR spectrum is useful in providing information about the behavior of metal ions in the perovskite lattice. The FT-IR spectra of NMO and NMO-BT composites in the wavenumber range of $400\text{-}1000\text{ cm}^{-1}$ are plotted in Fig. 7.3. The orthorhombic phase of manganites as described by factor group analysis consists of the following optical modes: $\Gamma = 7A_{\text{sym}}(R) + 7B_{1\text{sym}}(R) + 5B_{2\text{sym}}(R) + 5B_{3\text{sym}}(R) + 8A_{\text{unsym}}(IA) + 7B_{1\text{unsym}}(IR) + 8B_{2\text{unsym}}(IR) + 9B_{3\text{unsym}}(IR)$, where ‘sym’ and ‘unsym’ denotes gerade and ungerade optical modes. The FT-IR spectra of NMO show minimum or no splitting indicating high ordering in crystal lattice. The presence of strong peak at 556 cm^{-1} relating to non-symmetric vibrations of Mn-O-Mn bond generating from MnO_6 octahedra and broadening in region from $405\text{-}481\text{ cm}^{-1}$ relating to vibrations of Mn-O bond confirm the formation of manganite NMO [252]. The broad region is originated due to the John-Teller interactions which widens equatorial bond and shortens axial Mn-O bonds. Fig. 7.3 also shows the FT-IR spectra of NMO-10BT and NMO-20BT. It can be observed that the intense peak of 556 cm^{-1} increases to 562 cm^{-1} in NMO-10BT and shifts to 557 cm^{-1} in NMO-20BT. This shift in intense band located near 552 cm^{-1} relating to vibrations of Ti-O bond arising from TiO_6 octahedra confirms the formation of ferroelectric BT. Moreover, the broadening of this peak reduces with BT incorporation along with increased splitting in the widened region suggesting that Ti-O bonds of BT introduce additional vibrations in the NMO lattice. The reduction in broadening is linked to decrease in localized modes and charge carriers of Ti-O bonds hindering the optical modes of Mn-O-Mn bonds [253]. This softening of FT-IR spectra and increased splitting confirms the formation of NMO-BT composites as validated by XRD studies.

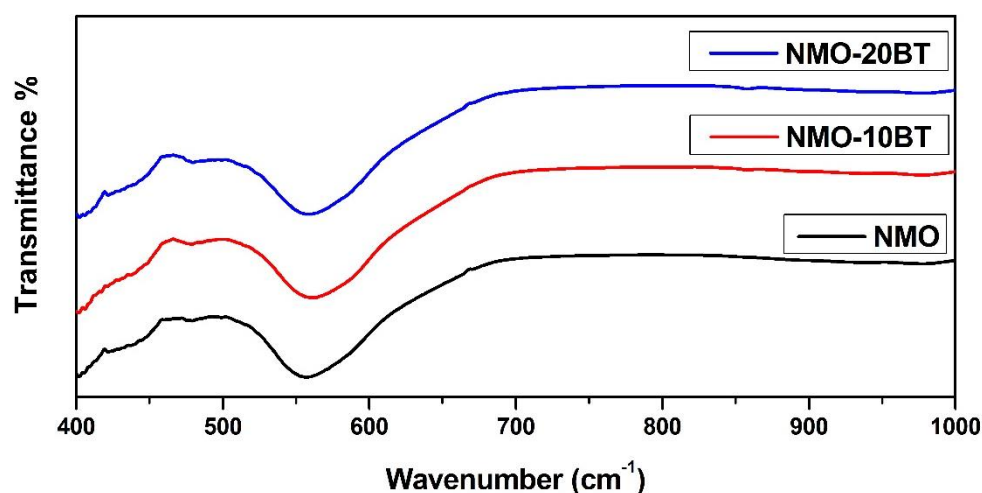


Figure 7.3. FT-IR spectra of NMO and NMO-BT composites

The room temperature Raman spectra of NMO and NMO-BT composites is shown in Fig. 7.4. The spectra show intense peak at 636 cm^{-1} of $B_{1\text{sym}}$ mode relating to O-O vibrations originating from John-Teller interactions and peak at 288 cm^{-1} of A_{sym} mode relating to tilting of MnO_6 octahedra. However, the usual peak at 480 cm^{-1} relating to second order non-symmetric stretching of O-O is absent. The Raman spectra of NMO-BT composites show an improvement in the peaks around 180, 260 and 512 cm^{-1} indicated by '*' relating to the transverse non-symmetry vibration Ti-O (A_T) of phonons and indicate infusion of tetragonal BaTiO_3 into orthorhombic NdMnO_3 lattice corroborating with XRD and FT-IR studies.

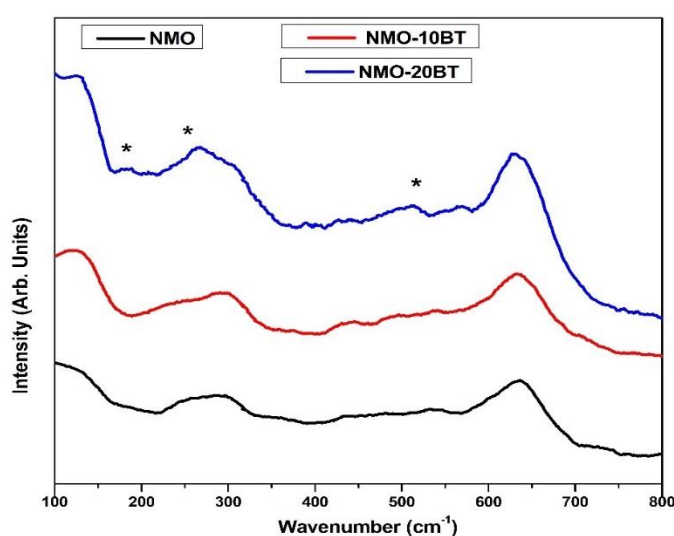


Figure 7.4. Raman spectra of NMO-BT composites

7.3.2. Dielectric Measurements

The dielectric properties of the composites are analyzed with the content of BT in NMO-BT composites. The frequency dependence plots of dielectric constant (ϵ') for NMO-BT composites is shown in Fig. 7.5. The NMO-BT composite samples show strong step like decrease above frequency of 10 kHz behavior indicating the presence of dipolar relaxation processes at all temperatures [252]. In the low frequency region, dielectric constant is more or less static as electric dipoles are following the oscillations of applied electric field. Furthermore, at higher frequencies, the dipoles are unable to follow the oscillations of electric field. The dielectric behavior of such non-Debye type can be represented as

$$\epsilon_r = \epsilon_{r\infty} + \frac{\epsilon_{rs} - \epsilon_{r\infty}}{1 + (i\omega\tau)^{1-\alpha}} \quad (7.2)$$

where, α is constant, τ is relaxation time, $\epsilon_{r\infty}$ is dielectric constant at very high

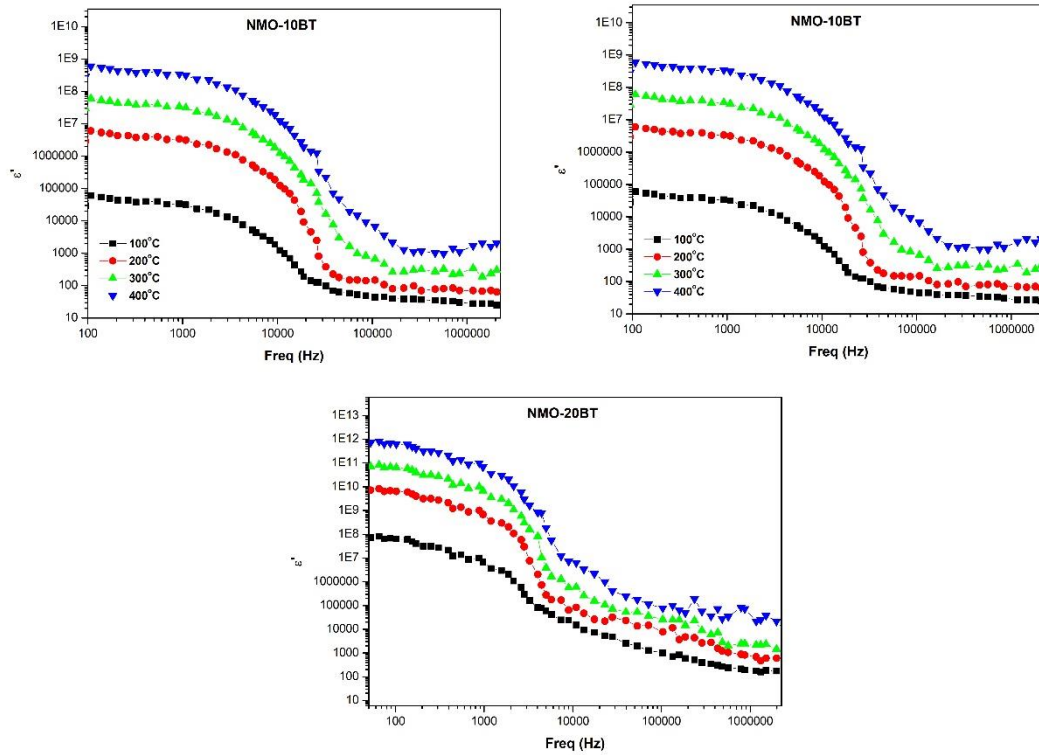


Figure 7.5 Frequency dependence of dielectric constant of NMO and NMO-BT composites.

frequencies and ϵ_{rs} is dielectric constant at static field [254]. The increase in the dielectric constant at high temperature is attributed to increased conduction in the NMO-BT composites. It can also be observed that the value of dielectric constant at

any measured temperature is more in NMO-BT composite than NMO due to the strong dielectric nature. The giant increase in dielectric constant is related to stabilization in the lattice in NMO-BT composite, as confirmed by structural measurements.

7.3.3. Impedance Measurements

The electrical properties in composite materials viz., grain and grain boundary contributions can be understood by examining the deviation in the response of impedance as function of applied oscillating field [164]. The real (Z') and imaginary (Z'') components of the complex impedance $Z^* = Z' - iZ''$, are plotted against each other and the corresponding Cole-Cole plots for NMO and NMO-BT composites are shown in Fig. 7.6. The effective contributions of grain and grain boundary in the material can be separated and pictured by fitting the Cole-Cole plot to an equivalent circuit consisting of resistors and capacitor as

$$Z^* = \frac{R_1}{1 + i\omega R_1 C_1} + \frac{R_2}{1 + i\omega R_2 C_2} \quad (7.3)$$

where ω is the angular frequency of the oscillating field. In the present work, all the samples show non-Debye nature and thus capacitor is substituted by constant phase element (CPE) [254]. The CPE impedance can be represented as $Z_{CPE}^* = \frac{1}{C_c(i\omega)^n}$, where C_c is the capacitance of CPE and n is the power exponent. The Cole-Cole plots of NMO and NMO-BT composites show partial as well as complete semi-circular arcs with their centers lying below the Z' axis. The display of lower curvature confirms the presence of different relaxation processes associated with non-ideal electric behavior in NMO and NMO-BT composites. In addition, the non-Debye behavior could be due to the presence of defects and vacancies in NMO-BT composites. All samples show a decrease in the radius of Cole-Cole plots with increase in temperature from 100 °C to 400 °C and indicate the presence of thermally dominated conduction mechanism. It is also interesting to note that the Cole-Cole plot of NMO-20BT alone doesn't start from origin indicating the improved and strong dielectric nature in the composite [83]. The experimental data has been fitted with R-CPE elements using the Equation (7.3) and the corresponding values can be construed. The experimental data along with equivalent circuit and fitted spectra are shown in Fig. 7.6. The measured data and R-CPE equivalent fitted spectra show good agreement with each other. The resistance of

grains is always greater than that of grain boundaries at all temperatures. The activation energy obtained from the thermal variation of resistance of grains is of the order of 0.46 eV for NMO sample.

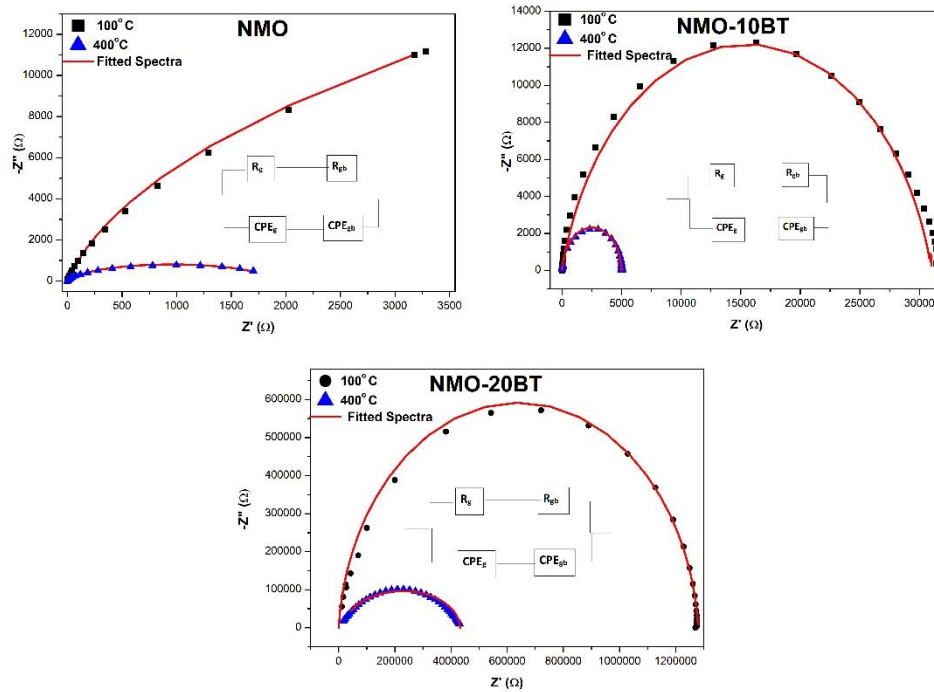


Figure 7.6. Cole-Cole plots and equivalent circuit with fitted spectra of NMO-BT composites.

Table 7.3. Fitted parameters for Cole–Cole plots of NMO-BT composites

Temp (°C)	R_g (Ω)	CPE_g	n_g	R_{gb} (Ω)	CPE_{gb}	n_{gb}
NMO						
100	2100000	1.1×10^{-9}	0.81	80000	8×10^{-9}	0.65
400	11625	5×10^{-8}	0.67	1150	5×10^{-7}	0.4
NMO-10BT						
100	3300000	2×10^{-9}	0.85	570000	9×10^{-9}	0.73
400	8000	8×10^{-8}	0.7	2796	3×10^{-7}	0.55
NMO-20BT						
100	435000	3×10^{-9}	0.89	6400	2×10^{-8}	0.85
400	4050	4×10^{-8}	0.73	190	8×10^{-7}	0.64

7.3.4. Conductivity Measurements

The transport behavior of charge carriers can be understood by studying the frequency dispersion of conductivity (σ') for NMO-20BT composite using Equation (2.10). The Fig. 7.7 shows static conductivity at all temperatures upto $\log \omega \approx 5 \text{ rad s}^{-1}$ and indicates dc conductivity. This dc behavior is correlated to the movement of charges across grain boundaries. The low value of conductivity in this region could be

due to charge accumulation at grain boundary / electrode interface. On the contrary, the conductivity in Fig. 7.7 shows strong dispersion and rapidly increases in the high frequency region indicating intensified mobility of multivalent charge carriers of Mn and Ti atoms. The increase in temperature decreases the conductivity suggesting temperature dependent conductivity phenomena of charge carriers.

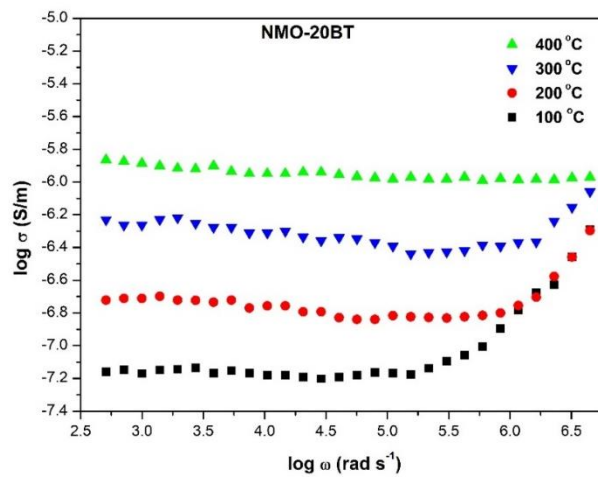


Figure 7.7. Variation of $\log \sigma'$ versus $\log \omega$ for NMO-20BT composite.

The temperature dependence of dc conductivity for NMO-BT is shown in Fig. 7.8 and the activation energy for NMO and NMO-BT composites obtained using the Arrhenius law. The activation energies of NMO and NMO-BT composites are less than unity and are mainly due to the presence of single oxidized ions from Mn and Ti atoms produced during synthesis as given by Kroger-Vink defect Equation (3.4).

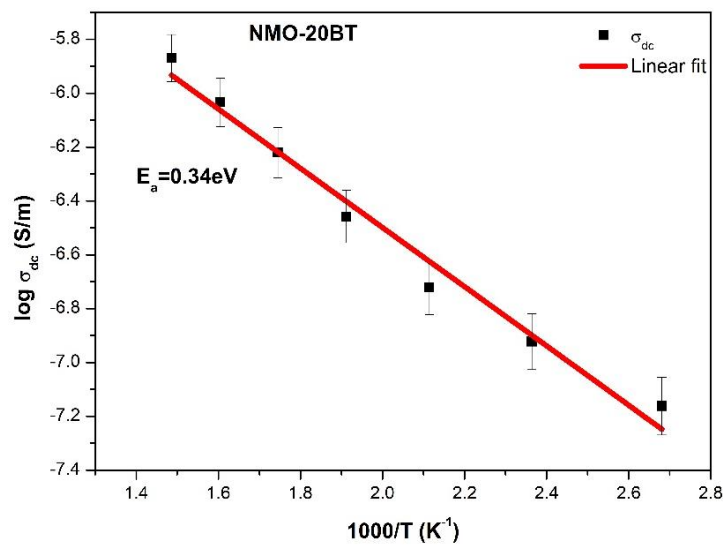


Figure 7.8. Plot of DC conductivity versus temperature for NMO-20BT composite.

The thermal variation of exponent n for NMO and NMO-BT composites is shown in Fig. 7.9. Based on the types of conduction mechanism discussed in section 3.3.4 and 4.3.4, it can be observed and understood that the composites display correlated barrier hopping between the neighboring sites through thermal activation. This hopping can be visualized as the movement of carriers between nearest neighboring localized sites via hopping mechanism. The values of n for NMO and NMO-BT composites remains less than unity and indicates translational motion of charge carriers [91].

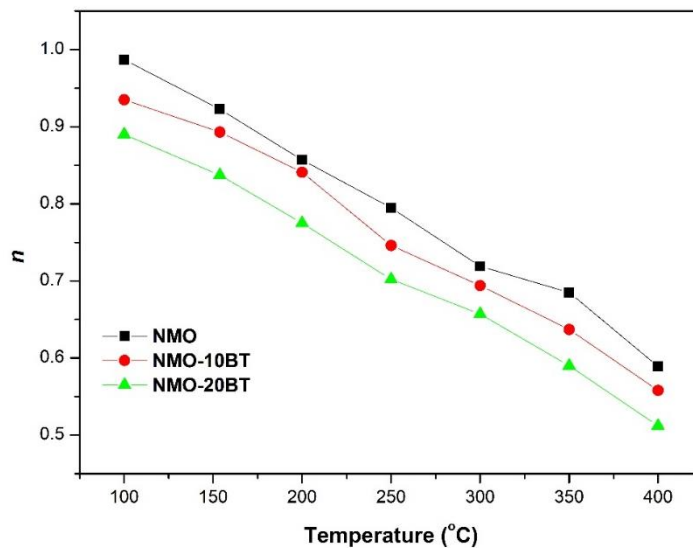


Figure 7.9. Variation of power exponent n with temperature for NMO and NMO-BT composites.

7.3.5. Magnetic Measurements

The room temperature magnetization measurements obtained using vibrating sample magnetometer studies magnetization (M) at a maximum field of 15000 Oe are plotted in Fig. 7.10. The M - H plots indicate that magnetization of the $\text{NdMnO}_3\text{-BaTiO}_3$ composites increases linearly with the field and confirms the antiferromagnetic behavior of NdMnO_3 . The occurrence of magnetization in NMO-BT composites is predominantly due to the antiferromagnetic nature of NMO. The maximum magnetization reduces on the addition of BT in NMO. The addition of non-magnetic BT creates spatial modifications in NMO, which lowers the maximum magnetization in the composites. The remnant magnetization is also found to decrease with BT content in NMO-BT composites. However, in case of NMO-20BT composite remnancy is more than NMO-10BT due to stabilization of spatial orderings NMO-20BT composite. Fig. 7.10 shows the enlarged image of M - H lines (inset of Fig. 7.10). This improved

magnetization shows potential for memory device applications. The coercivity of NMO-BT composites obtained by differentiating the M-H hysteresis curve resulting in dM / dH curves are in good agreement with each other. The coercivity of the NMO and NMO-BT composite remains the same suggesting that movements of domains walls don't get effected from spatial orderings.

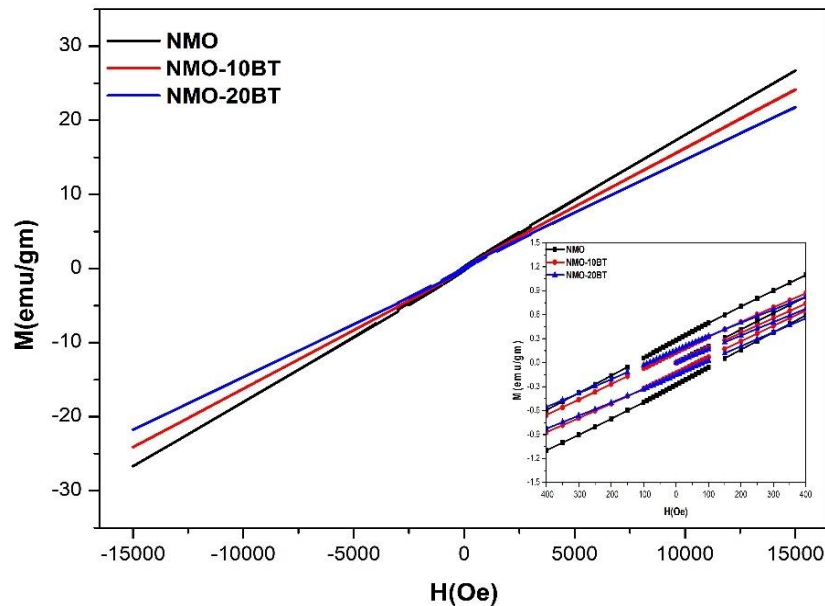


Figure 7.10. M-H hysteresis loops of NMO and NMO-BT composites. Inset shows enlarged M-H hysteresis loops of NMO and NMO-BT composites in the magnetic field range of ± 400 Oe.

7.3.6. Ferroelectric and Magnetoelectric Measurements

The ferroelectric properties of dielectrics are useful in determining polarization switching applications. The ferroelectric P-E hysteresis loop is studied employing the Sawyer–Tower technique [209] and the respective variations for NMO and NMO-20BT composite are plotted in Fig. 7.11. The P-E loop of NMO exhibits a low-lying flat loop suggesting its weak ferroelectric nature. It is interesting to note that the P-E loop of NMO-20BT composite display an improved saturation as well as polarization. This improvement can be attributed to incorporation of ferroelectric domain walls in an orthorhombic lattice of NMO results in decrease in the lattice strain, which stabilizes the lattice. This decrement in strain stabilizes as well as saturates the ferroelectric hysteresis loop. NMO displayed an energy storage density of 2.004 mJ/cm^3 with efficiency of 17.21 %. The NMO-20BT composite displays an enhanced energy storage density of 1.54 mJ/cm^3 with an improved efficiency of 50 %. The enhancement in

energy storage efficiency of NMO-20BT composite validates its potential for the energy storage devices.

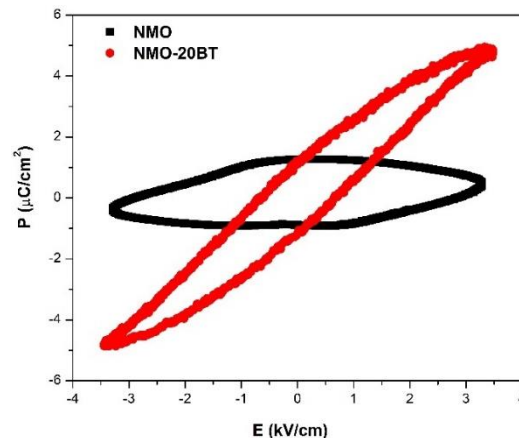


Figure 7.11 P-E hysteresis loops of NMO and NMO-20BT composite.

The evidence of magnetoelectricity in NMO-BT composites can be observed by varying the ferroelectric P-E hysteresis loop with external magnetic field. The measured maximum polarization at respective magnetic fields for NMO, NMO-BT composites is shown in Fig. 7.12. The relative variation of 93% in P_{\max} versus H is maximum for NMO, which decreases upto 46% for NMO-20BT composite. The blue line represents the fitted spectra for variation of NMO-BT composites. As the amount of BT is increased the percentage change of magnetoelectric coupling decreases indicating that the stabilization in the lattice decreases the strain originated from coupling amongst individual component phases. The maximum magnetoelectric coupling of 22 mV/cm/Oe was achieved for NMO-20BT composite.

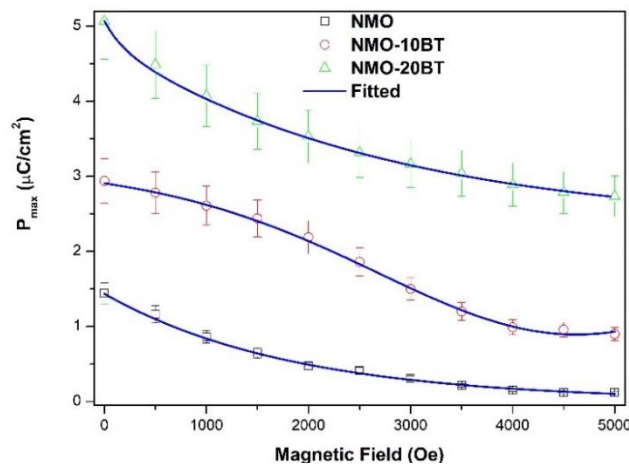


Figure 7.12. Variation of maximum polarization versus magnetic field for NMO and NMO-BT composites

Chapter - 8

Summary and Scope of Future Work

8.1. Summary

The objectives of this thesis work were to synthesize and characterize BaTiO₃ based magnetoelectric composites for energy storage applications. A variety of BaTiO₃ based magnetoelectric composites were successfully synthesized by choosing different host materials and using solid state reaction route. Importance was given to synthesize composites with highest purity.

As discussed in the previous chapters, magnetoelectric materials are one of the finest advance materials which offer multifunctionality and have potential for a numerous applications such as memory stage, gyration, sensing, filtering, resonating devices, MRAMs and energy storage devices [137,251]. In the present thesis, different BaTiO₃ based composites were prepared using solid state reaction route for optimizing magnetoelectric coupling. The structural, electrical and magnetic properties of these composites have been performed. In addition to this, the stoichiometry was varied in BaTiO₃ based composites to optimize as well as energy storage density as well as energy conversion efficiency.

Single phase magnetoelectrics suffer due to the weak coupling. One of the best ways to improve the magnetoelectric coupling is to prepare strong ferroelectric based composites. BaTiO₃ and PbZrTiO₃ are the ideal ferroelectrics for energy storage applications. Keeping in mind the environmental concerns, BaTiO₃ based composites are preferred for preparing composite materials for magnetoelectric as well as energy storage applications. Materials that exhibit strong magnetoelectric coupling display lower energy storage density. In the light of this, diverse magnetic constituents are chosen for preparing different magnetoelectric composites of (1-x) BaTiO₃ - xCoFe₂O₄ (0 ≤ x ≤ 0.05), (1-x) CoFe₂O₄ - x BaTiO₃ (0 ≤ x ≤ 0.3), (1-x) Co_{0.5}Ni_{0.5}Fe₂O₄ - x BaTiO₃ (0 ≤ x ≤ 0.2), (1-x) Bi_{0.85}La_{0.15}FeO₃ - x BaTiO₃ (0 ≤ x ≤ 0.3) and (1-x) NdMnO₃ - x BaTiO₃ (0 ≤ x ≤ 0.2) as well as for optimizing the energy parameters.

8.2. Important Findings of Research Work

The structural properties such as constituent phase, phase purity and crystallite size in BaTiO₃ based composites were explored by employing XRD. The XRD spectra of the prepared BaTiO₃ based composites in the present work are all in good agreement with their respective JCPDS files and confirm the formation of composites in these bi-phasic systems.

The dielectric and impedance investigations in these composites assisted in understanding the polarization mechanism in them. All the composites displayed Maxwell-Wagner space charge polarization with non-Debye type relaxation behavior. In most of the composites, the grains and grain boundaries played an important role in charge conduction. The conduction in these composites was due to singly ionized charges as confirmed from the low value of dc activation energy. The overall effect of incorporation of BaTiO₃ was to improve dielectric, impedance and conduction properties.

The magnetic measurements aided to comprehending the influence of BaTiO₃ in different composites. The major significant change was lowering in maximum magnetization due to increase in concentration of BaTiO₃. In addition, the incorporation of BaTiO₃ induced lattice disorder resulting in remanent magnetization and coercivity variations.

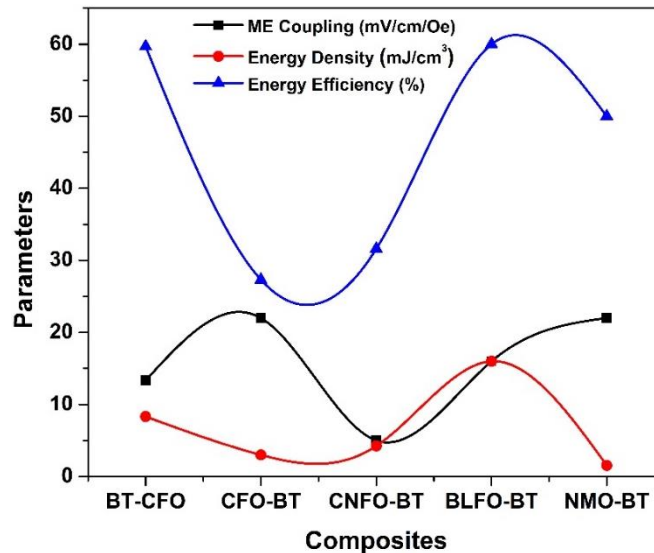


Figure 8.1. Comparison of different composites based on energy storage parameter and magnetoelectric coupling

The ferroelectric measurements supported in establishing the ferroelectric

nature, magnetoelectric coupling and energy storage density in BaTiO₃ based composites. All the composites displayed ferroelectric nature with an improvement due to BaTiO₃ addition. The comparison of magnetoelectric coupling and energy storage parameters of different composites studied in this thesis is displayed in Fig. 8.1. The maximum magnetoelectric coupling of 22 mV/cm/Oe was exhibited by 0.9CoFe₂O₄ - 0.1BaTiO₃ (CFO-10BT) and 0.8NdMnO₃ - 0.2BaTiO₃ (NMO-20BT). The maximum energy storage density of 16 mJ/cm³ and efficiency of 60% was displayed by 0.9Bi_{0.85}La_{0.15}FeO₃ - 0.1BaTiO₃ (BLFO-10BT) composite. The composites of 0.9Bi_{0.85}La_{0.15}FeO₃ - 0.1BaTiO₃ (BLFO-10BT) demonstrated optimum magnetoelectric coupling of 16 mV/cm/Oe along with highest energy storage parameters and can be considered as a potential magnetoelectric composite for energy storage applications.

8.3. Future Scope of the Work

1. Fabrication of prototype magnetoelectric device based on BLFO-BT for energy storage applications.
2. To synthesize BaTiO₃ doped magnetoelectric composites for energy storage applications.
3. To synthesize and characterize nanocomposite based on BaTiO₃.
4. To grow magnetoelectric thin films having large ME-constant on suitable substrates using pulsed laser deposition (PLD) techniques and by spin-coating and study of their physical properties.
5. To synthesize and to study the physical properties of layered magnetoelectric composites.
6. To utilize the optimized magnetoelectric composites to fabricate energy efficient devices.

References

- [1] Y. Qiu, Y. Lin, X. Liu, H. Yang, J. Alloys Compd. 797 (2019) 348–355.
- [2] H. Sun, X. Wang, Q. Sun, X. Zhang, Z. Ma, M. Guo, B. Sun, X. Zhu, Q. Liu, X. Lou, J. Eur. Ceram. Soc. 40 (2020) 2929–2935.
- [3] I. Calisir, A.A. Amirov, A.K. Kleppe, D.A. Hall, J. Mater. Chem. A 6 (2018) 5378–5397.
- [4] L.F. Zhu, B.P. Zhang, Z.C. Zhang, S. Li, L.J. Wang, L.J. Zheng, J. Mater. Sci. Mater. Electron. 29 (2018) 2307–2315.
- [5] C.M. Fernández-Posada, H. Amorín, C. Correias, O. Peña, M. Algueró, A. Castro, J. Mater. Chem. C 3 (2015) 2255–2266.
- [6] Y. Wang, S. Gao, T. Wang, J. Liu, D. Li, H. Yang, G. Hu, L. Kong, F. Wang, G. Liu, Ceram. Int. 46 (2020) 12080–12087.
- [7] T. Zhang, H. Aziguli, Y. Wu, J. Yin, P. Yu, J. Mater. Sci. 55 (2020) 2764–2771.
- [8] H. Yang, H. Qi, R. Zuo, J. Eur. Ceram. Soc. 39 (2019) 2673–2679.
- [9] T. Wang, X. Wei, Q. Hu, L. Jin, Z. Xu, Y. Feng, Mater. Sci. Eng. B Solid-State Mater. Adv. Technol. 178 (2013) 1081–1086.
- [10] Z.H. Shen, J.J. Wang, Y. Lin, C.W. Nan, L.Q. Chen, Y. Shen, Adv. Mater. 30 (2018) 1–6.
- [11] Q. Li, L. Chen, M.R. Gadinski, S. Zhang, G. Zhang, H. Li, A. Haque, L.Q. Chen, T. Jackson, Q. Wang, Nature 523 (2015) 576–579.
- [12] W. Eerenstein, N.D. Mathur, J.F. Scott, Nature 442 (2006) 759–765.
- [13] G. Catalan, J.F. Scott, Adv. Mater. 21 (2009) 2463–2485.
- [14] N.A. Spaldin, MRS Bull. 42 (2017) 385–390.
- [15] N.A. Spaldin, R. Ramesh, Nat. Mater. 18 (2019) 203–212.
- [16] N.A. Spaldin, Proc. R. Soc. A Math. Phys. Eng. Sci. 476 (2020) 20190542.
- [17] A. Ioachim, R. Ramer, M.I. Toacsan, M.G. Banciu, L. Nedelcu, C.A. Dutu, F. Vasiliu, H. V. Alexandru, C. Berbecaru, G. Stoica, P. Nita, J. Eur. Ceram. Soc. 27 (2007) 1177–1180.
- [18] C.J. Stringer, N.J. Donnelly, T.R. Shrout, C.A. Randall, E.F. Alberta, W.S. Hackenberger, J. Am. Ceram. Soc. 91 (2008) 1781–1787.
- [19] G. Ray, N. Sinha, B. Kumar, Mater. Chem. Phys. 142 (2013) 619–625.
- [20] K. Chandra Babu Naidu, V. Narasimha Reddy, T. Sofi Sarmash, D. Kothandan, T. Subbarao, N. Suresh Kumar, J. Aust. Ceram. Soc. 55 (2019) 201–218.

- [21] D. Pang, C. He, X. Long, *Ceram. Int.* 42 (2016) 19433–19436.
- [22] Y. Lin, D. Li, M. Zhang, S. Zhan, Y. Yang, H. Yang, Q. Yuan, *ACS Appl. Mater. Interfaces* 11 (2019) 36824–36830.
- [23] H. Qi, R. Zuo, *J. Mater. Chem. A* 7 (2019) 3971–3978.
- [24] S. Dong, J.M. Liu, S.W. Cheong, Z. Ren, *Adv. Phys.* 64 (2015) 519–626.
- [25] A.S. Zimmermann, D. Meier, M. Fiebig, *Nat. Commun.* 5 (2014) 1–6.
- [26] H. Schmid, *Ferroelectrics* 162 (1994) 317–338.
- [27] M. Fiebig, *J. Phys. D. Appl. Phys.* 38 (2005) R123–R152.
- [28] M.I. Bichurin, *Ferroelectrics* 161 (1997) 17–20.
- [29] B.D.H. Tellegen, *Philips Res. Rep.* 3 (1948) 81–101.
- [30] T.H. O'Dell, *The Electrodynamics of Magneto-Electric Media*, North-Holland, Amsterdam, 1970.
- [31] J. Zhang, C. Fang, G.J. Weng, *Proc. R. Soc. A Math. Phys. Eng. Sci.* 475 (2019) 0002.
- [32] P. Zhou, A. V Singh, Z. Li, M.A. Popov, Y. Liu, D.A. Filippov, T. Zhang, W. Zhang, P.J. Shah, B.M. Howe, M.E. Mcconney, G. Srinivasan, M.R. Page, A. Gupta, *Phys. Rev. Appl.* 054045 (2019) 1–15.
- [33] M. Bichurin, V. Petrov, *Modeling of Magnetoelectric Effects in Composites*, Springer, 2014.
- [34] C.W. Nan, M.I. Bichurin, S. Dong, D. Viehland, G. Srinivasan, *J. Appl. Phys.* 103 (2008) 031101.
- [35] M.I. Bichurin, D. Viehland, *Magnetoelectricity in Composites*, Springer, 2012.
- [36] M. Kumar, S. Shankar, G.D. Dwivedi, A. Anshul, O.P. Thakur, A.K. Ghosh, *Appl. Phys. Lett.* 106 (2015) 072903.
- [37] M. Kumar, S. Shankar, S. Kumar, O.P. Thakur, A.K. Ghosh, *J. Mater. Sci. Mater. Electron.* 27 (2016) 6849–6853.
- [38] C. Behera, R.N.P. Choudhary, P.R. Das, *J. Mater. Sci. Mater. Electron.* 25 (2014) 2086–2095.
- [39] R. Pandey, L.K. Pradhan, S. Kumar, S. Supriya, R.K. Singh, M. Kar, *J. Appl. Phys.* 125 (2019) 244105.
- [40] R. Gao, Q. Zhang, Z. Xu, Z. Wang, G. Chen, X. Deng, C. Fu, W. Cai, *Compos. Part B Eng.* 166 (2019) 204–212.
- [41] K. Osińska, J. Dzik, H. Bernard, B. Wodecka-Duś, A. Lisińska-Czekaj, D. Czekaj, *Ferroelectrics* 418 (2011) 60–69.

- [42] H.L. Mo, D.M. Jiang, C.M. Wang, W.G. Zhang, J. Sen Jiang, J. Alloys Compd. 579 (2013) 187–191.
- [43] Manjusha, K.L. Yadav, J. Mater. Sci. Mater. Electron. 27 (2016) 6347–6358.
- [44] N. Pulphol, R. Muanglua, S. Niemcharoen, W. Pecharapa, W.C. Vittayakorn, N. Vittayakorn, Adv. Mater. Res. 802 (2013) 22–26.
- [45] N. Pulphol, R. Muanglua, S. Niemcharoen, N. Vittayakorn, W. Vittayakorn, Ferroelectrics 488 (2015) 170–180.
- [46] S. Pachari, S.K. Pratihar, B.B. Nayak, RSC Adv. 5 (2015) 105609–105617.
- [47] S. Lather, A. Gupta, J. Dalal, V. Verma, R. Tripathi, A. Ohlan, Ceram. Int. 43 (2017) 3246–3251.
- [48] M.D. Chermahini, M.M. Shahraki, M. Kazazi, Mater. Lett. 233 (2018) 188–190.
- [49] D. Zhang, J. Cheng, J. Chai, J. Deng, R. Ren, Y. Su, H. Wang, C. Ma, C.S. Lee, W. Zhang, G.P. Zheng, M. Cao, J. Alloys Compd. 740 (2018) 1067–1076.
- [50] S. Liu, S. Yan, H. Luo, S. Huang, C. Liao, L. Deng, Mater. Lett. 212 (2018) 139–142.
- [51] J. van Suchtelen, Philips Res. Reports 27 (1972) 28–37.
- [52] M. Etier, C. Schmitz-Antoniak, S. Salamon, H. Trivedi, Y. Gao, A. Nazrabi, J. Landers, D. Gautam, M. Winterer, D. Schmitz, H. Wende, V. V. Shvartsman, D.C. Lupascu, Acta Mater. 90 (2015) 1–9.
- [53] R.E. Newnham, D.P. Skinner, L.E. Cross, Mater. Res. Bull. 13 (1978) 525–536.
- [54] S. Mohan, P.A. Joy, Ceram. Int. 45 (2019) 12307–12311.
- [55] M. Atif, S. Ahmed, M. Nadeem, M.K. Ali, M. Idrees, R. Grössinger, R.S. Turtelli, Ceram. Int. 42 (2016) 14618–14626.
- [56] Z. Cheng, J. Lin, Cryst. Eng. Comm. 12 (2010) 2646.
- [57] N. Ramadass, Mater. Sci. Eng. 36 (1978) 231–239.
- [58] S. Švarcová, K. Wiik, J. Tolchard, H.J.M. Bouwmeester, T. Grande, Solid State Ionics 178 (2008) 1787–1791.
- [59] J. Haines, J. Rouquette, V. Bornand, M. Pintard, P. Papet, F.A. Gorelli, J. Raman Spectrosc. 34 (2003) 519–523.
- [60] G. F.S., Structure, Properties and Preparation of Perovskite-Type Compounds: International Series of Monographs in Solid-State Physics, Elsevier, New York, 2013.
- [61] A.S. Bhalla, G. Rustum, Roy. R, Mater. Res. Innov. 3 (2000) 3–26.
- [62] C.E. Ciomaga, M. Airimioaei, I. Turcan, A. V Lukacs, S. Tascu, M. Grigoras,

- N. Lupu, J. Banys, L. Mitoseriu, J. Alloys Compd. 775 (2019) 90–99.
- [63] A. Guzu, C.E. Ciomaga, M. Airimioaei, L. Padurariu, L.P. Curecheriu, I. Dumitru, F. Gheorghiu, G. Stoian, M. Grigoras, N. Lupu, M. Asandulesa, L. Mitoseriu, J. Alloys Compd. 796 (2019) 55–64.
- [64] N.S. Negi, K. Bala, A. Yadav, R.K. Kotnala, J. Appl. Phys. 117 (2015) 164101.
- [65] K.E. Sickafus, J.M. Wills, N.W. Grimes, J. Am. Ceram. Soc. 82 (2004) 3279–3292.
- [66] Delmar Larsen, Book : Introduction To Inorganic Chemistry, LibreTexts, 2014.
- [67] D.L. Polla, L.F. Francis, Annu. Rev. Mater. Sci. 28 (1998) 563–597.
- [68] W.D. Callister, D.G. Rethwisch, Materials Science and Engineering: An Introduction, 9th ed., Wiley, 2014.
- [69] S.V. V Khikhlovskiy, G. Blake, The Renaissance of Multiferroics: Bismuth Ferrite (BiFeO_3)--a Candidate Multiferroic Material in Nanoscience., 2010.
- [70] A.J. Moulson, J.M. Herbert, Electroceramics: Materials, Properties and Applications, 2nd ed., Chichester, UK, John Wiley and Sons Ltd, 2003.
- [71] B. Kingery, H.K. Bowen, D.R. Uhlmann, Introduction to Ceramics, 2nd ed., Wiley-Interscience Publication, 1976.
- [72] M.M. Kumar, A. Srinivas, S. V. Suryanarayana, J. Appl. Phys. 87 (2000) 855–862.
- [73] Prof. Satish V. Kailas, in: Mater. Sci., NPTEL, 2012.
- [74] H. Adawi, Surface Effect of Ferromagnetic Nanoparticles on Transition Between Single- And Multi-Domain, Wright State University, 2017.
- [75] H.P. Wu, K.M. Deng, W.S. Tan, C.Y. Xiao, F.L. Hu, Q.X. Li, Chinese Phys. B 18 (2009) 5008–5014.
- [76] T. V Anuradha, E-Journal Chem. 7 (2010) 894–898.
- [77] F. Li, M. Zeng, H. Yu, H. Xu, J. Li, J. Mater. Sci. Mater. Electron. 27 (2016) 2836–2840.
- [78] T.K. Kundu, A. Jana, P. Barik, Bull. Mater. Sci. 31 (2008) 501–505.
- [79] Z. Fu, B.K. Moon, H.K. Yang, J.H. Jeong, J. Phys. Chem. C 112 (2008) 5724–5728.
- [80] B.P. Jacob, S. Thankachan, S. Xavier, E.M. Mohammed, J. Alloys Compd. 541 (2012) 29–35.
- [81] N.B. Velhal, N.D. Patil, A.R. Shelke, N.G. Deshpande, V.R. Puri, AIP Adv. 5 (2015) 097166.

- [82] A. Singh, V. Pandey, R.K. Kotnala, D. Pandey, *Phys. Rev. Lett.* 101 (2008) 1–4.
- [83] M. Kumar, S. Shankar, R.K. Kotnala, Om Parkash, *J. Alloys Compd.* 577 (2013) 222–227.
- [84] M. Atif, M. Nadeem, W. Khalid, Z. Ali, *Mater. Res. Bull.* 107 (2018) 171–179.
- [85] A. Jain, A.K. Panwar, A.K. Jha, *Mater. Res. Bull.* 100 (2018) 367–376.
- [86] L. V. Leonel, A. Righi, W.N. Mussel, J.B. Silva, N.D.S. Mohallem, *Ceram. Int.* 37 (2011) 1259–1264.
- [87] P. Puliová, J. Kováč, A. Voigt, P. Raschman, *J. Magn. Magn. Mater.* 341 (2013) 93–99.
- [88] M.D. Chermahini, H.A. Baghbaderani, M.M. Shahraki, M. Kazazi, *Ceram. Int.* 45 (2019) 5491–5495.
- [89] M.U.D. Rather, R. Samad, B. Want, *J. Mater. Sci. Mater. Electron.* 29 (2018) 19164–19179.
- [90] D. Pang, C. He, X. Long, *J. Alloys Compd.* 709 (2017) 16–23.
- [91] S. Shankar, M. Kumar, A.K. Ghosh, O.P. Thakur, *J. Mater. Sci. Mater. Electron.* 25 (2014) 4896–4901.
- [92] S. Ojha, W.C. Nunes, N.M. Aimon, C.A. Ross, *ACS Nano* 10 (2016) 7657–7664.
- [93] S. Shankar, M. Kumar, S. Kumar, O.P. Thakur, A.K. Ghosh, *J. Alloys Compd.* 694 (2017) 715–720.
- [94] A. Sathiya Priya, I.B. Shameem Banu, S. Anwar, *Mater. Lett.* 142 (2015) 42–44.
- [95] A. Prasatkhetragarn, P. Muangkonkad, P. Aommongkol, P. Jantaratana, N. Vittayakorn, R. Yimnirun, *Ceram. Int.* 39 (2013) 249–252.
- [96] D. Wang, A. Khesro, S. Murakami, A. Feteira, Q. Zhao, I.M. Reaney, *J. Eur. Ceram. Soc.* 37 (2017) 1857–1860.
- [97] N. Sharma, S. Kumar, A.K. Mall, R. Gupta, A. Garg, *Mater. Res. Express* 4 (2017) 015702.
- [98] K. Sen, K. Singh, A. Gautam, M. Singh, *Ceram. Int.* 38 (2012) 243–249.
- [99] A. Perejón, P.E. Sánchez-Jiménez, L.A. Pérez-Maqueda, J.M. Criado, J. Romero De Paz, R. Sáez-Puche, N. Masó, A.R. West, *J. Mater. Chem. C* 2 (2014) 8398–8411.
- [100] S.R. Das, R.N.P. Choudhary, P. Bhattacharya, R.S. Katiyar, P. Dutta, A. Manivannan, M.S. Seehra, *J. Appl. Phys.* 101 (2007) 3–10.
- [101] P.V.K.G.D. Jadav, C.S.L. Govindaraj, S.A.J.A. Bhalodia, *J. Mater. Sci. Mater.*

- Electron. 29 (2018) 8107–8134.
- [102] B. Vyas, H. Kundalia, M. Udeshi, P. Trivedi, M. Vagadia, S. Rayaprol, *Ceram. Int.* 43 (2017) 14962–14967.
- [103] G. Lalitha, P.V. Reddy, *Ultrasonics* 52 (2012) 706–711.
- [104] S. Chanda, S. Saha, A. Dutta, T.P. Sinha, *Mater. Res. Bull.* 48 (2013) 1688–1693.
- [105] J.M.D. Coey, M. Viret, S. von Molnár, *Adv. Phys.* 48 (1999) 167–293.
- [106] T. Kimura, S. Ishihara, H. Shintani, T. Arima, T. Takahashi, K. Ishizaka, Y. Tokura, *Phys. Rev. B - Condens. Matter Mater. Phys.* 68 (2003) 060403-1–4.
- [107] J.S.S. N. Aliouane, O. Prokhnenko, R. Feyerherm, M. Mostovoy, D.N.A. K. Habicht, K.C. Rule, E. Dudzik, A.U.B. Wolter, A. Maljuk, *J. Phys. Condens. Matter* 20 (2008) 434215.
- [108] M. Udeshi, S. V Katba, A. Ravalia, M. Vagadia, *AIP Conf. Proc.* 1591 (2014) 1303–1305.
- [109] A. Somvanshi, S. Husain, *AIP Conf. Proc.* 3 (2018) 030242-1–4.
- [110] Y. Tokura, *Reports Prog. Phys.* 69 (2006) 797–851.
- [111] B. Bouadjemi, S. Bentata, A. Abbad, W. Benstaali, *Solid State Commun.* 207 (2015) 9–15.
- [112] W. Hu, G. Zhou, W. Ren, D. Li, Z. Zhang, *J. Appl. Phys.* 110 (2012) 013904.
- [113] M. Faisal, A.A. Ismail, *Sci. Rep.* 9 (2019) 1–11.
- [114] H. Ogihara, C.A. Randall, S. Trolier-Mckinstry, *J. Am. Ceram. Soc.* 92 (2009) 1719–1724.
- [115] Z. Sun, C. Ma, X. Wang, M. Liu, L. Lu, M. Wu, X. Lou, H. Wang, C.L. Jia, *ACS Appl. Mater. Interfaces* 9 (2017) 17096–17101.
- [116] W.B. Li, D. Zhou, L.X. Pang, R. Xu, H.H. Guo, *J. Mater. Chem. A* 5 (2017) 19607–19612.
- [117] C.W. Ahn, G. Amarsanaa, S.S. Won, S.A. Chae, D.S. Lee, I.W. Kim, *ACS Appl. Mater. Interfaces* 7 (2015) 26381–26386.
- [118] J. Pan, K. Li, J. Li, T. Hsu, Q. Wang, *Appl. Phys. Lett.* 95 (2009) 8–11.
- [119] Q. Zhang, H. Tong, J. Chen, Y. Lu, T. Yang, X. Yao, Y. He, *Appl. Phys. Lett.* 109 (2016) 2–6.
- [120] V.S. Puli, D.K. Pradhan, D.B. Chrisey, M. Tomozawa, G.L. Sharma, J.F. Scott, R.S. Katiyar, *J. Mater. Sci.* 48 (2013) 2151–2157.
- [121] D.K. Pradhan, V.S. Puli, S. Narayan Tripathy, D.K. Pradhan, J.F. Scott, R.S.

- Katiyar, J. Appl. Phys. 114 (2013) 0–9.
- [122] Z.H. Zhou, J.M. Xue, W.Z. Li, J. Wang, H. Zhu, J.M. Miao, Appl. Phys. Lett. 85 (2004) 804–806.
- [123] J. van den Boomgaard, R.A.J. Born, J. Mater. Sci. 13 (1978) 1538–1548.
- [124] S. V. Suryanarayana, Bull. Mater. Sci. 17 (1994) 1259–1270.
- [125] H. Sharma, K. Kumari, S.N. Giri, Bull. Mater. Sci. 22 (1999) 757–759.
- [126] P.S.A. Kumar, J.J. Shrotri, S.D. Kulkarni, C.E. Deshpande, S.K. Date, Mater. Lett. 27 (1996) 293–296.
- [127] T. Takada, Y. Bando, M.K. And, T. Shinjo, in: Y. Hoshino, A. S. Iida, M. Sugimoo. (Eds.), Proc. Int. Conf. Ferrites, University of Tokyo Press, Japan, Japan, 1971, pp. 29–31.
- [128] C.M. Chiu, Y.H. Chang, Sensors Actuators B Chem. 54 (1999) 236–242.
- [129] H. Araki, Rigaku J 6 (1989) 34–42.
- [130] J. Epp, in: Mater. Charact. Using Nondestruct. Eval. Methods, Elsevier, 2016, pp. 81–124.
- [131] B.D. Cullity, Elements of X-Ray Diffraction, 2nd ed., Addison-Wesley Publishing Company Inc, New York, 1978.
- [132] M. Kumar, S. Shankar, O.P. Thakur, A.K. Ghosh, Mater. Lett. 143 (2015) 241–243.
- [133] M.A. Hayat, Principles and Techniques of Scanning Electron Microscopy : Biological Applications, First, John Wiley & Sons, 1978.
- [134] B. Techniques, M. Page, Module 3 Microscopic Techniques, NPTEL, 2013.
- [135] M. Stewart, M.G. Cain, P. Weaver, in: Characterisation Ferroelectr. Bulk Mater. Thin Film., Springer, 2014, pp. 1–14.
- [136] M. Kumar, S. Shankar, O. Parkash, O.P. Thakur, J. Mater. Sci. Mater. Electron. 25 (2014) 888–896.
- [137] M. Kumar, S. Shankar, Brijmohan, S. Kumar, O.P. Thakur, A.K. Ghosh, Phys. Lett. A 381 (2017) 379–386.
- [138] N. Hur, S. Park, P.A. Sharma, J.S. Ahn, S. Guha, S.W. Cheong, Nature 429 (2004) 392–395.
- [139] N.S. Kumar, R.P. Suvarna, K.C. Babu Naidu, Mater. Sci. Eng. B Solid-State Mater. Adv. Technol. 242 (2019) 23–30.
- [140] N. Suresh Kumar, R. Padma Suvarna, K. Chandra Babu Naidu, Mater. Chem. Phys. 223 (2019) 241–248.

- [141] D. Kothandan, R.J. Kumar, M. Prakash, K.C.B. Naidu, *Mater. Chem. Phys.* 215 (2018) 310–315.
- [142] N.S. Kumar, R.P. Suvarna, K.C. Babu Naidu, *Ceram. Int.* 44 (2018) 18189–18199.
- [143] S. Jabez, S. Mahalakshmi, S. Nithiyanantham, *J. Mater. Sci. Mater. Electron.* 28 (2017) 5504–5511.
- [144] C.A.F. Vaz, J. Hoffman, C.H. Ahn, R. Ramesh, *Adv. Mater.* 22 (2010) 2900–2918.
- [145] C. Behera, R.N.P. Choudhary, S.K. Parida, *J. Mater. Sci. Mater. Electron.* 30 (2019) 4069–4078.
- [146] A.S. Dzunuzovic, M.M. Vijatovic Petrovic, J.D. Bobic, N.I. Ilic, M. Ivanov, R. Grigalaitis, J. Banys, B.D. Stojanovic, *Ceram. Int.* 44 (2018) 683–694.
- [147] A.S. Dzunuzovic, M.M.V. Petrovic, B.S. Stojadinovic, N.I. Ilic, J.D. Bobic, C.R. Foschini, M.A. Zaghete, B.D. Stojanovic, *Ceram. Int.* 41 (2015) 13189–13200.
- [148] T.M. Amaral, E. Antonelli, D.A. Ochoa, J.E. García, A.C. Hernandez, *Ceram. Int.* 42 (2016) 8488–8494.
- [149] B.K. Kuanr, S.R. Mishra, L. Wang, D. Delconte, D. Neupane, V. Veerakumar, Z. Celinski, *Mater. Res. Bull.* 76 (2016) 22–27.
- [150] K.K. Bharathi, R.J. Tackett, C.E. Botez, C. V. Ramana, *J. Appl. Phys.* 109 (2011) 2012–2015.
- [151] S.G. Kakade, R.C. Kambale, Y.D. Kolekar, C. V. Ramana, *J. Phys. Chem. Solids* 98 (2016) 20–27.
- [152] S. Yoon, C. Pithan, R. Waser, J. Dornseiffer, Y. Xiong, D. Grüner, Z. Shen, S. Iwaya, *J. Am. Ceram. Soc.* 93 (2010) 4075–4080.
- [153] M. Etier, V. V. Shvartsman, S. Salamon, Y. Gao, H. Wende, D.C. Lupascu, B. Raveau, *J. Am. Ceram. Soc.* 99 (2016) 3623–3631.
- [154] N. Adhlakha, K.L. Yadav, R. Singh, *Smart Mater. Struct.* 23 (2014) 105024.
- [155] M. Naveed-Ul-Haq, V. V. Shvartsman, S. Salamon, H. Wende, H. Trivedi, A. Mumtaz, D.C. Lupascu, *Sci. Rep.* 6 (2016) 1–10.
- [156] D. Sun, X. Jin, H. Liu, J. Zhu, Y. Zhu, Y. Zhu, *Ferroelectrics* 355 (2007) 145–148.
- [157] G. Allaadini, S.M. Tasirin, P. Aminayi, *Int. Nano Lett.* 5 (2015) 183–186.
- [158] Z. Yao, H. Liu, Y. Liu, Z. Wu, Z. Shen, Y. Liu, M. Cao, *Mater. Chem. Phys.* 109 (2008) 475–481.

- [159] I. Coondoo, N. Panwar, H. Amorín, V.E. Ramana, M. Algueró, A. Kholkin, J. Am. Ceram. Soc. 98 (2015) 3127–3135.
- [160] B. Parija, T. Badapanda, S.K. Rout, L.S. Cavalcante, S. Panigrahi, E. Longo, N.C. Batista, T.P. Sinha, Ceram. Int. 39 (2013) 4877–4886.
- [161] W.B. White, B.A. DeAngelis, Spectrochim. Acta Part A Mol. Spectrosc. 23 (1967) 985–995.
- [162] Y. Shi, J. Ding, Z.X. Shen, W.X. Sun, L. Wang, Solid State Commun. 115 (2000) 237–241.
- [163] M. Chandrasekhar, D.K. Khatua, R. Pattanayak, P. Kumar, J. Phys. Chem. Solids 111 (2017) 160–166.
- [164] A. Kaur, L. Singh, K. Asokan, Ceram. Int. 44 (2018) 3751–3759.
- [165] T. Kimura, Y. Yoshida, J. Am. Ceram. Soc. 89 (2006) 869–874.
- [166] M. Suzuki, M. Miyayama, Y. Noguchi, T. Uchikoshi, J. Appl. Phys. 104 (2008) 014102.
- [167] Y.D. Kolekar, L.J. Sanchez, C. V. Ramana, J. Appl. Phys. 115 (2014) 1–12.
- [168] S. Mohanty, R.N.P. Choudhary, R. Padhee, B.N. Parida, Ceram. Int. 40 (2014) 9017–9025.
- [169] C. Nayek, P. Murugavel, S. Dinesh Kumar, V. Subramanian, Appl. Phys. A Mater. Sci. Process. 120 (2015) 615–622.
- [170] F. Mizouri, N. Abdelmoula, D. Mezzane, H. Khemakhem, J. Alloys Compd. 763 (2018) 570–580.
- [171] N. Raghuram, T.S. Rao, K.C. Babu Naidu, Mater. Sci. Semicond. Process. 94 (2019) 136–150.
- [172] Y.H. Gao, J. Yang, H. Shen, J.L. Sun, X.J. Meng, J.H. Chu, Appl. Phys. Lett. 104 (2014) 19–24.
- [173] H.S. Shulman, D. Damjanovic, N. Setter, J. Am. Ceram. Soc. 83 (2000) 528–532.
- [174] T. Mondal, S. Das, T. Badapanda, T.P. Sinha, P.M. Sarun, Phys. B Condens. Matter 508 (2017) 124–135.
- [175] M.F. Kotkata, F.A. Abdel-Wahab, H.M. Maksoud, J. Phys. D. Appl. Phys. 39 (2006) 2059–2066.
- [176] S. Sahoo, P.K. Mahapatra, R.N.P. Choudhary, M.L. Nandagoswami, A. Kumar, Mater. Res. Express 3 (2016) 1–20.
- [177] M. Chandrasekhar, Sonia, P. Kumar, Phys. B Condens. Matter 497 (2016) 59–

- [178] M. Kumar, S. Shankar, O.P. Thakur, A.K. Ghosh, *J. Mater. Sci. Mater. Electron.* 26 (2015) 1427–1434.
- [179] M.E. Lines, A.M. Glass, *Principles and Applications of Ferroelectrics and Related Materials*, Oxford University Press, 2001.
- [180] M. Dawber, K.M. Rabe, J.F. Scott, *Rev. Mod. Phys.* 77 (2005) 1083–1130.
- [181] E. Ascher, H. Rieder, H. Schmid, H. Stössel, *J. Appl. Phys.* 37 (1966) 1404–1405.
- [182] V.M. Petrov, V. V Gagulin, *Inorg. Mater.* 37 (2001) 93–98.
- [183] S.J. Kuang, X.G. Tang, L.Y. Li, Y.P. Jiang, Q.X. Liu, *Scr. Mater.* 61 (2009) 68–71.
- [184] T.H. O’Dell, *Philos. Mag.* 7 (1962) 1653–1669.
- [185] J.P. Rivera, *Ferroelectrics* 161 (1994) 165–180.
- [186] C. Schmitz-Antoniak, D. Schmitz, P. Borisov, F.M.F. de Groot, S. Stienen, A. Warland, B. Krumme, R. Feyerherm, E. Dudzik, W. Kleemann, H. Wende, *Nat. Commun.* 4 (2013) 2051.
- [187] A. Manjeera, M. Vittal, V.R. Reddy, G. Prasad, G.S. Kumar, *Ferroelectrics* 519 (2017) 15–22.
- [188] M.T. Rahman, C. V Ramana, *J. Appl. Phys.* 116 (2014) 164108.
- [189] S. Chandarak, A. Ngamjarurojana, S. Srilomsak, P. Laoratanakul, S. Rujirawat, R. Yimnirun, *Ferroelectrics* 410 (2010) 75–81.
- [190] T. Kimura, Y. Yoshida, *J. Am. Ceram. Soc.* 89 (2006) 869–874.
- [191] D.C. Sinclair, A.R. West, *J. Appl. Phys.* 66 (1989) 3850–3856.
- [192] B.G. Toksha, S.E. Shirsath, M.L. Mane, S.M. Patange, S.S. Jadhav, K.M. Jadhav, *J. Phys. Chem. C* 115 (2011) 20905–20912.
- [193] C. Murugesan, G. Chandrasekaran, *RSC Adv.* 5 (2015) 73714–73725.
- [194] F. Ahmed, S. Kumar, N. Arshi, M.S. Anwar, B. Heun Koo, *Cryst. Eng. Comm.* 14 (2012) 4016.
- [195] A. Goldman, *Handbook of Modern Ferromagnetic Materials*, Springer US, Boston, MA, 1999.
- [196] R.K. Singh, S. Sanodia, N. Jain, R. Kumar, *AIP Conf. Proc.* 1953 (2018) 1–5.
- [197] S. Briceño, W. Brämer-Escamilla, P. Silva, G.E. Delgado, E. Plaza, J. Palacios, E. Cañizales, *J. Magn. Magn. Mater.* 324 (2012) 2926–2931.
- [198] X.H. Li, C.L. Xu, X.H. Han, L. Qiao, T. Wang, F.S. Li, *Nanoscale Res. Lett.* 5

- (2010) 1039–1044.
- [199] A.G.A. Darwish, Y. Badr, M. El Shaarawy, N.M.H. Shash, I.K. Battisha, J. Alloys Compd. 489 (2010) 451–455.
 - [200] P. Ganguly, A.K. Jha, K.L. Deori, Solid State Commun. 146 (2008) 472–477.
 - [201] E. Barsoukov, J.R. Macdonald, Impedance Spectroscopy, Wiley, New York, 2005.
 - [202] W. Li, R.W. Schwartz, Appl. Phys. Lett. 89 (2006) 242906.
 - [203] A. Avogadro, F. Tabak, M. Corti, F. Borsa, Phys. Rev. B 41 (1990) 6137–6144.
 - [204] M.F. Kotkata, F.A. Abdel-Wahab, H.M. Maksoud, J. Phys. D. Appl. Phys. 39 (2006) 2059–2066.
 - [205] R.K. Panda, R. Muduli, S.K. Kar, D. Behera, J. Alloys Compd. 615 (2014) 899–905.
 - [206] C.M. Kanamadi, B.K. Das, C.W. Kim, D.I. Kang, H.G. Cha, E.S. Ji, A.P. Jadhav, B.E. Jun, J.H. Jeong, B.C. Choi, B.K. Chougule, Y.S. Kang, Mater. Chem. Phys. 116 (2009) 6–10.
 - [207] J. Neumeier, J. Cohn, Phys. Rev. B - Condens. Matter Mater. Phys. 61 (2000) 14319–14322.
 - [208] S. Singhal, K. Chandra, J. Solid State Chem. 180 (2007) 296–300.
 - [209] A. Peláiz-Barranco, J.D.S. Guerra, O. García-Zaldívar, F. Calderón-Piñar, M.E. Mendoza, D.A. Hall, E.B. Araújo, Solid State Commun. 149 (2009) 1308–1311.
 - [210] H. Inaba, J. Mater. Sci. 32 (1997) 1867–1872.
 - [211] Z. Hu, M. Tian, B. Nysten, A.M. Jonas, Nat. Mater. 8 (2009) 62–67.
 - [212] T. Putzeys, M. Wübbenhorst, Phys. Chem. Chem. Phys. 17 (2015) 7767–7774.
 - [213] J. Nie, G. Xu, Y. Yang, C. Cheng, Mater. Chem. Phys. 115 (2009) 400–403.
 - [214] R.P. Mahajan, K.K. Patankar, M.B. Kothale, S.C. Chaudhari, V.L. Mathe, S.A. Patil, Pramana - J. Phys. 58 (2002) 1115–1124.
 - [215] A. Khamkongkao, P. Jantaratana, C. Sirisathitkul, T. Yamwong, S. Maensiri, Trans. Nonferrous Met. Soc. China 21 (2011) 2438–2442.
 - [216] M. Parishani, M. Nadafan, Z. Dehghani, R. Malekfar, G.H.H. Khorrami, 7 (2017) 3619–3623.
 - [217] N. Kasapoglu, B. Birs, Cent. Eur. J. Chem. 5 (2007) 570–580.
 - [218] A. Kumar, P. Sharma, D. Varshney, Ceram. Int. 40 (2014) 12855–12860.
 - [219] R. Debnath, S.K. Mandal, A. Nath, Mater. Lett. 237 (2019) 80–82.
 - [220] C.G. Koops, Phys. Rev. 83 (1951) 121–124.

- [221] G. Catalan, *Appl. Phys. Lett.* 88 (2006) 1–4.
- [222] R. Gao, Q. Zhang, Z. Xu, Z. Wang, C. Fu, G. Chen, X. Deng, X. Luo, Y. Qiu, W. Cai, *J. Mater. Sci. Mater. Electron.* 30 (2019) 10256–10273.
- [223] G.D. Dwivedi, K.F. Tseng, C.L. Chan, P. Shahi, J. Lourembam, B. Chatterjee, A.K. Ghosh, H.D. Yang, S. Chatterjee, *Phys. Rev. B - Condens. Matter Mater. Phys.* 82 (2010) 3–8.
- [224] M. Sufyan, S. Atiq, S.K. Abbas, M. Younis, *Mater. Lett.* 238 (2018) 10–12.
- [225] B. Yang, L. Jin, R. Wei, X. Tang, L. Hu, P. Tong, J. Yang, W. Song, J. Dai, X. Zhu, Y. Sun, S. Zhang, X. Wang, Z. Cheng, *Small* 3 (2019) 1903663.
- [226] M.S. Bernardo, T. Jardiel, M. Peiteado, A.C. Caballero, M. Villegas, *J. Eur. Ceram. Soc.* 31 (2011) 3047–3053.
- [227] N. Kumar, B. Narayan, S. Kumar, K.C. Verma, R. Ranjan, J. Shah, R.K. Kotnala, *Mater. Res. Express* 4 (2017) 095701.
- [228] H. Wang, S. Nie, H. Li, R. Ali, J. Fu, H. Xiong, J. Li, Z. Wu, W.M. Lau, N. Mahmood, R. Jia, Y. Liu, X. Jian, *ACS Sensors* 4 (2019) 2343–2350.
- [229] Y. Guo, X. Jian, L. Zhang, C. Mu, L. Yin, J. Xie, N. Mahmood, S. Dou, R. Che, L. Deng, *Chem. Eng. J.* 384 (2020) 123371.
- [230] X. Jian, W. Tian, J. Li, L. Deng, Z. Zhou, L. Zhang, H. Lu, L. Yin, N. Mahmood, *ACS Appl. Mater. Interfaces* 11 (2019) 15869–15880.
- [231] A.B. Swain, S. Dinesh Kumar, V. Subramanian, P. Murugavel, *Phys. Rev. Appl.* 13 (2020) 1.
- [232] Y. Li, S.D. Zhou, H. Wu, Y.G. Wang, F.G. Chen, *J. Alloys Compd.* 809 (2019) 151799.
- [233] S.T. Dadami, S. Matteppanavar, I. Shivaraja, S. Rayaprol, S.K. Deshpande, M. V. Murugendrappa, B. Angadi, *J. Alloys Compd.* 724 (2017) 787–798.
- [234] M. Lorenz, V. Lazenka, P. Schwinkendorf, F. Bern, M. Ziese, H. Modarresi, A. Volodin, M.J. Van Bael, K. Temst, A. Vantomme, M. Grundmann, *J. Phys. D. Appl. Phys.* 47 (2014) 135303.
- [235] S. Hohenberger, V. Lazenka, S. Selle, C. Patzig, K. Temst, M. Lorenz, *Phys. Status Solidi Basic Res.* 20 (2020) 1900613.
- [236] T.E. Quickel, L.T. Schelhas, R.A. Farrell, N. Petkov, V.H. Le, S.H. Tolbert, *Nat. Commun.* 6 (2015) 1–7.
- [237] R. shuai Han, L. qian Qi, X. Hou, L. hu Liu, H. yuan Liu, X.N. Xian, G.X. Guo, H. yuan Sun, *J. Magn. Magn. Mater.* 420 (2016) 117–121.

- [238] R. Pandey, L.K. Pradhan, S. Kumar, S. Supriya, R.K. Singh, M. Kar, *J. Appl. Phys.* 125 (2019) 244105.
- [239] R. Pandey, L. Kumar Pradhan, S. Kumari, M. Kumar Manglam, S. Kumar, M. Kar, *J. Magn. Magn. Mater.* 508 (2020) 166862.
- [240] R. Pandey, L.K. Pradhan, M. Kar, *J. Phys. Chem. Solids* 115 (2018) 42–48.
- [241] S. V. Baryshnikov, E. V. Charnaya, A.Y. Milinskii, A.A. Antonov, A.S. Bugaev, *Compos. Part B Eng.* 80 (2015) 15–19.
- [242] J.C. Maxwell, *Electricity and Magnetism*, Oxford University Press, London, 1993.
- [243] K.W. Wagner, *Ann. Phys. (N. Y.)* 40 (1973) 817–819.
- [244] D. Dhayanithi, M. Muneeswaran, N. V. Giridharan, *Ferroelectrics* 518 (2017) 103–108.
- [245] T. Wang, J. Hu, H. Yang, L. Jin, X. Wei, C. Li, F. Yan, Y. Lin, *J. Appl. Phys.* 121 (2017) 084103.
- [246] F. Yang, G. Le Dong, Y.L. Sui, S.Y. Ye, P. Li, C.G. Chen, X.X. Gao, Z.M. Guo, *Rare Met.* 38 (2019) 770–775.
- [247] M.R. Islam, M.S. Islam, M.A. Zubair, H.M. Usama, M.S. Azam, A. Sharif, *J. Alloys Compd.* 735 (2018) 2584–2596.
- [248] O.D. Jayakumar, S.N. Achary, K.G. Girija, A.K. Tyagi, C. Sudakar, G. Lawes, R. Naik, J. Nisar, X. Peng, R. Ahuja, *Appl. Phys. Lett.* 96 (2010) 2–5.
- [249] A. Mukherjee, S. Basu, P.K. Manna, S.M. Yusuf, M. Pal, *J. Mater. Chem. C* 2 (2014) 5885–5891.
- [250] S. Thakur, O.P. Pandey, K. Singh, *Phase Transitions* 87 (2014) 527–540.
- [251] M.K. Kim, J.Y. Moon, S.H. Oh, D.G. Oh, Y.J. Choi, N. Lee, *Sci. Rep.* 9 (2019) 1–10.
- [252] S. Saha, S. Chanda, A. Dutta, T.P. Sinha, *Mater. Res. Bull.* 48 (2013) 4917–4923.
- [253] S. Joseph, R.E. John, K. V. Saban, *Ceram. Int.* 45 (2019) 21249–21262.
- [254] T. Chakraborty, R. Yadav, S. Elizabeth, H.L. Bhat, *Phys. Chem. Chem. Phys.* 18 (2016) 5316–5323.

CURRICULUM VITAE

PERSONAL INFORMATION:	
Name:	S. SHANKAR SUBRAMANIAN
Father's Name:	K. S. NATHAN
Date of Birth:	05th June, 1989
Nationality:	Indian
Sex:	Male
Marital Status:	Married
Address for Communication:	S. Shankar Subramanian H. No. 70, Capital Apartment, Pocket-6 Nasirpur, Dwarka Sec-1A, New Delhi-110 045, INDIA. Mob. No.: +91-9540794900
E-mail Address:	shankar3274@gmail.com
ACADEMIC PERFORMANCE:	
<ul style="list-style-type: none"> ➤ 2011: Received Master of Science (M.Sc.) degree in Physics with 85% (First division) from Sri Sathya Sai Institute of Higher Learning, A.P. – 505034 India. ➤ 2009: Received Bachelor of Science in Honours (B.Sc Hon's) degree with 77% (First division) from Sri Sathya Sai Institute of Higher Learning, A.P. – 505034 India. ➤ 2006: 10+2 with 85% (absolute – First division) from CBSE Board, New Delhi, India. ➤ 2004: Matriculation (10th std.) with 77% (First division) from CBSE Board, New Delhi, India. 	
TEACHING EXPERIENCE (2013- 2020):	
Post Designation : Assistant Professor (Physics) Institute/University: Atma Ram Sanatan Dharma College, University of Delhi, Delhi, India. Teaching Tenure : Since 17 th August 2013 till date	
HONORS/AWARDS:	
Commendable Research Award received for publication of research work, <i>S. Shankar, O. P. Thakur and M. Jayasimhadri, "Conductivity behavior and impedance studies in BaTiO₃-CoFe₂O₄ magnetoelectric composites," Materials Chemistry and Physics 234 (2019) 110–121. (Impact Factor = 3.408) at 3rd Research Excellence Awards by Delhi Technological University on 13th March 2020.</i>	

SCI JOURNAL PUBLICATIONS:

1. **S. Shankar**, M. Kumar, V. Tuli, O. P. Thakur and M. Jayasimhadri, “Energy storage and magnetoelectric coupling in ferroelectric–ferrite composites” **Journal of Material Science: Materials in Electronics** 29 (2018) 18352–18357. (**Impact Factor: 2.22**)
2. **S. Shankar**, O. P. Thakur and M. Jayasimhadri, “Conductivity behavior and impedance studies in $\text{BaTiO}_3\text{--CoFe}_2\text{O}_4$ magnetoelectric composites,” **Materials Chemistry and Physics** 234 (2019) 110–121. (**Impact Factor: 3.408**)
3. **S. Shankar**, M. Kumar, A. K. Ghosh, O. P. Thakur and M. Jayasimhadri, “Anomalous ferroelectricity and strong magnetoelectric coupling in CoFe_2O_4 -ferroelectric composites,” **Journal of Alloys and Compounds** 779 (2019) 918-925. (**Impact Factor: 4.65**)
4. **S. Shankar**, O. P. Thakur and M. Jayasimhadri, “Impedance Spectroscopy and Conduction Behavior in $\text{CoFe}_2\text{O}_4\text{--BaTiO}_3$ Composites,” **Journal of Electronic Materials** 49 (2020) 472–484. (**Impact Factor: 1.774**)
5. **S. Shankar**, O.P. Thakur and M. Jayasimhadri, “Structural, multiferroic, and magnetoelectric properties of $(1-x)\text{Bi}_{0.85}\text{La}_{0.15}\text{FeO}_3\text{--}x\text{BaTiO}_3$ composite ceramics,” **Journal of Material Science: Materials in Electronics** 31 (2020) 12226–12237. (**Impact Factor: 2.22**)
6. **S. Shankar**, I. Maurya, Abhishek Raj, O. P. Thakur and M. Jayasimhadri, “Dielectric and tunable ferroelectric properties in $\text{BiFeO}_3\text{--BiCoO}_3\text{--BaTiO}_3$ ternary compound,” **Applied Physics A** 126 (2020) 686. (**Impact Factor: 1.81**)

PUBLICATIONS COMMUNICATED TO SCI JOURNAL:

1. **S. Shankar**, O. P. Thakur and M. Jayasimhadri, “Magnetodielectric effect, impedance and magnetoelectric coupling in multiferroics $(1-x)\text{Co}_{0.5}\text{Ni}_{0.5}\text{Fe}_2\text{O}_4\text{--}x\text{BaTiO}_3$ bulk composites ($x=0, 0.10, 0.20$)”, Communicated to **Journal of Electroceramics**. (**Impact Factor: 2.58**).
2. **S. Shankar**, O. P. Thakur and M. Jayasimhadri, “Discursive investigations on structural, dielectric and multiferroic properties of $(\text{NdMnO}_3)_{1-x}\text{--}(\text{BaTiO}_3)_x$ composites”, Communicated to **Journal of Alloys and Compounds**. (**Impact Factor: 4.65**).

NATIONAL & INTERNATIONAL CONFERENCES:

1. **S. Shankar**, O. P. Thakur and M. Jayasimhadri, “Enhanced dielectric and energy storage properties of spinel ferrite based composites”, International e-Conference on Advanced Functional Materials and Optoelectronic Devices (ICAFMOD-20), organized by Centre for Renewable Energy, Prof. Rajendra Singh (Rajju Bhaiya) Institute of Physical Sciences for Study and Research, Veer Bahadur Singh Purvanchal University, Jaunpur-222003, U. P., India on 13-15th June 2020.
2. Manish Kumar, **S. Shankar**, Vinita Tuli, Srishti Mittal, Aditya, Amit Singh, O. P. Thakur and M. Jayasimhadri, “Structural and Energy Storage Analysis in Dielectric - Ferrite System”, 3rd International Conference on Science & Engineering of Materials (ICSEM-2019), organized by Physics Department, School of Basic Sciences & Research, Sharda University, Gr. Noida-201310, U.P., India on 19-21st July 2019.
3. **S. Shankar**, O. P. Thakur, M. Jayasimhadri, “Tunable dielectric and energy storage studies in NdMnO₃ based composites”, National Conference on Functional Materials Emerging Technologies and Applications in Materials Science (NCFM-2020), organized by Physics Department, School of Basic Sciences & Research, Sharda University, Gr. Noida-201310, U.P., India on 25-26th July 2020.
4. **S. Shankar**, O. P. Thakur, M. Jayasimhadri, “Improved dielectric and ferroelectric properties of spinel ferrite-based Composites” National Conference on Functional Materials Emerging technologies and applications in materials science (NCFM-2020), organized by Physics Department, School of Basic Sciences & Research, Sharda University, Gr. Noida-201310, U.P., India on 25-26th July 2020.